

DISSERTATION ZUR ERLANGUNG DES  
DOKTORGRADES DER NATURWISSENSCHAFTEN  
VORGELEGT BEIM FACHBEREICH BIOCHEMIE, CHEMIE UND PHARMAZIE  
DER GOETHE UNIVERSITÄT IN FRANKFURT AM MAIN, DEUTSCHLAND (D30)

NEUROPEPTIDERGIC CONTROL OF SYNAPTIC  
VESICLE FILLING AND BEHAVIOR IN THE  
NEMATODE *Caenorhabditis elegans*

THESIS

BY

WAGNER STEUER COSTA

BORN ON THE 17TH OF MAY 1986 IN SÃO PAULO, SP, BRASIL

DECEMBER 22, 2016

SUPERVISOR:

PROF. DR. ALEXANDER GOTTSCHALK



Vom Fachbereich Biochemie, Chemie und Pharmazie der  
Goethe-Universität als Dissertation angenommen.

Dekan: Prof. Dr. Michael Karas

Gutachter Prof. Dr. Alexander Gottschalk  
Prod. Dr. Martin Grininger

Datum der Disputation:



# Contents

<b>I. Eidesstattliche Erklärung</b>	<b>XV</b>
I.1. Versicherung . . . . .	XV
<b>Abstract</b>	<b>XVII</b>
<b>Zusammenfassung</b>	<b>XX</b>
<b>1. Introduction</b>	<b>1</b>
1.1. Neurobiology . . . . .	2
1.1.1. Synaptic transmission . . . . .	2
1.1.1.1. Gap junctions . . . . .	3
1.1.1.2. Chemical synapses . . . . .	3
1.1.2. The chemical pre-synapse and the synaptic vesicle cycle . . . . .	4
1.1.2.1. Neurotransmitters and their loading into the SV . . . . .	4
1.1.2.2. SV release machinery and release modes . . . . .	7
1.1.2.3. SV endocytosis modes . . . . .	12
1.2. Neurobiological techniques . . . . .	13
1.2.1. Genetic determinants of expression . . . . .	13
1.2.2. Optogenetics . . . . .	14
1.2.2.1. Opsin based tools . . . . .	14
1.2.2.2. Optogenetic neuronal silencing . . . . .	16
1.2.2.3. BLUF domain based tools . . . . .	17
1.2.2.4. Genetically encoded calcium indicators . . . . .	20
1.2.2.5. Optogenetic driven cell ablation . . . . .	21
1.2.3. Further genetically encoded tools for neurotransmission analysis . . . . .	22
1.3. The model organism <i>Caenorhabditis elegans</i> . . . . .	23
1.3.1. Neuronal organization . . . . .	25
1.3.1.1. SV quantal size modulation in <i>C. elegans</i> . . . . .	27

1.3.1.2.	Neuromuscular junction and excitation-inhibition balance . . . . .	28
1.3.1.3.	The neuronal network for locomotion . . . . .	30
1.3.1.4.	The GABAergic interneuron RIS . . . . .	33
1.3.1.5.	Role of RIS in a sleep-like state in larvae . . . . .	35
1.4.	Objectives . . . . .	37
<b>2.</b>	<b>Materials and Methods</b>	<b>39</b>
2.1.	Materials . . . . .	39
2.1.1.	Reagents . . . . .	39
2.1.2.	Buffers and Media . . . . .	40
2.1.3.	Kits . . . . .	41
2.1.4.	Equipment . . . . .	42
2.1.5.	Enzymes . . . . .	43
2.1.5.0.1.	Restriction enzymes . . . . .	43
2.1.5.0.2.	Miscellaneous enzymes . . . . .	44
2.1.6.	Organisms . . . . .	44
2.1.7.	Transgenic <i>C. elegans</i> strains . . . . .	44
2.1.8.	Oligonucleotides . . . . .	48
2.1.9.	Plasmids . . . . .	52
2.1.10.	Miscellaneous Materials . . . . .	53
2.1.11.	Software . . . . .	54
2.2.	Methods . . . . .	55
2.2.1.	Molecular and Microbiological methods . . . . .	55
2.2.1.1.	Genomic DNA extraction from <i>C. elegans</i> . . . . .	55
2.2.1.1.1.	DNA extraction for Whole Genome Sequencing . . . . .	55
2.2.1.2.	Polymerase Chain Reaction . . . . .	56
2.2.1.2.1.	Primer design . . . . .	58
2.2.1.2.2.	Colony PCR of transgenic bacteria . . . . .	58
2.2.1.2.3.	RT-PCR . . . . .	58
2.2.1.3.	Site-directed mutagenesis . . . . .	59
2.2.1.4.	Gel electrophoresis . . . . .	59
2.2.1.5.	DNA gel extraction . . . . .	59
2.2.1.6.	DNA purification . . . . .	60
2.2.1.6.1.	PCA Extraction . . . . .	60
2.2.1.6.2.	PCR product purification . . . . .	60

2.2.1.7.	DNA restriction digest . . . . .	60
2.2.1.8.	Measurement of DNA concentration . . . . .	61
2.2.1.9.	DNA dephosphorylation . . . . .	61
2.2.1.10.	DNA fragment ligation . . . . .	61
2.2.1.11.	Heat shock transformation . . . . .	62
2.2.1.12.	Plasmid DNA preparation . . . . .	62
2.2.1.13.	Small region DNA sequencing . . . . .	63
2.2.2.	<i>C. elegans</i> handling . . . . .	63
2.2.2.1.	Cultivation . . . . .	63
2.2.2.1.1.	Male generation . . . . .	64
2.2.2.1.2.	Crosses . . . . .	64
2.2.2.1.3.	Genotyping . . . . .	64
2.2.2.1.4.	Decontamination . . . . .	64
2.2.2.2.	DNA micro injection in <i>C. elegans</i> . . . . .	65
2.2.2.2.1.	Injection mix . . . . .	65
2.2.2.2.2.	Injection . . . . .	65
2.2.2.3.	Extrachromosomal array integration by UV irradiation . . . . .	66
2.2.2.4.	EMS mutagenesis . . . . .	67
2.2.2.5.	<i>C. elegans</i> cell dissociation and culture . . . . .	67
2.2.2.6.	RNAi . . . . .	67
2.2.3.	Microscopy . . . . .	67
2.2.3.1.	Stereo microscopy . . . . .	67
2.2.3.2.	DIC microscopy . . . . .	67
2.2.3.3.	Qualitative analysis of fluorescence . . . . .	68
2.2.3.4.	Quantitative analysis of fluorescence . . . . .	68
2.2.4.	<i>C. elegans</i> behavior analysis . . . . .	69
2.2.4.1.	Analysis of swimming behavior . . . . .	69
2.2.4.2.	Multimodal Illumination Tracker . . . . .	69
2.2.4.3.	Multi Worm Tracker . . . . .	70
2.2.4.4.	Spot Tracker . . . . .	70
2.2.4.5.	Contraction assays . . . . .	70
2.2.4.5.1.	bPAC C1V1 co-expression experiment. . . . .	70
2.2.5.	Cholinergic survival upon sustained cAMP signaling induced by bPAC photostimulation . . . . .	71
2.2.6.	Miscellaneous methods . . . . .	71
2.2.6.1.	Light power measurement . . . . .	71

2.2.6.2.	Light wavelength measurement . . . . .	71
2.2.7.	Data analysis . . . . .	72
2.2.7.1.	Video pre-processing . . . . .	72
2.2.7.2.	Behavioral phenotype analysis by clustering . . . . .	72
2.2.7.3.	WGS Data analysis . . . . .	72
2.2.7.4.	RNA-Seq data analysis . . . . .	73
2.2.7.5.	Manual tagging of EM images and data analysis . . . . .	73
2.2.7.6.	3D reconstruction and analysis of synapses . . . . .	74
2.2.7.7.	Analysis of mPSC kinetic parameters . . . . .	74
2.2.8.	Statistical inference . . . . .	75
2.2.8.1.	Multiple testing correction . . . . .	77
2.2.8.2.	Effect size . . . . .	77
2.2.8.3.	Statistical analysis software . . . . .	77
<b>3.</b>	<b>Results</b>	<b>79</b>
3.1.	cAMP modulates cholinergic synaptic output . . . . .	79
3.1.1.	bPAC enhances neuronal output . . . . .	80
3.1.1.1.	Swimming bout frequency increase . . . . .	80
3.1.1.2.	Speed and body posture modulation on solid substrate . . . . .	81
3.1.1.2.1.	bPAC effect on body posture persists after light deactivation. . . . .	83
3.1.1.2.2.	bPAC photoactivation elicits a small body contraction. . . . .	83
3.1.1.2.3.	bPAC effect is not LITE-1 dependent. . . . .	84
3.1.1.2.4.	bPAC requires intrinsic depolarization for behavioral modulation. . . . .	85
3.1.1.2.5.	bPAC augments opsin mediated optogenetic depolarization of cholinergic neurons. . . . .	86
3.1.1.2.6.	Increased cAMP degradation impairs bPAC-induced effects . . . . .	87
3.1.1.3.	$G_{\alpha S}$ gain of function coupled to homeostatic adaptation not present in acutely induced bPAC effects . . . . .	88
3.1.1.4.	Enhancement of miniature postsynaptic currents amplitude upon bPAC photostimulation . . . . .	90



3.1.2.	bPAC induced effects require neuropeptidergic signaling at the presynapse . . . . .	91
3.1.2.1.	Muscle excitability is not changed upon bPAC photoactivation. . . . .	95
3.1.2.2.	mPSC kinetic parameters were not changed during bPAC photoactivation . . . . .	96
3.1.3.	bPAC photoactivation elicits ultrastructural changes at the presynapse . . . . .	97
3.1.3.1.	bPAC photostimulation leads to increased SV size . . . . .	102
3.1.3.2.	SV size increase observed during bPAC photostimulation is UNC-31 dependent . . . . .	104
3.1.3.3.	mPSC amplitude increase induced by bPAC is dependent on acute modulation of vAChT . . . . .	106
3.1.4.	Synapsin is required for cAMP mediated modulation of behavior	107
3.1.4.1.	Behavioral analysis of mutants for defective bPAC photostimulation response revealed synapsin involvement in signal transduction . . . . .	107
3.1.4.2.	Synapsin is required for neuropeptidergic signaling induced by bPAC photoactivation . . . . .	109
3.1.4.3.	Defective vesicle mobilization in synapsin mutant synapses	110
3.1.4.4.	Analysis of the SNN-1B(S9A) PKA phosphorylation site mutant . . . . .	116
3.1.4.5.	NLP-21 deficiency affected cAMP-induced behavior as observed in SNN-1B(S9A) animals . . . . .	117
3.1.5.	Brief conclusion . . . . .	119
3.2.	Characterization of the interneuron RIS . . . . .	119
3.2.1.	Single cell expression system . . . . .	119
3.2.1.1.	Cre/LoxP based expression system . . . . .	119
3.2.1.2.	Expression on a further cell in male animals . . . . .	121
3.2.2.	Acute RIS photoactivation induces locomotion pause behavior in adult animals . . . . .	122
3.2.2.1.	Transgenic animals cease swimming behavior . . . . .	122
3.2.2.2.	Motility inhibition on solid substrate . . . . .	123
3.2.2.3.	Body elongation during RIS depolarization . . . . .	125
3.2.2.4.	High light dosage additionally inhibited pharynx pumping . . . . .	126

3.2.2.5.	RIS induced phenotypes are bypassed by mechanosensory stimuli . . . . .	127
3.2.2.6.	No inhibition of behavior during RIS hyperpolarization	129
3.2.3.	Identification of signaling pathways within or involving RIS . .	129
3.2.3.1.	Canonical mutant analysis shows neuropeptidergic signal requirement . . . . .	129
3.2.3.2.	The LIM-6 transcription factor is required for RIS::ChR2 induced phenotypes in adult animals . . . . .	131
3.2.3.3.	Cell specific RNA sequencing revealed putative neuropeptides required for RIS function . . . . .	134
3.2.4.	Analysis of the intrinsic activity of RIS . . . . .	139
3.2.5.	bPAC photoactivation in RIS led to increased locomotion stop probability . . . . .	140
3.2.5.1.	No acute locomotion inhibition upon RIS::bPAC photostimulation . . . . .	141
3.2.5.2.	Probability of stop increased during RIS::bPAC photostimulation . . . . .	143
3.2.6.	Brief conclusion . . . . .	143
<b>4.</b>	<b>Discussion</b>	<b>145</b>
4.1.	Modulation of cholinergic neurons function by light-evoked activity of bPAC/cAMP generation . . . . .	145
4.1.1.	bPAC's low dark activity may still modulate behavior . . . . .	145
4.1.2.	A new model for cholinergic SV quantal size regulation . . . . .	146
4.1.3.	Possible role of Synapsin in neuropeptidergic signaling . . . . .	150
4.1.4.	bPAC as an enhancer of rhodopsin based optogenetic tools . . . . .	152
4.1.5.	bPAC long time photostimulation induced necrosis . . . . .	153
4.2.	Possible roles of RIS in the neuronal network of <i>C. elegans</i> . . . . .	154
4.2.1.	RIS activity correlates with locomotion stop . . . . .	155
4.2.2.	Serotonin reduced RIS activity, as monitored by calcium imaging	156
4.2.3.	RIS inhibition did not modulate behavior . . . . .	158
4.2.4.	Possible auto-regulatory mechanism of RIS inactivation . . . . .	159
4.2.5.	Possible RIS role in the neuronal network of <i>C. elegans</i> . . . . .	160
4.2.5.1.	Information input on RIS . . . . .	161
4.2.5.2.	Processing in RIS . . . . .	163
4.2.5.3.	RIS output and modulation of behavior . . . . .	163

4.2.6. Comparison of RIS to similar modules in neuronal networks of species . . . . .	164
<b>5. Outlook</b>	<b>167</b>
5.1. Auto regulatory, neuropeptidergic signaling in cholinergic motoneurons	167
5.2. Synapsin requirement for neuropeptidergic signaling . . . . .	168
5.3. RIS role in behavior regulation . . . . .	168
<b>Bibliography</b>	<b>171</b>
<b>List of Figures</b>	<b>213</b>
<b>List of Tables</b>	<b>215</b>
<b>Glossaries</b>	<b>216</b>
Acronyms . . . . .	221
Contributors . . . . .	224
<b>Appendix</b>	<b>225</b>
<b>A. Methods performed by colleagues</b>	<b>225</b>
A.1. CRISPR/Cas9 genomic mutation . . . . .	225
A.2. Electrophysiology of body wall muscle cells . . . . .	225
A.3. EPG Measurements . . . . .	227
A.4. HPF-EM . . . . .	227
A.5. RIS isolation and RNA-Seq . . . . .	228
<b>B. Software</b>	<b>229</b>
B.1. KNIME Workflows . . . . .	229
B.1.1. KNIME Multimodal illumination tracker data analysis . . . . .	229
B.1.1.0.1. Pseudo code . . . . .	232
B.1.1.0.2. Workflow scheme . . . . .	233
B.1.2. KNIME Contraction assay analysis . . . . .	237
B.1.2.0.3. Pseudo code . . . . .	237
B.1.2.0.4. Workflow scheme . . . . .	238
B.1.3. KNIME Choreography and MWT . . . . .	240
B.1.3.0.5. Pseudo code . . . . .	240

	B.1.3.0.6. Workflow scheme . . . . .	241
B.1.4.	KNIME Circos . . . . .	243
	B.1.4.0.7. Pseudo code . . . . .	243
	B.1.4.0.8. Workflow scheme . . . . .	244
B.1.5.	KNIME EM analysis . . . . .	247
	B.1.5.0.9. Pseudo code . . . . .	249
	B.1.5.0.10. Workflow scheme . . . . .	251
B.1.6.	KNIME Image pre-processing . . . . .	263
	B.1.6.0.11. Pseudo code . . . . .	263
	B.1.6.0.12. Workflow scheme . . . . .	264
B.1.7.	KNIME Analysis of pump frequency through kymographs . . .	267
	B.1.7.0.13. Pseudo code . . . . .	268
	B.1.7.0.14. Workflow scheme . . . . .	270
B.1.8.	KNIME synchronization and analysis of mPSCs . . . . .	277
	B.1.8.0.15. Pseudo code . . . . .	278
	B.1.8.0.16. Workflow scheme . . . . .	279
B.2.	R Scripts . . . . .	285
B.2.1.	EM ROI distance calculation . . . . .	285
	B.2.1.1. EM ROI linear distance . . . . .	285
	B.2.1.1.1. Pseudo code . . . . .	285
	B.2.1.2. EM ROI distance through plasma membrane . . . . .	287
	B.2.1.2.1. Pseudo code . . . . .	287
B.2.2.	Multimodal illumination tracker data visualization . . . . .	289
	B.2.2.0.2. Pseudo code . . . . .	289
B.2.3.	Behavioral data cluster analysis . . . . .	290
	B.2.3.0.3. Pseudo code . . . . .	291
B.2.4.	Synchronize mPSCs . . . . .	292
	B.2.4.0.4. Pseudo code . . . . .	292
B.2.5.	Fit mPSCs . . . . .	293
	B.2.5.0.5. Pseudo code . . . . .	293
B.3.	MatLab Scripts . . . . .	295
B.3.1.	Minis to Histogram . . . . .	295
	B.3.1.0.6. Pseudo code . . . . .	295
B.4.	ImageJ scripts . . . . .	296
B.4.1.	EM ROI quantification . . . . .	296
	B.4.1.0.7. Pseudo code . . . . .	297

B.5. Canon G9 and Arduino code . . . . .	299
B.5.1. Canon G9 code . . . . .	299
B.5.2. Arduino code . . . . .	299
<b>C. Plasmid Charts</b>	<b>300</b>
<b>D. Publications and personal involvement</b>	<b>312</b>
<b>Acknowledgments</b>	<b>313</b>



# I. Eidesstattliche Erklärung

Ich erkläre hiermit, dass ich mich bisher keiner Doktorprüfung im Mathematisch-Naturwissenschaftlichen Bereich unterzogen habe.

Frankfurt am Main, den

---

Wagner Steuer Costa

## I.1. Versicherung

Ich erkläre hiermit, dass ich die vorgelegte Dissertation über

NEUROPEPTIDERGIC CONTROL OF SYNAPTIC VESICLE FILLING AND BEHAVIOR IN THE NEMATODE *Caenorhabditis elegans*

selbständig angefertigt und mich anderer Hilfsmittel als der in ihr angegebenen nicht bedient habe, insbesondere, dass alle Entlehnungen aus anderen Schriften mit Angabe der betreffenden Schrift gekennzeichnet sind.

Ich versichere, die Grundsätze der guten wissenschaftlichen Praxis beachtet, und nicht die Hilfe einer kommerziellen Promotionsvermittlung in Anspruch genommen zu haben.

Frankfurt am Main, den

---

Wagner Steuer Costa





# Abstract

This thesis reports on the results obtained by expression photoactivatable adenylyl cyclase from *Beggiatoa spp.* (bPAC) in cholinergic neurons from *Caenorhabditis elegans* (*C. elegans*) and the characterization of the role of a single neuron, RIS, during locomotion in the adult animal.

Pharmacological activation of adenylyl cyclases through Forskolin is known to induce increased neuronal output in diverse model organisms through a protein kinase A (PKA) dependent mechanism. Nevertheless, pharmacological assays are not spatially restricted, do not allow for precise and acute activation nor to cessation of the signal. Thus, an optogenetic approach for was selected through the expression of photoactivatable adenylyl cyclase from *Beggiatoa spp.* (bPAC) in cholinergic neurons of *Caenorhabditis elegans* (*C. elegans*). This model organism was chosen due to its transparency, ease of maintenance, fast generation cycles as well as for being an eutelic animal. Further, its genome has been fully sequenced and the connectome of the neuronal network is known, thus allowing for precise analysis of neuronal function. Furthermore, the molecular mechanisms governing neuronal functions are well conserved up to primates. Mainly two optogenetical tools were applied, bPAC and the light gated cation channel channelrhodopsin 2 (ChR2).

Behavioral assays of bPAC photostimulation in cholinergic neurons recapitulated previous work performed with the photoactivatable adenylyl cyclase from *Euglena gracilis* (EuPAC $\alpha$ ), in which swimming frequency and speed on solid substrate were increased. Electrophysiological recordings of body wall muscle (BWM) cells by Dr. Jana F. Liewald showed that bPAC photoactivation led to an increase in miniature postsynaptic current (mPSC) rate and, in contrast to ChR2 invoked depolarization, also amplitude. Analysis of mutants deficient in neuropeptidergic signaling (UNC-31) via electrophysiology performed by Dr. Jana F. Liewald showed that the increase in mPSC amplitude due to bPAC photoactivation requires neuropeptide release. This was confirmed by co-expression of bPAC with the neuropeptide marker NLP-21::Venus and subsequent fluorescence analysis of release, exploiting the fact

that released neuropeptides are ultimately degraded by scavenger cells (coelomocytes). These were enriched with NLP-21::Venus after bPAC photostimulation, but no fluorescence could be observed in the UNC-31 mutants.

Additional analysis of the electrophysiological data performed by myself showed no modulation of mPSC kinetics due to neuropeptidergic release induced by bPAC. Hence, neuropeptide release and action sites were in the cholinergic neurons, the latter including cholinergic motoneurons.

Dr. Szi-chieh Yu provided electron microscopy images of high pressure frozen, bPAC or ChR2 expressing animals. These were tagged by myself for automatic analysis of ultrastructural properties of the cholinergic presynapse, also during photoactivation of both optogenetic tools. Photoactivation of both induced a reduction of synaptic vesicles, with ChR2 showing a more severe effect. In contrast to ChR2, though, bPAC also reduced the amount of dense core vesicles (DCV), the neuropeptide transporters. Additionally, long bPAC photoactivation as well as ChR2 photoactivation led to the appearance of large vesicles (LV), presumably in response to the increased SV fusion rate. bPAC photostimulation also induced an increase in SV size, not observed after ChR2 photostimulation. In UNC-31 mutants, bPAC photostimulation could not lead to the SV size increase, a further argument for the presynaptic effect of the released neuropeptide. Additional analysis of electrophysiology paired with pharmacology, performed by Dr. Jana F. Liewald, showed that mPSC amplitude increase requires the function of the vesicular acetylcholine transporter.

A further effect observed in the ultrastructure of bPAC photostimulated cholinergic presynapses was a shift in the distribution of SV regarding the dense projection. An analysis of cAMP pathway mutants showed that synapsin is required for bPAC induced behavior effects. Synapsin is known to mediate SV tethering to the cytoskeleton. Here, I show evidence for a new role of synapsin in controlling the availability of DCVs for fusion and thus, in neuropeptidergic signaling.

In the second part of my thesis I characterized the function of the GABAergic interneuron RIS in the neuronal network of *C. elegans*. RIS was shown to induce lethargus, a sleep-like state, during all larval molts, but its function in the adult animal was not yet described. Specific RIS expression of ChR2 achieved by a recombinase based system allowed to acutely depolarize the neuron during locomotion, which led to an acute behavioral stop. Diverse signal transduction pathway mutants were analyzed showing that the phenotype was induced by neuropeptidergic signaling. Through mutagenesis followed by whole genome sequencing data analysis as well as analysis

of RIS specific RNA sequencing data further narrowed the signal transduction pathway to mediate the locomotion stop behavior. Since the neuropeptide and, to some extent, the neuron are conserved across nematodes, an argument is outlined in favor of the conservation of this sleep-like state.

In addition, since ChR2 could induce neuropeptidergic signaling from RIS, secretion of vesicles is regulated by variable pathways depending on the neuronal identity. Nevertheless, expression of *bpAC* in RIS allowed to optogenetically increase the probability of short stops, as observed by expression of a calcium sensor (GCaMP) in RIS and analysis of its intrinsic activity in the adult animal.

# Zusammenfassung

Die hier vorliegende Arbeit charakterisiert die Verwendung einer lichtaktivierbaren Adenylylcyclase (englisch: photoactivatable adenylyl cyclase from *Beggiatoa* spp. (bPAC)) in cholinergischen Motoneuronen und die dadurch entstehende Steigerung des neuronalen Signals. Bei verschiedenen Organismen konnte bereits nachgewiesen werden, dass das Protein Kinase A (PKA) eine Steigerung der Neurotransmitterfreisetzung ermöglicht. PKA wird wiederum durch das Produkt von Adenylylcyclasen, das cyclische Adenosinmonophosphat (cAMP), aktiviert. Die pharmakologische Zugabe von Forskolin führt zur Stimulation der meisten Adenylylcyclasenklassen, somit auch von PKA und letztlich zu einer Steigerung der synaptischen Transmission. Pharmakologische Experimente in frei beweglichen Tieren stellen aus verschiedenen Gründen eine Herausforderung dar, dazu zählen, dass die akute Zugabe oft gepaart ist mit Verletzungen des Gewebes; eine Begrenzung des Pharmakons auf die zu untersuchenden Zellen oft nicht realisierbar ist und eine akute Inaktivierung des Pharmakons selten erfolgreich ist.

Deshalb wurde nach einer Möglichkeit gesucht, cAMP akut, nicht-invasiv, und zeitlich begrenzt in der zu untersuchenden Zellgruppe zu erhöhen. Diese Anforderungen werden durch Anwendung der Optogenetik erfüllt. Bei der Optogenetik werden im wesentlichen zwei Methoden angewandt. Das "Opto" stellt eine Referenz auf die Verwendung lichtaktivierbarer Proteine als Effektoren dar. Dazu zählen lichtgesteuerte Membrankanäle, beispielweise Channelrhodopsin 2 (ChR2), oder lichtaktivierbare Adenylylcyclasen, wie bPAC. "Genetik" bezeichnet die Referenz auf die verwendeten Methoden zur Expression des lichtaktivierbaren Proteins in den zu untersuchenden Zellen. Darüber hinaus existieren die Methoden zur Applikation von Lichtsignalen, durch die diese Proteine aktiviert werden können.

Die Untersuchung der präsynaptischen Prozesse die zur Steigerung des Signals nach PKA-Aktivierung führen, wurden in dem neuronalen Netzwerk des Nematoden *Caenorhabditis elegans* (*C. elegans*) durchgeführt. *C. elegans* ist ein etwa 1 mm langes, transparentes, eutelisches Tier, das einfach in der Handhabung ist und eine kur-

ze Generationszeit von etwa drei Tagen aufweist. Zusätzlich ist das Genom bereits komplett sequenziert und das Expressionsverhalten diverser Proteine charakterisiert. Ferner sind viele molekulare Prozesse konserviert bis hin zu denen der Primaten. Dadurch ist *C. elegans* ein idealer Modellorganismus, um mittels Optogenetik die basalen Prozesse zur Regulation neuronaler Signale zu untersuchen.

Zu Beginn der vorliegenden Arbeit wurde bPAC erst in alle cholinergen Neuronen exprimiert, um einen Vergleich mit bereits publizierten Ergebnissen herzuleiten, die mithilfe lichtaktivierbarer Adenylyl cyclase aus *Euglena gracilis* (EuPAC $\alpha$ ) erhalten worden waren. Diese Untersuchung der EuPAC $\alpha$  hat aufgezeigt, dass cAMP nicht nur die Rate der synaptischen Vesikel-Fusion beeinflusst, sondern auch deren Effekt in der neuromuskulären Endplatte potenziert. Da EuPAC $\alpha$  jedoch bereits im Dunkeln eine hohe Aktivität aufweist, hatte dies zur Folge, dass im Rahmen der vorliegenden Arbeit, diese Auswirkungen anhand eines anderen Effektorproteins untersucht werden sollten. Durch die Verwendung von bPAC konnte nachgewiesen werden, dass dieses die gleichen Verhaltenseffekte hervorruft, nämlich eine Steigerung der Schwimmfrequenz und der Bewegungsgeschwindigkeit auf festem Untergrund. Zusätzlich wurde eine zeitabhängige Komponente in der Bewegung auf festem Untergrund charakterisiert, nämlich die Steigerung der Biegungswinkel während der undulatorischen Fortbewegung von *C. elegans*.

Diese durch die bPAC-Photoaktivierung hervorgerufenen Effekte sind abhängig von dem intrinsischen neuronalen Muster, denn die Hyperpolarisation der cholinergischen Neuronen mittels der Protonenpumpe MAC führt zur Inhibition des Effekts durch bPAC. Desweiteren kommt es unter der Verwendung von bPAC nicht zu tetanischen Kontraktionen wie der Chr2-Depolarisation der cholinergischen Neuronen. Durch diese Erkenntnisse konnte ausgeschlossen werden, dass bPAC eine Depolarisation des Neurons hervorruft. Übereinstimmend mit diesen Ergebnissen ist die Potenzierung der Muskelkontraktion bei Co-Photoaktivierung von bPAC und die durch den Einsatz mittels grünem Licht aktivierbaren Opsin C1V1 im Vergleich zur Aktivierung von C1V1 alleine. Dadurch ist nachgewiesen, dass die Aktivierung von bPAC nicht auf den Depolarisationszustand des Neurons wirkt, sondern die Wahrscheinlichkeit der Freisetzung synaptischer Vesikel beeinflusst.

Elektrophysiologische Messungen von Dr. Jana F. Liewald bestätigten diese Erkenntnisse. Sie hat die Körperwandmuskeln von *C. elegans* mittels der Patch-Clamp-Technik untersucht. Ihre Messungen zeigen eine erhöhte Anzahl an miniatur-post-synaptischen Strömen (mPSC) während der Photoaktivierung von bPAC, welche eben-

falls durch die Chr2 induzierte neuronale Depolarisation zustande kommt. Im Gegensatz zu Chr2 werden durch die bPAC-Photoaktivierung auch die Amplituden der mPSCs erhöht. Beide Effekte stehen im Einklang mit den durch EuPAC $\alpha$  induzierten mPSC-Änderungen. Desweiteren konnte durch die Elektrophysiologie gezeigt werden, dass der durch bPAC induzierte Effekt von der Modulation der cholinergischen Präsynapsen und nicht von dem GABAergischen Signal abhängig ist. Dies ist notwendig, da in *C. elegans* die cholinergen Motoneuronen den inhibitorischen, GABAergischen Motoneuronen vorgeschaltet sind.

Um den Stoffwechselweg zu untersuchen und nachzuweisen, dass die bPAC-Photoaktivierung letztendlich zu erhöhten Amplituden in mPSC-Messungen führt, wurden verschiedene bekannte cAMP Signaltransduktionsproteinmutanten untersucht. Die Inhibition der Neuropeptidfreisetzung durch Mutation des Ca<sup>2+</sup>-abhängigen Sekretionsaktivatorproteins (in *C. elegans* UNC-31) führte zur partiellen Inhibition des durch bPAC induzierten Effekts. Dieses Ergebnis wurde durch elektrophysiologische Messungen von Dr. Jana F. Liewald bestätigt. Zusätzlich konnte sie zeigen, dass Neuropeptide für die erhöhten mPSC Amplituden verantwortlich sind.

Diese Erkenntnisse wurden durch ein Experiment mit einem fluoreszierenden Protein, das an ein in cholinergischen Motoneuronen exprimierendes Neuropeptid gekoppelt ist (NLP-21::Venus), bestätigt. Im *C. elegans* Pseudocoel sekretierte Neuropeptide werden durch spezialisierte Fresszellen (Coelomozyten) aufgenommen und zersetzt. Dadurch kann die Fluoreszenz von Coelomozyten als Indikator für die NLP-21::Venus Sekretion verwendet werden. Eine Photoaktivierung von bPAC führte zur Sekretion von NLP-21::Venus und erhöhte die Fluoreszenz von Coelomozyten, während eine Chr2-vermittelte Depolarisation cholinergischer Motoneuronen dies nicht erreichen konnte. Ferner konnte keine bPAC abhängige Coelomozyten Fluoreszenz in UNC-31 Mutanten ermittelt werden. Verschiedene pharmakologisch gestützte elektrophysiologische Messungen, durchgeführt von Dr. Jana F. Liewald, zeigten weiter, dass die von bPAC sekretierten Neuropeptide keinen Einfluss auf die Kinetik der postsynaptischen Rezeptoren in der Körperwandmuskulatur hatten.

Die elektrophysiologischen Messungen wurden herangezogen, um darüber hinaus zeigen zu können, dass die kinetischen Parameter der mPSCs nicht von der bPAC-Photoaktivierung beeinflusst worden sind.

Die Ergebnisse deuteten auf einen präsynaptischen Effekt hin. Um dies zu überprüfen, hat Dr. Szi-chieh Yu verschiedene Gruppen von bPAC und Chr2 exprimierenden Tieren mittels Hochdruck eingefroren und für die Elektronenmikroskopie vorberei-

tet. Die von ihr bereitgestellten Abbildungen cholinergischer Präsynapsen wurden von mir markiert und analysiert. Die Photoaktivierung beider optogenetischer Tools führte zur Verringerung der Anzahl der synaptischen Vesikel, wobei Chr2 einen stärkeren Effekt aufwies. Im Gegenzug dazu führte die alleinige Verwendung von bPAC zur Verringerung der Anzahl an Vesikeln mit dichtem Kern (englisch: dense core vesicle, DCV). Diese Vesikel sind verantwortlich für die Sekretion von Neuropeptiden, sodass die bisherigen Ergebnisse bestätigt werden konnte. Desweiteren wurden große, für Elektronen transparente Vesikel (englisch: large vesicle, LV) nach Photoaktivierung beider Tools gefunden, wobei bPAC diese erst nach langer Belichtungszeit erreicht hat. Dies ist womöglich darauf zurückzuführen, dass die von Chr2 bedingte Depolarisation zur massiven Ausschüttung synaptischer Vesikel geführt hat, während bPAC nur die Freisetzungswahrscheinlichkeit erhöht hat. Diese großen Vesikel sind wahrscheinlich auf den erhöhten Bedarf an synaptischer Vesikelendozytose zurückzuführen.

Ein weiterer Effekt der bPAC-Photoaktivierung ist die Vergrößerung der synaptischen Vesikel. Dies wurde weder in UNC-31 Mutanten noch nach einer Chr2 evozierten Depolarisation der cholinergen Motoneuronen gemessen. In Kombination zu den bisherigen Ergebnissen deutet dies auf einen autoregulatorischen Effekt in cholinergen Motoneuronen hin. Eine weitere pharmakologisch gestützte elektrophysiologische Messung, durchgeführt von Dr. Jana F. Liewald, zeigte, dass die mPSC Amplitudensteigerung von den vesikulären Acetylcholintransportern (vAChT) abhängig ist. Eine Blockierung der vAChT durch Vesamicol hatte keinen Einfluss auf die bPAC abhängige Steigerung der mPSC Rate, wohingegen deren Amplitudenerhöhung verhindert wurde.

Anhand der beschriebenen Experimente kann zwar nicht unterschieden werden, ob die Motoneuronen die Neuropeptide freisetzen oder ob diese aus einer anderen Gruppe cholinergischer Neuronen entstanden sind. Nichtsdestotrotz wird die Signaltransduktion vom Neuropeptid nicht über cAMP weitergeleitet, da ansonsten der bPAC-Photoaktivierungseffekt nicht von der DCV-Freisetzung und UNC-31 abhängig wäre. Desweiteren führt der Signaltransduktionsweg zur erhöhten Auffüllung synaptischer Vesikel mit Acetylcholin.

Zusätzlich konnte eine Veränderung der Position der im Zytoplasma befindlichen synaptischen Vesikel in Relation zum synaptischen Band (englisch: dense projection) nach unterschiedlichen bPAC-Photoaktivierungsdauern nachgewiesen werden. Dies deutet darauf hin, dass strukturelle Elemente an der cAMP-Signalweiterleitung be-

teilt sind. Deswegen wurden Synapsine, strukturelle präsynaptisch vorkommende Proteine, untersucht. Hierfür wurde erst eine Deletionsmutante des einzigen homologen *C. elegans* Gens untersucht (*snn-1*). In Verhaltensexperimenten sowie elektrophysiologischen Messungen von Dr. Jana F. Liewald ähnelten die Ergebnisse denen, die bei UNC-31 Mutanten erhalten wurden. Desweiteren konnte bPAC, gemessen an der Fluoreszenz der Coelomozyten, keine Neuropeptide freisetzen. Eine ultrastrukturelle Analyse der Präsynapse in Zusammenarbeit mit Dr. Szi-chieh Yu zeigte ebenfalls keine Reduktion der DCV nach einer bPAC-Photoaktivierung. Dazu wurde die Änderung der Positionierung der synaptischen Vesikel durch eine bPAC-Photoaktivierung gestört. Eine der beiden Synapsin-Isoformen in *C. elegans* beinhaltet ein konserviertes Serin, das von PKA phosphoryliert wird. Eine Mutante für diese Phosphorylierungsstelle zeigte während der Verhaltensexperimente einen ähnlichen Phänotyp zur zusätzlich getesteten NLP-21-Deletionsmutante. Beide Phänotypen unterscheiden sich aber von den Synapsin- und den UNC-31-Mutanten. Dies deutet darauf hin, dass Synapsin eine, zumindest in *C. elegans*, bisher unbekannte Rolle in der Freisetzung der Neuropeptide spielt.

Ein weiterer Teil dieser Arbeit befasst sich mit der Untersuchung eines GABAergen Interneurons, genannt RIS. RIS ist notwendig für die Reduktion der Bewegung während der vier Larvenzwischenphasen in der Entwicklung von *C. elegans*. Dieser schlafähnliche Zustand wird durch die Freisetzung von FLP-11 Neuropeptiden reguliert. Die Rolle von RIS im adulten neuronalen Netzwerk ist aber bisher unbekannt gewesen.

Im Rahmen dieser Arbeit wurde zunächst ChR2 spezifisch mittels einer Kombination zweier Transkriptionspromotoren und des Rekombinations-Systems Cre/loxP exprimiert. Die Photoaktivierung von ChR2 in RIS führte zum akuten Ausfall der Bewegung und der pharyngalen Pumpen. Dieses Phänomen wurde sowohl während des Schwimmens, als auch während der Bewegung auf festem Untergrund ermittelt. Zudem wurde dieser Effekt in Mutanten für den vesikulären GABA-Transporter gemessen und ist somit nicht durch GABA vermittelt. Daher ist zu vermuten, dass das Signal von RIS im adulten Tier ebenfalls durch Neuropeptide weitergeleitet wird. Anders als in cholinergen Neuronen aber, konnte eine Depolarisation von RIS mittels ChR2 ebenfalls eine neuropeptidogene Sekretion herbeiführen, was darauf hindeutet hat, dass die Regulation der DCV-Sekretion in verschiedenen Zellen unterschiedlich durchgeführt wird.

Aufgrund der Tatsache, dass lange Pausen in der Bewegung adulter Tiere unty-



pisch sind, stellte sich die Frage nach der intrinsischen Aktivierung von RIS. Eine weitere Möglichkeit der Optogenetik ist die Verfolgung intrazellulärer Calciumsignale durch Calciumsensoren als Stellvertreter für neuronale Aktivität. Als Reporter wurde GCaMP, ein cyclisch permutiertes, grün fluoreszierendes Protein (GFP) in Kombination mit einer M13-Helix aus Myosin-leichte-Kette sowie ein Calmodulinfragment, ausgewählt. Die Bindung von Calcium am Calmodulinfragment führt zur konformationellen Änderung und Rekonstitution des Fluorophors im GFP. Die Messungen mit GCaMP zeigten eine RIS-Aktivität in der Region des Nervenrings kurz bevor die Bewegung anhielt.

Um weiter die molekulare Signalkaskade zu charakterisieren wurde eine Mutagenese durchgeführt und dadurch neun unabhängige Mutationen erhalten. Eine dieser Mutationen wurde im Rahmen der vorliegenden Arbeit ausgewählt und durch Analyse der Sequenzierung des gesamten Genoms ausgewertet. Dadurch konnte eine Punktmutation in der DNA-Bindedomäne eines in RIS exprimierenden Transkriptionsfaktors charakterisiert werden, LIM-6. Dessen Mutation hat weder die Morphologie von RIS, noch die zellspezifische Expression darin gestört. Zusätzlich wurde eine RIS-Linie für die zellspezifische RNA-Sequenzierung erstellt. Diese Methode ergab eine Liste verschiedener Gene, die putativ an der Signalkaskade beteiligt und für die Funktion von RIS im adulten Tier notwendig sind.

bPAC wurde spezifisch in RIS exprimiert, da es sich um ein neuropeptiderges Neuron handelt. Dessen Photoaktivierung führte zu einer erhöhten Wahrscheinlichkeit eines kurzen Anhaltens der Bewegung während eines Verhaltensexperimentes auf festem Untergrund. Da FLP-11 in Nematoden konserviert ist und mit RIS vergleichbare Zellen in anderen Spezies ebenso zu finden sind, wurden Parallelen zur Bewegungskontrolle, genauer über deren Aufhebung, in Nematoden gezogen. Des Weiteren ist dieser schlafähnliche Zustand in anderen Organismen ebenfalls durch neuropeptidergene Neuronen reguliert. Der dazu zuständige molekulare Mechanismus ist weitgehend konserviert, bis hin zu Primaten.



# 1. Introduction

Animals move in order to sustain life, be it foraging for food, seeking a mate or escaping from predators. Thus, behavior is the output of the processing of information in an organism, a task mainly performed by neurons (figure 1.1).

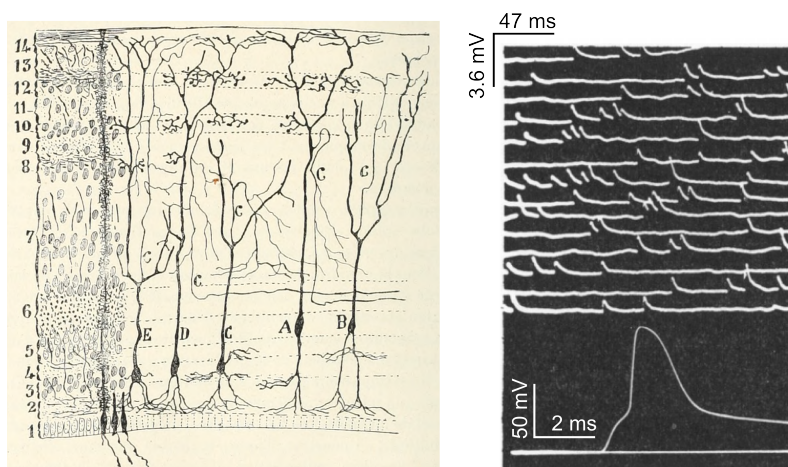


**Figure 1.1.: The legacy of Cajal and Katz.**

Santiago Ramón y Cajal's work led to the notion of the neuron as the information processing cell in an animal (left: optic lobe of chameleon, drawing of distinct neuronal morphologies). Bernard Katz first described the miniature post-synaptic potential, which defined the quantal nature of chemical neurotransmission (top right: muscle intracellular recording of spontaneous potential. Bottom right: evoked excitatory postsynaptic potential).

Figure left [1, p. 124], right adapted from [2].

Neurobiology was greatly influenced by the work of Santiago Ramón y Cajal and colleagues, who proved the neuron theory and provided insights into the variety of neuronal shapes encountered in animals [1]. Further outstanding work was performed by Bernard Katz and colleagues, who provided the experimental proof on the quantal nature of neurotransmission in the neuromuscular junction (NMJ) (figure 1.1) [2]. Both researchers were awarded the Nobel Prize in Physiology or Medicine

(1906, 1970, respectively). Albeit in the focus of research for over half a century, the exact mechanism by which neurons modulate their information output is not yet fully understood.

The work performed in the nematode *C. elegans* is reported in the following parts:<sup>1</sup>

1. An advance in the understanding of how cholinergic motoneurons regulate their output using the second messenger cyclic adenosine monophosphate (cAMP) (section 3.1, p. 79).
2. Characterization of the neuron RIS regarding its role in adult behavior (section 3.2, p. 119).
3. Description of the personal involvement on published projects performed during this thesis (section D, p. 312).

## 1.1. Neurobiology

Nervous systems are made of specialized cell types that process information from the environment and the organism itself to optimize behavior and find an adequate response to external stimuli. The term neuron was defined by Heinrich Wilhelm Gottfried von Waldeyer-Hartz, while working with Camillo Golgi and Santiago Ramón y Cajal [4]. Their neuron theory established the definition of the cell type ubiquitously required for information processing in the animal kingdom (figure 1.1 left [1, p. 124]). Neurons are found in all Eumetazoa [5], although neuronal cell markers are found across all Animalia [6]. Thus, fast inter-cellular communication is required to rapidly adapt to the environment. The conduction velocity of a voltage change varies from about  $1 \text{ mm s}^{-1}$  in sponges to about  $1 \text{ m s}^{-1}$  in Ctenophores and up to  $100 \text{ m s}^{-1}$  in mammalian nerves [7]. Nonetheless, transmission of information alone does not modulate behavior, information therefore must be evaluated.

### 1.1.1. Synaptic transmission

Information is conveyed between two neurons at synapses, of which two major types exist.

---

<sup>1</sup>Protein names are abbreviated with the nomenclature for mammalian and their *C. elegans* counterparts, as long as only one main gene is present in *C. elegans*. For example, protein kinase C (PKC) has four isoforms in *C. elegans*, TPA-1, PKC-1, PKC-2 and PKC-3, thus only the abbreviation PKC is used [3]

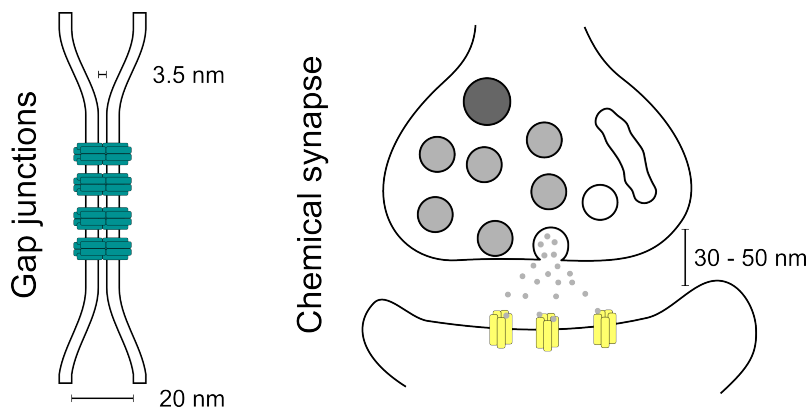


**Figure 1.2.: Synaptic transmission types.**

Two major synapse types exist. In gap junctions the plasma membrane of both interacting cells is bridged by proteins forming a pore. These synapses allow fast and reliable voltage step transmission in the  $\mu\text{s}$  range, as well as the exchange of small molecules (left). Chemical synapses, on the other hand use neurotransmitters to convey signals from the pre- to the post-synaptic side and transmit information in the range of ms (right).

Figure based on [8].

#### 1.1.1.1. Gap junctions

The first type is an electrical synapse, or gap junction (figure 1.2, left). Gap junctions are protein generated pores in the membrane of two cells that are aligned to connect the cytoplasm of both cells and thus allow transport of small molecules as well as reliable transmission of voltage steps between them; they are found in all animals [9]. Importantly, Gap junctions may act as rectifiers, allowing voltage steps only in one direction of the junction [10, 11]. This process might be mediated by a stomatin-like protein that effectively blocks the channel pore [12]. Of note, gap junctions have independent origins in vertebrates and nematodes [13].

#### 1.1.1.2. Chemical synapses

The second type is a chemical synapse (figure 1.2, right). These are specialized membrane domains in two neurons: the pre- and post-synapse, which are aligned to each other across the synaptic cleft. The pre-synapse releases small chemical molecules, neurotransmitters, that are recognized in the post-synapse by receptors, i.e. ligand gated ion channels, and “converted” into a voltage change [8]. Neurotransmitters are then either retrieved from or degraded in the synaptic cleft, hence terminating

transmission of information. Notably, retrograde signaling from the post- to the pre-synapse is possible, for instance through gaseous signaling molecules (nitric oxide (NO), [14]).

In contrast to classical chemical transmission, volume transmission does not rely on the juxtaposition of pre- and post-synapse. In volume transmission synapses, neurotransmitters are released into the extra-cellular space and diffuse to their sites of action [15, 16]. This modality is the slowest information transmission that can have delays of up to several min, compared to the delays of  $\mu\text{s}$  in Gap junctions and ms in chemical synapses [15].

Noteworthy, neuropeptidergic signaling resembles volume transmission, as their site of release must not be in vicinity to their site of action. In contrast to volume transmission though, neuropeptides may be released without a classical pre-synaptic specialization [17, 18]. However, neuropeptides may also be secreted in synapses as synaptic transmitters [19]. Neuropeptidergic signaling is therefore dependent on the neuronal subtype and the same organism might secrete different neuropeptides at distinct neuronal specializations.

### **1.1.2. The chemical pre-synapse and the synaptic vesicle cycle**

The pre-synapse machinery in a chemical synapse is optimized for the release of neurotransmitters upon depolarization as well as membrane retrieval after fusion. Synaptic vesicle (SV) precursors originate in the Golgi apparatus and are actively transported to the region where synapses are formed [20]. After initial fusion and membrane cargo delivery to the plasma membrane, a SV cycles through many exocytosis steps delivering neurotransmitters to the synaptic cleft [21, 22].

#### **1.1.2.1. Neurotransmitters and their loading into the SV**

A subset of neurotransmitters is well conserved in the animal kingdom. Acetylcholine (ACh) was the first characterized neurotransmitter [23] and is genetically prominent considering the conservation of the cholinergic gene locus (CGL) [24, 25]. This locus codes for the vesicular acetylcholine transporter (vAChT) and the choline acetyltransferase (ChAT/CHA-1), both required for cholinergic transmission. In addition, at least gamma-aminobutyric acid (GABA), glutamate and serotonin — all major neurotransmitters — are conserved signal molecules also in plants [26–28].

Most neurotransmitters are loaded into SVs by secondary active transporters driven

by the electrochemical gradient generated by vacuolar-type  $H^+$ -adenosine triphosphatase (v-ATPase) [8]. On average, SVs contain one copy of the v-ATPase [29]. The v-ATPase itself consists of two major sub-complexes: the membrane bound, proton transporting  $V_0$  and the cytosolic ATPase  $V_1$  (figure 1.3 left) [30,31]. Regulation of the assembly of both sub-complexes to a functional unit is dependent on the acidification state of the SV. Further, the assembled v-ATPase inhibits exocytosis of the SV [32]. Interestingly, blockage of the  $V_0$  complex with Bafilomycin A1 (Baf A1) leads to disruption of the v-ATPase and thus allows SV release without proper filling, likely due to Baf A1 blockage of the predicted proton binding sites in  $V_0$  [33]. This is not the case if the proton motive force is disrupted with Nigericin, a  $K^+$  ionophore (figure 1.3 right) [32,34]. The missing dissociation of both complexes leads to inhibition of SV release. A specific subunit of  $V_1$ , VHA-12, is required for exocytosis, since deletion mutants of the gene *vha-12* lead to increased SV protonation coupled with strongly reduced SV release in *C. elegans* [35].

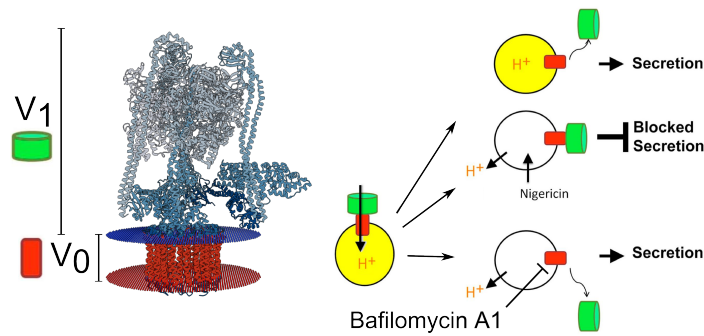


**Figure 1.3.: The v-ATPase control of SV loading and release.**

Two major sub-complexes of v-ATPase are described: the membrane bound, proton transporting  $V_0$  and the cytosolic ATPase  $V_1$  (left). SV release requires dissociation of these two components. Inhibition of the proton pump with Baf A1 allows exocytosis, while proton motive force disruption with Nigericin does not. Figure adapted from: left [31], right [36].

As described above, SVs are loaded by secondary active transporters and evidence argues for a model where an equilibrium state is achieved between electrochemical gradients and modulation of the transport itself. The latter for instance through increased transporter count per vesicle [37]. The equilibrium is further shifted by the possibility of SV swelling [37,38], wherefore the synaptic proteoglycan SV2A is required [39]. Further, GABAergic synapses of the chicken retina were shown to have variable SV quantal size that is not explained by the post-synaptic receptor proper-

ties but rather due to variable SV filling states [40]. Thus, SV quantal size is a crucial modulator of synaptic strength. SV filling may also be dependent on additional transporters present in the SV, i.e. the chloride-proton-antiporter family of proteins [41,42]. Further, transporters may switch from sym- to anti-porter configuration in response to changes in cytosolic chloride concentration, modulating equilibrium levels [43]. These determinants of SV loading may themselves be regulated, for instance through G protein-coupled receptor (GPCR) signaling pathways [44].

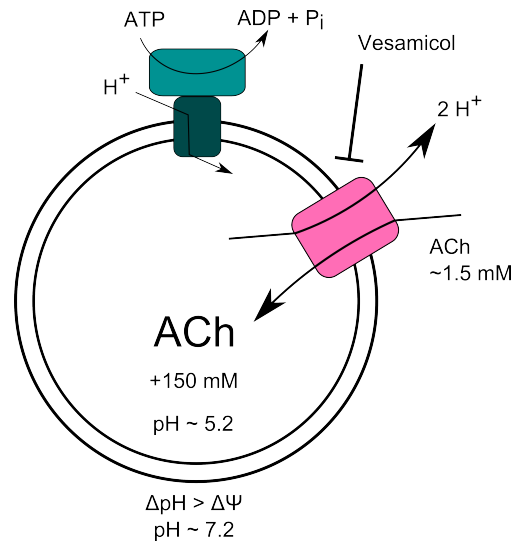


**Figure 1.4.: Neurotransmitter loading as exemplified for ACh.**

ACh is transported into SVs by the vAChT. vAChT itself is an antiporter that exchanges 2 H<sup>+</sup> for each ACh molecule. For function, the antiporter requires the proton motive force generated by the v-ATPase. A typical SV has about 200 proteins (not shown). The final ACh concentration ratio is similar to the H<sup>+</sup> concentration ratio achieved by the v-ATPase, that is, about 100 fold of the cytosolic concentration. In the median, one copy of v-ATPase and vAChT are present per SV (green and pink, respectively). The vAChT is blocked by vesamicol. Figure data from [29,45–49].

SV filling is described by the example of ACh transport into by vAChT. Two protons are exchanged for one ACh molecule [47]. The antiporter itself is rather slow ( $v_{\max}$  about 0.5 to 2 nmol min<sup>-1</sup> mg<sup>-1</sup> and  $K_M$  about 1 mM), although these low rates may be due to experimental setup or missing regulation otherwise present *in vivo* [45,48]. vAChT is allosterically inhibited by Vesamicol [45,50,51], and a single point mutation in the last cytoplasmic loop leads to insensitivity to the blocker [52]. Further, vAChT may be regulated by cystein S-nitrosylation, as this treatment led to re-



duced SV neurotransmitter content in an *ex vivo* nitrosylation model [52]. vAChT can be phosphorylated by PKC at the C-Terminus and this phosphorylation was shown to affect sorting of vAChT into large vesicles for transport and trafficking [53, 54]. Its transport and localization might also be regulated by C-terminal poly-Q sequences [49]. Noteworthy, neither the phosphorylation site preceding the conserved di-leucine motive, nor the poly-Q sequence are conserved in *C. elegans* [55].

In contrast to the aforementioned small neurotransmitters, neuropeptides are less conserved across species, but found in all animals [56]. They represent the category with the largest diversity and number of unique molecules among the neurotransmitters so far described [57].

Neuropeptides are unique in their biosynthesis, since they are derived from propeptides that are processed in dense core vesicles (DCVs). The latter originate from the Golgi apparatus in the cell soma and are actively transported to the site of release. Additionally, neuropeptides usually have a higher affinity to their cognate receptors than the remaining neurotransmitters [57].

It is important to note that distinct neurotransmitter transporters may co-exist in a single synapse, and since these might be modulated by different pathways, chemical neurotransmission allows for complex information integration [58]. Further, the action of a given neurotransmitter in the postsynaptic cell is defined by the receptor expressed therein. For instance, dopamine has two major types of receptors. D<sub>1</sub>-like family receptors are G<sub>S</sub> alpha subunit (G<sub>αS</sub>) coupled while D<sub>2</sub>-like family receptors are G<sub>I</sub> alpha subunit (G<sub>αI</sub>) coupled, inducing and inhibiting adenylyl cyclase activity, respectively [59]. It is this variability, among other mechanisms, that empowers a neuronal network to compute converging information: a neuron may signal to two downstream partners with differing expression patterns and thus these might ultimately respond with opposing voltage steps to the same pre-synaptic signal. In sum, a variety of pathways allows for tight control of SV filling state, hence modulating quantal size. Notwithstanding, for a given system, only a few aspects of the aforementioned regulatory pathways may be relevant.

#### 1.1.2.2. SV release machinery and release modes

SVs are categorized by their probability of release, defining specific SV pools (figure 1.5). The reserve pool contains SVs that do not partake in fusion events but rather act as a buffer of proteins required for the SV cycle [60]. This pool is segregated from the recycling pool by Synapsin / SNN-1 (SNN-1) [61,62]. The recycling pool contains

SVs that are scattered throughout the terminal, but highly mobile and releasable upon stimulation through tethering to the release machinery. Neuronal activity is required for SNN-1 detachment from the SVs to allow reserve pool maturing into recycling pool [63]. The last pool is the readily releasable pool (RRP), a class of SVs that are docked or primed at release sites and ready to fuse [64]. Only a small fraction of the SVs recycle *in vivo* [65]. The modulation of the relative populations between SV pools is achieved by diverse factors, i.a. presynaptic calcium influx [66], specific phospholipids [67] and free radicals [68].

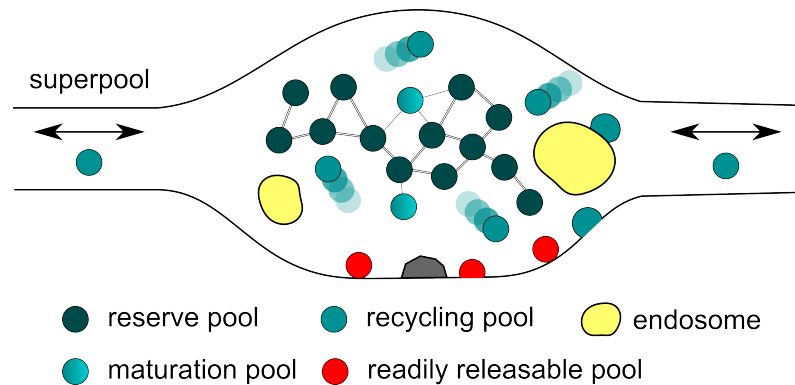


**Figure 1.5.: SV pools.**

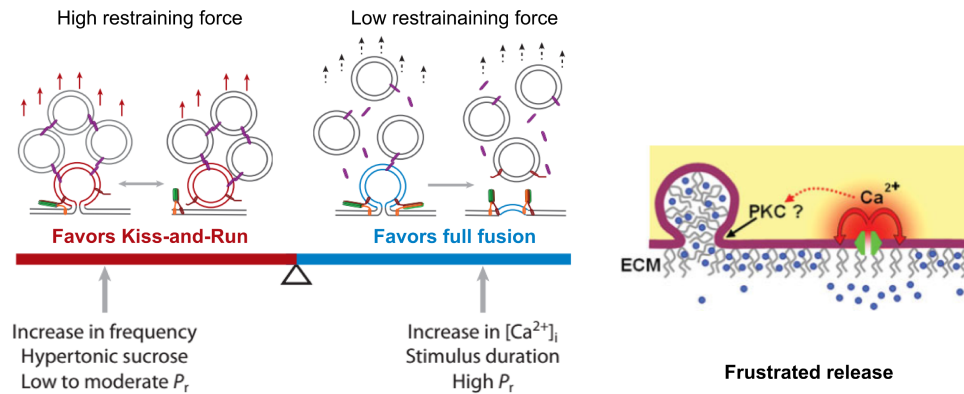
SVs are distributed in the synapse into three pools, defined by their probability of release. A specific SV switches pools depending on local circumstances. The total of SVs across synapses is further described as the super pool. Endosomes are an intermediate step in the recycling pool.

Figure adapted from [69].

The SV release machinery allows for distinct release mechanisms (figure 1.6). Complete fusion of SV membrane with the plasma membrane (PM) releases the full content of the vesicle into the synaptic cleft [70]. In cholinergic neurons and in presence of glycosylated SV2A protein, it is also possible that a full SV fusion to the PM leads to a frustrated release — ACh is coordinated by the keratan sulfate and only released upon a following depolarization of the membrane [71–73]. Further, the fusion event must not be a complete one, thus allowing for direct retrieval of the SV membrane for a further cycle; this event is called Kiss-and-Run model [74]. Hence, full fusion and Kiss-and-Run are dependent on the same release machinery and are differentiated only by the specific conditions during depolarization. For instance, high frequency neurotransmission, low stimulus duration and lower intra-cellular calcium concentrations promote Kiss-and-Run over full fusion events [74,75]. In contrast, frustrated

release requires supplementary components and is an additional regulatory mechanism for neurotransmission.

Apart from the required protein machinery discussed below, the SV cycle is significantly modulated by lipids and sterols [76]. Nevertheless, these will not be discussed in detail, as the primary targets of cAMP are proteins.



**Figure 1.6.: SV release modes.**

Fusion of SV with the plasma membrane leads to release of neurotransmitters. In the Kiss-and-Run model, the fusion pore is opened and neurotransmitter is released, but the SV is endocytosed before the full membrane fusion is performed (left). In the frustrated SV release model the SV is fully fused, but the neurotransmitter remains coordinated to the membrane by proteoglycans. A further depolarization is required to release neurotransmitter to the synaptic cleft (right). This mode requires additional components, while full fusion and Kiss-and-Run depend on the same set of release machinery, solely discerned by the distinct conditions during release.

Figures adapted from [73,75].

In common to these modes of transmitter release is the requirement of the SV fusion machinery (figure 1.7). The first step before fusion is vesicle docking and priming (figure 1.7 top left). Therefore, Rab3-interacting molecule (RIM/UNC-10) and RIM binding protein (RIM-BP/RIMB-1) tether calcium channels in the presynapse [77,78], in close proximity to SV plasma membrane tethering sites, a process regulated by SUMOylation [79]. The complex is attached to the SV protein Rab3 (Rab3/RAB-3) through mammalian unc13 (Munc13/UNC-13) [80], recruiting the SV to the RRP [81]. Munc13/UNC-13 has two variants, where the long version promotes fast SV release, while long and short versions mediate slow SV release. The spatial distribution of Munc13/UNC-13 favors the long version next to the dense projection (DP) [82]. In addition, slow release is inhibited by syntaxin-binding protein 5 /

Tomosyn (STXBP5/TOM-1), which itself is inhibited by protein kinase A (PKA/KIN-1) phosphorylation [83,84]. Further, syntaxin-binding protein 1 (STXBP1/UNC-18) interacts with syntaxin (STX1/UNC-64), displacing STXBP5/TOM-1 and promoting vesicle fusion [85].

The attained proximity of SV to the PM in combination to the stability of the STX1/-UNC-64 and STXBP1/UNC-18 complex enables the soluble NSF attachment protein receptor (SNARE)-complex to be formed [86]. The SNARE-complex is formed by three proteins, from which synaptobrevin (SNB-1) is located in the SV while the PM contributes with two proteins: STX1/UNC-64 and synaptosomal-associated protein 25 (SNAP-25/RIC-4). These three proteins create a tetra- $\alpha$ -Helix bundle with the latter contributing two  $\alpha$ -Helices [87]. PKA/KIN-1 phosphorylation of SNAP-25/RIC-4 modulates the probability of release by discerning between docked and primed vesicles [88–90]. The SNARE-complex interacts with Munc13/UNC-13 through STX1/-UNC-64 [91]. Further, the SNARE-complex is held in a “super-primed” state by complexin (CPLX1/CPX-1) binding, thus inhibiting spontaneous vesicle fusion [92]. Upon further increase of local calcium concentration, CPLX1/CPX-1 and synaptotagmin (SYT/SNT-1) bind calcium ions. The former releases the SNARE-complex while the latter promotes membrane fusion through electrostatic interaction [93,94]. CPLX1/CPX-1 is an additional PKA/KIN-1 target: Upon phosphorylation of the CPLX1/CPX-1 C terminus the probability of SV fusion is increased [95]. Furthermore, tension of the PM, propagated by the actin cytoskeleton is an additional force that promotes SV fusion [96].

SYT/SNT-1 itself does not contain a PKA/KIN-1 phosphorylation site [99]. Hence, PKA/KIN-1 induced release may be mediated by SYT/SNT-1 interactors, for example, cystein-string proteins (CSPs) [100–102] and Snapin [103]. Indeed, vesicle priming is disturbed in Snapin (Snapin/SNPN-1) mutants [104] and Snapin/SNPN-1 PKA/KIN-1 phosphorylation increases the probability of release [105]. In murine chromaffin cells, deletion of Snapin/SNPN-1 led to reduced vesicle release under low intracellular calcium concentrations as well as loss of synchronized release in murine neuronal cell culture [106].

The amount of SNARE-complexes required for vesicle fusion has been proposed to be between 3 to 15 [107–110], based on different *in vitro* assays and theoretical considerations. The variability observed in SNARE-complex numbers required for fusion might reflect the difference between a full fusion and a Kiss-and-Run event [75]; however, it may result from the fact that such studies are done *in vitro* reconstituted

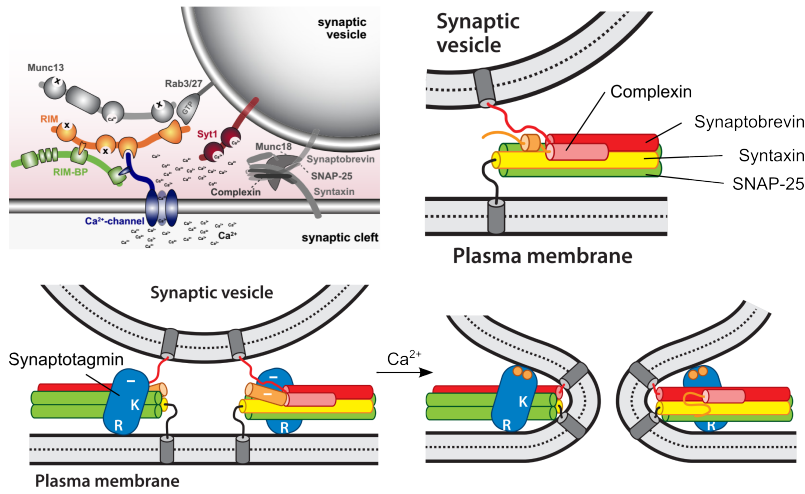


**Figure 1.7.: SV release machinery.**

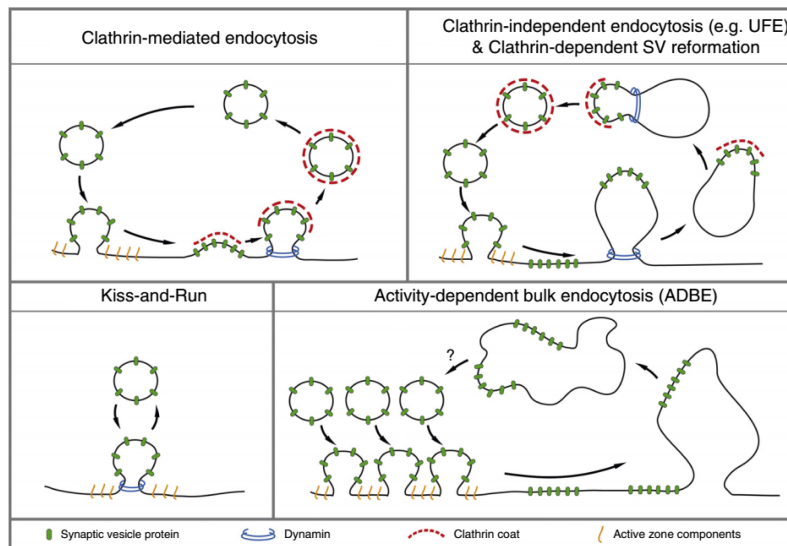
SV tethering to the vicinity of calcium channels is performed by RIM/UNC-10 and RIM-BP/RIMB-1 (top left). Both interact with Rab3/RAB-3 and Munc13/UNC-13, the later also interacts with the SNARE complex (not shown). The SNARE complex is formed by SNB-1, STX1/UNC-64 and SNAP-25/RIC-4 and fusion is inhibited by CPLX1/CPX-1 (top right). The SNARE complex is then bound by SYT/SNT-1. Upon further calcium addition, CPLX1/CPX-1 is displaced from the SNARE complex, allowing fusion.

Figure adapted from: top left [97], remaining [98].

systems, which can only partly reflect the *in vivo* situation. In fact, analysis of SNARE-complex *in vitro* proposed that a single complex is sufficient to create and stabilize a fusion pore [111,112]. Noteworthy, the studies used differing methods and cell types as membrane donors for their analysis, with lower SNARE-complex counts for the studies analyzing DCV release. This discrepancy might be due to a regulatory difference between these vesicle types. For instance, release of SVs and DCVs in *C. elegans* are regulated by different proteins (Munc13/UNC-13 and Ca<sup>2+</sup>-dependent activator protein for secretion / UNC-31 (CAPS/UNC-31), respectively) [18,113–115]. In mammalian cells, CAPS/UNC-31 is also required for neuropeptidergic signaling [116], a process regulated by SUMOylation, likely of SYT/SNT-1 [117]. Thus, these distinctions might be conserved and allow for co-transmission of neuropeptides with chemical neurotransmitters across species.

### 1.1.2.3. SV endocytosis modes

Once a vesicle is fused, the SNARE complex has to be dissociated. This is performed by the ATPase N-ethylmaleimide sensitive factor / NSF-1 (NSF) and the adaptor protein a soluble NSF attachment protein / SNAP-1 (a-SNAP) [118, 119]. NSF is recruited to the SNARE complex by a-SNAP and dissociates the core complex. The SNARE complex is likely dissociated before SV membrane retrieval [120]. The SV membrane is retrieved through different processes, with all modes requiring dynamin, a GTPase mediating membrane constriction and fission [121–124]. Endocytosis is possibly also dependent on SYT/SNT-1, as has been described for *Drosophila melanogaster* (*D. melanogaster*) [125]. The mechanism by which the membrane is retrieved is dependent on the stimulus that led to release, e.g. the local calcium concentration and subsequent depolarization.



**Figure 1.8.: SV endocytosis modes.**

Clathrin mediated endocytosis directly at the PM (top left) or in an early endosome, after bulk endocytosis, e.g. in ultrafast endocytosis (top right). Clathrin independent pathways also occur. In a Kiss-and-Run cycle the fusion pore is only transiently opened and, before full fusion occurs, the SV is detached by dynamin (lower left). Further, SVs may be retrieved from endosomes without clathrin. Figure adapted from [126].

Full fusion events require that the whole membrane is retrieved, a process mediated mainly by bulk endocytosis. Bulk endocytosis is dependent on dynamin and

actin cytoskeleton that generates PM invaginations and early endosomes. Ultrafast endocytosis is further dependent on clathrin to reform the SV from the endosomal structures, it operates in the range of 50 ms to 100 ms [127–130]. In addition, SVs may form from endosomal structures without the requirement for clathrin but for calcium efflux from the endosome and calcineurin activity [131, 132].

SV recovery by clathrin from endosomal structures as well as the less common clathrin mediated endocytosis require early factors like intersectins. These recruit clathrin adapter proteins, for instance AP180 / UNC-11 (AP180), to form a clathrin coated pit. Mutations of AP180 may result in enlarged SVs [133]. The fully coated vesicle is fissioned from the PM by dynamin, that itself is recruited by endophilins, amphiphysins and synaptojanins. The process is dependent on phosphatidylinositol 4,5-bisphosphate [134]. Although clathrin mediated endocytosis is slow, in the range of 3 s to 30 s [134], there specialized synapses in retinal bipolar cells with clathrin primed SVs that allow for an order of magnitude faster endocytosis [135].

Kiss-and-Run vesicles have their pore closed by dynamin and may change in size [75]. The endocytic process does not require clathrin [134] and is fast, in the range of 400 ms to 900 ms [136, 137].

## 1.2. Neurobiological techniques

A plethora of techniques are applied in neuroscience that contribute to the body of knowledge attained so far. A subset of these were used during this work and are introduced in this section, while methods performed by colleagues are described in the appendix section A, p. 225.

### 1.2.1. Genetic determinants of expression

Genetic targeting of proteins of interest must be regulated by specific promoters. First, promoters are characterized for their cell specificity by expression of fluorescent proteins and analysis of their expression pattern [138, 139]. If no promoter is specific for the neuron(s) in question, a combination of two promoters that co-express in the cell(s) of interest can drive cell specific expression through a recombinase based system [140, 141]. The Cre/LoxP recombination system was used during this thesis for cell specific expression in the neuron RIS (results section 3.2.1.1, p. 119).

In *C. elegans*, transgenesis may generate extrachromosomal arrays with an unde-

fixed number of copies of the gene in question [142]. If required, expression can be regulated by copy number restriction [143] and also by inducible promoters [144]. Stability of the transgene over generations may be achieved by integration into the genome [143,145,146].

### 1.2.2. Optogenetics

Optogenetics describes methods that use genetic approaches described above to express light modulated proteins in the target cell, therefore allowing for a spatiotemporal control of its function.

First approaches to achieve light-control of neurons were based on caged chemical compounds that could be released upon photostimulation. Thus, expression of otherwise not represented receptors allows for optical neuronal control [147]. The limitation of such approaches is the requirement for caged compound delivery, often by an invasive method. An advantage is the use of chemically linked photoswitches to engineered receptors [148, 149]. An additional development is the use of non-tethered photoswitches that are specific for a set of receptors [150]. Further, photoswitches were implemented into diacylglycerols, allowing for Munc13/UNC-13 mediated synaptic modulation in *C. elegans* [151]. Nonetheless, these methods require addition of complex chemicals and are thus not easily modifiable and, if not genetically targeted, broadly active.

Optogenetics as defined above started with the characterization of two genes in *Chlamydomonas reinhardtii* (*C. reinhardtii*) [152–155], named channelrhodopsin 1 (ChR1) and channelrhodopsin 2 (ChR2), followed by the first application *in vivo* in mechanosensory neurons and body wall muscle (BWM) from *C. elegans* [156].

#### 1.2.2.1. Opsin based tools

Channelrhodopsin-like optogenetic tools are based on the light-gated ion channel ChR2. ChR2 is a seven-transmembrane protein that requires the co-factor all-trans-retinal (ATR) for function [153]. Upon blue light illumination, ATR photoisomerization is induced and the channel is opened (figure 1.9 right) [157, 158]. Importantly the green light absorbance in the open state can lead to faster channel closure. Hence, multiple variations of ChR2 were generated that modified the photocycle by stabilizing intermediate states or changing the ion pore selectivity. The opsin variants applied throughout this thesis are summarized in table 1.1.



Noteworthy are the following three ChR2 variants. First, the gain of function mutation ChR2(H134R) with improved expression in *C. elegans* [156]. Second, the step function opsin ChR2(C128S) and its variants, with significantly increased closing times, thus remaining open after light application [159]. These variants can be turned off by yellow light photoactivation (figure 1.9 photocycle). Third, the chloride channel iC1C2 and its step function variant SwiChR, based on the structure of C1C2 [160,161].

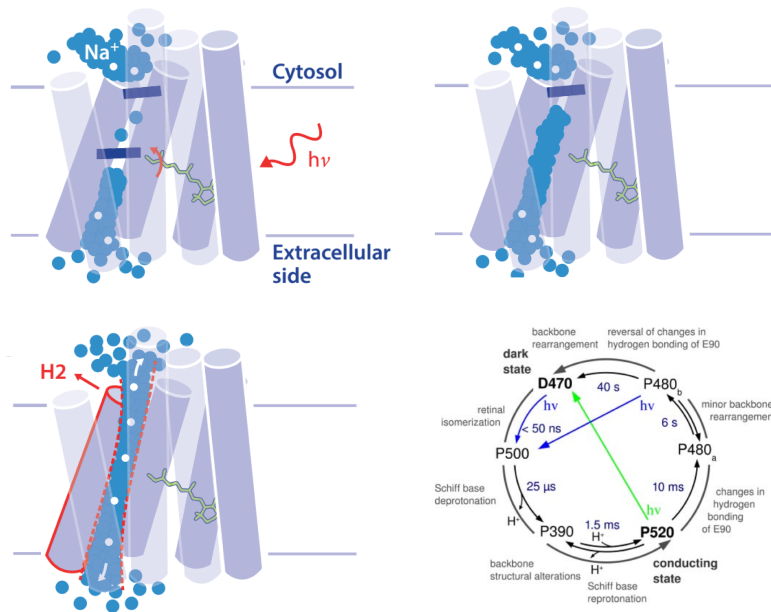


**Figure 1.9.: Suggested mechanism of ChR2 pore formation and the ChR2 photocycle.**

Photon absorption by ATR leads to its isomerization (top left). The outward directed barrier is opened (top right) and  $\alpha$ -Helix 2 is displaced, opening the inward directed barrier (bottom left). ChR2 photocycle with  $\tau$  values for the transitions at pH = 6. Blue light photoactivation leads to opening of the channel pore. Green light absorbance can lead to faster channel closure (bottom right). Figure adapted from [162], left. [158], right.

Other algae express homologs of ChR2 [163–167], for example *Volvox carteri* with the opsins VChR1 and VChR2. Although VChR1 has lower photocurrents than ChR2, a chimera composed of ChR1 and VChR1 with designed point mutations (C1V1-ETET) is capable of photoactivating neurons with green excitation light [168]. This allowed for concomitant expression of two optogenetic tools that could be separately activated by their excitation wavelength, thus allowing bimodal photoactivation

of neuronal subpopulations in *C. elegans* [169].

A screen performed by Klapoetke and colleagues found four new channelrhodopsins with increased photocurrents compared to either ChR2 or C1V1 with blue or green photoactivation, respectively: *Stigeoclonium helveticum* ShChR (Chronos), *Chlamydomonas noctigama* CnChR1 (Chrimson), *Chloromonas oogama* CoChR and *Chloromonas subdivisa* CsChR [166]. Furthermore, they reported the first channelrhodopsin with peak excitation at yellow wavelengths, *Chlamydomonas noctigama* CnChR1. CoChR and Chrimson were concomitantly expressed in distinct neuronal subgroups of *C. elegans*, also allowing bimodal photoactivation with the added benefit of lower photoactivation light intensities due to the intrinsic properties of the channelrhodopsins [170].

#### 1.2.2.2. Optogenetic neuronal silencing

Apart from iC1C2 and its derivatives described above, additional opsins are available that drive neuronal silencing or hyperpolarization upon photostimulation.

The halorhodopsin from *Natronomonas pharaonis* NpHR is an inward light-driven chloride pump [171]. The structural similarity to ChR2 suggested that it could be used as a neuronal hyperpolarizer, which was shown by Feng Zhang and colleagues in mammalian cell culture and *C. elegans* neurons [172]. Since NpHR has a peak absorbance in yellow wavelengths, this tool was effectively used in combination to ChR2.

A further hyperpolarizer type is the proton pumping bacteriorhodopsin: the blue-green light activatable pump from *Leptosphaeria maculans* Mac and the yellow light activatable pumps *Halorubrum sodomense* Arch and *Halorubrum* strain TP009 ArchT [173–175]. From these, Mac was the first successfully applied tool in combination with ChR2 in *C. elegans* to modulate behavior [176], albeit Mac efficiency for long time neuronal hyperpolarization in *C. elegans* is not matching that of Arch [177]. Arch and NpHR are similarly effective in *C. elegans*, with Arch requiring slightly less light power [177, 178]. In contrast, Mac has a broader activation spectrum in *C. elegans*, with some activation also in blue wavelengths [177].

It is important to note that selection of a hyperpolarizing optogenetic tool must take the neuronal network in consideration. On the one hand, NpHR will modulate the effect of GABA receptors due to the reduced chloride electrochemical gradient on the membrane, up to reversal potential [179]. On the other hand, bacteriorhodopsins may alkalize the pre-synaptic cytosol through the export of H<sup>+</sup>. The resulting  $\delta\text{pH}$  is

sufficient to trigger calcium influx and thus synaptic vesicle release [180], a process likely depended on pre-synaptic N-methyl-D-aspartate (NMDA) receptors [181].

A recent option to the above mentioned tools is BLINK1, an engineered blue light activatable potassium channel. In addition, BLINK1 is saturated with below 1 % of the light dosage required for the activity of NpHR [182]. Nonetheless, the blue light activation of BLINK1 does neither allow concomitant expression with ChR2, nor with bPAC.

The subsequent table summarizes the opsins and their variants applied in the studies leading to this thesis (table 1.1).

**Table 1.1.:** Opsins and their variants for optogenetics

<b>Name or variant</b>	<b>Description</b>
ChR2(H134R)	Expression of the ATR-bound protein in <i>C. elegans</i> improved and higher Na <sup>+</sup> conductance [156, 169, 183].
ChR2(C128S)	Step-function rhodopsin, inactivation with yellow light [159].
ChR2(C128S;H134R)	Step-function rhodopsin with expected improved expression in <i>C. elegans</i> .
ChR2(L132C) (CatCh)	Increased photocurrents, Mg <sup>2+</sup> and Ca <sup>2+</sup> conductance [184].
ChR2(T159C)	Higher affinity to ATR, increased photocurrents, reduced degradation [185, 186].
C1V1(E122T;E162T)	Green light activated opsin [168].
NpHR	Yellow light activated chloride pump [171, 172].
Mac	Blue-green light activated proton pump [173].
Arch	Yellow light activated proton pump [174].

### 1.2.2.3. BLUF domain based tools

The sensors of blue-light using FAD (BLUF) type of photoreceptors have a non-covalently bound flavin adenine dinucleotide (FAD) [187] and are mainly found in prokaryotes, with the exception of *Euglena gracilis* (*E. gracilis*) [188, 189]. The domain structure was determined in a few proteins [190–192] and molecular modeling predicted an unusual property of the BLUF domain photocycle, namely, a glutamine tautomerisation upon photoactivation [193]. Indeed, a recent study by Domratcheva and colleagues confirmed the tautomerisation process in BLUF domains (figure 1.10 top) [194]. This process leads to kinetic energy transfer through the conserved tyrosine and the FAD to the effector domain linked to the photoreceptor domain (figure 1.10 bottom left) [193]. In addition to both aforementioned residues, a trypto-

phane is highly conserved, mutation thereof either leading to higher photoactivation wavelengths or the inability to transduce the absorbed energy into  $\beta$ -sheet displacement [195,196].

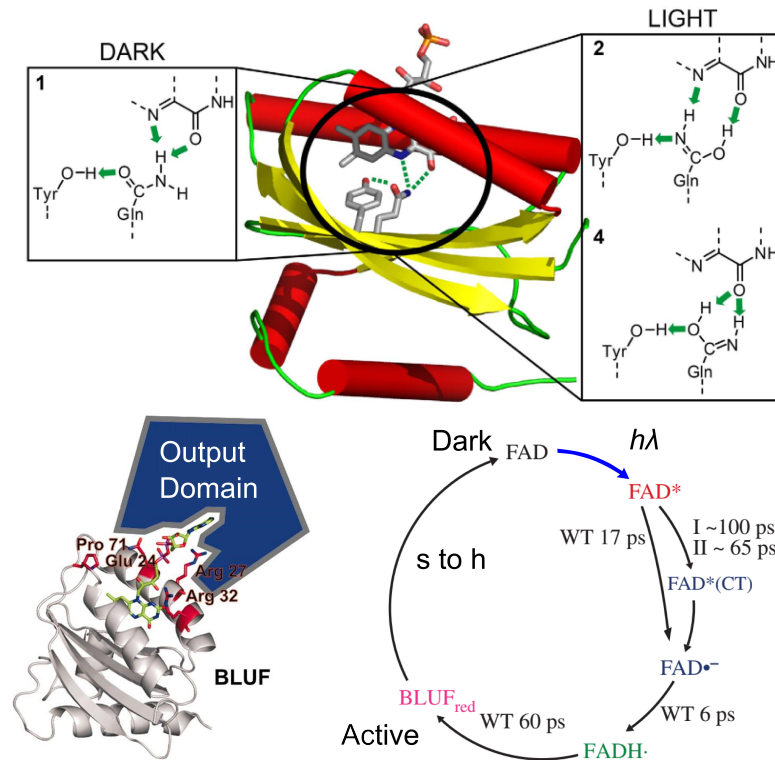


**Figure 1.10.: BLUF domain light induced tautomerization and signal transduction.**

Upon illumination, the FAD co-factor absorbs the photon and induces a tautomerisation of a conserved glutamine residue (top). The adjacent tyrosine modulates the  $\beta$ -sheet structure of the domain, relaying the energy to the effector domain (bottom left). The photocycle of the domain has a sub-ns proton transfer and a protein dependent relaxation constant (bottom right).

Figures adapted from top [194], bottom left [191], bottom right [197].

The relaxation of BLUF domains does not involve photon absorbance and is highly dependent on the specific structure in question. It is proposed that relaxation from light to dark state is dependent on a proton transfer from the tyrosine to the glutamine, leading to the enol form of glutamine and reversal of the tautomerisation [198]. Although photoactivation is performed in the sub ns range, relaxation varies from a few s to h and may be determined by amino acids outside of the FAD binding

pocket (figure 1.10 bottom right) [199].

The modular aspect of the BLUF domain evolved to modulate the activity of diverse proteins, ranging from adenylyl cyclases; cyclic GMP and cyclic-di-GMP sensors; putative amino acid sensors to further photoreceptors. From these, the BLUF-activated photoactivatable adenylyl cyclase  $\alpha$  from *E. gracilis* (EuPAC $\alpha$ ) and EuPAC $\beta$  were of particular interest, since these could be used as optogenetic tools [187]. EuPACs have the structure BLUF-cyclase-BLUF-cyclase (figure 1.11 inset), while a heterotetramer of ePAC $\alpha_2\beta_2$  is formed in *E. gracilis* [200]. Expression of the isolated monomers led to functional ePACs in *Xenopus laevis* (*X. laevis*) oocytes, with EuPAC $\alpha$  showing a 100-fold adenylyl cyclase activity increase in comparison to EuPAC $\beta$  [201]. The time constants for maximal cAMP concentration during photoactivation as well as decay time after light was turned off were later measured to be about 250 ms and 2 s, respectively [202]. EuPAC $\alpha$  was thus selected as an optogenetic tool to modulate cAMP in mammalian cell culture, *Aplysia*, *D. melanogaster* and *C. elegans* [201, 203, 204]. Photoactivation of EuPAC $\alpha$  in *C. elegans* cholinergic motoneurons led to augmented behavioral output, in line with  $G_{\alpha S}$  gain of function mutations (figure 1.11 left) [204, 205]. However, EuPAC $\alpha$  adenylyl cyclase is also active in the dark state, increasing the cAMP concentration in *X. laevis* oocytes by about 20-fold, while blue light stimulation further increased it by ten-fold [201]. Indeed, this dark activity of EuPAC $\alpha$  might have induced compensatory adaptation to the high basal cAMP concentration in *C. elegans*, as transgenic animals had reduced motility before photoactivation and effect strength was positively correlated with EuPAC $\alpha$  expression level [204]. Importantly BWM electrophysiological analysis of miniature post synaptic current (mPSC), representing the quantal content of a SV fusion event, was increased during EuPAC $\alpha$  photoactivation in *C. elegans* [204], an effect not present during ChR2 mediated cholinergic neuron depolarization [206].

Hence, a light activatable adenylyl cyclase with reduced dark activity was desired for further analysis of the mechanism leading to the increased quantal size observed. The later described bPAC has a single BLUF domain followed by an adenylyl cyclase domain [202, 207]. bPAC has a lower dark activity compared to EuPAC $\alpha$ . Treatment with 3-isobutyl-1-methylxanthine (IBMX), a phosphodiesterase inhibitor, did not lead to increased cAMP concentration due to bPAC in the dark state. This was not the case for EuPAC $\alpha$ , where IBMX treatment during dark state increased cAMP concentration. In contrast to EuPAC $\alpha$ , bPAC has increased on-set and decay time constants, about 750 ms and 20 s, respectively [202]. Nonetheless, due to the minimal dark activity

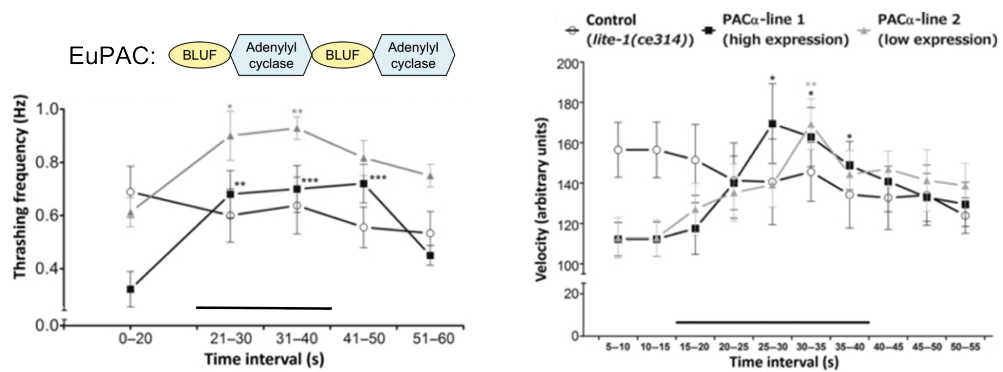


**Figure 1.11.: Motility modulation by EuPAC $\alpha$  expression in cholinergic neurons of *C. elegans*.**

BLUF/cyclase domain organization in EuPACs (inset). Photoactivation of EuPAC $\alpha$  in cholinergic motoneurons from *C. elegans* led to increased swimming rate (left) and speed on solid substrate (right). Due to the dark activity of EuPAC $\alpha$ , compensatory effects reduced basal motility of these animals. Figures adapted from [204], inset [187].

present in bPAC and its relative small size, bPAC was selected as the optogenetic tool for light induced cAMP production in *C. elegans* for this thesis.

Noteworthy, a regulation mechanism of both mRNAs coded by the CGL by cAMP may be relevant for the experimental design of the work performed during this thesis [208–210]. Increase of cAMP concentration and PKA/KIN-1 activation leads to increased mRNAs levels from ChAT/CHA-1 and vAChT, as well as stimulated ChAT/CHA-1 activity. Thus, all experiments conducted during the work presented herein were measured upon acute exposure to induced cAMP concentration increase.

Further, Mac was selected as a hyperpolarizer for concomitant expression with bPAC for two reasons: First, Mac lower efficiency was desired so that minimal neuronal hyperpolarization in combination with bPAC photoactivation was possible.

#### 1.2.2.4. Genetically encoded calcium indicators

In addition to neuronal control, optogenetics may be used to monitor neuronal activity. Since SV fusion requires calcium, an indirect measurement of activity is thus performed by genetically encoded Ca<sup>2+</sup> indicators (GECIs). Two main types of GECIs are used.

First, the single fluorophore G-CaMP (GCaMP), is based on the M13 fragment of

myosin light chain kinase, a circularly permuted GFP and calmodulin [211]. M13 and calmodulin interact upon calcium binding and the fluorophore of the GFP can form (figure 1.12). Further improvements of dynamic range, signal to noise and kinetics were attained [212–214].

Second, the Förster resonance energy transfer (FRET)-based sensors use calmodulin or troponin C as linker between a FRET donor and acceptor [215,216]. Calcium binding to the linker domain leads to an approximation and/or a change in the relative orientation of both fluorophores and thus enables radiation-less energy transfer. The measurement is ratiometric by design, but the dynamic range of FRET optimized GECIs reaches only about half of the GCaMP values [212,217].

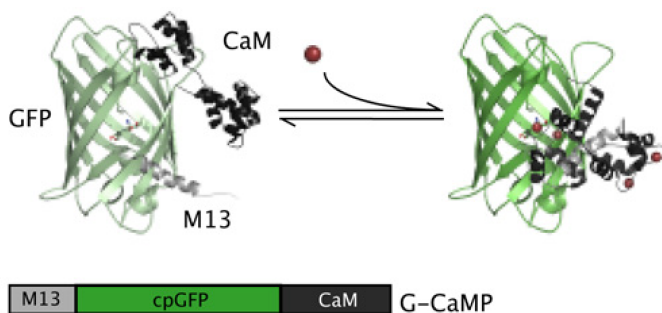


**Figure 1.12.: The genetically encoded calcium indicator GCaMP.**

The circularly permuted GFP fluoresces upon calcium-induced M13 and calmodulin interaction.

Figure adapted from [218].

#### 1.2.2.5. Optogenetic driven cell ablation

Chromophore-assisted light inactivation (CALI) is the method of optically inducing protein destruction [219]. The first optogenetic tool for CALI was described by Pletnev and colleagues: the red fluorescent, reactive oxygen species (ROS) generating protein KillerRed [220]. In contrast to laser beam cell ablation [221], optogenetic cell ablation allows for a higher throughput and acute effects. KillerRed was successfully used in light-driven cell ablation in *C. elegans* [222]. However, KillerRed requires dimerization for functional expression, is large (26.4 kDa) and long photostimulation time of about 2 h with  $2.5 \text{ mW mm}^{-1}$  of green light is required for cell ablation [222]. A monomeric version of KillerRed, named SuperNova, was generated, allowing to tag specific proteins without inducing dimerization [223]. However, the same study

showed that SuperNova was not capable of driving cell ablation in *C. elegans*.

The green fluorescing mini singlet oxygen generator (miniSOG), engineered from *Arabidopsis thaliana* phototropin 2, is a small (13.9 kDa), monomeric, ROS producing protein (figure 1.13). The fluorescence quantum yield is reduced compared to GFP, but  $^1\text{O}_2$  quantum yield is above 0.5. Further, fusion proteins with miniSOG were correctly localized [224]. Targeting of miniSOG to the mitochondrial outer membrane allowed to induce cell death by incubation with  $0.5 \text{ mW mm}^{-1}$  of blue light for 15 min [225]. Thus, miniSOG is superior to KillerRed and SuperNova, unless spectral overlap is a concern. In addition, miniSOG allows for correlated light and electron microscopy analysis by catalyzing a reaction that produces an osmium aggregating polymer [224].

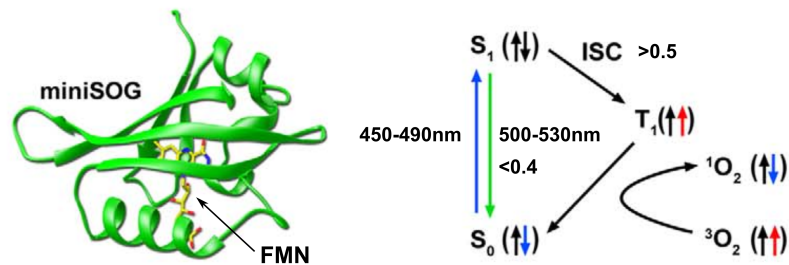


**Figure 1.13.: Light induced ROS production with miniSOG.**

MiniSOG requires flavin mononucleotide (FMN) for function (left). Photoactivation of miniSOG leads to green fluorescence as well as to intersystem crossing (ISC). The later produces ROS during relaxation with a quantum yield above 0.5 (right).

Figure adapted from [224].

### 1.2.3. Further genetically encoded tools for neurotransmission analysis

A few further genetically encoded tools were applied during this work and are briefly introduced here.

In cases where neuronal cell ablation did not require temporal precision, genetically induced apoptosis was used. Cell specific expression of interleukin-1  $\beta$  converting enzyme (ICE) leads to FAS/ZYG-8-mediated apoptosis [226–229]. However, if promoter expression patterns are not well characterized, apoptosis can be driven in unspecific targets. Furthermore, ICE leads to apoptosis upon expression. Since



most neurons in *C. elegans* are born before the end of the first of four larval stadia (L1) [230,231], compensatory effects may appear.

Tetanus toxin (TeTX) can be selectively expressed in cases where chemical synaptic transmission of a distinct neuronal population needs to be abolished [232]. TeTX is a zinc protease that cleaves SNB-1, thus inhibiting SV release [233] and impairing neurotransmission *in vivo* [234]. Nonetheless, TeTX also cleaves Cellubrevin/VAMP3 that does not participate in evoked SV release and results must thus be interpreted with caution [235,236].

In addition, neuronal silencing in *C. elegans* can be triggered by histamine gated chloride channel 1 (HisCl1) [237], since histamine could not yet be found as a neurotransmitter in *C. elegans* [238]. However, there is a reduced temporal control inherent to a pharmacological application of histamine, albeit histamine itself is not inducing an observable effect on *C. elegans* behavior [237]. Nonetheless, HisCl1 augments optogenetic analysis in *C. elegans*, since it allows complex neuronal challenge paradigms that would otherwise not be feasible through an all-optical approach.

### 1.3. The model organism *Caenorhabditis elegans*

The basis of knowledge in the neuroscience is derived from experiments in diverse model organisms, of which *C. elegans*, *D. melanogaster*, *Danio rerio* (*D. rerio*) and *Mus musculus* (*M. musculus*) are summarized in figure 1.14. These organisms have in common the sequenced genome, ontologies for behavior and phenotype description as well as detailed information of their neuronal circuitry. Further, the methodological tractability of these model organisms is similar.

*C. elegans* is a 1.1 mm  $\pm$  0.1 mm long, non-parasitic nematode that feeds on bacteria. It is an eutelic animal with 959 cells for the hermaphrodite and 1031 cells in the adult male [230,251]. It achieves adulthood in about 4 d with a ratio of hermaphrodites to males of about 1000:1 in laboratory conditions (figure 1.15 hermaphrodite adult and life cycle). Hermaphrodite animals lay about 300 eggs by self-fecundation and this number can increase up to 1200 eggs with additional male fecundation, thus breeding and genetic variant crossing are exceptionally easy compared to other model organisms. In addition, transparency, defined connectome, and ease of mutagenesis and transgenesis combined with optimal properties for optogenetical, electrophysiological and ultrastructural analysis were pivotal for selection of *C. elegans* as the model organism for the studies presented herein [142,156,230,231,252–259].

	<i>C. elegans</i>	<i>D. melanogaster</i>	<i>D. rerio</i>	<i>M. musculus</i>
<b>Life cycle</b>	± 56 hours	± 12 days	± 50 days	± 50 days
<b>Brood size</b>	± 140 eggs/day	± 120 eggs/day	± 200 eggs/week	6 to 12 pups/month
<b>Genome</b>				
<b>Annotated</b>	Reference genome	Reference genome	>90% sequenced	No reference
<b>Length</b>	103 Mbp	143 Mbp	1464 Mbp	3482 Mbp
<b>Coding genes</b>	20362	13918	25790	22643
<b>Homology to <i>H. sapiens</i></b>	± 43 %	± 61 %	± 76 %	> 95 %
<b>Methods</b>				
<b>Optogenetics</b>	Transparent	Larva translucent	Larva translucent	Invasive
<b>HPF-EM</b>	Yes	Larva	Larva	Brain slices
<b>Electrophysiology</b>	Immobilized	Immobilized	Immobilized	Freely behaving
<b>Neuroscience</b>				
<b>Behavior and phenotypes</b>	Ontology	Ontology	Ontology	Ontology
<b>Nervous system structure</b>	Nerve ring, nerve	Brain / Ganglia	Brain / Spinal cord	Brain / Spinal cord
<b>Neurons per adult</b>	302	± 2.5 x 10 <sup>5</sup>	± 1 x 10 <sup>7</sup>	± 7.1 x 10 <sup>7</sup>
<b>Synapses per adult</b>	>7283	± 10 <sup>7</sup>	± 10 <sup>9</sup>	± 10 <sup>12</sup>
<b>Connectome</b>	Complete	Partial	Partial	Partial

Figure 1.14.: Comparison of model organisms in neuroscience.

Data from: *C. elegans* [239–242], *D. melanogaster*, [241–245], *D. rerio* [241, 242, 246–248] and *M. musculus* [242, 249, 250]

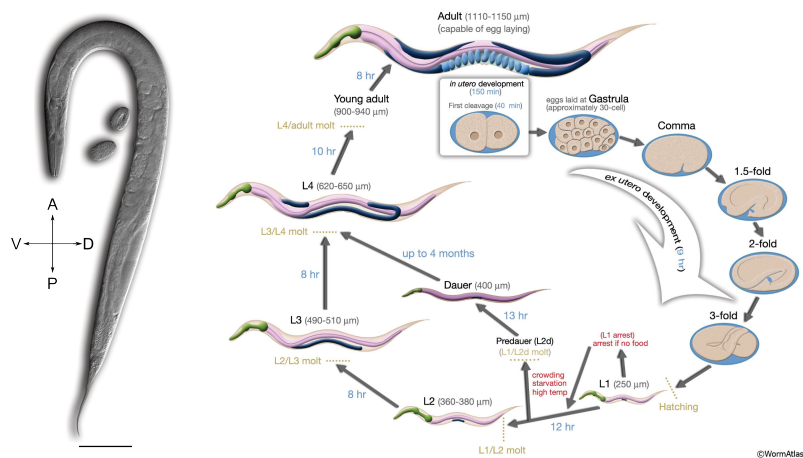
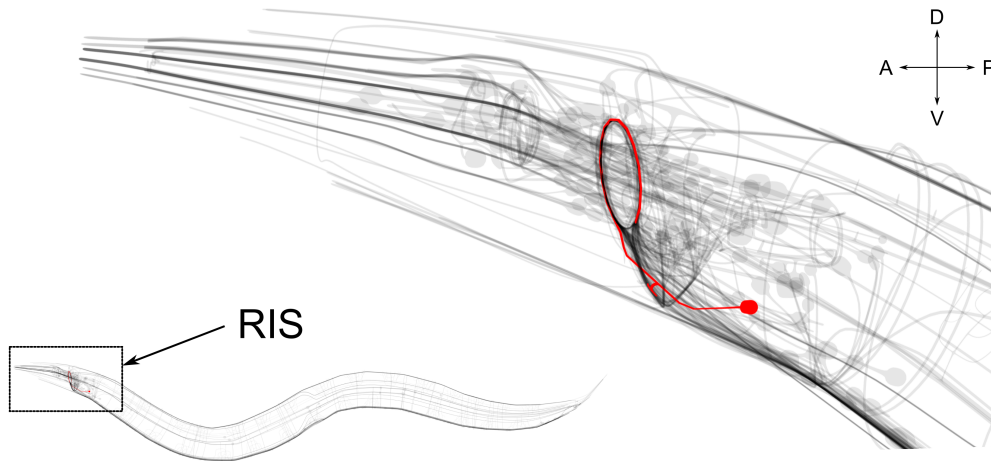


Figure 1.15.: *Caenorhabditis elegans* life cycle.

DIC imaged adult hermaphrodite *C. elegans* (left). Life cycle of *C. elegans* with time points regarding cultivation at 20 °C (right). Figures adapted from [260]. Scale bar = 0.1 mm.

### 1.3.1. Neuronal organization

The neuronal organization of *C. elegans* was described by analysis of serial transverse sections imaged by electron microscopy by John G. White and co-workers [257]. Neurons were named with two to three uppercase letters plus, in a few cases, a number indicating their class. Radially symmetric neuronal classes have a three letter code and are followed by a position letter (L: left, R: right, D: dorsal and V: ventral). The resulting connectome describes 302 neurons in two main networks of the hermaphrodite animal. Both networks are interconnected by a single neuron. The somatic nervous system consists of 282 neurons divided in 118 classes [257], from which one single neuron, RIS, is characterized in this thesis and discussed below (section 1.3.1.4, p. 33, figure 1.16).



**Figure 1.16.:** Representation of *C. elegans* neurons along the body depicting the position of RIS. The cell body and main process location of *C. elegans* neurons in the head as well as for the whole neuronal system (inset: full animal, RIS red). Figure created with data from [261].

Another classification method is based on the neurotransmitter expression pattern. The main neurotransmitters used by *C. elegans* are glutamate, ACh and GABA, produced by 265 neurons (figure 1.17) [262–264]. Further 23 neurons utilize known biogenic amines as neurotransmitters: dopamine, tyramine, octopamine and serotonin [265–269]. One additional pair of neurons is also aminergic, but the neurotransmitter is not yet known [264].

The presence of more small neurotransmitters cannot be completely excluded, the

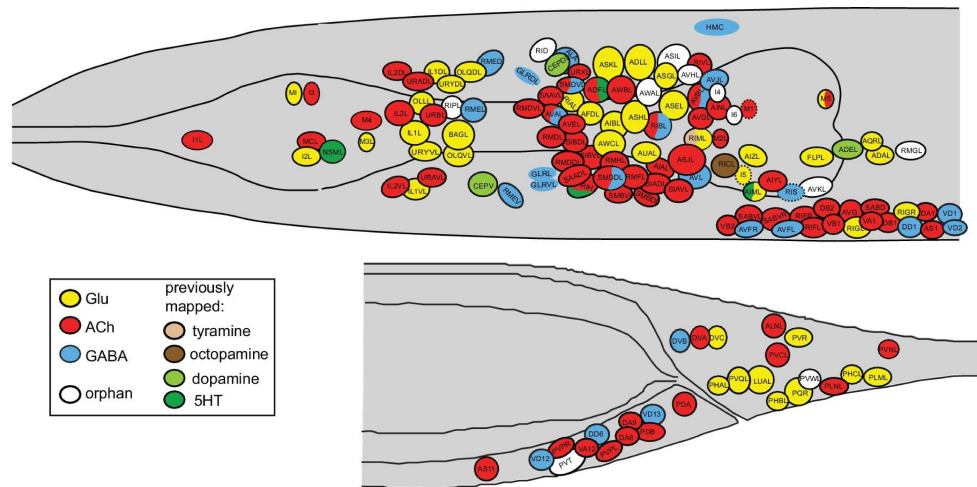


**Figure 1.17:** *C. elegans* neuronal cell bodies and neurotransmitters. The cell body position of head and tail neurons, with color coded indication of their use of neurotransmitter. Only neurons on the left side are shown, unless the neuronal class is exclusively located to the right (dotted line). Figure adapted from [264].

most probable being melatonin. Melatonin is a biogenic amine that does have an effect on *C. elegans* behavior, even though no known transmembrane receptor orthologs are found in the genome [270]. Nonetheless, melatonin might transduce information through nuclear hormone receptors in *C. elegans*, in accordance to the circadian rhythm of melatonin production [271].

The remaining 12 orphan neurons may be purely neuropeptidergic. For example, the neuron class AVK expresses the neuropeptide FLP-1, through which body undulation amplitude is modulate [272, 273]. Further, RID expresses, among others, the neuropeptide FLP-14 and its function is to maintain forward movement [274]. The *C. elegans* genome has 113 genes encoding for neuropeptides. These are further subdivided in three categories, based on the encoded peptide properties: 40 insulin-like peptides (INs), 31 FMRF-like peptides (FLPs) and 42 neuropeptide-like protein (NLP) genes [275–279]. It is important to note that most neurons express neuropeptides in addition to small molecule neurotransmitters [280]. Thus, neuropeptidergic signaling has an important modulatory role in the neuronal circuit of *C. elegans*.

### 1.3.1.1. SV quantal size modulation in *C. elegans*

*C. elegans* neuronal information transmission is mainly graded depending on the input signal [281,282]. In the NMJ, neurotransmission from cholinergic and GABAergic motoneurons can be analyzed by electrophysiological measurements of the BWMs (section A.2, p. 225). Single SV release events result in mPSCs. These have a broad distribution of amplitudes, ranging from  $\leq 10$  pA to  $\geq 200$  pA, partly due to the receptor type in the BWM cell (figure 1.18) [283].

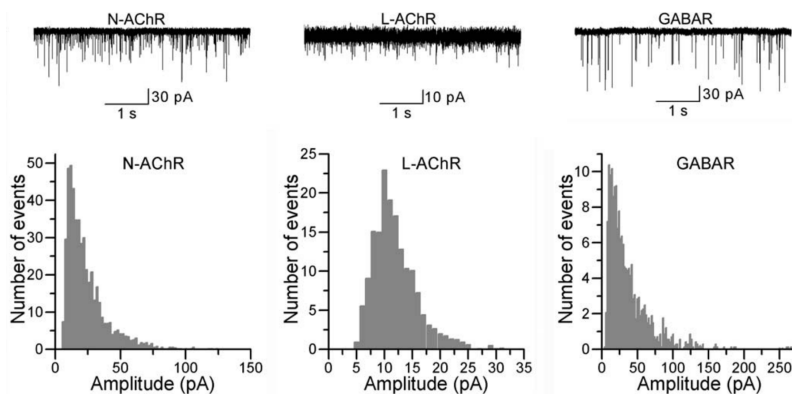


**Figure 1.18.: BWM cell recording and SV quantal size.**

High variability in mPSC size as measured by electrophysiology of BWM cells is an indication of SV quantal size modulation. Three types of receptors are expressed in BWM cells: N-AChR nicotine-sensitive acetylcholine receptor; L-AChR levamisole-sensitive acetylcholine receptor and GABAR GABA receptor. Original recording for these receptor types (top) and distribution of amplitudes (bottom). Figure adapted from [283].

The amplitude of mPSCs was shown to be modulated by cAMP [204]. Thus, this variability may be caused by modulation of SV quantal content in the pre-synapse. Indeed, pre-synaptic calcium signal mediated by the ryanodine receptor (RyR/UNC-68) is required for occurrence of mPSCs of  $\geq 50$  pA [284]. The mechanism leading to modulation of SV quantal size, triggered by cAMP signaling was investigated as part of the work described in this thesis.

It is important to note that no ortholog of SV2 has been found in invertebrates to date. Nonetheless, the SVOP-1 protein is similar to the SV2-family of protein with sequence identity of about 20%. SVOP-1 lacks the glycosylation sites present in SV2-family of proteins, though [285]. Since for SV2, the keratan sulfate glycosylation is required for coordination of ACh [71,286], the function of SVOP-1 in *C. elegans* may

not fully resemble the function of SV2. This is specifically the case for the frustrated SV release model described above, that is probably absent in *C. elegans* (figure 1.6). Nonetheless, SVOP-1 may still allow for the SV2A dependent SV size increase observed upon vesicle loading [39]

Another potential candidate protein that may control SV release is SNN-1. Synapsin is a major component of the presynaptic terminal that tethers SVs to themselves and to the actin cytoskeleton [287,288]. Synapsin in *C. elegans* occurs in two splice variants that resemble mammalian synapsin I and synapsin II long and short isoforms. One of them, SNN-1B, is the long form and contains a conserved PKA/KIN-1 phosphorylation site required for SV association (Serine 9 in SNN-1B) [289]. Ch'ng and colleagues suggested that SNN-1 in *C. elegans* associates with SVs that are either distal to the DP or associates with them following endocytosis [290]. This would be in accordance with the previously reported Synapsin colocalization with actin during endocytosis in the spinal cord of lampreys [288]. Thus, SNN-1 could be a major, PKA/KIN-1 modulated, regulator for exocytosis in *C. elegans*. This hypothesis would be in line with experiments performed in *D. melanogaster* [291] and mammalian neurons [61, 292], where Synapsin controls availability of SVs for fusion. Further, Synapsin mutation was shown to reduce neuropeptidergic signaling in mammals [293]. Nevertheless, the neuropeptide in question, brain-derived neurotrophic factor (BDNF), has no ortholog in nematodes, albeit other neurotrophic factors being conserved [294,295].

### 1.3.1.2. Neuromuscular junction and excitation-inhibition balance

In contrast to the mammalian skeletal NMJ, the *C. elegans* NMJ is an *en passant* pre-synaptic differentiation with a muscle arm as the post-synaptic structures. In adult animals, each BWM cell sends about four muscle arms to the next neuronal cord [296]. Opposing this morphological distinction, the *C. elegans* NMJ is interposed by a basement membrane constituted of proteins with orthologs in vertebrates [297,298]. Further, the basement membrane is required for synapse formation [299]. Noteworthy in an *en passant* synapse is that a super-pool of SVs is a likely consequence. Thus, vesicle recruiting and retention to the pre-synapse is of particular interest.

*C. elegans* has 95 BWM cells organized in four quadrants along the anterior-posterior axis and each quadrant consists of two rows of BWM cells (figure 1.19) [296]. The main synaptic input is cholinergic and GABAergic [257], the former leading to muscle contraction and the later to muscle relaxation. BWM cells also express diverse neuropeptide receptors [300], for example FRPR-4. This receptor was recently char-

acterized as a receptor for the neuropeptide FLP-13 and required for behavior quiescence [301]. In addition, BWM cells are connected by gap junctions to their neighboring BWM cells and its disruption leads to uncoordinated behavior [302,303].

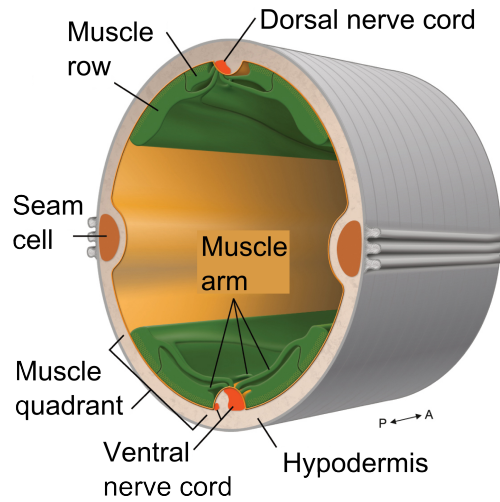


**Figure 1.19.: Schematic of body wall muscle organization.**

*C. elegans* BWM are organized in four quadrants of two cell rows. Each BWM cell contact the nearest neuronal cord.

Figure adapted from [260].

A further peculiarity of the *C. elegans* connectome is a feed-forward network of cholinergic and GABAergic motoneurons (figure 1.20) [304]. This excitation-inhibition allows the contraction and relaxation of opposing BWM required for locomotion and is tightly regulated [305,306].

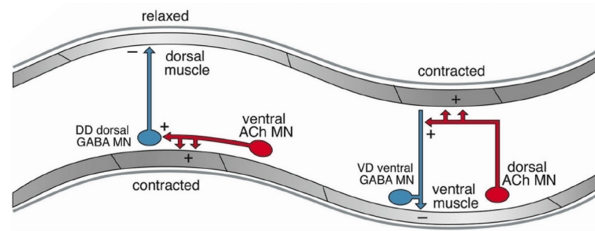


**Figure 1.20.: Cholinergic to GABAergic motoneuron feed-forward network.**

The cholinergic motoneurons from the ventral nerve cord innervate GABAergic neurons. This feed-forward network generates contraction and relaxation of opposing dorsoventral muscles during locomotion. Further, motoneurons in each body section are coupled to the vincinal sections (not shown). Figure adapted from [307].

### 1.3.1.3. The neuronal network for locomotion

The motoneurons in the ventral nerve cord (VNC) innervate the ventral and dorsal BWM cells. They are subdivided into eight classes in accordance to their connectivity [303, 304, 308, 309]:

- AS — Synapses in the dorsal nerve cord, cholinergic
- DA — Pre-synapses mainly in the dorsal nerve cord, cholinergic
- DB — Synapses mainly in the dorsal nerve cord, cholinergic, proprioceptive
- DD — Synapses in both nerve cords, GABAergic
- VA — Synapses in the ventral nerve cord, cholinergic
- VB — Synapses in the ventral nerve cord, cholinergic, proprioceptive
- VC — Synapses in the ventral nerve cord and vulva muscles, cholinergic and serotonergic
- VD — Synapses in both nerve cords, GABAergic

These neurons, together with the BWM cells, are organized in functional subsets [310]. Each section couples to its predecessor and processes proprioceptive information on the state of body segment curvature [303]. The activity of these motoneurons is controlled by two groups of command interneurons with their main classes being AVB, for forward locomotion, and AVA, for backward locomotion (figure 1.21 top) [311]. Noteworthy, the head and neck BWM cell are connected to moto-interneurons in the head instead of AVA and AVB [257]. This connectivity pattern of the foremost muscle cells enables wave propagation independent head movements, for instance



during food search [312].

The neuronal network can be organized according to the signal flow through chemical and electrical synapses (figure 1.21 bottom) [239]. This computational analysis suggests AVA and AVB above the motoneurons, in accordance to the natural neuronal network layout and confirmed further experimntal fidings [239]. Hence, such analysis could be used to infer a function of a unspecified neuron in the neuronal network. Nonetheless, these computations do not take into account the effect of neuropeptidergic or aminergic signaling. In fact, serotonergic signaling was shown to inhibit a neuropeptidergic signal by Flavell *et al.* [313]. This inhibition leads to increased dwelling of the animals in a restricted area. Without the serotonergic signal, animals have a higher propensity to roaming, a state where locomotion is performed with low angular speed and few reorientation events. Recent connectivity analysis implemented a draft connectome of monoaminergic signaling as well as a dozen neuropeptide receptors. The extent of connectivity between neurons compared to the synaptic connectome alone was more than doubled [314]. Hence, the connectome does not perfectly depict the function of a given neuron and analysis of a second layer interneuron is very complex. This is due to the second layer of interneurons being hidden, without direct sensory input and, in some cases, also lacking connectivity to motoneurons. Nonetheless, some neurons cannot be easily categorized: RIS, for example, is connected to only 15 neuronal classes, but these are comprised of sensory neurons, interneurons in all layers as well as motoneurons.

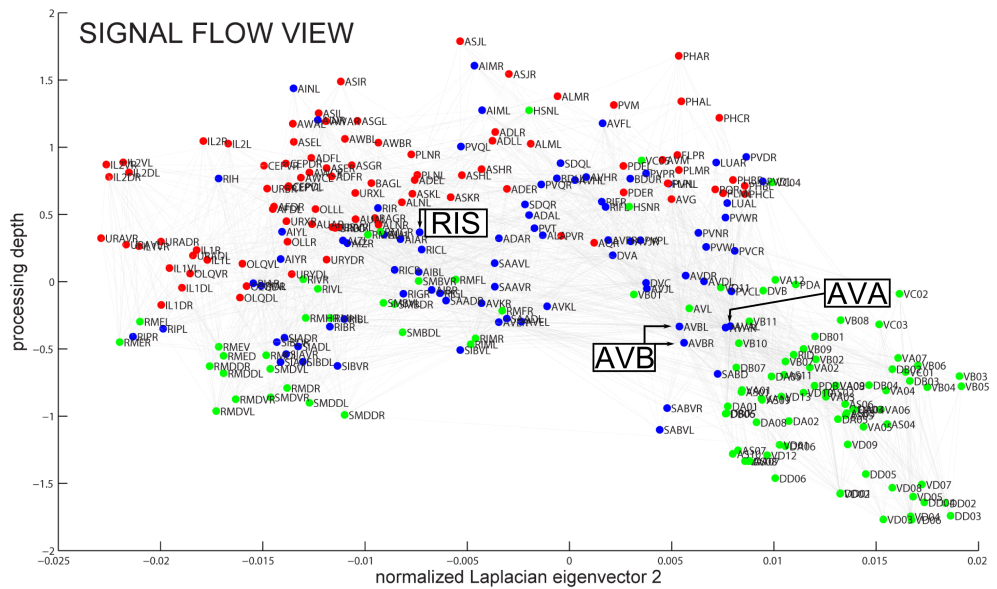
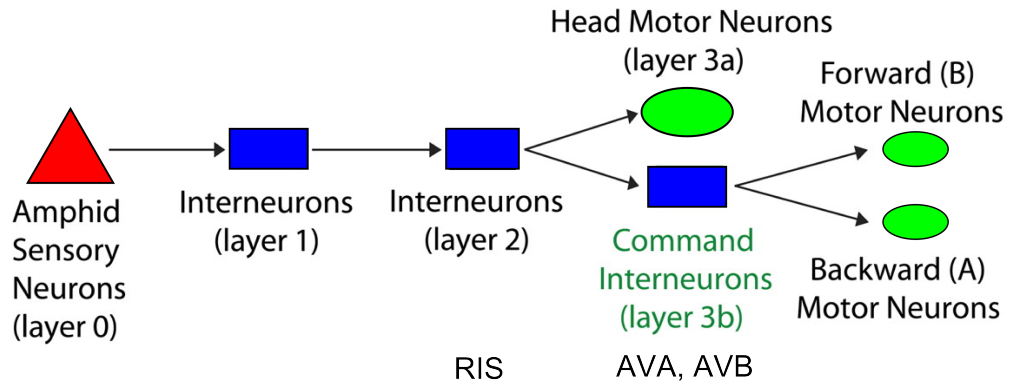


**Figure 1.21.: Neuronal network topology and signal flow.**

The scheme of *C. elegans* neuronal network composed of sensory neurons, three interneuron layers and motoneurons.

Computed signal flow view through all somatic neurons of *C. elegans* (bottom) with information flow mostly downward.

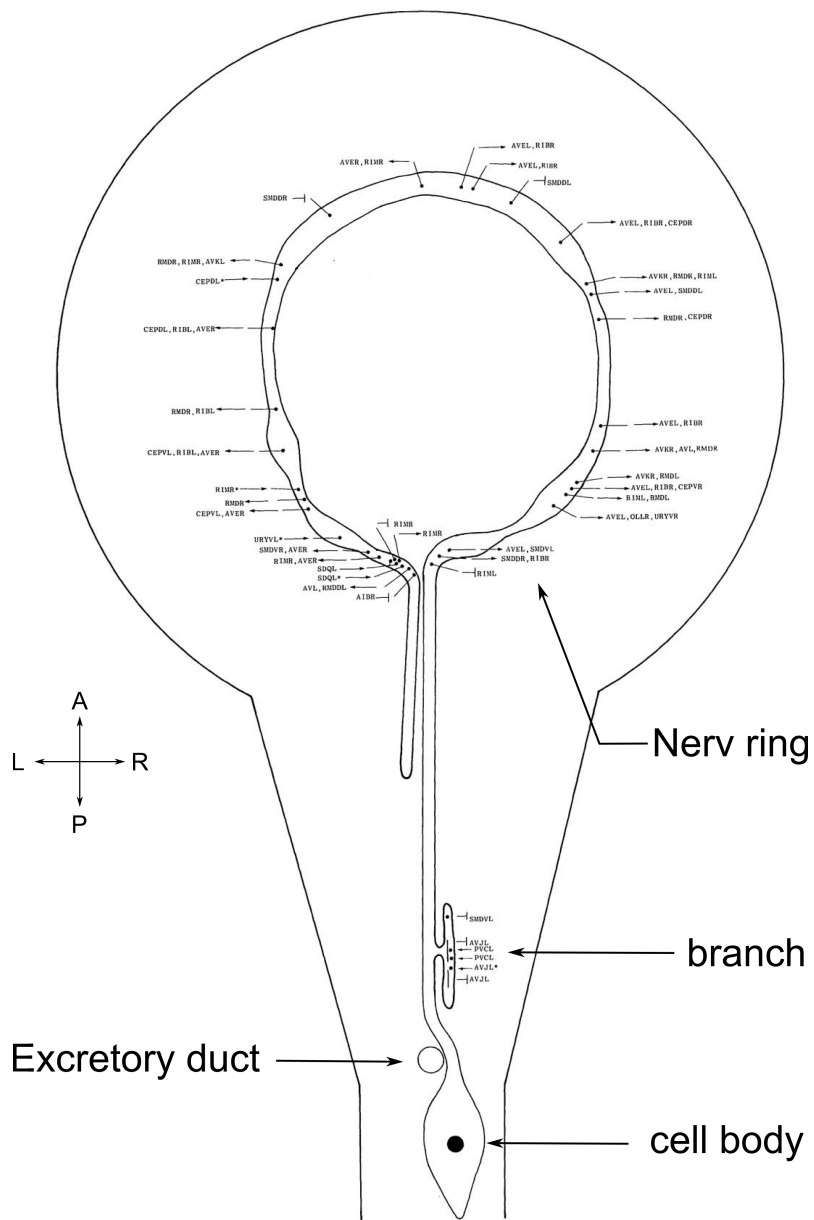
Neuron colored red: sensory neurons; blue: interneurons; green: motoneurons.

Figure adapted from: top [312], bottom [239].

#### 1.3.1.4. The GABAergic interneuron RIS

RIS was the first characterized GABAergic interneuron in *C. elegans* [264,315]. In contrast to most other neuronal classes, RIS is a single neuron localized at the right side of the animals (figure 1.16 anatomical positioning). The left hand side counterpart to the cell that gives rise to RIS, amongst others, undergoes programmed cell death during embryonic development [231]. RIS has a single process that runs through the nerve cord, where most synapses are formed, as well as a small branch to the ventral nerve cord with a few characteristic gap junctions [257, pp. 268-269]. RIS is considered part of the interneuron network associated with motoneurons in the head of *C. elegans* [257, p. 45]. *In silico* analysis of signal flow in the neuronal network from *C. elegans* placed RIS in the center of the network, albeit without a further indication on the role of RIS in information processing (figure 1.21, bottom) [239].

A study performed by Tsalik and co-workers analyzed the circuitry associated with motoneurons in the nerve ring as described above [316]. Laser ablation of RIS did not have an effect on reversal behavior. Further laser ablation studies elucidated the head neuronal circuit associated with locomotion, without providing indications of a role of RIS in locomotion behavior [312].



**Figure 1.22.: Schematic location of RIS in the adult hermaphrodite.**

The RIS cell body is located on the right side of the ventral ganglion, behind the excretory duct. It sends one process to the nerve ring with a small branch to the ventral nerve cord.

Figure adapted from [257, pp. 268-269].

### 1.3.1.5. Role of RIS in a sleep-like state in larvae

Although the role of RIS in adult behavior is not uncovered, the neuron is required for a larval sleep-like state during molt phases. Sleep is a debated concept of a natural, periodic state in behavior in which an animal is less responsive to outward stimuli coupled to muscular inactivity [317]. It is neither coupled to metabolic rate reduction (hibernation) nor to the inability of arousal (coma). Sleep and sleep-like states are encountered throughout animal species: molluscs [318, 319], crustaceans [320], insects [321, 322], fish [323], reptiles [324, 325], amphibians [326], birds [327] and mammals [328] sleep. It is important to note that although sleep and sleep-like states have a similar phenotype across species, they may be acquired independently through evolution [329].

There are two sleep-like states described in *C. elegans*. Lethargus, also called developmentally timed sleep (DTS), occurs during larval molt transitions [330]. In contrast, stress-induced sleep (SIS) is a response of adult animals to cellular stress [331]. Both states are behaviorally similar with a lack of locomotion and feeding paired with increased arousal threshold [332], and they are regulated by distinct neuropeptidergic pathways (DTS: NLP-22, SIS: FLP-13) [330, 333]. Interestingly, NLP-22 requires the PKA/KIN-1 inhibitory subunit (KIN-2) for function [330], while FLP-13 signal transduction is not well characterized. The latter may signal through the tachykinin-related family receptor NPR-22, although the receptor has higher affinity to other neuropeptides [334]. Further, photoactivation of RIS was shown to induce lethargus in larvae [335] (note that Channelrhodopsin expression achieved in this work was not exclusive to RIS and affected four additional pairs of neurons). Nonetheless, GABA-signaling from RIS was not necessary for the inhibition of locomotion in these larvae. Additional analyses showed the FLP-11 neuropeptide requirement for sleep-like behavior and its (increased) release following over-expression was sufficient to induce lethargus [336]. FLP-11 activates at least three receptors of *C. elegans*: NPR-22 (with higher affinity than FLP-13) [334], FRPR-3 (with no detected FLP-13 affinity) [337] and NPR-4 (with lowest affinity to FLP-11) [338].

It is interesting to note that sleep and sleep-like behavior as well as arousal is encoded by neuropeptidergic and aminergic neurotransmitters [339, 340]. In mammals, sleep is mainly regulated in the ventrolateral preoptic nucleus, where GABAergic and galaninergic neurons inhibit orexin/hypocretin releasing neurons during sleep and inversely during wakefulness [341, 342]. Further, the cycle is coupled to and influenced by molecular clocks as well as the duration of wakefulness states itself [343].

However, orexins were neither found in *C. elegans* nor in *D. melanogaster*, but it was shown that pigment dispersing factor (PDF) neuropeptides could mediate arousal in these species [344–346], while the aforementioned neuropeptides promote sleep-like states.

The pathway leading to intrinsic RIS activity may be modulated by dopamine and serotonin signaling. The former may lead to cAMP production, since RIS expresses the dopamin D<sub>1</sub>-like family receptor DOP-1 [347,348]. In contrast, serotonin activates the SER-4 receptor in RIS, an ortholog of mammalian 5-HT<sub>1</sub> metabotropic serotonin receptors [347]. SER-4 attenuates the adenylyl cyclase function in *C. elegans* [349]. It is possibly further coupled to G<sub>βγ</sub>, inhibiting SV release, as has been shown for this class of serotonin receptors in mammals [350]. Expression of both receptors in RIS is regulated by the transcription factor LIM-6 [347]. LIM-6 also induces the expression of the transcription factor APTF-1, the latter required for FLP-11 expression [336].

Hence, RIS might be involved in locomotion cessation in response to diverse factors, from sensory input to neuropeptidergic signaling and internal state of the neuronal network. The output of RIS in the adult animal could enable a change of locomotion directionality.

## 1.4. Objectives

Two main objectives were pursued during this thesis. First, the expression and characterization of bPAC in cholinergic motoneurons of *C. elegans*. bPAC photoactivation in cholinergic neurons should be compared to  $G_{\alpha S}$  gain of function mutations, thereby delineating the requirement for an acute cAMP modulation. The characterization of presynaptic modulation through cAMP pathway should then be performed utilizing canonical mutations and a stable expression strain with a genome integrated transgene array. Specifically, the effect of bPAC photoactivation regarding mPSC amplitude was expected to depend on neuropeptidergic signaling, since in a previous electrophysiological study, cAMP transduction pathway and Chr2 mediated depolarization in motoneurons did not induce the same effects. Hence, an optical readout method for neuropeptidergic signal should be applied and compared to Chr2 induced depolarization of cholinergic neurons.

In addition, multiple improvements in data analysis were required in order to measure subtle effects in behavioral, electrophysiological and ultrastructural data. These should be combined to workflow automation methods, improving data analysis throughout this work.

Second, the characterization of the interneuron RIS in respect to its function in the adult neuronal system of *C. elegans*. RIS was shown to induce lethargus in during larval molts but this behavior is not part of the repertoire of adult animals. Therefore, optogenetic analysis with Chr2 elicited depolarization as well as Arch elicited hyperpolarization of RIS should be performed. In order to achieve single cell expression, a combinatorial, recombinase based system should be generated.

Albeit GABAergic, RIS had been shown to mainly use neuropeptidergic signaling during larval states. To test whether GABAergic or neuropeptidergic signaling was the main transducer of RIS function in adult animals, independent methods should be applied. In the case that bPAC manipulated neuropeptidergic release, expression of bPAC specifically in RIS should be performed and hence, specifically modulating neuropeptide release. In addition, analysis of canonical mutants in both pathways should be applied in combination to the optogenetic tools above.

Lastly, expression of a genetically encoded calcium indicator in RIS should allow to measure its intrinsic activity during behavior. With this tool-set, analysis of signal transduction should be performed, thereby characterizing not only RIS function in the neuronal network, but also its effector pathways.





## 2. Materials and Methods

The Material and Methods section contains passages from my Diploma Thesis in Biochemistry (2010) at the University of Frankfurt, Germany, with updated procedures where applicable. Both, my Diploma Thesis and this work, were performed under the supervision of Prof. Alexander Gottschalk.

### 2.1. Materials

#### 2.1.1. Reagents

Table 2.1.: Reagents.

Name	Supplier
Acetic acid	Carl Roth
Agar	AppliChem
Agarose	Biozym
Ampicillin sodium salt	AppliChem
Bovine serum albumin (BSA)	NEB
Calcium chloride	Carl Roth
Cholesterol	Merck
Desoxy nucleotide triphosphate (dNTP)	Invitrogen
Ethylene-diamine-tetra-acetic acid (EDTA)	Carl Roth
Ethanol	Carl Roth
Ethanol (AR grade)	AppliChem
Ethidium bromide	Carl Roth
GeneRuler 1 kb DNA Ladder	Fermentas
GeneRuler 1 kb Plus DNA Ladder	Fermentas
Halocarbon oil	Halocarbon
Yeast extract	Carl Roth
Isopropanol	Carl Roth
Potassium acetate	Carl Roth
Potassium citrate	Carl Roth
Potassium chloride	Carl Roth
Dipotassium phosphate	Carl Roth

**Table 2.1.:** (continued)

<b>Name</b>	<b>Supplier</b>
Monopotassium phosphate	Carl Roth
Magnesium sulfate	Fermentas
Magnesium chloride	Carl Roth
Sodium acetate	Carl Roth
Sodium azide	Carl Roth
Sodium chloride	Carl Roth
Disodium phosphate	Carl Roth
Nystatin	Sigma-Aldrich
Oligonucleotides	Eurofins MWG
Phenol chloroform isoamyl alcohol (50:49:1)	Carl Roth
Polyethylene glycol (PEG) 6000	Carl Roth
Polystyrene beads (0.1 $\mu\text{m}$ )	POLYCIENCES
Nitrogen	Linde
Streptomycin	AppliChem
Tris-(hydroxymethyl)-aminomethane (TRIS)	Carl Roth
TRIZOL	
Tryptone/Peptone from Casein	Carl Roth

### 2.1.2. Buffers and Media

**Table 2.2.:** Buffers and Media specifications.

<b>Name</b>	<b>Contents/ Supplier</b>
Antartic phosphatase (AP) Buffer (10x)	NEB
Buffer Tango (10x)	Fermentas
DNA loading dye 6x	Fermentas
dNTP Mix	10 mM dATP 10 mM dCTP 10 mM dGTP 10 mM dTTP
HF-Buffer (5x)	Finnzymes
Injection buffer (10x)	20 % (w/v) PEG 200 mM Tripotassium phosphate 0.33 mM Calcium chloride 0.33 mM Magnesium sulfate
Klenow reaction buffer	Fermentas
Lysogeny broth (LB) medium	0.5 % (w/v) Yeast extract 1 % (w/v) Tryptone/Peptone 1 % Sodium chloride 1.5 % (w/v) Agar Optional, after autoclaved: + 100 $\mu\text{g mL}^{-1}$ Ampicillin + 200 $\mu\text{g mL}^{-1}$ Streptomycin

**Table 2.2.:** (continued)

<b>Name</b>	<b>Contents / Supplier</b>
NEB cutsmart buffer (10x)	NEB
Nematode growth medium (NGM)	0.25 % (w/v) Tryptone/Peptone 0.3 % Sodium chloride 1.7 % (w/v) Agar 1 mM Calcium chloride 1 mM Magnesium sulfate 25 mM Potassium phosphate buffer 0.0005 % (w/v) Cholesterol (in ethanol) 0.001 % (w/v) Nystatin
M9 buffer	1 mM Magnesium sulfate 20 mM Monopotassium phosphate 40 mM Disodium phosphate 85 mM Sodium chloride
Phusion HF-buffer (5x)	Finzymes
Potassium phosphate buffer (1 M, pH 7.5)	1 M Monopotassium phosphate 1 M Dipotassium phosphate mixed to about 1:5.5 until pH 7.5
Single egg/worm lysis buffer (SEWLB)	2.5 mM Magnesium chloride  10 mM TRIS-HCl (pH 8.3) 50 mM Potassium chloride 0.05 % (w/v) Gelatine 0.45 % (v/v) Tween-20
T4 DNA ligase buffer (10x)	Fermentas
TRIS acetate EDTA (TAE) buffer (50x)	40 mM TRIS/Acetic acid 2 mM EDTA at pH 8.5
Transformation buffer	0.1 M Calcium chloride

### 2.1.3. Kits

**Table 2.3.:** Used kits.

<b>Kit</b>	<b>Manufacturer</b>
AccuScript High Fidelity 1st Strand cDNA Synthesis Kit	Agilent Technologies Inc., Santa Clara, CA (USA)
Expand Long Template PCR Kit	F. Hoffmann-La Roche AG, Basel (CH)
In-Fusion™ Dry-Down PCR Cloning Kit	Clontech Laboratories Inc., Mountain View, CA (USA)
Gel/PCR DNA Fragments Extraction Kit	Avagene life sciences, Teheran (IR)
NucleoBond PC 100	Macherey-Nagel GmbH & Co. KG, Düren (DE)

**Table 2.3.:** (continued)

<b>Kit</b>	<b>Manufacturer</b>
NucleoSpin Plasmid Kit	Macherey-Nagel GmbH & Co. KG, Düren (DE)
Q5 <sup>®</sup> Site-Directed Mutagenesis Kit	New England BioLabs GmbH, Frankfurt am Main (DE)
TOPO <sup>®</sup> TA Cloning <sup>®</sup> Kit	Life Technologies, Darmstadt (DE)

## 2.1.4. Equipment

**Table 2.4.:** Equipment used

<b>Name</b>	<b>Contents</b>	<b>Supplier</b>
Autoclave	Serie FVS 5075 ELVC	Fedgari Tuttnauer
Bunsen burner	Type 1010	Usebeck
Cameras	AxioCam MRm DC290 Zoom em-c <sup>2</sup> ORCA-Flash2.8 ORCA-Flash4.0 PowerShot G9	Zeiss Kodak Rolera Hamamatsu Hamamatsu Canon
Centrifuges	Biofuge Pico 17 Biofuge Primo R Centrifuge 5415R Microcentrifuge Rotanta Mikro 200R	Heraeus Heraeus Eppendorf Carl Roth Hettich Hettich
ddH <sub>2</sub> O equipment	Milli-Q Plus	Millipore
Electrophoresis chamber	Varia 1	Carl Roth
Filter sets	540 nm Band pass F36-525 (GFP) F41-007 (mCherry) F41-028 (YFP)	Thor Labs AHF Analysetechnik AHF Analysetechnik AHF Analysetechnik
Glass capillaries	1B100 F-4	World Precision Instruments
Incubator	3015 FOC 225E Refrigerated Incubator Kelvitron T Unitron Vinothek	GFL VELT Scientifica Heraeus Heraeus Liebherr
Lamps	HBO 50 Mercury-vapor HBO 100 Mercury-vapor UVT-20 M/W	Osram Osram Herolab

Table 2.4.: (continued)

Name	Contents	Supplier
Magnetic stirrer	Stuart CB162	Bibby Scientific
Micromanipulator	MMJ rechts with 1/2"-Klammer	Märzhäuser
Micropipette puller	Modell P97	Sutter
Microscopes	Axiovert 40 CFL	Zeiss
	Axiovert 200	Zeiss
	CLSM Axiovert 200	Zeiss
	Leica MZ 16F	Leica
	SMZ 645	Nikon
Microwave oven	Generic	MikroMaxx
pH meter	Cyberscan pH 510	Eutech
Photometer	NanoDrop ND-1000	Thermo Scientific
	Genova	Jenway
Optical power meter	PM100	Thor Labs
	S120UV	Thor Labs
	S130A	Thor Labs
	ESC10-9, 9 V DC 1.1 A	Generic
Shutter	Shutter	Sutter Instrument Company
Thermal cycler	MyCycler Personal Thermal Cycler	Bio-Rad
UV lightbox	BioView	BioView
Vortexer	Vortex Genie 2	Scientific Industries
Weighing machine	Analysewaage 770	Kern

## 2.1.5. Enzymes

**2.1.5.0.1. Restriction enzymes** All restriction enzymes were obtained from NEB or Thermo Fischer and used according to suppliers recommendation. The restriction enzymes utilized during this work are: *AarI*, *AatII*, *Acc65I*, *AccI*, *Acil*, *AcuI*, *AfeI*, *AflII*, *AgeI*, *AhdI*, *AlwNI*, *ApaI*, *ApoI*, *AscI*, *AvaI*, *AvaII*, *AvrII*, *BamHI*, *BbvCI*, *BccI*, *BciVI*, *BclI*, *BfaI*, *BglI*, *BglII*, *BmgBI*, *BmtI*, *BpmI*, *Bpu1102I*, *BsaAI*, *BsaBI*, *BsaI*, *BseGI*, *BseRI*, *BsgI*, *BsiWI*, *BsII*, *BsmI*, *Bsp1286I*, *BspEI*, *BspHI*, *BspMI*, *BspQI*, *BsrDI*, *BsrGI*, *BssHII*, *BssKI*, *Bst1107I*, *BstBI*, *BstEII*, *BstNI*, *BstXI*, *BstZ17I*, *Bsu36I*, *BtgZI*, *ClaI*, *DdeI*, *DpnI*, *DraI*, *DraIII*, *EagI*, *EcoNI*, *EcoO109I*, *EcoRI*, *EcoRV*, *FatI*, *FspI*, *HincII*, *HindIII*, *HpaI*, *Hpy188I*, *HpyCH4V*, *KasI*, *KpnI*, *MboI*, *MfeI*, *MluI*, *MnII*, *MscI*, *MseI*, *MspA1I*, *MspI*, *NaeI*, *NarI*, *NcoI*, *NgoMIV*, *NheI*, *NmeAIII*, *NotI*, *NruI*, *NsiI*, *NspI*, *PacI*, *PasI*, *PciI*, *PmeI*, *PmlI*, *PshAI*, *PsiI*, *PspOMI*, *PspXI*, *PstI*, *PvuI*, *PvuII*, *RsrII*, *SacI*, *SacII*, *SalI*, *SbfI*, *SexAI*, *SfaNI*, *SfoI*, *SgrAI*, *SmaI*, *SnaBI*, *SpeI*, *SphI*, *SspI*, *StuI*, *StyI*, *Tsp509I*, *XbaI*, *XcmI*, *XhoI*, *XmaI*, *XmaJI*, *XmnI*.

**2.1.5.0.2. Miscellaneous enzymes** All further enzymes used that are not components of specific kits (table 2.3) or restriction enzymes, were obtained from NEB, Sigma-Aldrich or Thermo Fischer and used according to suppliers recommendation. Miscellaneous enzymes used during this work are: Klenow fragment, Phusion Polymerase, Pronase, Proteinase K, T4 DNA Ligase, Taq Polymerase.

## 2.1.6. Organisms

**Table 2.5.:** Organisms

Species	Strain	Source
<i>C. elegans</i>	Bristol N2 (N2)	CGC
<i>C. elegans</i>	CB4856 isolate (Hawaiian strain)	CGC
<i>E. coli</i>	DH5a	Invitrogen
<i>E. coli</i>	OP50-1	CGC

## 2.1.7. Transgenic *C. elegans* strains

Note that for the sake of readability, gene names are not formatted in italics in the following table.

**Table 2.6.:** Transgenic *C. elegans* strains.

Strain	Genotype	Source
ZX1459	cels33 [rab-3::Tpde-4d (+) cDNA]	Dr. Kenneth Miller
ZX1460	zxIs53[punc-17::bPAC::YFP, pmyo-2::mCherry]	This work
ZX1461	zxIs53[punc-17::bPAC::YFP, pmyo-2::mCherry] cels33 [rab-3::Tpde-4d (+) cDNA]	This work
ZX1462	lim-6(nr2073)	Caenorhabditis Genetics Center (CGC)
ZX1463	epac-1(ok655)	CGC
ZX1464	flp-13(tm2448)	National Bioresource Project (NBRP)
ZX1465	snn-1(tm2557)	NBRP
ZX1466	lite-1(ce314) zxIs55 [pggr-1::Cre; pggr-2::flox::ChR2(H134R)::mCherry::SL2::GFP; pmyo-2::mCherry]	This work
ZX1467	tdc-1(n3419) lite-1(ce314) zxIs55 [pggr-1::Cre; pggr-2::flox::ChR2(H134R)::mCherry::SL2::GFP; pmyo-2::mCherry]	This work

**Table 2.6.:** (continued)

<b>Strain</b>	<b>Genotype</b>	<b>Source</b>
ZX1468	unc-47(e307) lite-1(ce314) zxls55 [pggr-1::Cre; pggr-2::flox::ChR2(H134R)::mCherry::SL2::GFP; pmyo-2::mCherry]	This work
ZX1469	unc-31(n1304) lite-1(ce314) zxls55 [pggr-1::Cre; pggr-2::flox::ChR2(H134R)::mCherry::SL2::GFP; pmyo-2::mCherry]	This work
ZX1470	lite-1(ce314); zxis52 [pmyo-3::Rcamp 35] zxls55 [pggr-1::Cre; pggr-2::flox::ChR2(H134R)::mCherry::SL2::GFP; pmyo-2::mCherry]	This work
ZX1556	lite-1(ce314) pmec-4::ChR2(H134R)::mCherry::SL2::GFP; pmyo-3::RCaMP35	This work
ZX1557	unc-31(n1304) zxls55 [pggr-1::Cre; pggr-2::flox::ChR2(H134R)::mCherry::SL2::GFP; pmyo-2::mCherry]	This work
ZX1558	tdc-1(n3419) zxls55 [pggr-1::Cre; pggr-2::flox::ChR2(H134R)::mCherry::SL2::GFP; pmyo-2::mCherry]	This work
ZX1559	unc-9(e101) zxls55 [pggr-1::Cre; pggr-2::flox::ChR2(H134R)::mCherry::SL2::GFP; pmyo-2::mCherry]	This work
ZX1560	zxis52 [pmyo-3::Rcamp 35] zxls55 [pggr-1::Cre; pggr-2::flox::ChR2(H134R)::mCherry::SL2::GFP; pmyo-2::mCherry]	This work
ZX1561	zxls55 [pggr-1::Cre; pggr-2::flox::ChR2(H134R)::mCherry::SL2::GFP; pmyo-2::mCherry]	This work
ZX1562	zxEx355 [pggr-2::GCaMP6::SL2::RFP]	Caspar-Elias Glock
ZX1563	zxEx356 [pggr-1::Cre; pggr-2::flox::GCaMP6::SL2::RFP]	Caspar-Elias Glock
ZX1564	zxEx357 [pggr-1::Cre; pggr-2::flox::miniSOG::SL2::GFP]	Caspar-Elias Glock
ZX1565	zxEx358 [pggr-1::mCherry; pggr-2::GCaMP3]	Caspar-Elias Glock
ZX1566	lite-1(ce314) zxEx350 [punc-17::bPAC::YFP; pmyo-2::mCherry]	This work
ZX1567	lite-1(ce314) zxEx351 [punc-17::bPAC::YFP; pmyo-2::mCherry]	This work
ZX1568	lite-1(ce314) zxEx352 [punc-17::bPAC::YFP; pmyo-2::mCherry]	This work
ZX1569	lite-1(ce314) zxls53[punc-17::bPAC::YFP; pmyo-2::mCherry]	This work
ZX1570	unc-31(n1304) lite-1(ce314) zxls53[punc-17::bPAC::YFP; pmyo-2::mCherry]	This work
ZX1572	zxls53[punc-17::bPAC::YFP; pmyo-2::mCherry] zxls53[punc-17::bPAC::YFP; pmyo-2::mCherry]; zxEx359 [punc-17::C1V1(E122T;E162T)::YFP; pmyo-3::CFP]	This work
ZX1573	tom-1(ok285) lite-1(ce314) zxls53[punc-17::bPAC::YFP; pmyo-2::mCherry]	Dr. Szi-chieh Yu
ZX1574	unc-47(e307) zxls53[punc-17::bPAC::YFP; pmyo-2::mCherry]	This work
ZX1575	ZW129 zxls53[punc-17::bPAC::YFP; pmyo-2::mCherry]	This work
ZX1576	zxls60[pggr-1::Cre; pggr-2::flox::GCaMP6::SL2::RFP]	This work
ZX1577	lite-1(ce314) zxEX360 [pggr-1::Cre; pggr-2::flox::ChR2(H134R)::mCherry::SL2::GFP]	This work
ZX1578	zxEx361 [pggr-1::Cre; pggr-2::flox::GCaMP6::SL2::mCherry]	Caspar-Elias Glock
ZX1579	npr-19(ok2068)	CGC

**Table 2.6.:** (continued)

<b>Strain</b>	<b>Genotype</b>	<b>Source</b>
ZX1813	lite-1(ce314) zxEX620[punc-17::Mac::YFP; elt-2::mCherry]; zxIs53[punc-17::bPAC::YFP; pmyo-2::mCherry]	Dr. Szi-chieh Yu
ZX1815	snn-1(tm2557) zxIs6 [punc-17::ChR2 (H134R)::YFP; lin-15]	Dr. Szi-chieh Yu
ZX1816	snn-1(tm2557); lite-1(ce314) zxIs6 [punc-17::ChR2 (H134R)::YFP; lin-15]	Dr. Szi-chieh Yu
ZX1831	unc-68(r1162)V zwIs108[myo-3p::Myc::RYR-1 + myo-3p::GFP]	CGC
ZX1832	unc-68(r1162)V zwIs100[rab-3p::Myc::RYR-1 + myo-3p::GFP]	CGC
ZX1859	lite-1(ce314) zXEx362[pggr-1::Cre; pggr-2::flox::HisCl1::GFP]	This work
ZX1860	ZW64 zxIs53[punc-17::bPAC::YFP; pmyo-2::mCherry]	This work
ZX1861	flp-13(tm2427)	NBRP
ZX1862	vglu-3(tm3990)	NBRP
ZX1863	unc-17(e113) zxIs53[punc-17::bPAC::YFP; pmyo-2::mCherry]	This work
ZX1864	unc-25(e156) zxIs55 [pggr-1::Cre; pggr-2::flox::ChR2(H134R)::mCherry::SL2::GFP; pmyo-2::mCherry]	This work
ZX1865	unc-17(e113) lite-1(ce314) zxIs53[punc-17::bPAC::YFP; pmyo-2::mCherry]	This work
ZX1866	lite-1(ce314)EMS Mutagenesis zxIs55 [pggr-1::Cre; pggr-2::flox::ChR2(H134R)::mCherry::SL2::GFP; pmyo-2::mCherry]	This work
ZX1867	epac-1(ok655) zxIs53[punc-17::bPAC::YFP; pmyo-2::mCherry]	This work
ZX1868	snn-1(tm2557) lite-1(ce314)	This work
ZX1869	zxis52 [pmyo-3::Rcamp 35] zxIs53[punc-17::bPAC::YFP; pmyo-2::mCherry]	Dr. Sebastian Wabnig
ZX1870	unc-31(n1304) zxIs53[punc-17::bPAC::YFP; pmyo-2::mCherry]	This work
ZX1871	snn-1(tm2557) lite-1(ce314) zxIs53[punc-17::bPAC::YFP; pmyo-2::mCherry]	This work
ZX1873	kyEx14206[tag-168::HisCl2::SL2::GFP; tag-168::HisCl1::SL2::GFP; myo3::mCherry. tag-168]	Hernan Jaramillo
ZX1874	lite-1(ce314)EMS Mutagenesis zxIs55 [pggr-1::Cre; ChR2(H134R)::mCherry::SL2::GFP; pmyo-2::mCherry]	This work
ZX1875	lite-1(ce314)EMS Mutagenesis zxIs55 [pggr-1::Cre; ChR2(H134R)::mCherry::SL2::GFP; pmyo-2::mCherry]	This work
ZX1876	lite-1(ce314)EMS Mutagenesis zxIs55 [pggr-1::Cre; ChR2(H134R)::mCherry::SL2::GFP; pmyo-2::mCherry]	This work
ZX1877	lite-1(xu7) xuIs28[Pnpr-9::chr2::yfp + Pnpr-9::Dsred2b + Punc-122::gfp]	This work
ZX1878	zxIs53[punc-17::bPAC::YFP; pmyo-2::mCherry] zxIs53[punc-17::bPAC::YFP; pmyo-2::mCherry]; zxEx359 [punc-17::C1V1(E122T;E162T)::YFP; pmyo-3::CFP]	This work
ZX1879	lite-1(ce314)EMS Mutagenesis zxIs55 [pggr-1::Cre; ChR2(H134R)::mCherry::SL2::GFP; pmyo-2::mCherry]	This work
ZX1880	unc-17(e113); lite-1(ce314)	This work
ZX1881	zxIs61[pggr-1::Cre; pggr-2::flox::GFP]	This work
ZX1882	ZIM294 [punc-31::NLS-GCaMP5K]	Prof. Manuel Zimmer



**Table 2.6.:** (continued)

<b>Strain</b>	<b>Genotype</b>	<b>Source</b>
ZX1883	lite-1(ce314) zxE364 [pggr-1::Cre, pggr-2::flox::Chr2(H134R)::mCherry::SL2::GFP; pflp-1::flp-1::mCherry]	This work
ZX1884	lite-1(ce314) zxE365 [pggr-1::Cre, pggr-2::flox::Chr2(H134R)::mCherry::SL2::GFP; pggr-2::flox::Arch::YFP; pmyo-2::mCherry]	This work
ZX1885	lite-1(ce314) zxE366 [pntr-2::Cre; pggr-2::flox::Chr2(H134R)::mCherry::SL2::GFP; pmyo-2::mCherry]	This work
ZX1886	lite-1(ce314) zxE367 [pggr-1::Cre; pggr-2::flox(Chr2(C128S; H134R)::mCherry::SL2::GFP; pmyo-2::mCherry]	Jatin Nagpal
ZX1988	zxE368[pggr-1::mCherry; pggr-2::GFP]	This work
ZX1989	zxls62[pggr-1::mCherry; pggr-2::GFP]	This work
ZX1990	lite-1(ce314) zxls53[punc-17::bPAC::YFP; pmyo-2::mCherry] nuls183[Punc-129::NLP-21::Venus; myo-2::NLS::GFP]	This work
ZX1991	snn-1(tm2557) lite-1(ce314) zxls53[punc-17::bPAC::YFP; pmyo-2::mCherry] nuls183[Punc-129::NLP-21::Venus; myo-2::NLS::GFP]	This work
ZX1992	unc-68(r1162) zxls53[punc-17::bPAC::YFP; pmyo-2::mCherry]	This work
ZX1993	lite-1(ce314) zxE369[pggr-1::Cre, pggr-2::flox::bPAC::SL2::GFP, pmyo-2::mCherry]	This work
ZX1994	lite-1(ce314) zxE370[pggr-1::Cre, pggr-2::flox::bPAC::SL2::GFP, pmyo-2::mCherry]	This work
ZX1995	zxls63[pggr-1::mCherry; pggr-2::GFP]	This work
ZX1996	zxls64[pggr-1::mCherry; pggr-2::GFP]	This work
ZX1997	zxls62[pggr-1::mCherry; pggr-2::GFP]	This work
ZX2064	zxls65[pggr-1::mCherry; pggr-2::GFP]	This work
ZX2065	zxls106[pggr-1::mCherry; pggr-2::GFP]	This work
ZX2066	zxls107[pggr-1::mCherry; pggr-2::GFP]	This work
ZX2067	lite-1(ce314) EMS Mutagenesis zxls55 [pggr-1::Cre; pggr-2::flox::Chr2(H134R)::mCherry::SL2::GFP; pmyo-2::mCherry]	This work
ZX2068	lite-1(ce314) EMS Mutagenesis zxls55 [pggr-1::Cre; pggr-2::flox::Chr2(H134R)::mCherry::SL2::GFP; pmyo-2::mCherry]	This work
ZX2069	lite-1(ce314) EMS Mutagenesis zxls55 [pggr-1::Cre; pggr-2::flox::Chr2(H134R)::mCherry::SL2::GFP; pmyo-2::mCherry]	This work
ZX2070	lite-1(ce314) EMS Mutagenesis zxls55 [pggr-1::Cre; pggr-2::flox::Chr2(H134R)::mCherry::SL2::GFP; pmyo-2::mCherry]	This work
ZX2071	lite-1(ce314) EMS Mutagenesis zxls55 [pggr-1::Cre; pggr-2::flox::Chr2(H134R)::mCherry::SL2::GFP; pmyo-2::mCherry]	This work
ZX2072	SNN-1B(S9A) NU721	Knudra (section A.1, p. 225)
ZX2073	SNN-1B(S9A) zxls53[punc-17::bPAC::YFP; pmyo-2::mCherry]	This work
ZX2074	SNN-1B(S9A) zxls53[punc-17::bPAC::YFP; pmyo-2::mCherry]	This work
ZX2075	SNN-1B(S9A) zxls53[punc-17::bPAC::YFP; pmyo-2::mCherry]	This work
ZX2076	pde-4(tm2525) zdls5[pmec-4::GFP]	Dr. Anindya Ghosh Roy
ZX2077	pde-4(tm2536)	Dr. Anindya Ghosh Roy

**Table 2.6.:** (continued)

Strain	Genotype	Source
ZX2078	nlp-21(tm2569) zxls53[punc-17::bPAC::YFP; pmyo-2::mCherry]	This work
ZX2079	nlp-21(tm2569) snn-1(tm2557) zxls53[punc-17::bPAC::YFP; pmyo-2::mCherry]	This work
ZX2080	lite-1(ce314) zxls22[punc-17::Chr2 C128S::YFP; lin-15] nuls183[Punc-129::NLP-21::Venus; myo-2::NLS::GFP]	Dr. Szi-chieh Yu
ZX2081	snn-1(tm2557) lite-1(ce314) zxls22[punc-17::Chr2 C128S::YFP; lin-15] nuls183[Punc-129::NLP-21::Venus; myo-2::NLS::GFP]	Dr. Szi-chieh Yu

### 2.1.8. Oligonucleotides

Oligonucleotides named oWSCX were created during this work. Oligonucleotides named oWSC\_AHX were created with Anke Hermann, while oWSC\_JWX were created with Jonas Pascal Weil.

**Table 2.7.:** Oligonucleotides

Name	Sequence	Comment
oCS121	CAC GTG AGA ATG GAT ACC	pr ptrx-1b
oCS121 2	GAT CTT CTC CGG ATG TTG AC	pr ptrx-1b 2
oMB8	GAA GCC AGC AGC AAG CCA TT	Rev, am 5' von Chr2(H134R)
oONA58	GAT CAT TCA CTT TTT CCA G	Prof. Harald Hutter
oONA62	GAT GGT TGT TGA ATT GTT GG	Prof. Harald Hutter
oWSC30	TTG TCC ACC TTC TCG TTC TC	Seq rev, bPGC
oWSC31	TCA CGC TAG CAT GAT GAA GCG GCT GGT G	nnnn BmtI Ini bPAC
oWSC32	TCA CGA TAT CCA GGA ACA GGT GGT GGC G	nnnn EcoRV End RFP
oWSC33	AGA TGC TAG CTA CCC AGC TTG CTT GTT C	BgPAC::tdimer2RF (Pair) f
oWSC34	TGC TGA TAT CGA CTC CAT TCG GGT GTT C	BgPAC::tdimer2RF (Pair) r
oWSC35	GGA TCC TAC CGC TGT CTC ATC C	pEntr - bicistronic (Pair) BamHI f for bicistronic
oWSC36	GGA TCC CGG TAC AGC AGT TTC C	pEntr - bicistronic (Pair) BamHI r for bicistronic
oWSC37	GAA ATG AAA TAA GCT TAG GCA ACC GTG TGC TCT GGC	In Fusion pPD95.79 HindIII pggr-1 forward
oWSC38	ATC CTC TAG AGT CGA CTC AAT AAT TAA AGT ATG CAG TTG A	In Fusion pPD95.79 Sall pggr-1 reverse low TM, 0 bp to atg of ggr-1
oWSC39	ATC CTC TAG AGT CGA CTG GTG GAA CTG GGG CAG AAG GA	In Fusion pPD95.79 Sall pggr-1 reverse high TM, 78 bp to atg of ggr-1

Table 2.7.: (continued)

Name	Sequence	Comment
oWSC40	AAT GAA ATA AGC TTG CAT GCT CTT CCG GCA GAT GCG CTG TT	In Fusion pPD95.79 SphI pggr-2 forward
oWSC41	ATC CTC TAG AGT CGA CGC CGT CGT GGT AAG ACG TTA TAG TT	In Fusion pPD95.79 Sall pggr-2 reverse
oWSC42	AGT GGG GTA AAG CTT GTC CTA GGC	nested pggr-1 forward
oWSC43	TCT GCC TGA CCC AGG ACG CA	nested pggr-1 reverse
oWSC44	TCT CTC CGC GCT GAC CAA GT	nested pggr-2 forward
oWSC45	TGG CAC CGG TTC GCT CCT ACT	nested pggr-2 reverse
oWSC46	GAA ATG AAA TAA GCT TAG AAA CTT CGG GTT ACT CAG CGT	pstr-2 forward InFusion pPD95.79 HindIII
oWSC47	ATC CTC TAG AGT CGA CAT GGA TCA CGA GTA TTC GGA CA	pstr-2 reverse InFusion pPD95.79 Sall
oWSC48	ACC GGT CCT GCA AAC AGG TTC A	pstr-2 nested forward
oWSC49	CTC GTG CAG CCA CAC CAG GC	pstr-2 nested reverse
oWSC50	GCC GGA AAG CAA ATG TTG CGT CTG	psrsx-3 forward nested
oWSC51	GTG CTG TGC TCA TGG CAC CTG	psrsx-3 reverse nested
oWSC52	ATC AGT CGA CGT ATT CTT ATG GTC TTA GAA CAA	psrsx-3 reverse Sall
oWSC53	ATC GAA GCT TCT CTA TGT AGT CAT GCA ATT TA	psrsx-3 forward HindIII
oWSC54	ATC GGC AAG GTG TCC ATC	Forward sequencing of bPGC (bPAC), bind to ini
oWSC55	ATC GAT GGG CTG GGA TGA GTC TAA CC	pgcy-8 forward
oWSC56	GGA TCC TTT GAT GTG GAA AAG GTA GAA TC	pgcy-8 reverse
oWSC57	TAA TTG CGG GCA AGG TAC TC	pgcy-8 forward nested
oWSC58	GGC ACG CTG CCA AAT AAA TC	pgcy-8 reverse nested
oWSC59	CAT TCG TAG AAT TCC AAC TG	pggr-2 forward InFusion RCaMP
oWSC60	GCC GTC GTG GTA AGA CGT TA	pggr-2 reverse InFusion RCaMP
oWSC61	TCT TAC CAC GAC GGC GAT AAC TTC GTA TAG CAT AC	pggr-2 forward InFusion RCaMP for flox
oWSC62	ATA ACT TCG TAT AAT GTA TG	pggr-2 reverse InFusion RCaMP for flox
oWSC63	ATT ATA CGA AGT TAT GCG GCC GCC ACC ATG GGT T	pggr-2 forward InFusion RCaMP for RCaMP
oWSC64	GGA ATT CTA CGA ATG GAA TTC CGG TTA CTT CGC TG	pggr-2 reverse InFusion RCaMP for RCaMP
oWSC65	AAT AAG CTT TCA CGC CCG TCC GGT GAA AC	pgcy-31 forw
oWSC66	CGG AAG CTT GGC GGT GTG AAA ATT GAA AAT GAA AAT GTT G	pgcy-31 rev
oWSC67	GCC CGT ATT GCC CAC GCG A	pgcy-31 forw nested
oWSC68	TCG GTG ACC CCC GAC ACG AA	pgcy-31 rev nested

Table 2.7.: (continued)

Name	Sequence	Comment
oWSC69	GCG GCC GCC ACC ATG TAA GTA CAA CTA GTA AGA GCT CA	forward infusion primer bc btw bpgc and yfp
oWSC70	CCC TTG CTC ACC ATG GTA CAG CAG TTT CCC TGA AT	reverse infusion primer bc btw bpgc and yfp
oWSC71	CAT TTT CAT TTT CAA TTT TCA CAC CGC CAA TGG TGA GCA AGG GCG AGG A	fusionspcr pgcy-31 cGMP sensor
oWSC72	TTA ATT AAG CTT GTG CCC CAG TTT GC	fusion pcr pgcy-31 cGMP sensor
oWSC73	ACT GTT AAT TAA TAC CGC TGT CTC ATC C	PacI Bicistronic forward
oWSC74	ACT GGC ATG CGA TCA TTC ACT TTT TCC AG	SphI ONA58 prig-5a/b with two first exons
oWSC75	CCT GTT AAT TAA GAT GGT TGT TGA ATT GTT GG	PacI ONA62 rev prig-5a/b with first two exons
oWSC76	TCG GGT TGG GAA AGC AAA CG	genomic rig-5 forw (nested)
oWSC77	CAG ACA TTG GCA GCA GTT GG	genomic rig-5 rev (nested)
oWSC78	GAC TGC ATG CTA CGC CAA GCT ATC AAC	prab-3 forward SphI for pGH8
oWSC79	GAC TCC CGG GCA AAC TTG TCA TCT GAA AA	prab-3 Xmai reverse for pGH8
oWSC80	CAG TTG ATG GAG CAA GAG ATG G	Genotyping deg-3(u701) forward
oWSC81	GAG ATA TGA TGT GCG TGT CAG G	Genotyping deg-3(u701) reverse
oWSC82	CGC CAT TGG TAG AAG TTC GTC CAC	Genotyping deg-3(u773) for- ward, from Emiliano Cohen
oWSC83	GTG CCA TTC TGC CAA CGA GAA TGA G	Genotyping deg-3(u773) reverse, from Emiliano Cohen
oWSC84	CTG CAT GCA TCA GAG ATT GTC TCC TCT	pntr-2 forward
oWSC85	ATC CCG GGC GTG TTG TTG TTC ATG CTG AAA TC	pntr-2 reverse
oWSC86	ACT ATC ATC ACC GCC GTT TG	nested pntr-2 forward
oWSC87	ACG TCA GCA CGT TCT AAA CC	nested pntr-2 reverse
oWSC88	TCC GTC TGC GTG GAG ATA C	geno tdc-1(n3419) fwd
oWSC89	GCG GAA CCT GGT GAT TGT G	geno tdc-1(n3419) rev
oWSC90	TGC CAC TGA TGA AAG GAG TG	geno epac-1(ok655) fwd from WormBase
oWSC91	GTG GAG GAA GAC CGT GTT GT	geno epac-1(ok655) rev from WormBase
oWSC92	TCA AAT CTG CCT CCG CTG TTC	unc-25(e156) flanking fwd
oWSC93	CAG GCA TAA CTC GCC TCG AAG	unc-25(e156) flanking rev
oWSC98	CGT CGT CGC CAT TCA GGC CTT TG	Geno flp-13 fw
oWSC99	GGA GCT GAT GAA GCA CGT CCG AAG	Geno flp-13 rev
oWSC100	GGT TGA TGG CTG GAA ATA GG	npr-19(ok2068) fwd
oWSC101	AGG CTT GAA GAC CAA ACG	npr-19(ok2068) rev
oWSC102	CTT CTC ACC TCA CCG GTC ATT CTC ATT CGT CTG TC	Q5SDM_1/10/2014_F Chr2 HR → Chr2 CS HR

Table 2.7.: (continued)

Name	Sequence	Comment
oWSC103	CCA CTC GGC GTA ACG CAA	Q5SDM_1/10/2014_R Chr2 HR → Chr2 CS HR
oWSC104	GAA GCA TGG GTC AAG GGA GAC	snn-1 genotyping fw
oWSC105	GTC ATT TCG CTG CTT ACT TGC ATT G	snn-1 genotyping rev
oWSC106	TGA TAC GGG AAA AGC TAC GC	OK1598_external_left from WormBase
oWSC107	TGG AAC ACT TCC CCA AAC TC	OK1598_external_right from WormBase
oWSC108	AAT TGG CAG AGT TGT TTC GG	OK1598_internal_left from WormBase
oWSC109	GGA AGC AGT TTG CTC TCC AG	OK1598_internal_right from WormBase
oWSC110	ATG AGA TGG CTG CCT GCT AC	nr2073 OH110 forward
oWSC111	CCC TGG CCG ATT ACT TCA GG	nr2073 OH110 reverse
oWSC112	GAC GCA GGC GGT ACA AGA CTC CGA CAG AAC	snn-1 gene rev primer
oWSC113	TGT GTT GGC ACC ATC AAC ACG TTC TGA AGG	snn-1 gene forward primer
oWSC114	ACG CAG CAT GCT GAA GCG GCT GGT GTA CAT C	bPAC in RIS forward
oWSC115	GGT ACC TTA GCC AGG TCC TCC TCC GAG ATC AGC	bPAC in RIS rev
oWSC116	CCC ATT TAC CTC CCA GAT TC	dpy-3 forward
oWSC117	GGC TCA CAT CTC GTA ATG AC	dpy-3 reverse
oWSC118	CCT TAG CTT CAA CCC CTC CAG ACA C	SNN-1(S9A) forward
oWSC119	GCT CAA GGC GGC CTA GGT TTG GAA T	SNN-1(S9A) reverse
oWSC120	TCC CTT CGG TAG CAA TAG C	pkc-1(ok563) f
oWSC121	GGG TGG CAT TAC ACA ACT G	pkc-1(ok563) r
oWSC122	GGC TGC AAT CGA CTC TTA TG	pkc-1(wt) f
oWSC123	CCG GTG CTG TCC ATG ATG TAG	pde-4 fwd
oWSC124	AGC AGC CAC CAC CAA CAA G	pde-4 rev
oWSC_AH01	ATG GGC GCA CCC AAG AAG AAG	Only for design of oWSC_AH04
oWSC_AH02	CCG CTT ACA GAC AAG CTG TGA C	fusions-pcr pntr-2 cre utr reverse
oWSC_AH03	CTT CTT CTT GGG TGC GCC CAT CGT GTT GTT GTT CAT GCT GAA ATC	fusions-pcr ntr-2 reverse
oWSC_AH04	GAT TTC AGC ATG AAC AAC AAC ACG ATG GGC GCA CCC AAG AAG AAG	fusions-pcr cre forward
oWSC_AH05	ATT ACG CCA AGC TTG TCA GAG ATT GTC TCC TCT	infusion fwd
oWSC_AH06	CCT TTG GCC AAT CCC CGT GTT GTT GTT CAT GCT GAA ATC	infusion rev
oWSC_JW01	GAC GTG CAT GCT TCC CCC CCT CTG ACG ACT ACT	Upstream Primer ser-4

Table 2.7.: (continued)

Name	Sequence	Comment
oWSC_JW02	GTC ACG CAC CGG TGA GAA GTC ACA GAC CAC GAC	Downstream Primer ser-4
oWSC_JW03	TCG ATA CCG GTC ACC CTT ATA GGC AGA TG	fwd RNAi lim-6 sense
oWSC_JW04	GCT AGT CCG GGA GGC GTG CAA AGA TTA GAG	rev RNAi lim-6 sense
oWSC_JW05	GCT AGT CCG GGA CAC CCT TAT AGG CAG ATG	fwd RNAi lim-6 anti sense
oWSC_JW06	TCG ATA CCG GTG GCG TGC AAA GAT TAG AG	rev RNAi lim-6 anti sense
oWSC_JW07	TGA GAT GGC TGC CTG CTA CC	Nested lim-6
oWSC_JW08	CAC AAG CAC GGA CCG TAT CG	Nested lim-6 rev
oWSC_JW09	AAC GTT ATT CGC TTC GGG GTC CTA TTC TGC	Nested fwd pser-4
oWSC_JW10	ACC CCC GGC GTG GCA ATT TAT TT	Nested rev pser-4

### 2.1.9. Plasmids

Plasmids used during this work are listed in table 2.8. Plasmids named pWSCX were cloned during this work. For these constructs, a plasmid chart is presented in the appendix chapter C.

Table 2.8.: Plasmids

Name	Description	Source
	<i>pelt-2::mCherry</i>	Prof. Alexander Gottschalk
	<i>pmyo-3::RCaMP19</i>	Dr. Sebastian Wabnig
	<i>ptab-1::Chr2(H134R)::YFP</i>	Prof. Alexander Gottschalk
	pBAD-blaC	Prof. Mark Gomelsky
	pBAD-blgC	Prof. Mark Gomelsky
	bPAC	Dr. Manuela Stierl
pAG56	<i>pmec-4::Chr2(H134R)::YFP</i>	Prof. Alexander Gottschalk
pPD95.79	GFP (promoterless)	Prof. Andrew Fire, Addgene
pNP165	<i>pgr-1::flox-stop::Chr2(H134R)::mCherry</i>	Prof. Cori Bargmann
pNP259	<i>pgap-14::Cre</i>	Prof. Cori Bargmann
pNP403	<i>ptag-168::HisCl::SL2::GFP</i>	Prof. Cori Bargmann
pUC19	DNA material without an effect in <i>C. elegans</i> , added as supplement.	NEB
pWSC13	<i>pmyo-3::bPGC::YFP</i>	
pWSC14	<i>ptrx-1::trx-1::bPGC::YFP</i>	
pWSC15	<i>pggr-1::GFP</i>	
pWSC16	<i>punc-17::flox::Arch::YFP</i>	

Table 2.8.: (continued)

Name	Description	Source
pWSC17	<i>pggr-2</i> ::GFP	
pWSC18	bPAC::RFP::TOPO	
pWSC19	<i>pggr-1</i> ::Cre	
pWSC20	<i>pggr-1</i> ::mCherry	
pWSC21	<i>pnpr-9</i> ::RCaMP19	
pWSC22	<i>punc-17</i> ::bPAC::YFP	
pWSC23	<i>pggr-2</i> ::flox::Arch::YFP	
pWSC24	<i>pggr-2</i> ::flox::Chr2::SL2::GFP	
pWSC25	SL2::Arch::YFP	
pWSC26	<i>prig-5ab</i> ::SL2::Arch::YFP	
pWSC27	<i>pmyo-2</i> ::bPAC::YFP	
pWSC28	<i>pggr-2</i> ::GCaMP3	
pWSC29	<i>pggr-2</i> ::miniSOG::SL2::GFP	
pWSC34	pCR4::SL2	
pWSC37	<i>pggr-2</i> ::flox::GFP	
pWSC38	<i>pggr-2</i> ::flox::Chr2(C128S::H134R)::SL2::GFP	
pWSC42	<i>pggr-2</i> ::HisCl::SL2::GFP	
pWSC43	<i>pggr-2</i> ::flox::HisCl::SL2::GFP	
pWSC44	bPAC::SL2::GFP	
pWSC45	<i>pggr-2</i> ::flox::bPAC::SL2::GFP	

## 2.1.10. Miscellaneous Materials

Table 2.9.: Miscellaneous materials

Description	Type	Supplier
Centrifuge tube	15 ml and 50 ml	Greiner Bio-One International GmbH, Kremsmünster (AT)
Cover Slip	Squared cover slip 22 mm	Carl Roth GmbH + Co. KG, Karlsruhe (DE)
HighPower-LED	Blue 3 W 30 lm 10° 3.1 V	ledxon GmbH, Landshut (DE)
Glass capillary	1B 100F-4	World Precision Instruments Inc. Sarasota, FL (USA)
Glass pipettes	5 ml 10 ml and 25 ml	Brand GmbH + Co. KG, Wertheim (DE)
Microcentrifuge tube	200 µl	Sarstedt AG and Co, Nümbrecht (DE)
Microcentrifuge tube	Row of 8x or 12x 200 µl	neoLab Migge GmbH, Heidelberg (DE)
Microcentrifuge tube	1.5 ml and 2 ml	Carl Roth GmbH + Co. KG, Karlsruhe (DE)
Microcentrifuge plate	96x 200 µl	Carl Roth GmbH + Co. KG, Karlsruhe (DE)
Microscope slide	Microscope slide	Carl Roth GmbH + Co. KG, Karlsruhe (DE)
Protective gloves	Rotiprotect latex and nitrile gloves	Carl Roth GmbH + Co. KG, Karlsruhe (DE)
Objective immersion oil	Immersol 518F	Carl Zeiss Microscopy GmbH, Oberkochen (DE)

Table 2.9.: (continued)

Description	Type	Supplier
Parafilm	Parafilm M	VWR International GmbH, Darmstadt (DE)
Disposable tips	All plastic tips	Carl Roth GmbH + Co. KG, Karlsruhe (DE)

### 2.1.11. Software

Table 2.10.: Software

Name	Version	Developer / Reference
Argus X1	3	Biostep GmbH, Burkhardtshof (DE)
APBS	1.4.2	Holst group software [351]
Axio Vision	4.5	Carl Zeiss Microscopy GmbH, Oberkochen (DE)
Circos	0.64	Martin Krzywinski, Canada's Michael Smith Genome Sciences Centre [352]
Citavi	4.4.0.28	Swiss Academic Software GmbH, Wädenswil (CH)
Clone Manager	9	Scientific & Educational Software, Denver CO (USA)
Fiji	Update 06/2016	Fiji contributors [353]
Galaxy	usegalaxy.org	usegalaxy.org [354]
Group-based Prediction System	2.1	The CUCKOO Workgroup [355]
ImageJ	1.47v	Wayne Rasband [356]
Inkscape	0.48.4 r9939	The Inkscape Team
Integrative Genomics Viewer	2.3.6	Broad Institute [357]
KNIME Desktop	2.12	KNIME.com AG, Zurich (CH) [358]
LSM Image Browser	4.2	Carl Zeiss Microscopy GmbH, Oberkochen (DE)
Mathematica	10	Wolfram Research, Champaign, IL (USA)
MATLAB	R2007a	The MathWorks, Inc., Natick, MA (USA)
Micro-Manager	1.4	Open Imaging, Inc. [359]
Microsoft Office	12.0.6607.1000	Microsoft Corporation, Redmond (USA)
MiKTeX	2.9	Christian Schenk
Neuroptikon	0.9.9	Janelia Farm Research Campus, Ashburn, VA (USA) [360]
Notepad++	6.5.5	Notepad++ team
Origin	9.1	OriginLab Corporation, Northampton, MA (USA)
Origin Viewer	9.1	OriginLab Corporation, Northampton, MA (USA)
PDB2PQR	2011	Holst group software [361,362]
Prism	5	GraphPad Software, Inc., La Jolla, CA (USA)
ProSA	ProSA-web	University of Salzburg [363,364]
PyMOL	0.99rc6	DeLano Scientific LLC
R	3.2.1	R Core Team [365]
RStudio	0.99.465	RStudio, Inc., Boston, MA (USA)
Serial Cloner	2.6	Serial Basics



**Table 2.10.:** (continued)

<b>Name</b>	<b>Version</b>	<b>Developer / Reference</b>
Strawberry Perl	5.18.2.1	strawberryperl.com
TeXnicCenter	2.02	The TeXnicCenter Team
VirtualDub	1.10.4	Avery Lee
ZEN 2012	8.0.0273 black edition	Carl Zeiss Microscopy GmbH, Oberkochen (DE)
ZEN lite 2012	1.1.1.0 blue edition	Carl Zeiss Microscopy GmbH, Oberkochen (DE)

## 2.2. Methods

### 2.2.1. Molecular and Microbiological methods

This section comprises of the methods used for analysis of deoxyribonucleic acid (DNA) sequences and DNA cloning.

#### 2.2.1.1. Genomic DNA extraction from *C. elegans*

Genomic DNA was extracted with the following protocol adapted from Worm-Book [366]. Ten animals from a sample plate were pooled into 2.5 µl of single egg worm lysis buffer (SEWLB) with 2% (v/v from 10 mg ml<sup>-1</sup>) Proteinase K and frozen for 20 min at -80 °C. Following freeze fracture of the animals' cuticle, animals were incubated for 1 h at 60 °C enabling Proteinase K activity. Inactivation of Proteinase K was performed in a 15 min incubation at 95 °C. Positive tested plates had their genotype confirmed by single worm analysis of at least eight sample animals; lysis procedure was as described above.

**2.2.1.1.1. DNA extraction for Whole Genome Sequencing** A variation of the genomic DNA extraction was performed for WGS analysis. The protocol was obtained from Dr. Baris Tursun, briefly:

1. Plates were rinsed with M9 and collected into an Eppendorf tubes
2. Centrifuged for 3 min at
3. Rinsed 3x with M9
4. Incubated for 2 h in M9
5. Rinsed 3x with M9

6. Centrifuged for 3 min at
7. Removed supernatant
8. Combined precipitates into 15 ml Falcon tube
9. Performed genomic DNA purification using “Gentra Puregene Kit” (Qiagen) with protocol “DNA Purification from Tissue”.

#### 2.2.1.2. Polymerase Chain Reaction

polymerase chain reaction (PCR) is a method for exponentially amplifying DNA *in vitro* using two oligonucleotides, called primers, flanking the region of interest. Different DNA polymerases were used during this work, depending on either their suitability for the template length, desired result quality or cost per reaction. Genotyping was performed with Taq polymerase or, in case of failure or single point mutants that had to be sequenced, Phusion polymerase. PCR based cloning was performed with Phusion polymerase or Extend long template DNA polymerase mix depending on product length.

The basic PCR reaction content is listed in table 2.11. The reaction volume was adapted as required by the specific conditions. The volume for analytical PCRs was scaled to a total between 20  $\mu\text{l}$  and 50  $\mu\text{l}$ , while the reaction volume for PCRs for a subsequent DNA gel extraction were scaled between 100  $\mu\text{l}$  and 500  $\mu\text{l}$ . Further, a reaction tube contained a maximum of 100  $\mu\text{l}$  and higher PCR volumes were equally distributed across multiple reaction tubes.

**Table 2.11.:** Basic PCR reaction mix.

Substance	Volume [ $\mu\text{l}$ ]
DNA Template (10 ng $\mu\text{l}^{-1}$ )	1
DNA Polymerase	0.5
Polymerase Buffer	10
Forward primer (10 pM)	0.5
Reverse primer (10 pM)	0.5
dNTP	2
ddH <sub>2</sub> O	add to 50

The PCR mix was then inserted into a . The program depended on the length of the PCR product and the DNA polymerase used. Genotyping with Taq polymerase was performed according to table 2.12. PCR products of up to 4 kbp in length were

created with the Phusion polymerase according to table 2.13. Longer PCR products were created with the Extend long template DNA polymerase mix according to table 2.14.

**Table 2.12.:** PCR reaction conditions using Taq polymerase.

<b>Process</b>	<b>Temperature [°C]</b>	<b>Time [s]</b>	<b>Repeat</b>
Initial denaturation	95	300	
Denaturation	95	15	
Primer annealing	Primer specific	30	35 times
Primer extension	68	PCR product dependent	
Final extension	68	600	
Pause	4	∞	

**Table 2.13.:** PCR reactions condition using Phusion polymerase.

<b>Process</b>	<b>Temperature [°C]</b>	<b>Time [s]</b>	<b>Repeat</b>
Initial denaturation	98	30	
Denaturation	98	10	
Primer annealing	Primer specific	30	35 times
Primer extension	72	PCR product dependent	
Final extension	72	300	
Storing	4	∞	

**Table 2.14.:** PCR reaction conditions using Extend long template DNA polymerase mix.

Process	Temperature [°C]	Time [s]	Repeat
Initial denaturation	93	120	
Denaturation	93	10	
Primer annealing	Primer specific	30	10 times
Primer extension	68	PCR product dependent	
Denaturation	93	15	
Primer annealing	Primer specific	30	25 times
Primer extension	68	PCR product dependent + i * 20	
Final extension	68	420	
Storing	4	∞	

**2.2.1.2.1. Primer design** All primers were designed using the built in functions from the program Clone Manager 9 . Further, all primers intended for genomic PCR were validated using the tool Primer-BLAST at NCBI <sup>1</sup>. This tool uses the algorithm Primer3 to find primer binding sites in a user defined database. In this case, primer pair specificity was checked against the genomes of *C. elegans* and *Escherichia coli* (*E. coli*). All primers were provided by Eurofins Genomics GmbH (Ebersberg, Germany).

**2.2.1.2.2. Colony PCR of transgenic bacteria** Colony PCR was applied to quickly screen 25 or more transformant bacteria colonies for a plasmid of interest. Reaction mix and conditions were as described for a Taq polymerase PCR reaction (2.11 and 2.12) with one distinction. A transformant bacteria colony of interest was picked with a sterile pipette tip and the latter briefly sunk into the reaction mix. The remaining bacteria on the pipette tip were deployed on a fresh LB-agar plate with the appropriate selection antibiotic and generated the backup from which colony PCR positive samples could be obtained from.

**2.2.1.2.3. RT-PCR** RNA was extracted with TRIZOL<sup>®</sup> according to suppliers recommendation. RNA purity was assessed by the  $A_{260}/A_{230}$  ratio, while RNA quantity was calculated from the  $A_{260}/A_{280}$  ratio. First strand cDNA synthesis was achieved with 200 ng template RNA and the AccuScript<sup>™</sup> kit according to manufacturer's specification. The cDNA was used as template for a PCR.

<sup>1</sup>[\\*http://www.ncbi.nlm.nih.gov/tools/primer-blast/](http://www.ncbi.nlm.nih.gov/tools/primer-blast/)

### 2.2.1.3. Site-directed mutagenesis

Site-directed mutagenesis was performed with Q5 polymerase according to the specifications from “Q5<sup>®</sup> Site-Directed Mutagenesis Kit”.

### 2.2.1.4. Gel electrophoresis

Gel electrophoresis of DNA is a method to measure DNA length. The gel was produced by dissolving between 1 % and 3 % agarose (w/v) in 1x TAE buffer with heat from a microwave oven. Agarose concentration was chosen as a function of the expected DNA size, with higher agarose content for smaller DNA fragments. After cooling the solution to about 50 °C, it was poured to a chamber with a linear grid to make pockets in which the samples could be pipetted to. Each sample was added one sixth in volume of loading dye before pipetting it to the pockets. In a separate pocket, 5 µl to 10 µl of either “GeneRuler 100 bp DNA ladder” or “GeneRuler 1 kb DNA ladder” from Fermentas has been pipetted as a reference for DNA length. Electroporation was conducted at 5 V cm<sup>-1</sup> to 8 V cm<sup>-1</sup> for 45 min in 1x TAE buffer.

After the electrophoresis, the DNA in the gel was colored with the marker ethidium bromide (EtBr) in a 0.1 % (w/v) water solution during an incubation of at least 10 min. After staining, the agarose gel was imaged with a . Image acquisition parameters were set for optimal DNA band pattern analysis. DNA fragment size was inferred from the ladder size, if required through ImageJ gel analysis tool .

In case of a subsequent DNA gel extraction, the EtBr solution was renewed prior to staining. UV exposure was limited to 30 % light intensity and exposure time was reduced to as low as possible. The gel was photographed as mentioned above after the bands of interest had been excised from the gel.

### 2.2.1.5. DNA gel extraction

DNA fragment extraction from agarose gel was performed according to the manual from “Gel/PCR DNA Fragments Extraction Kit”, with the following modifications. All centrifugation steps but drying and elution were performed at 1500 RCF. DNA elution was performed with 25 µl of elution buffer preheated at 70 °C for at least five minutes on a heat block set also at 70 °C. In case that a high DNA yield was required, a second elution step was performed as described above, increasing the average DNA concentration by about 30 %.

#### 2.2.1.6. DNA purification

The following methods were used to purify DNA:

**2.2.1.6.1. PCA Extraction** Phenol chloroform isoamyl alcohol (PCA) extraction is a method to separate DNA of salts and proteins. 0.5 volumes of a phenol:chloroform:isoamyl alcohol (25:24:1) were added to the solution containing DNA. The solution was emulsified by 1 min on a vortexer. The emulsion was then centrifuged for five minutes at 16 200 RCF. 2.5 volumes of 0.12 mM sodium acetate in Ethanol were added to the water phase and the solution was stored at  $-80^{\circ}\text{C}$  for 30 min. A further centrifugation for 1 hour at  $4^{\circ}\text{C}$  and 16 200 RCF pelleted the DNA. The pellet was washed with 500  $\mu\text{l}$  70 % ethanol and a centrifugation step for 1 h at  $20^{\circ}\text{C}$  and 16 200 RCF pelleted the purified DNA. The supernatant was disposed and the DNA dried at  $20^{\circ}\text{C}$  for 1 h. The pellet was then reconstituted in  $\text{ddH}_2\text{O}$ .

**2.2.1.6.2. PCR product purification** The PCR product purification was done as described in the manual of the "Gel/PCR DNA Fragments Extraction Kit". In order to enhance the amount of DNA extracted from the solution, all centrifugation steps but drying and elution were performed at 1500 RCF. DNA elution was performed with 25  $\mu\text{l}$  of elution buffer preheated at  $70^{\circ}\text{C}$  for at least five minutes on a heat block set also at  $70^{\circ}\text{C}$ .

#### 2.2.1.7. DNA restriction digest

DNA restriction digest allows to specifically cut DNA according to recognition sites of restriction enzymes, producing linear DNA for analysis or further processing. All restriction digests were performed according to suppliers recommendation. Concurrent usage of two enzymes in one restriction digest preparation were planned either with Double Digest Finder - NEB<sup>2</sup> and DoubleDigest Calculator - Thermo Fisher Scientific<sup>3</sup>. Sequential digest with a PCA purification in between were performed when activity of one of the restriction enzymes was below 50 % in the recommended buffer according to the above mentioned tools. Analytical or preparative restriction digests were planned respectively with at least 5 or 20 fold over digestion.

<sup>2</sup><https://www.neb.com/tools-and-resources/interactive-tools/double-digest-finder>

<sup>3</sup><https://www.thermofisher.com/de/de/home/brands/thermo-scientific/molecular-biology/thermo-scientific-restriction-modifying-enzymes/restriction-enzymes-thermo-scientific/double-digest-calculator-thermo-scientific.html>

### 2.2.1.8. Measurement of DNA concentration

DNA concentration was measured either in a NanoDrop ND-1000 or a Genova photometer. During this work the DNA probe used had a  $^{260}/_{280}$  absorbance ratio of  $1.8 \pm 0.1$ .

### 2.2.1.9. DNA dephosphorylation

DNA dephosphorylation was achieved with the enzyme antarctic phosphatase according to suppliers recommendation. Reaction contents for the dephosphorylation were as described in table 2.15 and reaction conditions were as described in table 2.16.

**Table 2.15.:** AP reaction condition.

Substance	Volume [ul]
DNA	1 $\mu$ l to 28 $\mu$ l ( $1 < x < 10 \mu$ g)
AP reaction buffer	1 $\mu$ l
AP	1 $\mu$ l
ddH <sub>2</sub> O	add to 30 $\mu$ l

**Table 2.16.:** Dephosphorylation conditions.

Process	Temperature [°C]	Time [min]	Information
Dephosphorylation	37	5 x	x from table 2.15
Enzyme inactivation	65	5	
Pause	4	$\infty$	

### 2.2.1.10. DNA fragment ligation

The ligation of DNA ends was performed with the reaction contents described in table 2.17. The reaction was performed by an incubation for 1 h at room temperature or for 16 h at 16 °C followed by a T4 ligase inactivation during an incubation period of 10 min at 65 °C. A 2x ligation buffer was preferred, usage depended on availability of highly concentrated educts. For ligation reactions, a certain DNA fragment was considered vector when the fragment also coded for a resistance gene.

[ $\mu$ l] is the volume of DNA to be used in the ligation in  $\mu$ l. It was calculated with following formula:

**Table 2.17.:** T4 ligation reaction condition.

<b>Substance</b>	<b>Amount</b>
Linear insert DNA	100 fmol to 300 fmol
Linear vector DNA	20 fmol to 60 fmol
T4 ligase	1 $\mu$ l
2x or 10x ligation buffer	10 $\mu$ l or 2 $\mu$ l
ddH <sub>2</sub> O	add to 20 $\mu$ l

$$[\mu l] = \frac{660[\frac{g}{mol * bp}] * [fmol] * [bp]}{[\frac{\mu g}{\mu l}]} * 10^9 \quad (2.1)$$

Where  $660[\frac{g}{mol * bp}]$  is the average molecular weight of a nucleotide pair, [fmol] is the amount of DNA for the reaction, [bp] is the DNA length in base pairs and  $[\frac{\mu g}{\mu l}]$  is the stock DNA concentration.

#### **2.2.1.11. Heat shock transformation**

Heat shock transformation of chemical competent *E. coli* DH5 $\alpha$  strain was the usual method for transformations during this work. The bacteria were stored in aliquots of 200  $\mu$ l at  $-80^\circ\text{C}$ . For transformation, an aliquot was allowed to thaw on ice. About 1 ng of plasmid were mixed to the bacteria, followed by an incubation of 30 min on ice. Then a heat shock was applied for 45 s at  $42^\circ\text{C}$ . The bacteria were again incubated on ice for 2 min. 500  $\mu$ l of LB-medium were pipetted to the bacteria, followed by an incubation for 1 h at  $37^\circ\text{C}$  in a shaker. The bacteria were then centrifuged for 5 min at 1500 RCF, 500  $\mu$ l of medium was discarded and the bacteria were re-suspended to the remaining medium. The medium was then plated on a LB-agar plate containing the antibiotic corresponding to the resistance gene. The plates were incubated for 16 h at  $37^\circ\text{C}$  and stored at  $4^\circ\text{C}$ .

The products from the In-Fusion<sup>TM</sup> PCR Cloning were heat-shock transformed in supplied *E. coli* bacteria as described in the accompanying manual.

#### **2.2.1.12. Plasmid DNA preparation**

Plasmid DNA preparation was performed according to suppliers recommendation using one of the following two kits: NucleoSpin Plasmid Kit for volumes about 5 ml



and NucleoBond PC 100 for volumes about 100 ml of *E. coli* culture (table 2.3). The former was used to test plasmids after transformation and growth of bacteria colonies in LB-agar plates, while the latter was used to prepare great quantities of plasmid for further usage. Notably, DNA intended for *C. elegans* micro injection was obtained with the NucleoBond PC 100 kit, since the propanol precipitation step lead to a high purity product.

#### 2.2.1.13. Small region DNA sequencing

Small region sequencing assignments were sent to Eurofins Genomics GmbH (Ebersberg, Germany) according to their recommendations. Briefly, 15  $\mu\text{l}$  sample DNA were mixed with 2  $\mu\text{l}$  of 10 pmol  $\mu\text{l}^{-1}$  sequencing primer and sent in a 1.5 ml safe-lock tube. The usual sequencing length was around 1 kbp.

### 2.2.2. *C. elegans* handling

This section comprises of the methods used for cultivation and handling of *C. elegans*. For microscopy imaging see section 2.2.3, for behavior analysis see section 2.2.4.

#### 2.2.2.1. Cultivation

*C. elegans* animals were cultivated based on the protocols described in WormBook [367] as follows. Animals were cultivated on NGM supplemented with 0.019 % (w/v) streptomycin sulfate [252] petri dish ((20, 60 and 140) mm in diameter according to required animal quantity). These plates have been kindly provided by Heike Fettermann, Mona Höret and Kerstin Zehl with help from Negin AzimiHashemi, Anke Hermann and Tim Phillip Waldow. About 300  $\mu\text{l}$  of *E. coli* bacteria, strain OP50-1, were seeded in the previous day to the NGM petri dish as food source for *C. elegans*. Animals were transferred to a seeded plate either with an ethanol sterilized eyelash (eyelash pick, single animal), a heat sterilized platinum wire (worm pick, few animals) or a heat sterilized spatula (piece of NGM with many animals, “to chunk”). Animals were kept at 16 °C for up to two weeks as backup for the main lineage cultivated at 20 °C. Some strains or experiments required higher growth temperatures and were therefore incubated at 25 °C. Transgenic animals that required ATR were incubated in the dark in plates inoculated with 300  $\mu\text{l}$  of OP50-1 bacteria with 2  $\mu\text{l}$  ATR (stock: 100 mM ATR in ethanol) [156, 206]. Plates containing histamine were

poured as previously described [237]. All plates were sealed with paraffin foil and, if darkness was required, wrapped in aluminum foil. Handling of light sensitive strains was performed in a darkened room with residual light intensities below the threshold required for activation of the light sensor.

**2.2.2.1.1. Male generation** Male animals were generated either by incubation of L4 larvae animals at 30 °C for about 4 h or by incubation in M9 buffer supplemented with 10% ethanol (v/v) for 30 min. The L4 animals were singled to seeded plates and incubated for one generation. The males from the first generation were used in a cross with their own genotype to generate a higher yield of males for subsequent crosses.

**2.2.2.1.2. Crosses** Crosses between two genotypes were performed in NGM plates with a torus shaped OP50-1 bacteria lawn ( $R \approx 7$  mm and  $r \approx 3$  mm). Up to 7 hermaphrodite L4 animals from the first strain and a five fold amount of male adult animals from the second strain were transferred to the center of the torus. The hermaphrodites were singled into fresh plates after an incubation for 1 d at 20 °C and cross efficiency was assessed by the amount of hermaphrodites that generated male animals. Depending on the genotype, F1 heterozygous males were used in a second cross or F1 heterozygous hermaphrodites were singled into seeded plates. The F2 animals were singled to seeded plates in an amount sufficient to reduce the probability of not finding a homozygous animal with all required traits to below 0.5%.

**2.2.2.1.3. Genotyping** *C. elegans* genotyping was performed with the genomic DNA (2.2.1.1) as template for a PCR (2.2.1.2) flanking the mutation of interest. Single point mutants that could not be analyzed by differential restriction enzyme recognition site (2.2.1.7) were sent for sequencing (2.2.1.13).

**2.2.2.1.4. Decontamination** Decontamination was performed depending on the contamination present. For mold contamination, a piece of affected NGM was transferred with a spatula to one side of a seeded plate. After about 15 min, adult animals that reached the other side of the plate were transferred to a new seeded plate. Bacteria and yeast contamination were cleaned by pipetting 20  $\mu$ l of 1:1 1 N sodium hydroxide (NaOH) : 5% sodium hypochlorite (NaClO) (v/v) to an *E. coli* free region of a seeded plate and transferring approximately 50 gravid adult animals to the droplet.

After about 1 d, young larvae were transferred to new seeded plates. In both cases, plates were scored for successful decontamination about five days after the decontamination procedure.

### 2.2.2.2. DNA micro injection in *C. elegans*

DNA micro injection into young adult hermaphrodite *C. elegans* gonads is a standard technique to obtain transgenic animals [368] with an extrachromosomal DNA array [369]. Transgenic F2-worms were isolated to create a new *C. elegans* transgenic strain. Extrachromosomal DNA is not transmitted to the whole offspring, therefore transgenic strains have to be maintained through selection. This selection occurs on a marker co-injected with the DNA of interest. During this work, either a fluorescent protein or a morphology mutant recovery marker was co-injected. DNA micro injection was performed as described by Mello *et al.* [142].

**2.2.2.2.1. Injection mix** DNA was prepared into injection mixes of 30  $\mu\text{l}$  volume as described in table 2.18 with a final concentration  $\geq 100 \text{ ng } \mu\text{l}^{-1}$ . The injection mix was centrifuged for 15 min at 16 200 RCF and the upper 15  $\mu\text{l}$  were transferred to a new 1.5 ml tube and used for injections.

**Table 2.18.:** Injection mix content.

Substance	Volume or final concentration
Injection buffer	3 $\mu\text{l}$
Marker plasmid	1 $\text{ng } \mu\text{l}^{-1}$ to 100 $\text{ng } \mu\text{l}^{-1}$
Plasmid(s) of interest	1 $\text{ng } \mu\text{l}^{-1}$ to 150 $\text{ng } \mu\text{l}^{-1}$
pUC19 <sup>4</sup>	add to 100 $\text{ng } \mu\text{l}^{-1}$
ddH <sub>2</sub> O	add to 30 $\mu\text{l}$

**2.2.2.2.2. Injection** Glass needles were made with the puller prior to micro injections. About 0.3  $\mu\text{l}$  of the injection mix was pipetted over the opening of the needle. During loading, a cover slip with a dry agar pad (2% (w/v) agar in ddH<sub>2</sub>O) was fixed to a microscope slide. The breath moistened agar pad was then carved at one edge

<sup>4</sup>Empty vector used for increasing the DNA concentration, if required.

and a droplet of halocarbon oil was applied in its vicinity. The filled needle was attached to the air pressure outlet, which was itself fixed to the micro manipulator. The microscope slide containing the agar pad was placed in the Zeiss Axiovert 40 CFL and the tip of the needle was aligned to one of the carvings in the agar pad under the halocarbon oil. The needle tip was broken upon contact to the agar carving and air pressure application.

One to five young adult hermaphrodite worms were transferred to the halocarbon oil with the eyelash pick and their bodies were cleansed from bacteria. Animals were transferred to clean region of the agar pad and the DNA was injected to both gonads. 3  $\mu$ l of M9-buffer were pipetted to release the animals from the agar and the animals were transferred with the eyelash pick to seeded plates. The NGM-plates were cultivated at 20 °C for 3 d to 5 d. The selection was done based on the marker used in the injection mix. Injections for this thesis were partially performed by Dr. Elisabeth Fischer, Dr. Sebastian Wabnig, Dr. Christian Schultheis, Negin AzimiHashemi, Jatin Nagpal.

#### **2.2.2.3. Extrachromosomal array integration by UV irradiation**

100 L4 animals were transferred to a NGM plate without bacteria and placed in a Stratagene UV crosslinker (Stratalinker) with the lid removed. Animals were irradiated with two pulses of 33.3 mJ interspaced by 30 s. Worms were transferred in batches of 5 animals to seeded plates and cultivated at 20 °C until starvation (F3 generation). Plates were chunked to seeded 140 mm plates and allowed to grow for 3 d at 20 °C. 800 transgenic, mosaicism free animals were singled to seeded plates and cultivated at 20 °C until the F2 generation grew up. Plates were screened for the pervasive presence of the transgenic marker and, if possible, no obvious behavioral or morphological deficit. Integrated arrays were back-crossed into the background strain used during injection for at least 4 times before further experiments were performed. The strain with the lowest transmission was selected for this procedure in cases where more than one strain coding for the same transgene, but with a different extrachromosomal array and all other strain properties being equal, had to be selected for array integration.

#### **2.2.2.4. EMS mutagenesis**

Ethyl methanesulfonate (EMS) mutagenesis was performed as described earlier with double the amount of animals screened [370].

#### **2.2.2.5. *C. elegans* cell dissociation and culture**

Cell dissociation and culture from L4 stadium animals was performed as described earlier [371, 372]. Cell culture was performed to access the practicability of RIS cell enrichment for cell specific RNA sequencing. Large scale animal cultivation, RNA extraction, RNA sequencing and data compilation were performed by Rebecca D. McWhirter, Kalen J. Petersen and David M. Miller, III.. Results were provided as part of a cooperation for analysis in this work (section A.5, p. 228).

#### **2.2.2.6. RNAi**

RNA Interference (RNAi) by feeding was performed as described earlier [373].

### **2.2.3. Microscopy**

This section comprises of the microscopy imaging techniques used for qualitative and quantitative analysis of *C. elegans* performed during this work.

#### **2.2.3.1. Stereo microscopy**

A SMZ 645 stereo microscope (Nikon) was used for *C. elegans* handling. Illumination and synchronized image acquisition were performed with a system based on an Arduino shutter developed and described in my Diploma Thesis. The required code is listed in appendix B.5.

#### **2.2.3.2. DIC microscopy**

Differential interference contrast (DIC) microscopy facilitated DNA micro injection 2.2.2.2 and swimming assays 2.2.4.1. For imaging, an Axiovert 200 (Zeiss) with a 10x (Zeiss A-Plan 10x / 0.25) or a 100x oil immersion (Zeiss C-Plan 100x / 1.3 oil) objective was used together with an AxioCam MRm (Zeiss) camera and AxioVisionAC

4.5 software or a Canon PowerShot G9 camera attached in place of one ocular with costume firmware controlled by a costume Arduino based signal generator .

### 2.2.3.3. Qualitative analysis of fluorescence

Qualitative fluorescence microscopy was used to handle and analyze transgenic *C. elegans* worms expressing fluorescent proteins. Extrachromosomal array expression level, transmission efficiency and mosaicism rate were inferred from the analysis in a Leica MZ 16F microscope equipped with filter sets for red fluorescent protein (RFP), green fluorescent protein (GFP) and cyan fluorescent protein (CFP)..

### 2.2.3.4. Quantitative analysis of fluorescence

Quantitative imaging were performed in one of the following systems, depending on the required resolution for downstream analysis.

- Axiovert 200 (Zeiss) with a 10x (Zeiss A-Plan 10x / 0.25) or a 100x oil immersion (Zeiss C-Plan 100x / 1.3 oil) objective together with an AxioCam MRm (Zeiss) camera and AxioVisionAC 4.5 software.
- Axio Observer Z1 (Zeiss) with a 10x (Zeiss A-Plan 10x / 0.25) or a 100x oil immersion (Zeiss C-Plan 100x / 1.3 oil) objective together with a ORCA-Flash2.8 (Hamamatsu) or an ORCA-Flash4.0 (Hamamatsu).
- Zeiss Cell Observer SD with a 100x oil immersion (alpha Plan-Apochromat 100x/1.46 Oil DIC (UV)) objective, Laser 488 nm and two Rolera EM-C2 cameras.

The worms were paralyzed in order to suppress *C. elegans* movement during acquisition by either 2.5% agar pad (w/v in ddH<sub>2</sub>O) with 10 µl 50 mM sodium azide (NaN<sub>3</sub>) in M9 buffer or 10% agar pad (w/v in ddH<sub>2</sub>O) with polystyrene beads on a microscope slide. The latter restrained the animals, but did not completely abolish movement, therefore it was applied when neuronal and or muscle activity was desired, i.e. for calcium imaging experiments or coelomocyte fluorescence analysis. Images for quantification experiments were acquired with the same settings in a single microscope.

## 2.2.4. *C. elegans* behavior analysis

All behavior assays were performed with young adult animals (up to 2 d after L4 stadium), unless otherwise stated. Experiments were repeated at least thrice in different weeks to account for intrinsic variability of *C. elegans* population.

### 2.2.4.1. Analysis of swimming behavior

The assay was performed on a 96 flat bottom well plate. Up to 10 animals were scored per well and an according amount of wells were prepared by adding 80  $\mu$ l of melted NGM. After solidification, 80  $\mu$ l of M9 buffer were added to the wells. Animals were transferred to the well under red light (650 nm  $\pm$  50 nm) and incubated for at least 15 min in dark. A video of the whole well was acquired with a Canon G9 camera on an Axiovert 200 (Zeiss) microscope using red transmission light (650 nm  $\pm$  50 nm). A HBO 50 lamp (Zeiss, 470 nm  $\pm$  20 nm and 0.2  $\mu$ W mm<sup>-2</sup>) was used for blue light activation. The video was opened in VirtualDub and the number of thrashes (defined as a complete sinusoid movement in a swimming cycle) were counted per 10 s and calculated in Hz for each time bin. Further, quiescent animals in a 10 s time bin were attributed a swimming frequency of 0 Hz. Therefore, the analysis also takes into account the episodic nature of swimming behavior in *C. elegans* [374].

### 2.2.4.2. Multimodal Illumination Tracker

Analysis of single worm posture and locomotion parameters were performed with a variant of a previously described worm tracker [176,375]. The addition of a mechanical shutter, between projector and microscope, synchronized to the light stimulation as well as a band pass filter (650 nm  $\pm$  50 nm) for the transmission light, ensured an ambient light power during tracking below 20  $\mu$ W mm<sup>-2</sup> (measured between 200 nm and 1000 nm). Single animals were transferred to unseeded NGM plates under red light (650 nm  $\pm$  50 nm) in a dark room and incubated for 15 min in darkness. Tracking was performed as described. A Konstanz Information Miner (KNIME) workflow was created as part of this thesis to filter data points from erroneously evaluated movie frames and streamline data analysis B.1.1. Briefly, velocity of animals was allowed to be between  $-2000 \mu\text{m s}^{-1}$  to  $2000 \mu\text{m s}^{-1}$ ; the length variation was allowed to be 10 % or 25 % of the mean length before photoactivation (for experiments where length variation was not or was expected, respectively). Data points were further excluded when time and level were not consistent with illumination protocol. If a

movie had more than 15 % of its data points excluded by the criteria mentioned, then the whole movie was excluded from further analysis.

Stop was defined as a movement rate below 0.04 worm lengths per second, with worm length defined as the mean length across all data points or across all data points before photoactivation, for experiments where length variation was not or was expected, respectively. This threshold is equivalent to a speed of  $45 \mu\text{m s}^{-1}$  and a body length of  $1150 \mu\text{m}$ . The speed threshold was used by Caspar-Elias Glock in his master thesis. The length-normalized stop definition used here also takes into account the difference in size across animals.

#### 2.2.4.3. Multi Worm Tracker

Population wide tracking of *C. elegans* was performed on a multi worm tracker [376]. Tracking was performed with red transmission light ( $650 \text{ nm} \pm 50 \text{ nm}$ ). The data analysis procedure was streamlined with a KNIME workflow B.1.3.

#### 2.2.4.4. Spot Tracker

Tracking of a fluorescent spot in freely behaving animals on NGM was achieved by a custom built system based on the image-free opto-mechanical tracker [377].

#### 2.2.4.5. Contraction assays

Analysis of *C. elegans* body contraction was performed with a module from the single worm tracker 2.2.4.2 [176]. Movie acquisition with a higher resolution was attained with a 10x objective in a tradeoff to manual control of the stage position. The data analysis procedure was streamlined with a KNIME workflow B.1.2.

**2.2.4.5.1. bPAC C1V1 co-expression experiment.** Body contraction analysis for co-expression of bPAC and C1V1, a red-shifted rhodopsin, were performed in dim light conditions. Light intensities were set to such levels, that C1V1 photoactivation alone was not enough to elicit a detectable body contraction. Further, bPAC photostimulation was reduced to 10 s to minimize the bPAC induced contraction observed upon long stimulation protocols. Yellow light ( $530 \text{ nm}$ ) for C1V1 photoactivation was set to  $100 \mu\text{W mm}^{-2}$  and applied from 10 s to 30 s. Blue light ( $470 \text{ nm}$ ) for bPAC photoactivation was set to  $70 \mu\text{W mm}^{-2}$  and applied from 20 s to 30 s. Mean body length



before illumination was calculated from the first 3 s, while body length during illumination was calculated from 37 s to 30 s (figure 2.1). The ratio of both lengths was calculated and used as descriptor for body contraction enhancement due to bPAC photoactivation concomitant to C1V1 activity.

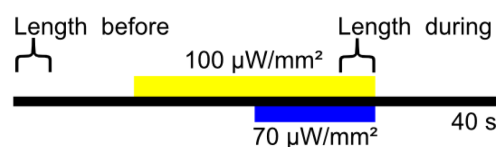


**Figure 2.1.:** Contraction assay protocol for bPAC and C1V1 co-photostimulation. The ratio between the last three seconds of illumination to the first three seconds of the experiment was calculated. Light intensities were set such, that C1V1 alone could not elicit detectable body contraction.

## 2.2.5. Cholinergic survival upon sustained cAMP signaling induced by bPAC photostimulation

Animals were exposed to  $800 \mu\text{W mm}^{-2}$  blue LED light (470 nm) for up to 40 h on an OP-50 seeded NGM plate. At designated time points animals were scored for spontaneous pharyngeal pumping as a marker for survival. Dead animals were excluded from further analysis. Three consequent mechanical stimuli were applied to the posterior end of the live animals and reaction to any of the stimuli was scored as survival of cholinergic neurons.

## 2.2.6. Miscellaneous methods

### 2.2.6.1. Light power measurement

Light power was measured with a powermeter at the focal plane while the sensor was positioned at the expected worm's position. Ambient light power was measured by pointing the sensor to the brightest source of ambient light, no spectral correction was performed.

### 2.2.6.2. Light wavelength measurement

Light wavelength measurement was performed with a Compact Fiber Spectrometer with the fiber end positioned at the expected worm's position. Ambient light spec-

trum was measured by randomly pointing the sensor in the room while the spectrometer was set to persistence mode to acquire the different ambient light wavelengths. The later measurement was qualitative and only used in conjunction to the quantitative measurement of ambient light power.

### **2.2.7. Data analysis**

This section contains information on advanced data analysis or where multiple methods generated the data for a single analysis. Further, analysis performed on data contributed by colleagues (see appendix A) is described here.

#### **2.2.7.1. Video pre-processing**

Low contrast, low signal to noise ratio videos were pre-processed to improve tracker reliability. First, avi videos were converted to image sequences in VirtualDub, this process was automated by an ImageJ script contributed by Dr. Christian Schultheis. Image background was subtracted and noise was reduced with a Gaussian blur in an automated workflow in KNIME B.1.6. The enhanced images were converted into avi video files for processing in the tracker software of choice.

#### **2.2.7.2. Behavioral phenotype analysis by clustering**

Data from the Multimodal illumination tracker 2.2.4.2 from different group of animals was analyzed for similarity in behavior over time in response to a light stimulus. Analysis was performed on the mean speed and mean bending angle changes upon photostimulation. The mean response of a group over time was passed to a dynamic time warping (DTW) algorithm [378] to quantify the resemblance of behavior between groups. A hierarchical clustering algorithm further quantified the difference between multiple groups. The data similarity was plotted in a dendrogram while the mean change of behavior is visualized in a heat map. This analysis was performed in R B.2.3.

#### **2.2.7.3. WGS Data analysis**

The analysis of whole genome sequencing (WGS) data was performed in the Galaxy server [354]<sup>5</sup>, with the workflow for variant calling CloudMap implemented [379].

---

<sup>5</sup><https://usegalaxy.org/>

Result tables were processed in a KNIME workflow B.1.4 for visualization in Circos [352].

#### 2.2.7.4. RNA-Seq data analysis

The RIS-enriched set of genes was analyzed for the presence of neuronal receptor and neuropeptide genes. An overview of the data set was generated by gene ontology (GO) term enrichment by WormMine [380] and visualization with the tool REViGO [381]. There, GO term size was selected from the *C. elegans* database and the semantic similarity measure was performed by a Resnik algorithm with normalized output [382].

#### 2.2.7.5. Manual tagging of EM images and data analysis

High pressure freezing followed by electron microscopy (HPF-EM) images with feature calling were obtained from Dr. Szi-chieh Yu (figure 2.2, section A, p. 225). Features were tagged in ImageJ as follows. SV and docked synaptic vesicle (docked SV) were tagged with an oval selection. DCV, docked dense core vesicle (docked DCV), large vesicle (LV), endosome (ENDO), unknown feature type 1 (unknown-type-1) and unknown feature type 2 (unknown-type-2) were tagged either with an oval or elliptical selection. LV and ENDO were also marked with a spline fitted polygon selection, in cases where oval or elliptical selections were not optimal. DP and PM were tagged with a spline fitted polygon selection. The selections were stored as region of interest (ROI) files and analyzed by an automated ImageJ script B.4.1. Image overlays were also exported for manual verification. The resulting feature descriptions and ROI coordinates were processed by a KNIME workflow B.1.5 with distance calculations performed in R B.2.1. Note that the DP ROI was set comprising of an extracellular area that is not existent in reality (figure 2.2, right). Therefore, DP ROIs sizes were not analyzed. The extension of the ROI was performed to facilitate distance calculations. The distance of a docked SV to the DP through the PM was calculated to the nearest border cross between DP and PM.

The shape of the PM was analyzed by the isoperimetric quotient, which describes the ratio from the perimeter of the PM divided by the perimeter of a circle with equal area as the feature of interest. The range of the isoperimetric quotient is from 1 to  $+\infty$ , where a circle has a value of 1 and a line equals  $+\infty$ . The isoperimetric quotient was calculated as described in formula 2.2:

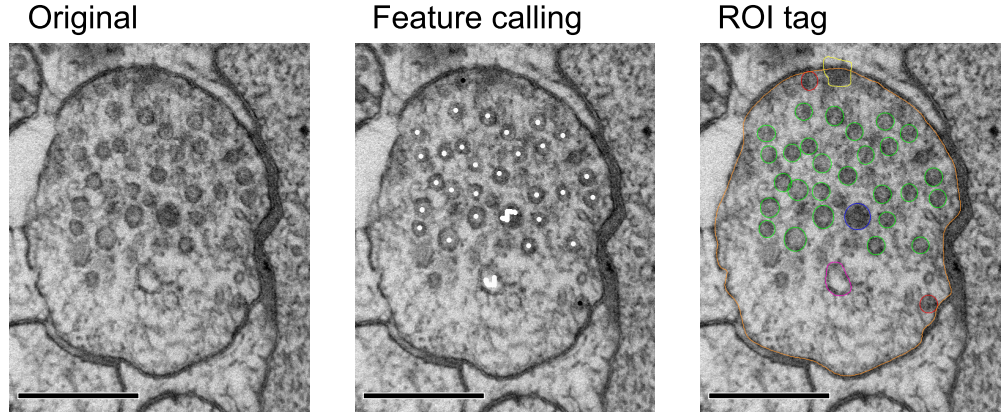


**Figure 2.2.: EM quantitative image analysis.**

Ultrastructure of cholinergic synapses was analyzed in EM images (left: original image). Feature calling was performed by Dr. Szi-chieh Yu (center). ROIs were defined for each feature of interest and stored for quantitative analysis of the synaptic profile (right). Green: SV, red: docked SV, blue: DCV, yellow: DP, orange: PM, magenta: LV. Scale bar 200 nm.

Left and center provided by Dr. Szi-chieh Yu, right generated by myself.

$$\text{Isoperimetric quotient} = \frac{\text{Perimeter}}{2 \times \pi \times \sqrt{\frac{\text{Area}}{\pi}}} \quad (2.2)$$

The volume of SVs was calculated using the diameter of an equiareal circle and considering membrane thickness of 3.4 nm, as described in formula 2.3:

$$\text{SV}_{\text{Volume}} = \frac{4}{3} \times \pi \times \left( \frac{2 \times \sqrt{\frac{\text{SV}_{\text{Area}}}{\pi}} - 6.8}{2} \right)^3 \quad (2.3)$$

#### 2.2.7.6. 3D reconstruction and analysis of synapses

#### 2.2.7.7. Analysis of mPSC kinetic parameters

Original recordings and mPSC data were obtained from Dr. Jana F. Liewald (section A, p. 225). mPSC location was obtained from the mPSC data files and used to export a range of data points containing the mPSC from the original recording. mPSC were synchronized to the maximum amplitude and descriptive statistics were calculated. Furthermore, the kinetic parameters  $\tau_{on}$  and  $\tau_{off}$  were analyzed based on a fit

of a mono-exponential growth or decay function, respectively. Data analysis was automated in a KNIME workflow (section B.1.8, p. 277). Constraints for analysis were that mPSC must neither have another mPSC in the same time window, nor in the rise or decay time as described in the mPSC data file. Further, only kinetic data for mPSC with a fit quality of  $p \leq 0.001$  were analyzed, exemplary fit quality plots for  $\tau_{off}$  are shown in figure 2.3 (green and blue passed fit quality constraints). Further, only mPSCs that had both,  $\tau_{on}$  and  $\tau_{off}$  successfully calculated were analyzed.

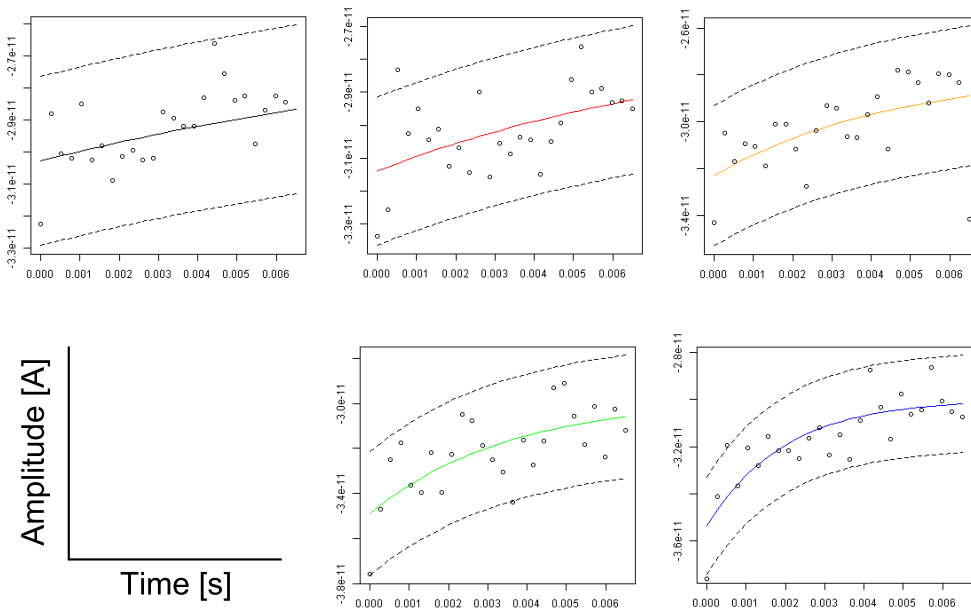


**Figure 2.3.:** Exemplary fit curves for mPSC kinetic analysis of  $\tau_{off}$ .

26 data points starting at the peak amplitude of a mPSC were fitted with a mono-exponential decay curve. Fit curves are shown with 95% confidence interval (CI). Mono-exponential fit color as description of the fit quality as follows. Black:  $p > 0.05$ , red:  $p \leq 0.05$ , yellow:  $p \leq 0.01$ , green:  $p \leq 0.001$  and blue:  $p \leq 0.0001$ .

## 2.2.8. Statistical inference

Frequentist inference was applied during this work and significance is given as p-value (not significant  $ns$  :  $p \geq 0.05$ ; \* :  $p \leq 0.05$ ; \*\* :  $p \leq 0.01$ ; \*\*\* :  $p \leq 0.001$ ). Statistical analysis was performed with a test suitable for the data set, based on a decision tree by Field *et al.* [383]. A description for parametric (table 2.19) and non-parametric (table 2.20) tests performed during this thesis follows. Some data

visualizations throughout this thesis use 95 % CI.

**Table 2.19.:** Data type and statistical hypothesis test performed for when assumptions of parametric tests were met.

<b>Data type</b>	<b>Statistical hypothesis test</b>
One categorical predictor (more than two categories, different entities) and one continuous response variables.	One-way independent ANOVA
One categorical predictor (more than two categories, same entities) and one continuous response variables.	One-way repeated measures ANOVA
One categorical predictor (two categories, different entities) and one continuous response variables.	Independent Student's T-Test
One categorical predictor (two categories, same entities) and one continuous response variables.	Dependent Student's T-Test
One categorical predictor and one categorical response variables.	Pearson $\chi^2$
One continuous predictor and one continuous response variables.	Pearson correlation
Two categorical predictor and one continuous response variables.	Two-way ANOVA
Two or more categorical predictor and one continuous response variables.	Factorial ANOVA <sup>6</sup>
Two or more categorical predictor and two or more continuous response variables.	Factorial MANOVA

**Table 2.20.:** Data type and statistical hypothesis test performed for when assumptions of parametric tests were not met.

<b>Data type</b>	<b>Statistical hypothesis test</b>
One categorical predictor (more than two categories, different entities) and one continuous response variables.	Kruskal-Wallis Test
One categorical predictor (more than two categories, same entities) and one continuous response variables.	Friedman's ANOVA
One categorical predictor (two categories, different entities) and one continuous response variables.	Mann-Whitney U Test
One categorical predictor (two categories, same entities) and one continuous response variables.	Wilcoxon matched-pairs Test
One categorical predictor and one categorical response variables.	Pearson $\chi^2$
One continuous predictor and one continuous response variables.	Bootstrap correlation
Two or more categorical predictor and one continuous response variables.	Robust factorial ANOVA <sup>7</sup>
Two empirical cumulative distribution functions (eCDFs).	Two-sample Kolmogorov-Smirnov Test

<sup>6</sup>Further specified in repeated, independent or mixed, depending if the same, different or mixed predictor category, respectively.

<sup>7</sup>Further specified in repeated, independent or mixed, depending if the same, different or mixed predictor category, respectively.

### 2.2.8.1. Multiple testing correction

Multiple testing correction has been performed with Bonferroni correction in preliminary tests and where required. Tukey's HSD and Dunnett's test were used for multiple pairwise comparisons where possible.

### 2.2.8.2. Effect size

The effect size  $d_{Cohen}$  was calculated with formula 2.4 as described by [384], where  $m_1$  and  $m_2$  are the means of both distributions and  $s_{pol}$  is the pooled standard deviation, as given by formula 2.5. There,  $n_1$  and  $n_2$  are the group sizes and  $s_1$  and  $s_2$  the respective group standard deviations. The 95% CI was calculated as described by formula 2.7 [385].

$$d_{Cohen} = \frac{m_1 - m_2}{s_{pol}} \quad (2.4)$$

$$s_{pol} = \sqrt{\frac{((n_1 - 1) \times s_1^2) + ((n_2 - 1) \times s_2^2)}{n_1 + n_2 - 2}} \quad (2.5)$$

$$\sigma = s_{pol} \times \sqrt{\frac{n_1 + n_2 - 2}{n_1 + n_2}} \quad (2.6)$$

$$CI_{95\%} = d_{Cohen} \pm 1.96 \times \sqrt{\frac{\sigma}{\sqrt{n_1 + n_2}}} \quad (2.7)$$

### 2.2.8.3. Statistical analysis software

Statistical analysis presented in this thesis was performed either in KNIME, Mathematica, MATLAB, Microsoft Excel, Origin, Prism or R (section 2.1.11, p. 54).





## 3. Results

Neuronal modulation of the presynapse is crucial for an organism to adapt to its environment.

In this work I used photoactivatable adenylyl cyclase from *Beggiatoa spp.* (bPAC) as a modulator of the second messenger cAMP in cells of *C. elegans*. Specifically in neurons, this acute optogenetic manipulation of cAMP levels conferred the possibility to analyze the signal transduction pathway that leads to presynaptic modulation with a spatiotemporal resolution not achievable by pharmacological assays.

Firstly, the subset of cholinergic neurons in *C. elegans* was selected as model for analysis of the mechanisms of presynaptic modulation. Secondly, characterization of a GABAergic interneuron with hitherto unknown function in adult *C. elegans* behavior was performed.

### 3.1. cAMP modulates cholinergic synaptic output

Characterization of cholinergic presynaptic modulation by cAMP signaling pathway activation required expression of bPAC in *C. elegans* neurons.

Expression in cholinergic neurons was achieved by subcloning the coding sequence for bPAC YFP fusion protein into a vector with the promoter of *unc-17*. In order to facilitate animal care, the bPAC construct was injected in combination with a plasmid coding for mCherry expression in the pharynx of the *C. elegans*. Thus, transgenic animals could be selected by red fluorescence without bPAC photoactivation during animal handling. Three extrachromosomal arrays were obtained, from which one was selected for integration. One integration event was obtained and out-crossed four times into N2 and *lite-1(ce314)* genotypes, further referenced as bPAC N2 and bPAC *lite-1(ce314)*, respectively.

bPAC was found in neuronal cell bodies and processes, as expected for a soluble protein expressed under the promoter of *unc-17* (figure 3.1) .

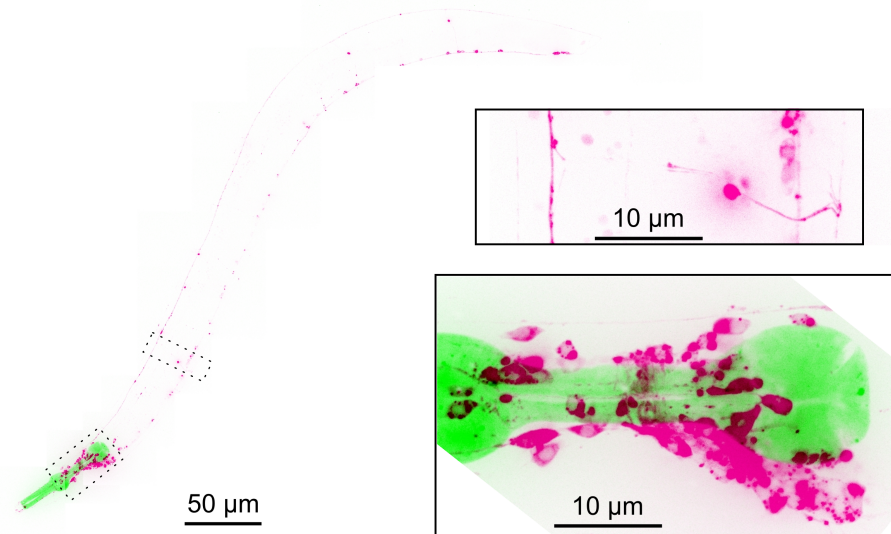


**Figure 3.1.: Expression of bPAC in cholinergic neurons.**

YFP tagged bPAC was present in cholinergic neuron cell bodies and processes, as well as in commissures (upper inset). Furthermore, the promoter specific for cholinergic neurons also expressed bPAC in cholinergic interneurons in the head (lower inset). The pharynx was labeled with a red co-injection marker.

Maximum intensity projection, magenta: bPAC::YFP, green: mCherry co-injection marker. Scale bar 50 µm, inset 10 µm.

### 3.1.1. bPAC enhances neuronal output

#### 3.1.1.1. Swimming bout frequency increase

Swimming behavior of *C. elegans* in low viscosity liquids is more sensitive to changes in locomotion than its behavior on solid substrate [386]. Therefore, a primer experiment for behavioral modulation is the analysis of swimming bout frequency. bPAC N2 animals frequently coiled during the swimming assays (data not shown), thereby hindering analysis. In order to overcome this problem, animals expressing bPAC in mutants of the intrinsic light receptor from *C. elegans*, LITE-1, were analyzed. These animals have an intrinsically lower swimming rate than N2 wild type (wt) worms. Nonetheless, bPAC *lite-1(ce314)* animals increased their swimming frequency by 60% upon photoactivation (figure 3.2). This effect reverted to wt levels in the first ten seconds after termination of photoactivation.

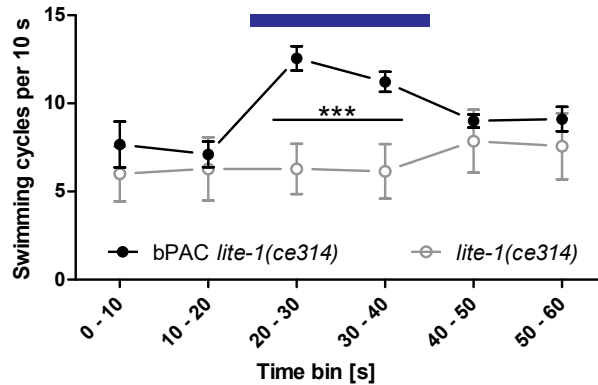


**Figure 3.2.: bPAC photoactivation enhances swimming behavior.**

bPAC photoactivation increases swimming bout frequency by 60%. The effect reverted after termination of photoactivation.

Photoactivation denoted by blue bar.  $n_{\text{bPAC}} = 9$ ,  $n_{\text{control}} = 7$  Mean  $\pm$  SEM. ANOVA, Bonferroni correction. \*\*\* :  $p \leq 0.001$ .

### 3.1.1.2. Speed and body posture modulation on solid substrate

Since bPAC photoactivation increased swimming bout frequency, analysis of behavioral modulation on solid substrate allows richer data acquisition and analysis. bPAC photoactivation increased locomotion speed for about 5 s, 2 s after light onset (figure 3.3 top left). The speed returned to wt levels thereafter, but in conjunction with an increase in the mean bending angle of the animal (figure 3.3 bottom left). The increased bending angles were visible by eye (figure 3.3 top right). The calculation of the mean bending angle implemented in the tracker [176, 387] is summarized in the schematic in the bottom left of figure 3.3. Briefly, the image of the animal is binarized and thinned to a single pixel backbone (orange line). Then, 13 equidistant points are placed on the backbone (pink) and the deviation from  $180^\circ$  is calculated for all 11 angles (first angle  $\alpha$  shown in blue). The mean deviation from  $180^\circ$  ( $\bar{\alpha} = \sum_{i=1}^{11} |\alpha_i|$ ) is calculated and for simplicity further referenced as mean bending angle. The linear correlation between mean speed and mean bending angle between 20 s to 40 s is highly significant, with Pearson  $r = -0.87$  ( $p < 0.0001$ , two-tailed Students' T-Test).

Both these behavior effects had a high signal to noise ratio and thus were selected for further analysis and later for the mutant screening.

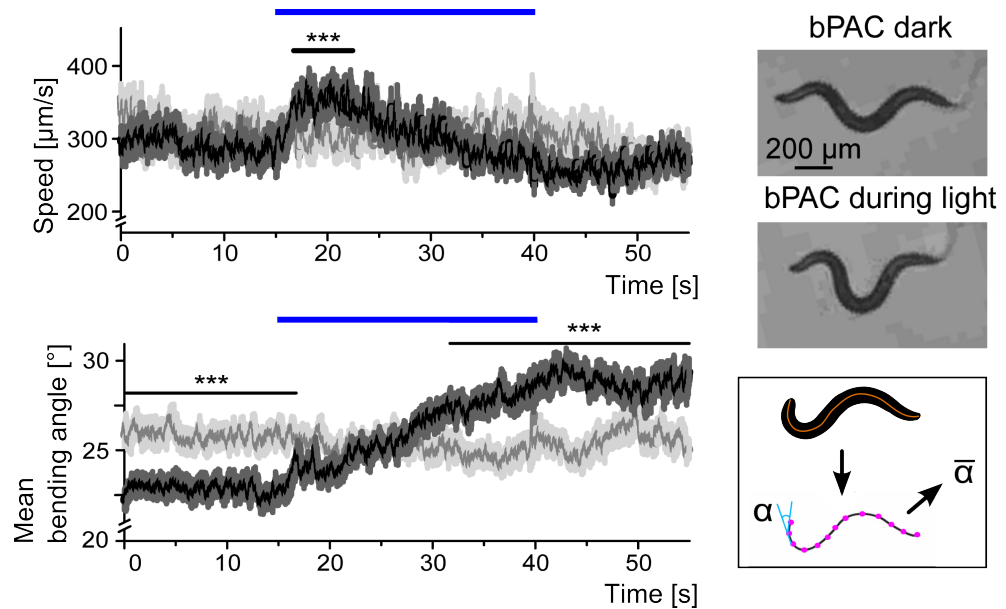


**Figure 3.3.: Transient speed increase followed by stronger body bending during bPAC photostimulation.**

The mean speed of transgenic animals was transiently increased for about 5 s during photostimulation (top left). The speed reverted to wt levels during photoactivation while the mean bending angle increased. The increased bending angles are sustained after photoactivation (bottom left). Representative image depicting the increased bending angles during bPAC photostimulation (top right). Schematic illustrating the calculation of the mean bending angle from 11 equally distributed angles on the skeleton of the animal is shown in the bottom right (only first angle marked).

$n \geq 45$ . Mean  $\pm$  SEM. Students' T-Test, Bonferroni correction. *ns* :  $p \geq 0.05$ ; \* :  $p \leq 0.05$ ; \*\* :  $p \leq 0.01$ ; \*\*\* :  $p \leq 0.001$ , significance region with at least 95 % of data points meeting p-value description.

**3.1.1.2.1. bPAC effect on body posture persists after light deactivation.** The increase in bending angles persisted after the end of photostimulation. In order to identify to which extent this effect could still be observed, movies with 90 s acquisition post illumination were analyzed. The increased bending angle was observed up to 35 s after photostimulation (figure 3.4).

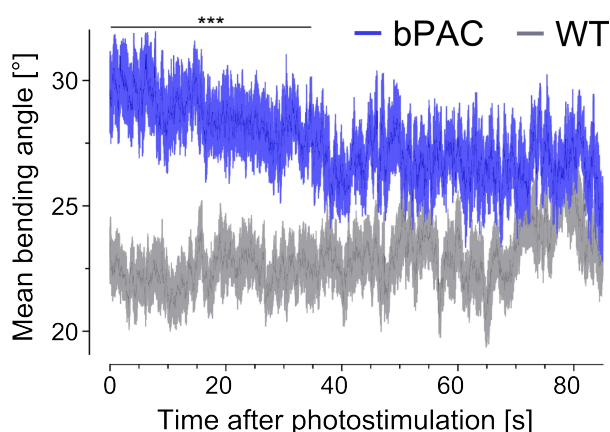


**Figure 3.4.: Increase in bending angles observed up to half a minute after light deactivation.** bPAC photoactivation induced increase in bending angles compared to wt was observed up to 35 s after light was turned off.  $n \geq 15$ . Mean  $\pm$  SEM. Students' T-Test, Bonferroni correction. *ns* :  $p \geq 0.05$ ; \* :  $p \leq 0.05$ ; \*\* :  $p \leq 0.01$ ; \*\*\* :  $p \leq 0.001$ , significance region with at least 95 % of data points meeting p-value description.

Although a significant change in mean bending angle could be observed for such extended periods, tracking and video acquisition reliability were reduced, i.e. due to animals crawling to the edge of the plate. Thus, a compromise was chosen, with analysis of 15 s after end of the photoactivation. This protocol could nonetheless indicate mutants that reverted to the behavior before illumination in significantly shorter periods than wt.

**3.1.1.2.2. bPAC photoactivation elicits a small body contraction.** Furthermore, during the last ten seconds of bPAC photoactivation in cholinergic neurons, a small contraction of the body to about 2 % in the mean could be detected (figure 3.5). This contraction persisted after the end of the photostimulation, but could not be discerned for as long as the increased bending angles described above (section 3.1.1.2.1, p. 83), due to the lower signal to noise ratio. A significant contraction was observed up to 10 s after end of the illumination.

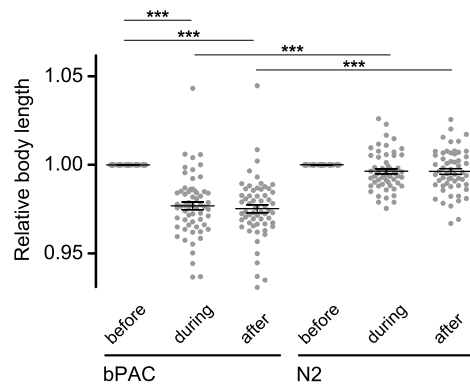


**Figure 3.5.: bPAC elicits a small body contraction.**

bPAC photoactivation leads to 2% contraction that persists after photostimulation light deactivation. Only the last 10 s of stimulation were analyzed during illumination.

$n_{\text{bPAC}} = 61$ ,  $n_{\text{N2}} = 56$ . Scatter plot with mean  $\pm$  SEM. ANOVA, Bonferroni correction. \*\*\*:  $p \leq 0.001$ .

Due to the low signal to noise in the body length measurements, body length was also not an appropriate descriptor for the characterization of mutants that impaired bPAC evoked behavioral modulation. bPAC induced behavioral changes in speed and mean bending angle during crawling on solid substrate were selected for mutant characterization.

**3.1.1.2.3. bPAC effect is not LITE-1 dependent.** *C. elegans* light perception is mainly conferred by the protein LITE-1. Upon exposure to UV- and blue light this receptor induces an avoidance behavior, which encompasses change in movement directionality and speed.

On the one hand, the data quality obtained from the multimodal illumination tracker (section 2.2.4.2, p. 69) enables to study the cAMP signaling pathway triggered by bPAC in cholinergic neurons ultimately leading to the behavior modulation described above. On the other hand, a few canonical mutations planned for subsequent analysis were known to emphasize the light avoidance behavior, i.e. the CAPS/UNC-31 mutant *unc-31(n1304)*. bPAC is  $K_M$  is at light intensities were about one quarter of response caused by LITE-1 was observed [202,388]. Therefore, the light insensitive *lite-1(ce314)* variant was crossed with these mutants to ensure that the behavior elicited by photoactivation is due to bPAC and cAMP signaling.

The bPAC elicited behavior modulation in wild type was compared to the effect in *lite-1(ce314)* mutants. The increased speed and bending angles observed in N2 background were very similar in *lite-1(ce314)* background, albeit the later had a reduced basal speed (figure 3.6). Since the elicited effect on behavior was similar also in its progression through time, analysis of mutant strains could be performed either in N2 or *lite-1(ce314)* background, depending on the known light sensitivity of the mutant

in question.

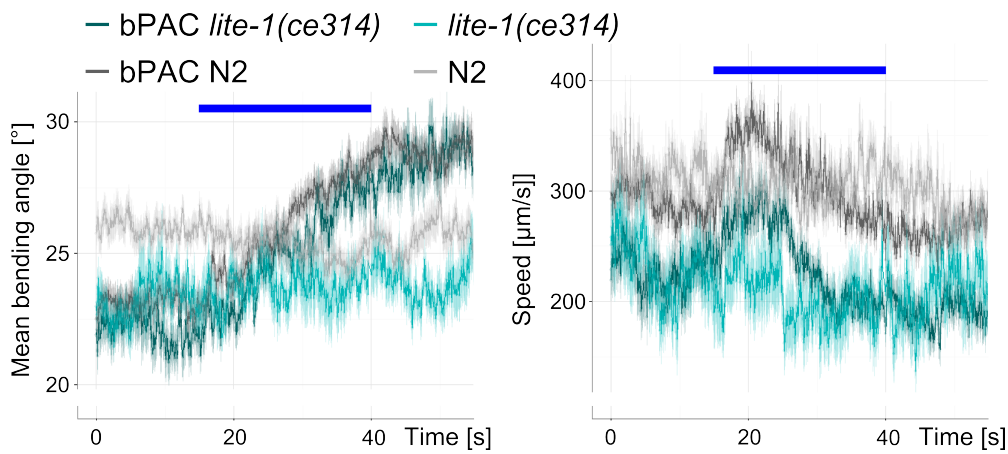


**Figure 3.6.: Modulation of behavior by bPAC is LITE-1 independent.**

bPAC *lite-1(ce314)* animals showed a similar modulation of behavior upon photostimulation compared to bPAC N2 animals. The mean speed was increased in the same time domain as in bPAC N2 animals, albeit bPAC *lite-1(ce314)* animals displayed a lower basal speed before illumination (left). The bending angle was increased as in bPAC N2 animals (right).  
n  $\geq$  15. Mean  $\pm$  SEM.

**3.1.1.2.4. bPAC requires intrinsic depolarization for behavioral modulation.** To test if the effects of bPAC photostimulation require intrinsic neuronal activity, bPAC was co-expressed with the hyperpolarizing, yellow light activated rhodopsin H<sup>+</sup>-pump MAC. bPAC photoactivation in absence of the MAC chromophore ATR led to significant body contraction in the range of 1.25%. In presence of ATR, though, bPAC and MAC elicited a significant body elongation that was not different to the elongation observed by hyperpolarization of cholinergic neurons in animals solely expressing MAC (figure 3.7 left). Furthermore, bPAC MAC co-activation lead to a reduction of movement speed, in contrast to the speed increase observed in bPAC MAC co-expressing animals without ATR (figure 3.7 right). Consequently, bPAC elicited effects require neuronal intrinsic depolarization and thus bPAC could be used to augment opsin mediated optogenetic depolarization.

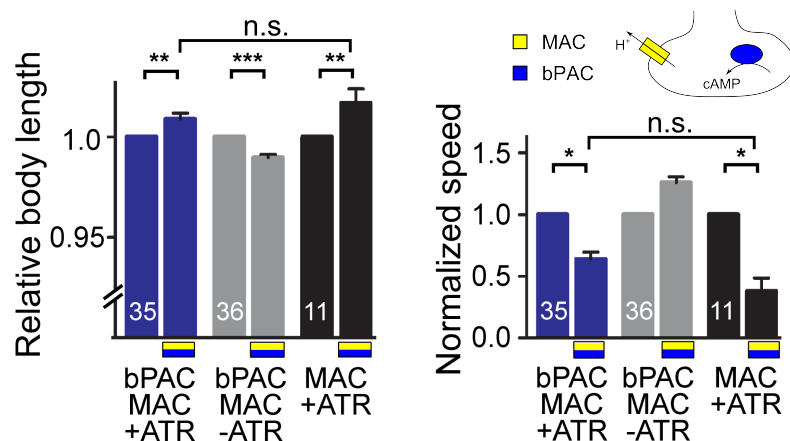


**Figure 3.7.: bPAC co-expression with the hyperpolarizer MAC shows bPAC dependency to intrinsic depolarization.**

bPAC MAC co-activation without the MAC chromophore ATR led to body contraction. In contrast, in presence of ATR, co-activation led to body elongation equivalent to MAC photoactivation alone (left). Co-activation of bPAC and MAC reduced speed similar to MAC photoactivation alone, in contrast to bPAC MAC photostimulation without ATR, where speed was increased (right).

Pictogram of experiment (top right). MAC+ATR hyperpolarized the pre-synapse, inhibiting the effect of bPAC on behavior.

All conditions with MAC, bPAC as indicated. Mean  $\pm$  SEM. ANOVA, Bonferroni correction. *ns* :  $p \geq 0.05$ ; \* :  $p \leq 0.05$ ; \*\* :  $p \leq 0.01$ ; \*\*\* :  $p \leq 0.001$ .

### 3.1.1.2.5. bPAC augments opsin mediated optogenetic depolarization of cholinergic neurons.

As described above, bPAC requires intrinsic neuronal depolarization and thus co-expression of a cation channel with bPAC could increase the neuronal output upon (optogenetic) depolarization. To test this hypothesis, bPAC was co-expressed with the light activated channelrhodopsin chimera C1V1 and body length ratio before and during illumination was calculated (section 2.2.4.5.1, p. 70). Light intensities were set to such levels, that C1V1 photoactivation alone could not induce a detectable body contraction. Neither did bPAC photostimulation with each or both light sources led to a detectable body contraction, nor did bPAC C1V1 co-photostimulation with yellow light do so (figure 3.8). Accordingly, bPAC can be used to modulate the neuronal output during (optogenetically) induced depolarization.



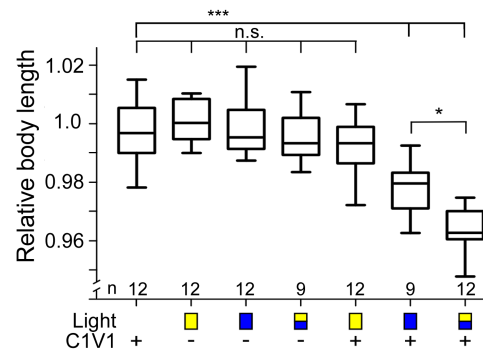


**Figure 3.8.: bPAC augments C1V1 induced depolarization.**

bPAC photostimulation for 10s did not lead to a detectable body contraction (box 2 to 4), and neither did bPAC C1V1 co-photostimulation with yellow light (box 5). A small body contraction was observed when bPAC and C1V1 were co-photoactivated with blue light (box 6). bPAC further enhanced the contraction upon co-photostimulation with both light colors (box 7) and therefore might be used to enhance rhodopsin based optogenetic cholinergic neuron stimulation.

All groups express bPAC in cholinergic neurons, illumination and C1V1 expression as denoted. Median, IQR, whiskers: 2.5 to 97.5. ANOVA, Bonferroni correction. *ns* :  $p \geq 0.05$ ; \* :  $p \leq 0.05$ ; \*\* :  $p \leq 0.01$ ; \*\*\* :  $p \leq 0.001$ .

**3.1.1.2.6. Increased cAMP degradation impairs bPAC-induced effects** In order to confirm that the effect of bPAC to behavior was mediated by cAMP, bPAC N2 animals were crossed into a PDE-4D<sub>gof</sub> expression strain. This strain has reduced basal cAMP levels in all neurons. In cholinergic neurons, bPAC photoactivation led to an increase of cAMP that was promptly degraded by the PDE-4D<sub>gof</sub>. bPAC PDE-4D<sub>gof</sub> animals show a transient increase in the mean bending angle (figure 3.9 left) as well as an increased speed upon photoactivation (figure 3.9 right). This is in contrast to bPAC N2 animals, where a transient increase in speed is observed, as well as lasting increase in bending angles. Thus, expression of PDE-4D<sub>gof</sub> impaired the effect of bPAC on behavior upon photostimulation and confirmed that the bPAC-induced effects were cAMP dependent.

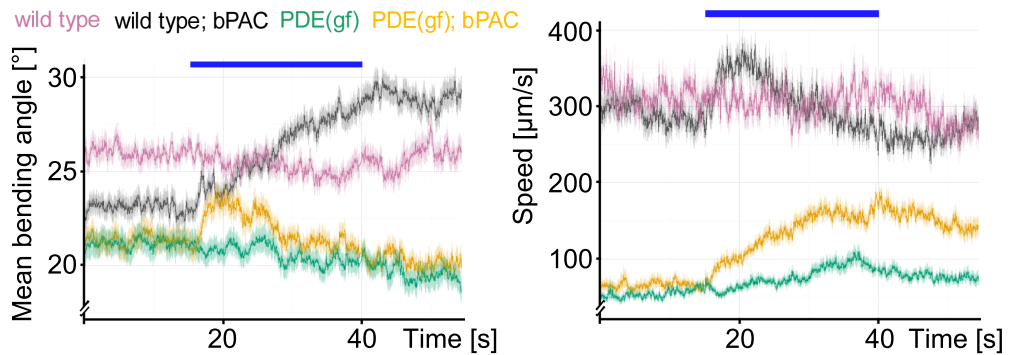


**Figure 3.9.: Expression of PDE-4D<sub>gof</sub> impairs the effect of bPAC on behavior.**

Upon photoactivation a transient increase in mean bending angles and a lasting increase in speed were observed, in contrast to the photoactivation of bPAC in N2 animals. Hence, bPAC-induced effects were cAMP dependent.

n = 64, 77, 69 and 64. Mean ± SEM.

### 3.1.1.3. G<sub>αS</sub> gain of function coupled to homeostatic adaptation not present in acutely induced bPAC effects

In order to compare the effects of constantly increased cAMP concentration onto behavior, we analyzed the a G<sub>αS</sub> constitutive active mutant, *acy-1(ce2)* (ACY-1(P260S)) [205]. The gain of function mutation of the adenylyl cyclase leads to increased body bends during locomotion. In our hands, these animals also display an increased body bend count per second, in the same range as reported in the literature (about 20% compared to wt, figure 3.10 top left). In addition, equally aged adult animals are smaller than their wt counterpart and do not show an increased absolute speed (figure 3.10 top right and bottom left). In contrast to wt animals, *acy-1(ce2)* mutants show significantly increased mean body angles (figure 3.10 bottom right), although not as strongly as the increased bending angle observed due to bPAC photostimulation. In contrast to bPAC without photostimulation, the mean bending angle is increased in *acy-1(ce2)* animals. This might be due to an adaptation to different levels of cAMP production of *acy-1(ce2)* versus bPAC in the dark state. Indeed, a gain of function mutation of the acetylcholine receptor (AChR) subunit ACR-2, expressed in some classes of cholinergic motoneurons in the ventral cord [305], leads to an imbalance of neuronal activity. A homeostatic, neuropeptidergic pathway is activated to modulate the excitation-inhibition imbalance posed by ACR-2(gf) by increasing the expression of *flp-18* and *flp-1* [389]. Both neuropeptides act on GABAergic cells to increase their SV fusion probability, therefore dampening the effect of ACR-2(gf) mutant [389]. FLP-18

peptides also act on BWM cells, likely inducing relaxation [389]. Since this homeostatic pathway is activity dependent [389], it is likely triggered in *acy-1(ce2)* mutants.

Therefore, analysis of the effect of cAMP on the pre-synaptic neuromodulation must be achieved by an acute stimulus. bPAC photoactivation allows to increase pre-synaptic output without activation of homeostatic pathways.

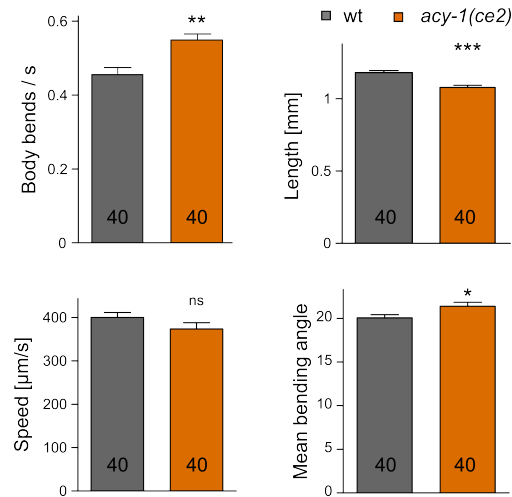


**Figure 3.10.: Adenylyl cyclase gain of function mutant.**

Behavior and morphology analysis of the gain of function mutation of the neuronal adenylyl cyclase, *acy-1(ce2)*.

An additional difference between ACY-1(gf) and bPAC induced behavior is that ACY-1 is expressed in neurons and BWMs of *C. elegans* and localized to the membrane [390], while bPAC was expressed solely in cholinergic neurons and is a soluble protein. *C. elegans* has only one gene coding for the PKA/KIN-1 catalytic and regulatory subunit (*kin-1* and *kin-2*, respectively), but these genes produce each 12 and 3 protein isoforms [391, 392]. The usual organization of PKA/KIN-1 holoenzyme restricts its diffusion by binding to the  $\alpha$ -kinase anchoring protein (AKAP), as well as by N-myristoylation of the regulatory domain [392, 393] and thus membrane anchoring. This organization ensures localized cAMP signaling, for instance by targeting of PKA/KIN-1 to the vicinity of  $G_{\alpha S}$  [393]. Thus, in addition to possible different basal cAMP levels between *acy-1(ce2)* and bPAC expressing animals in the dark, protein localization might lead to the discrepancy in observed phenotypes.

Hence, the adaptation to increased cAMP signaling observed in *acy-1(ce2)* animals in the form of low increase in the mean bending angle as well as the lack in absolute

speed increase reinforce the requirement of temporal control of cAMP concentration in order to achieve behavioral modulation.

#### 3.1.1.4. Enhancement of miniature postsynaptic currents amplitude upon bPAC photostimulation

The behavior experiments confirmed that the effect of bPAC is cAMP pathway dependent and requires intrinsic neuronal depolarization (section 3.1.1.2, p. 81). Thus, bPAC probably acts upstream of the synaptic vesicle release machinery.

To further characterize the pathway, electrophysiology measurements of BWM cells during bPAC photoactivation in cholinergic neurons were performed by Dr. Jana F. Liewald. She also measured Chr2(H134R) in cholinergic neurons for a comparison of the effect of both actuators on mPSCs. Both optogenetic tools increased the mPSC rate during photostimulation (figure 3.11 left). In contrast to Chr2(H134R), though, bPAC photostimulation increased the mPSC amplitude by about 30 % (figure 3.11 center). Further, Chr2(H134R) photostimulation led to a peak depolarization in the range of 1200 pA at the start of the illumination and a constant, albeit lower, depolarization throughout photostimulation. This depolarization was not present in animals expressing bPAC, during photostimulation (figure 3.11 right).

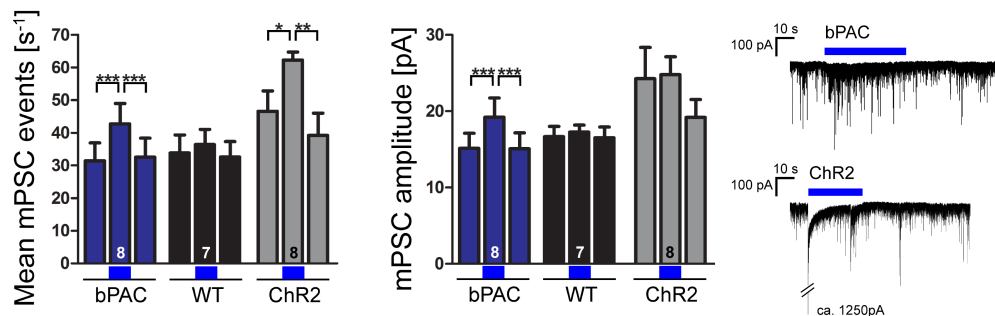


**Figure 3.11.: Body wall muscle cell voltage clamp measurements for bPAC or Chr2 stimulated cholinergic neurons.**

bPAC as well as Chr2(H134R) photoactivation increased the mPSC rate (left). bPAC, in contrast to Chr2(H134R), also increased the mPSC amplitude during photostimulation (center). wt mPSCs were not affected by illumination. Original recording from bPAC (top right) and Chr2(H134R) (bottom right), where bPAC lacked depolarization caused by photoactivation, as observed in Chr2(H134R). Mean  $\pm$  SEM. Intra group = paired Student's T-Test, inter group = Student's T-test. *ns* :  $p \geq 0.05$ ; \* :  $p \leq 0.05$ ; \*\* :  $p \leq 0.01$ ; \*\*\* :  $p \leq 0.001$ . Measurement and analysis by Dr. Jana F. Liewald.

Due to the patch pipette solution composition, the source of the mPSCs could not be discerned between cholinergic and GABAergic origin. Since cholinergic and GABAergic neurons are in a feed-forward neuronal network in *C. elegans*, it is important to distinguish if the effect of bPAC is due to modulation of the cholinergic synapse or due to (additional) GABAergic potentiation. I generated therefore a strain expressing bPAC in cholinergic neurons with mutant vesicular GABA transporter (*unc-47(e307)*). Photoactivation of bPAC in the *unc-47(e307)* background led to increased body contraction (Mean  $\pm$  SEM: 3.7%  $\pm$  0.9%, n = 14. About 85% increase compared to bPAC wt). This increased contraction is in accordance to the inability of muscle relaxation, but behavior measurement is not sensitive enough that we could rule out a GABAergic potentiation. Hence, Dr. Jana F. Liewald measured a comparable relative increase in mPSC rate and amplitude in these mutants compared to bPAC expressed in wt animals (figure 3.12). The absolute mPSC rate was reduced in *unc-47(e307)* animals, since GABAergic neurons are impaired in filling SVs with GABA and could thus not be measured.

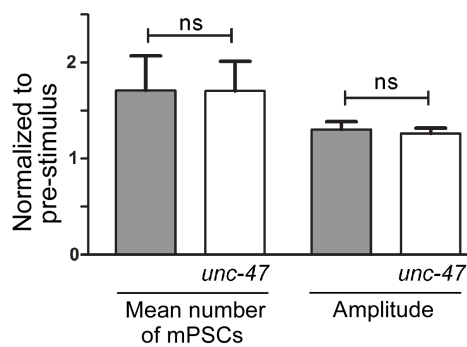


**Figure 3.12.: bPAC effect on mPSCs is not dependent on GABAergic feedback.**

The relative change in mPSC rate (left) and amplitude (right) is not dependent on GABAergic neurotransmission.

All groups with bPAC expression.  $n_{wt} = 8$ ,  $n_{unc-47(e307)} = 11$ . Mean  $\pm$  SEM. Student's T-test. ns:  $p > 0.05$ . Measurement and analysis by Dr. Jana F. Liewald.

### 3.1.2. bPAC induced effects require neuropeptidergic signaling at the presynapse

The mPSC amplitude increase could be caused by neuropeptidergic modulation of either the pre- or postsynapse. In order to first determine if neuropeptide release was induced by cAMP signaling activation, a reporter system was co-expressed with bPAC. The reporter chosen is a fusion construct of *nlp-21* and the fluorescent protein Venus. The former is a gene coding for a neuropeptide expressed in cholinergic

neurons, while the latter is a YFP based fluorescent protein. Thus, DCV cargo in the cells of interest also contained Venus protein. Upon DCV release in *C. elegans*, neuropeptides (and Venus) diffuse through the pseudocoelom, until endocytosed and degraded by scavenger cells called coelomocytes. Since there is a delay between endocytosis and degradation by coelomocytes, accumulation of Venus in these cells can be used for a quantitative analysis of neuropeptide release (figure 3.13 scheme left).

Upon photostimulation of bPAC, neuropeptidergic signaling was enhanced, as observed by a higher fluorescence of the Coelomocytes (figure 3.13). Importantly, neither neuronal depolarization for an equivalent time frame by ChR2(C128S,H134R), nor illumination of animals without bPAC expression led to an increase of fluorescence in the coelomocytes. Thus, bPAC photostimulation and cAMP signaling induced neuropeptide release.

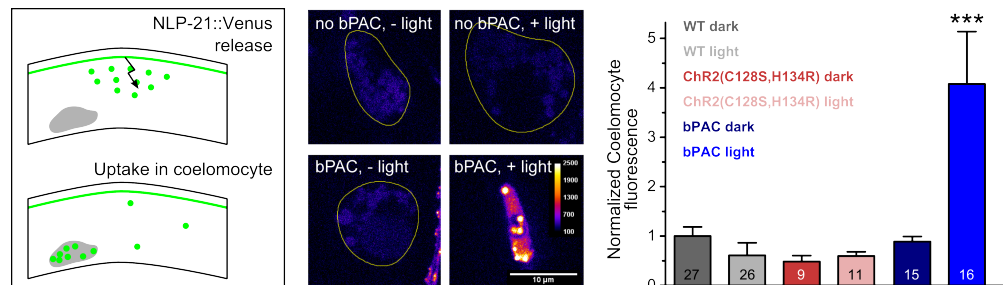


**Figure 3.13.: bPAC photostimulation led to neuropeptide secretion, as monitored by coelomocyte fluorescence.**

In *C. elegans*, neuropeptides released into the pseudocoelom are eventually endocytosed and degraded by scavenger cells called coelomocytes (scheme left). Normalized coelomocyte fluorescence was increased upon bPAC photoactivation (center, false colored representative coelomocyte image; right, quantification). In contrast, ChR2(C128S,H134R)-induced neuronal depolarization was not sufficient for neuropeptide release.

Normalized to wild type without photostimulation. Mean ± SEM. ANOVA, Bonferroni correction. \*\*\* :  $p \leq 0.001$ .

In *C. elegans*, DCV release is highly dependent on the CAPS/UNC-31 protein. Co-expression of bPAC and NLP-21::Venus in *unc-31(n1304)* mutants, lacking CAPS/UNC-31, inhibited bPAC-induced increase in coelomocyte fluorescence (figure 3.14, top left). This is in accordance to studies with unstimulated release of DCVs in *unc-31(e928)* mutants [394]. This was not due to reduced NLP-21::Venus expression in *unc-31(n1304)* mutants, since neuronal cell bodies and processes had an increased fluorescence compared to wt animals (figure 3.14 bottom left and center). Further,

bPAC photoactivation did not reduced the amount of fluorescent puncta in the VNC of mutant animals (figure 3.14 bottom right).

Furthermore, Dr. Jana F. Liewald measured the effect of bPAC photoactivation on mPSC in *unc-31(n1304)* mutant background. On the one hand, the mutant showed a reduced basal mPSC rate, but bPAC increased the rate upon photoactivation (figure 3.15 left). On the other hand, the bPAC induced increase in mPSC amplitude was abolished in the *unc-31(n1304)* mutant background (figure 3.15 right). Therefore, neuropeptidergic signaling was required to induce mPSC amplitude increase by bPAC and confirmed that the bPAC-elicited effect partially requires neuropeptidergic signaling. The next experiments were defined to discern between a pre- or post-synaptic neuropeptide receptor.

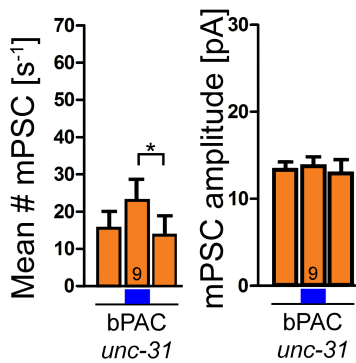


**Figure 3.15.: *unc-31(n1304)* impaired bPAC-induced mPSC amplitude increase.**

bPAC photoactivation increased the mPSC rate in *unc-31(n1304)* background, albeit the reduced basal rate (left). In contrast, bPAC photoactivation effect on mPSC amplitude was impaired by the *unc-31(n1304)* mutation (right).

Mean ± SEM. Intra group = paired Student's T-Test, inter group = Student's T-test. ns :  $p \geq 0.05$ ; \* :  $p \leq 0.05$ ; \*\* :  $p \leq 0.01$ ; \*\*\* :  $p \leq 0.001$ . Measurement and analysis by Dr. Jana F. Liewald.

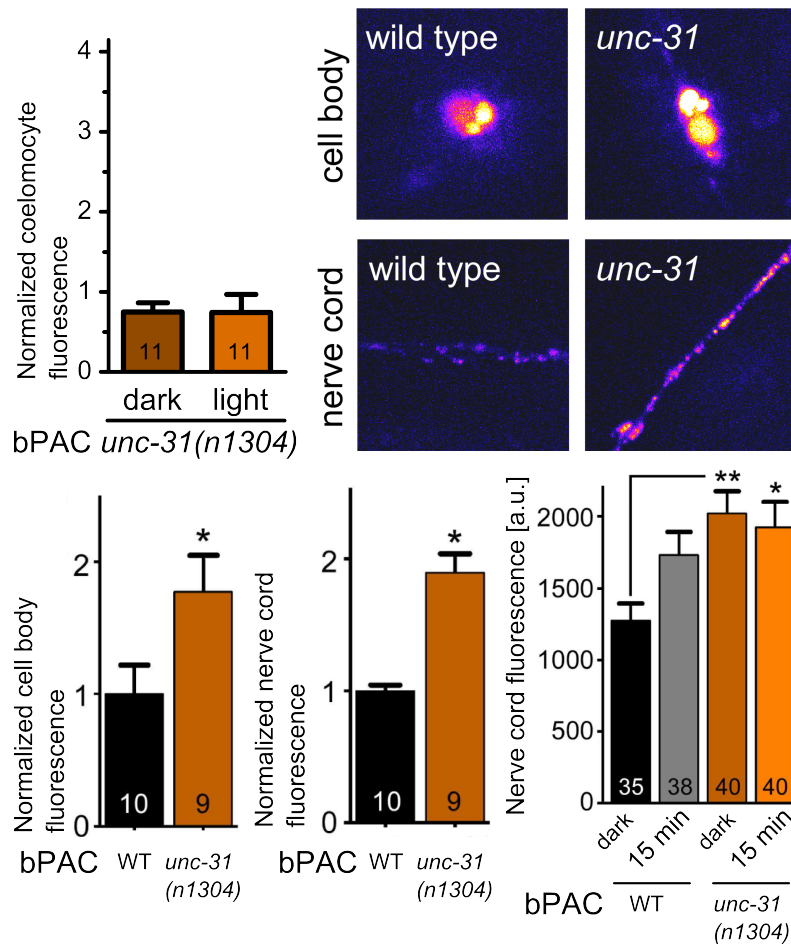


**Figure 3.14.: bPAC induced neuropeptide release required  $\text{Ca}^{2+}$ -dependent activator protein for secretion / UNC-31.**

Normalized coelomocyte fluorescence was not increased upon bPAC photostimulation in the *unc-31(n1304)* background (top left). This effect was not due to reduced expression of NLP-21::Venus in *unc-31(n1304)*, since fluorescence of neuronal cell bodies (bottom left) and processes (bottom center) was increased in the mutant background. Further, bPAC photoactivation did not reduce the amount of DCV fluorescence puncta in the nerve cord (bottom right). Top right: representative images.

Normalized and compared to wild type without photostimulation (figure 3.13). Mean  $\pm$  SEM. Student's T-test; Nerve cord fluorescence: Mann-Whitney U Test. ns :  $p \geq 0.05$ ; \* :  $p \leq 0.05$ ; \*\* :  $p \leq 0.01$ ; \*\*\* :  $p \leq 0.001$ .



### 3.1.2.1. Muscle excitability is not changed upon bPAC photoactivation.

Since bPAC photoactivation led to neuropeptide secretion, the increased mPSC amplitude observed could be due to neuropeptidergic post-synaptic modulation. To test this hypothesis, Dr. Jana F. Liewald measured BWM cell response to puff application of ACh after or during bPAC photostimulation (figure 3.16 left, bars 2 and 3, respectively). A second ACh puff application also did not change the excitatory post synaptic current (EPSC) amplitude significantly (bar 4). Nonetheless, the effects could be occluded by intrinsic GABAergic signaling. ACh puff application on bPAC *unc-47(e307)* did not increase the amplitude of the EPSC and therefore GABAergic signaling did not impair the measurement (bar 5). Further, the muscle cells could be desensitized, i.e. due to handling at low light level required for the patch procedure. Thus, I generated animals expressing bPAC in the *unc-17(e13)* background, missing the vAChT and therefore with impaired cholinergic transmission. Since there were no measurable changes in the EPSC amplitude after ACh puff application without or with bPAC photoactivation in these mutants, we can rule out a pre-desensitization of the BWM cells (bars 6 and 7, respectively).

*C. elegans* BWM cells express two types of ionotropic AChR, namely nicotine and levamisole sensitive AChR. The latter has lower peak currents and reduced desensitization compared to the former [395]. Therefore, ACh puff application might not address specific modulation of the L-AChR, since the signal difference might be below the noise caused by the N-AChR activity. In addition to that, bPAC-induced large bending angles are reminiscent of the phenotype displayed by a L-AChR gain of function strain [396]. Consequently, Dr. Jana F. Liewald measured EPSC amplitude after puff application of Levamisole. No change was observed due to bPAC photostimulation (figure 3.16 right).

Hence, bPAC-induced neuropeptidergic signaling is likely not targeted to the post-synapse.

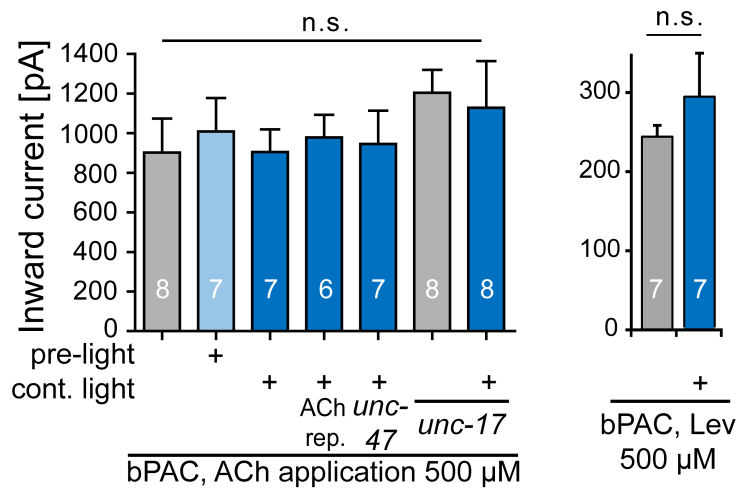


**Figure 3.16.: EPSC amplitude was not altered by bPAC photostimulation and agonist puff application in BWM recording.**

ACh puff application either after or during bPAC photoactivation elicits an EPSC with no observable amplitude modulation. Further, puff application of ACh in the mutant backgrounds *unc-47(e307)* and *unc-17(e13)*, lacking GABAergic and cholinergic transmission respectively, did not evoke a change in amplitude during bPAC photostimulation (left). During puff application of Levamisole probing the L-AChR, no changes in the EPSC amplitude could be observed (right).

Mean  $\pm$  SEM. Student's T-test. *ns* :  $p \geq 0.05$ . Measurement and analysis by Dr. Jana F. Liewald.

### 3.1.2.2. mPSC kinetic parameters were not changed during bPAC photoactivation

The lack of bPAC effect on the EPSC amplitude is an indication that the AChR were not modulated in their kinetics, localization or abundance. I further analyzed the kinetic properties of the AChR in an analysis of the  $\tau_{on}$  and  $\tau_{off}$  of mPSCs in wild type and *unc31(n1304)* mutant background with data kindly provided by Dr. Jana F. Liewald. Due to the low acquisition rate between 3 kHz to 5 kHz, analysis was performed with a mono-exponential growth and a mono-exponential decay ( $\tau_{on}$ ,  $\tau_{off}$ , respectively) fit (section 2.2.7.7, p. 74). After quality control, about 15% of the mPSCs were accepted for further analysis. There was no change in both kinetic parameters of the mPSCs during or after bPAC photoactivation in both genotypes (figure 3.17, left and center). Mean mPSC trace had an increased amplitude in wild type animals, an effect dependent on UNC-31 (figure 3.17, right). Therefore, bPAC photoactivation requires neuropeptidergic signaling but the target is located in the presynapse. Further,

the neuropeptidergic signal is transduced by a non  $G_{\alpha S}$  dependent pathway, since bPAC photostimulation would have bypassed the signal otherwise.

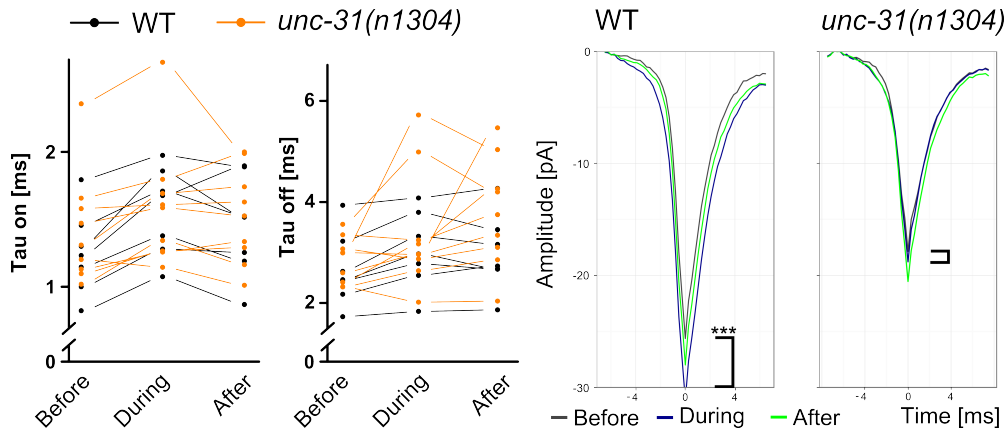


**Figure 3.17.: mPSC kinetic parameter analysis confirmed neuropeptidergic effect on the presynapse of the NMJ.**

bPAC did not change the mean mPSC  $\tau_{on}$  (left) or  $\tau_{off}$  (center) during or after photoactivation, neither in wild type (wt) nor in *unc-31(n1304)* background. Mean mPSC trace displayed an increased amplitude during bPAC photoactivation in wild type animals, but not in *unc-31(n1304)* background (right).

Left, center: Scatter plot, paired data; right: mean.  $n_{wt, unc-31(n1304)} = 7$  and 9 original recordings. Left, center: Kruskal-Wallis test, Dunn's Multiple Comparison Test; right: none performed. Amplitude comparison only between before and during light \*\*\* :  $p \leq 0.001$ . Data acquisition by Dr. Jana F. Liewald, compare figure 3.11

### 3.1.3. bPAC photoactivation elicits ultrastructural changes at the presynapse

In view of the presynaptic effect of bPAC photoactivation measured by electrophysiology, we measured the ultrastructure of cholinergic synapses with and without bPAC photostimulation (figure 3.18, section A.4, p. 227, image acquisition and feature calling by Dr. Szi-chieh Yu, feature quantification and data analysis by myself). Further, ChR2 photostimulated synaptic profiles were obtained for comparison to the bPAC-induced effect on ultrastructural level.

Three time points for bPAC photostimulation were frozen, namely 5 s, 30 s and 300 s of photostimulation. Additionally, a period of about 4 s was required for sample freezing. ChR2(H134R) was frozen 30 s and ChR2(C128S) frozen 1 s with added 4 s

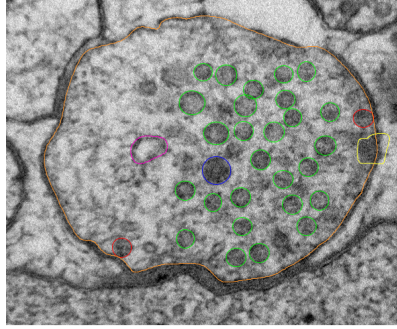


**Figure 3.18.: Representative thin section with ultrastructure of pre-synapse marked.**  
 Image and feature calling provided by Dr. Szi-chieh Yu, ultrastructure tagged by myself.  
 SV green, docked SV red, DCV blue, LV pink, DP yellow and PM orange.  
 Compare figure 2.2.

pause after photostimulation. The latter was equivalent to a depolarization for 9 s, due to the channel kinetics, and thus comparable to bPAC photostimulation for 5 s.

Firstly, the size of the profiles varied significantly across groups. Perimeter of the PM was increased upon bPAC photostimulation for 300 s (figure 3.19, left), while profile area change was not related to change in perimeter (figure 3.19, center). This discrepancy is due to a change in shape, with bPAC 300 s photostimulation group displaying an elongated profile cross section. This effect was also observed in both photoactivated ChR2 groups, albeit with reduced magnitude in the ChR2(H134R) group. Further, in the ChR2(C128S) group, the mean shape change was higher than in bPAC 300 s, but the variance of the later was higher leading to increased shape deformations in the bPAC 300 s group. Due to this variance, feature counts were normalized to a standard perimeter of 1548 nm and a standard area of 164 100 nm<sup>2</sup>. These values result in an ideal synaptic profile with an isoperimetric quotient of 1.078, similar to the mean isoperimetric quotient value for all analyzed control profiles ( $1.070 \pm 0.039$ , mean  $\pm$  SD,  $n = 511$ , formula 2.2). Correspondingly, distance calculations were normalized to these values. Analysis of the isoperimetric quotient better represented the change in the shape of the photostimulated profiles (figure 3.20).

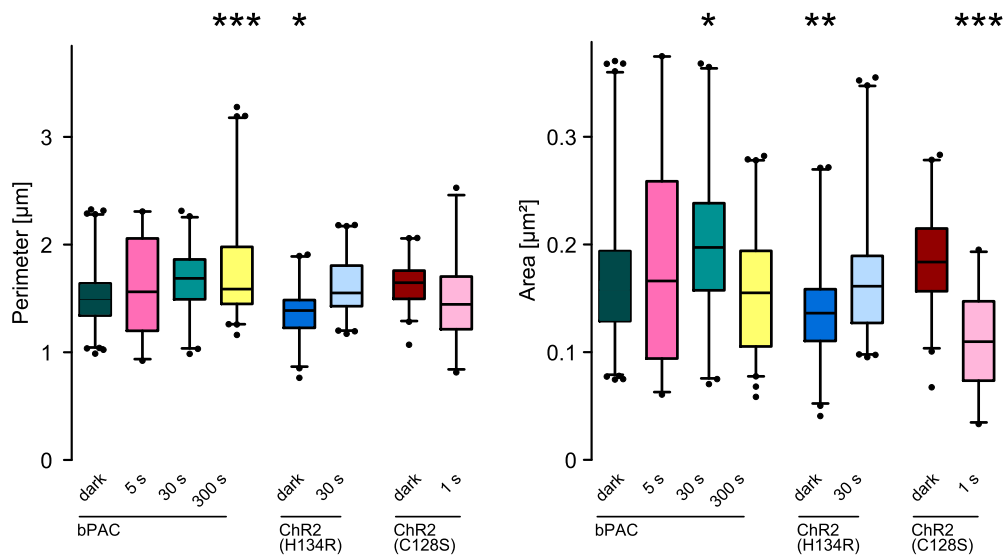


**Figure 3.19.: Perimeter and area of profiles analyzed by HPF-EM.**

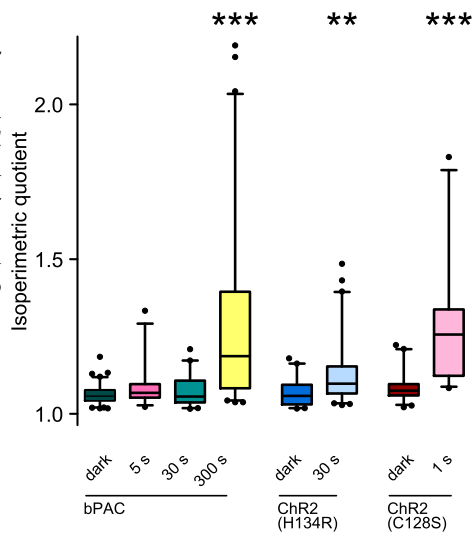
Mean perimeter and area of profiles analyzed by HPF-EM (left and right respectively). Both properties varied significantly across groups tested, with increased variance upon bPAC photostimulation.

$n = 168, 71, 94, 124, 89, 121, 95$  and  $68$ . Median, IQR, whiskers:  $2.5$  to  $97.5$ . ANOVA, Tukey's HSD.  $ns : p \geq 0.05$ ;  $* : p \leq 0.05$ ;  $** : p \leq 0.01$ ;  $*** : p \leq 0.001$ fig:methods.EMtagging.

**Figure 3.20.: Isoperimetric quotient of HPF-EM profiles.**

The isoperimetric quotient had a higher variation on long bPAC photostimulation periods as well as after ChR2(C128S) photoactivation.

$n = 168, 71, 94, 124, 89, 121, 95$  and  $68$ . Median, IQR, whiskers:  $2.5$  to  $97.5$ . ANOVA, Tukey's HSD.  $ns : p \geq 0.05$ ;  $* : p \leq 0.05$ ;  $** : p \leq 0.01$ ;  $*** : p \leq 0.001$ .



Secondly, the number of SVs was analyzed, since an increase in mPSC rate indi-

cates a higher SV turnover, and this could have an effect on their count. The mean count of SVs per profile was reduced after bPAC as well as Chr2 photoactivation. In contrast to Chr2(C128S) photoactivation, bPAC has not led to a depletion of SVs (figure 3.21 left, bPAC dark:  $21.4 \pm 6.0$ , bPAC 5 s:  $15.8 \pm 7.3$ , 26 % reduction versus Chr2(C128S) dark:  $18.7 \pm 5.9$ , Chr2(C128S) 1 s:  $7.2 \pm 5.4$ , 69 % reduction, mean  $\pm$  SD). Correspondingly, the count of docked SVs was also reduced upon photoactivation of bPAC and Chr2, but the relative reduction was similar (figure 3.21 center, bPAC dark:  $2.5 \pm 1.5$ , bPAC 5 s:  $0.9 \pm 1.1$ , 64 % reduction versus Chr2(C128S) dark:  $1.7 \pm 1.2$ , Chr2(C128S) 1 s:  $0.5 \pm 1.0$ , 71 % reduction, mean  $\pm$  SD). In both cases, Chr2(H134R) photoactivation did not reduce the SVs or docked SVs pools to such extents as Chr2(C128S), likely due to the delay between end of illumination and high pressure freezing, a time frame where depolarization of the neuronal cells was not sustained. In line with the electrophysiology results, photoactivation of bPAC induced release of SVs, partially depleting synapses from these vesicles.

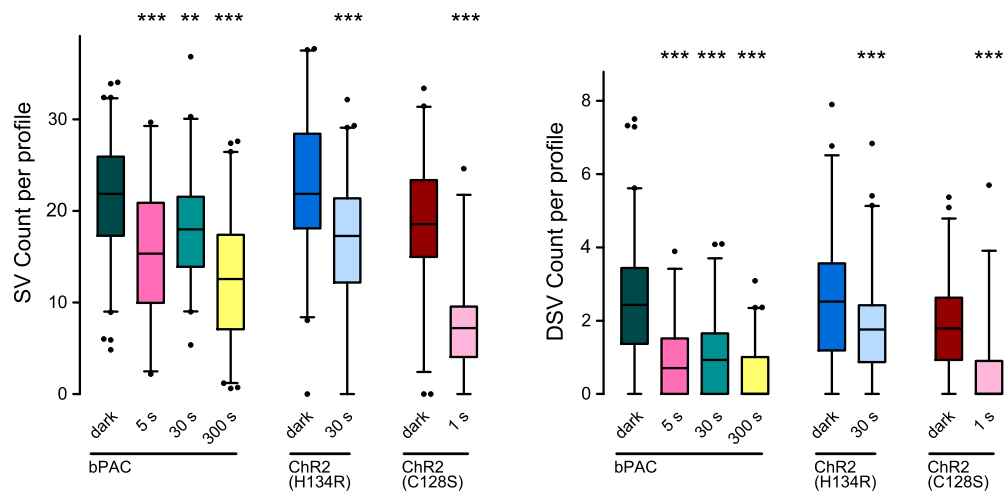
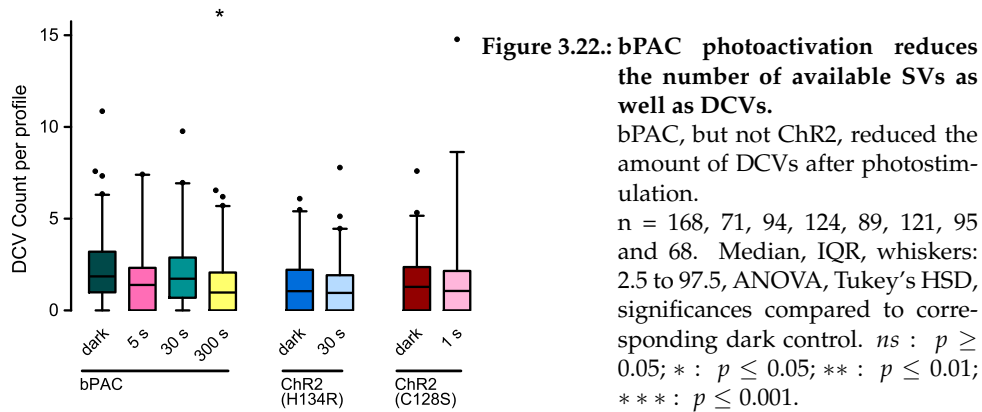


**Figure 3.21.: bPAC as well as Chr2 photoactivation reduced the number of available SVs and docked SVs.**

bPAC reduced the amount of SVs upon photostimulation, but this effect was not as ample as in the Chr2(C128S) 1 s group. Chr2(H134R) photostimulation effect was comparable to bPAC photostimulation (left). Both optogenetic tools also decreased the amount of docked SVs, where bPAC and Chr2(C128S) 1 s photostimulation elicited the highest depletion of docked SVs (right).

$n = 168, 71, 94, 124, 89, 121, 95$  and  $68$ . Median, IQR, whiskers:  $2.5$  to  $97.5$ . ANOVA, Tukey's HSD, significances compared to corresponding dark control.  $ns$  :  $p \geq 0.05$ ; \* :  $p \leq 0.05$ ; \*\* :  $p \leq 0.01$ ; \*\*\* :  $p \leq 0.001$ .

Since the bPAC effect was dependent on neuropeptidergic signaling, we also expected a reduction in the mean count of DCVs per profile. Their count per profile were variable and mostly of low abundance (bPAC dark:  $2.1 \pm 1.8$ , ChR2(H134R) dark:  $1.3 \pm 1.4$ , ChR2(C128S) dark:  $1.6 \pm 1.5$ , mean  $\pm$  SD). Since many profiles did not include a DCV, the acquired and analyzed number of profiles per group had a low power to statistically analyze their changes. Nonetheless, bPAC photoactivation for 300 s significantly reduced the DCV count after photoactivation compared to the dark control group (figure 3.22 right, bPAC 300 s:  $1.5 \pm 1.7$ , mean  $\pm$  SD. Effect size:  $d_{Cohen} = 0.34 \pm 0.22$  with 95 % CI, see formula 2.4). There was a tendency, albeit not significant, for DCV reduction in both shorter bPAC photostimulation groups (bPAC 5 s:  $1.6 \pm 1.7$  and bPAC 30 s:  $2.0 \pm 1.9$ , mean  $\pm$  SD) while ChR2 photostimulation did not lead to a change in the mean DCV count (ChR2(H134R) 30 s:  $1.2 \pm 1.3$  and ChR2(C128S) 1 s:  $1.6 \pm 2.3$ , mean  $\pm$  SD).



The increased vesicle release induced by photoactivation of bPAC after 300 s and ChR2(C128S) also promoted the generation of LVs (figure 3.23 left, bPAC dark:  $0.4 \pm 0.8$  versus bPAC 300 s:  $1.7 \pm 2.2$ , ChR2(C128S) dark:  $0.7 \pm 1.0$  versus ChR2(C128S) 1 s:  $2.6 \pm 3.0$ , mean  $\pm$  SD). These vesicles had a bilayer membrane and a electron-translucent core, similar to the 100 nm vesicles we reported for ChR2 photostimulation previously [397]. There, such 100 nm vesicles disappeared in about 8 s. This in agreement to the ChR2(H134R) stimulation protocol applied during this thesis, where no change in LV counts could be detected (ChR2(H134R) dark:  $0.5 \pm 0.8$  versus ChR2(H134R) 30 s:  $0.8 \pm 1.0$ , mean  $\pm$  SD). Further in agreement to Kittelmann *et al.* [397], the observed increase in LV count in ChR2(C128S) was associated with an increase in the vesicles largest diameter, (figure 3.23).

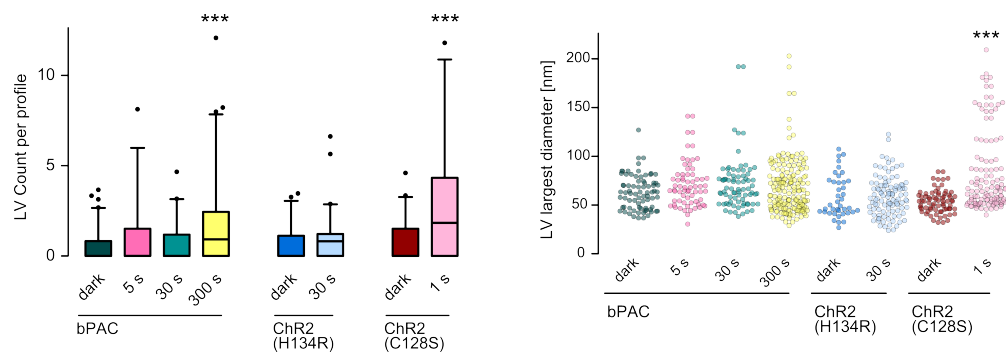


**Figure 3.23.: LVs with increased diameter present in bPAC long- and ChR2(C128S) photo-stimulation.**

bPAC 300 s as well as ChR2(C128S) 1 s photoactivation led to an increase in LVs count (left). Photoactivation of bPAC for 300 s as well as ChR2(C128S) for 1 s also led to an increased LV size (right).

$n_{\text{profiles}} = 168, 71, 94, 124, 89, 121, 95$  and  $68$ ;  $n_{\text{LVs}} = 76, 67, 77, 182, 40, 105, 72$  and  $119$ , respectively. Median, IQR, whiskers: 2.5 to 97.5, Scatter plot. ANOVA, Tukey's HSD test. \*\*\*:  $p \leq 0.001$ .

### 3.1.3.1. bPAC photostimulation leads to increased SV size

The ultrastructural effects of bPAC photoactivation described hitherto could not fully explain the increase in mPSC amplitude observed by electrophysiology. The reduction in DCV count was only observed after long photostimulation period, albeit the scarce absolute number of DCVs per profile. Therefore, we analyzed the size of SV in profiles with at least 10 SVs present. This constraint was required to exclude the effect of high systematic error in low SV count profiles. bPAC photostimulation for all periods measured significantly increased the mean SV Feret's diameter per profile, while this effect was not present under ChR2(C128S) photoactivation (figure 3.24). The calculated luminal SV volume increase is about 13% [formula 2.3,  $(7756.4 \pm 1139.8) \text{ nm}^3$ ,  $(8792.4 \pm 1037.8) \text{ nm}^3$ ,  $(8801.4 \pm 1298.9) \text{ nm}^3$  and  $(8781.3 \pm 1478.3) \text{ nm}^3$ , bPAC dark, 5 s, 30 s and 300 s and  $(7342.0 \pm 850.7) \text{ nm}^3$  and  $(8520.6 \pm 1472.3) \text{ nm}^3$ , ChR2(C128S) dark and 1 s, respectively, mean  $\pm$  SD,  $n = 173, 46, 87, 75, 105$  and  $48$ . Kruskal-Wallis test, Dunn's Multiple Comparison Test,  $p \leq 0.001, 0.001$  and  $0.01$  for bPAC dark versus 5 s, 30 s and 300 s, respectively,  $p > 0.05$  for ChR2(C128S) dark versus 1 s].

The increase in SV size could be linked to the enhanced quantal size and therefore explain the increased mPSC amplitude observed during bPAC photostimulation by electrophysiology experiments described above. Following this hypothesis, SV size



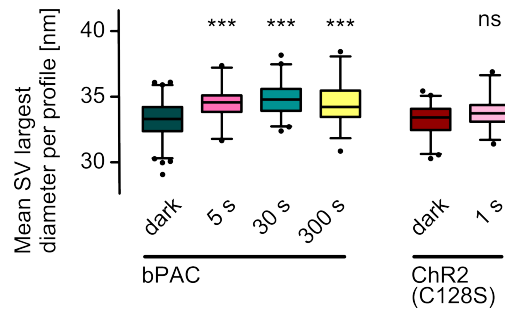


**Figure 3.24.: SV size increased after bPAC photoactivation.**

bPAC photoactivation increased the mean SV Feret's diameter per profile for profiles with at least 10 SVs. In contrast, ChR2(C128S) 1 s photoactivation did not significantly change the SV size, although few profiles were scored.

n = 173, 46, 87, 75, 105 and 48 profiles. Median, IQR, whiskers: 2.5 to 97.5. Kruskal-Wallis test, Dunn's Multiple Comparison Test, significances compared to corresponding dark control. *ns* :  $p \geq 0.05$ ; \* :  $p \leq 0.05$ ; \*\* :  $p \leq 0.01$ ; \*\*\* :  $p \leq 0.001$

should be dependent on neuropeptidergic signaling.

### 3.1.3.2. SV size increase observed during bPAC photostimulation is UNC-31 dependent

In order to test if the SV size increase observed by HPF-EM after bPAC photostimulation is dependent on neuropeptidergic signaling, we analyzed the ultrastructure of the synapse of cholinergic neurons in the *unc-31(n1304)* background. I generated bPAC *unc-31(n1304)* and Dr. Szi-chieh Yu provided HPF-EM images for two conditions, dark and 5 s photostimulation. Image tagging and subsequent data analysis were performed by myself.

First, we analyzed the isoperimetric quotient of bPAC *unc-31(n1304)* dark. This was significantly reduced compared to bPAC dark but there was no difference to bPAC *unc-31(n1304)* 5 s (formula 2.2, mean  $\pm$  SD =  $1.06 \pm 0.03$ ,  $1.04 \pm 0.02$  and  $1.06 \pm 0.02$ ,  $n = 168$ , 81 and 81. bPAC dark, bPAC *unc-31(n1304)* dark, bPAC *unc-31(n1304)* 5 s respectively; bPAC dark vs bPAC  $p \leq 0.01$ , bPAC *unc-31(n1304)* dark vs. bPAC *unc-31(n1304)* 5 s  $p > 0.05$ , bPAC dark vs. bPAC *unc-31(n1304)* 5 s  $p > 0.05$ , Kruskal-Wallis test, Dunn's Multiple Comparison Test). Therefore, all counts were normalized to the perimeter or area as specified above (section 3.1.3, p. 98).

The mean count of SVs or docked SVs per profile were not significantly reduced upon bPAC photostimulation in *unc-31(n1304)* background, in contrast to wt background (figure 3.25 left and center left, respectively). Nonetheless, there was a tendency in the reduction of SVs in the bPAC *unc-31(n1304)* 5 s compared to the dark control. Interestingly, the lack of reduction in the docked SVs upon bPAC photoactivation in *unc-31(n1304)* background is due to the intrinsic low count of docked SVs. bPAC *unc-31(n1304)* dark compared to bPAC dark has a significant reduction of observed docked SVs, that is not further modulated by bPAC ( $p \leq 0.001$ , ANOVA, Tukey's HSD test). This reduction is in agreement with data collected by Dr. Jana F. Liewald by BWM voltage clamp recording, where the mean mPSC rate was reduced in *unc-31(n1304)* background and the release rate increase mediated by bPAC was not significantly different than before stimulation (section 3.1.2, p. 93).

Further, bPAC photoactivation did not change the mean count of DCVs in the *unc-31(n1304)* background, but these were significantly increased compared to bPAC dark in wt (figure 3.25 center right, mean  $\pm$  SD =  $2.1 \pm 1.8$ ,  $3.3 \pm 1.8$  and  $2.9 \pm 2.2$ ,  $n = 168$ , 81 and 81, bPAC dark, bPAC *unc-31(n1304)* dark, bPAC *unc-31(n1304)* 5 s respectively; bPAC dark vs. bPAC  $p \leq 0.001$ , bPAC dark vs. bPAC *unc-31(n1304)* 5 s  $p \leq 0.05$ , bPAC *unc-31(n1304)* dark vs. bPAC *unc-31(n1304)* 5 s:  $p > 0.05$ , ANOVA, Tukey's HSD test). This result is in agreement with the NLP-21::Venus imaging of cholinergic,

neuronal processes, where an increased fluorescence was observed (section 3.1.2, p. 93). This apparent reduced exocytosis in *unc-31(n1304)* background was also paired with a reduced mean count of LVs, although bPAC photostimulation for 5 s had also not significantly increased LV counts (figure 3.25 right).

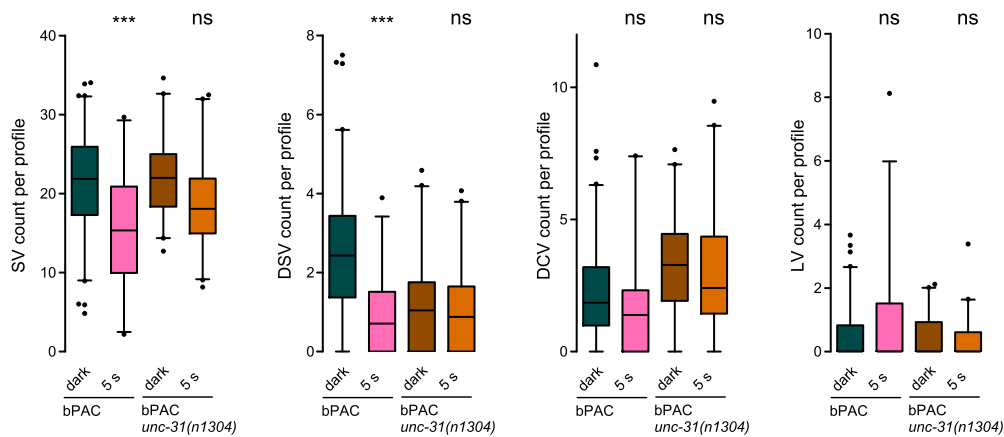


**Figure 3.25.: The observed bPAC effects on ultrastructure were UNC-31 dependent.**

The mean SV and docked SV counts per profile were not reduced in the *unc-31(n1304)* background (left and center left, respectively). In contrast, bPAC photoactivation for 5 s did not change the mean count of DCVs and LVs in the *unc-31(n1304)* background (center right and right, respectively).

n = 168, 71, 81 and 81. Median, IQR, whiskers: 2.5 to 97.5. ANOVA, Tukey's HSD test, significances compared to corresponding dark control. ns :  $p \geq 0.05$ ; \* :  $p \leq 0.05$ ; \*\* :  $p \leq 0.01$ ; \*\*\* :  $p \leq 0.001$ .

Importantly, the lack of neuropeptidergic transmission in the *unc-31(n1304)* background impaired the bPAC induced increase in SV size (figure 3.26, mean  $\pm$  SD =  $31.47 \pm 0.87$  and  $31.68 \pm 0.99$ , n = 100 and 98, bPAC *unc-31(n1304)* dark and bPAC *unc-31(n1304)* 5 s,  $p > 0.05$ , Kruskal-Wallis test, Dunn's Multiple Comparison Test, analysis of profiles with at least 10 SVs). Accordingly, there was no increase in SV luminal volume after photoactivation of bPAC in the *unc-31(n1304)* background (mean  $\pm$  SD =  $6232.0 \pm 672.8$  and  $6334.0 \pm 759.0$ , n = 100 and 98, bPAC *unc-31(n1304)* dark and bPAC *unc-31(n1304)* 5 s,  $p > 0.05$ , Kruskal-Wallis test, Dunn's Multiple Comparison Test, analysis of profiles with at least 10 SVs). Interestingly, the mean SV size in bPAC *unc-31(n1304)* dark was significantly reduced compared to bPAC dark.

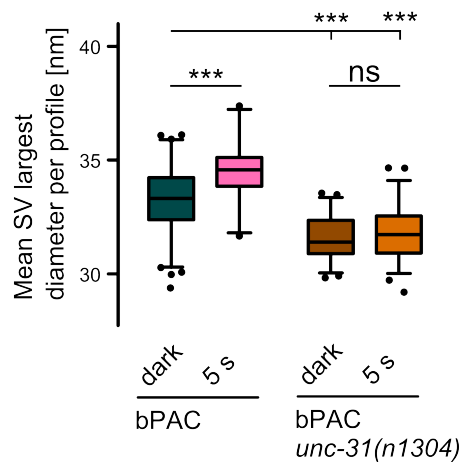


**Figure 3.26.: Neuropeptidergic signaling required for bPAC-induced increase of SV size.**

bPAC photoactivation in *unc-31(n1304)* background did not increase SV size. Rather, the mean SV size per profile was reduced in the *unc-31(n1304)* background compared to bPAC dark.

n = 159, 46, 75 and 77. Median, IQR, whiskers: 2.5 to 97.5. Kruskal-Wallis test, Dunn's Multiple Comparison Test, analysis of profiles with at least 10 SVs. ns :  $p \geq 0.05$ ; \* :  $p \leq 0.05$ ; \*\* :  $p \leq 0.01$ ; \*\*\* :  $p \leq 0.001$ .

### 3.1.3.3. mPSC amplitude increase induced by bPAC is dependent on acute modulation of vAChT

The above mentioned ultra-structure analysis confirmed the neuropeptidergic effect in the presynapse. To further probe if SV quantal size modulation was due to increased neurotransmitter content, we required measurements by electrophysiology. Therefore, Dr. Jana F. Liewald recorded from BWM cells with acute application of pharmacological blockers of either the v-ATPase or the vAChT. The former was blocked by application of Baf A1, while the latter by Vesamicol. Both substances were applied to the patch clamp bath solution prior to measurement with an incubation time of  $7 \text{ min} \pm 1 \text{ min}$  prior to recording (discrepancy due to individual patch conditions). Both substances reduced the mPSC rate (figure 3.27 left), while only Vesamicol inhibited the bPAC dependent mPSC amplitude increase (figure 3.27 right). Therefore, bPAC photostimulation led to a neuropeptide dependent modulation of the vAChT that increased the quantal size of SVs. Since Baf A1 did not inhibit this process, the residual acidification of the SVs is sufficient to increase SV loading with ACh upon bPAC photostimulation and thus vAChT probably does not fill SVs to its kinetic optimum. This was only possible due to the acute inhibition of the v-ATPase in the Baf A1 application experiment.

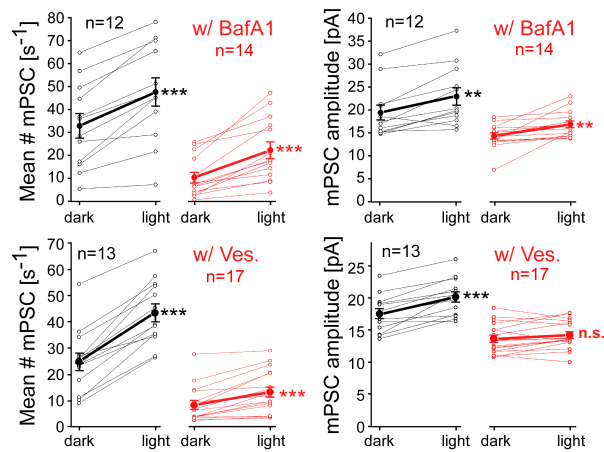


**Figure 3.27.: Acute inhibition of vAChT with Vesamicol inhibits the bPAC-induced increase in mPSC amplitude.**

Upon acute inhibition of either the v-ATPase by Baf A1 or of the vAChT by Vesamicol, the mean rate of mPSCs measured by electrophysiology was reduced (left). Only Vesamicol and the consequent blockage of vAChT inhibited the bPAC-induced increase in mPSC amplitude, an evidence for the neuropeptidergic modulation of the vAChT upon bPAC photostimulation (right).

Mean  $\pm$  SEM, scatter plot. Paired sample Student's T-Test. *ns* :  $p \geq 0.05$ ; \* :  $p \leq 0.05$ ; \*\* :  $p \leq 0.01$ ; \*\*\* :  $p \leq 0.001$ . Measurement and analysis by Dr. Jana F. Liewald.

### 3.1.4. Synapsin is required for cAMP mediated modulation of behavior

The characterized effect of bPAC photoactivation on cholinergic neurons is partially dependent on presynaptic modulation through a  $G_{\alpha S}$  independent pathway. Nonetheless, not all effects caused by bPAC and observed by behavior analysis could be abolished by CAPS/UNC-31 mutation, indicating either a partial  $G_{\alpha S}$ , and thus cAMP signaling dependency, or a direct modulation of SV release probability.

#### 3.1.4.1. Behavioral analysis of mutants for defective bPAC photostimulation response revealed synapsin involvement in signal transduction

To further test the bPAC-induced modulation of ACh release, a behavioral analysis of putative cAMP and PKA/KIN-1 targets was performed. The analyzed genes were synapsin, Ryanodine Receptor and exchange protein activated by cyclic AMP

(EPAC) (mutants *snn-1(tm2557)*, *unc-68(r1162)* and *epac-1(ok655)*, respectively). The effects of bPAC photoactivation in these mutants were compared to those observed in wt, *lite-1(ce314)*, *unc-31(n1304)* and PDE-4D<sub>gof</sub> backgrounds described above. The mean speed as well as the mean bending angle change upon photoactivation for each group were calculated and clustered for similarity (section 2.2.7.2, p. 72). bPAC photoactivation in these groups led to behavioral modulation that was clustered into the same category as bPAC in wt, with the exception of bPAC PDE-4D<sub>gof</sub> and bPAC *snn-1(tm2557)* (figure 3.28, magenta versus black cluster, respectively). Further, bPAC *unc-31(n1304)* clustered to bPAC PDE-4D<sub>gof</sub> in the speed response to photoactivation but to the bPAC wt in the mean bending angle response to photoactivation.

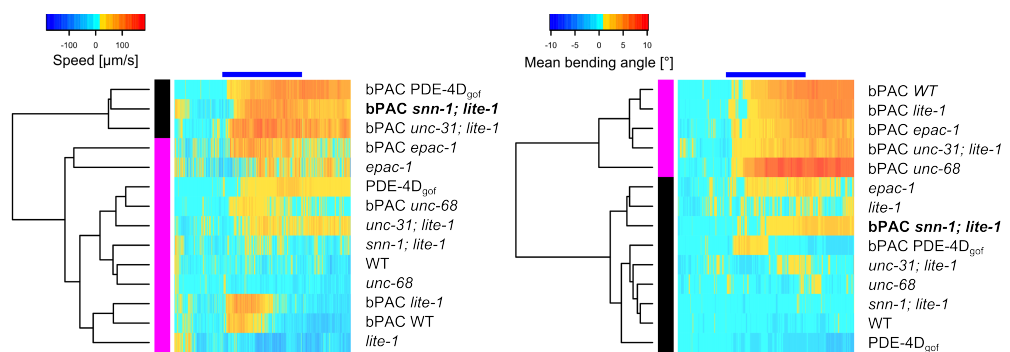


**Figure 3.28.: Analysis of behavioral response of several mutants to bPAC photostimulation revealed the requirement of synapsin for behavior modulation.**

Clustered speed and mean bending angle behavior response to photoactivation (left and right, respectively). bPAC expressing animals clustered to the same group in both behaviors, with the exception of bPAC *snn-1(tm2557)* and bPAC PDE-4D<sub>gof</sub>. Further, bPAC *unc-31(n1304)* clustered with the aforementioned strains in the speed analysis. bPAC *snn-1(tm2557)* trace highlighted in bold in both graphs.

bPAC expression denoted by “bPAC”. See text for gene variants. Photoactivation denoted by blue bar. Similarity calculated by DTW and clustered by hierarchical clustering.  $n \geq 29$ .

Hence, the behavioral clustering confirmed the hypothesis that the bPAC mediated effect is only partially dependent on neuropeptidergic signaling. In addition, the cluster analysis indicated the requirement of synapsin for both modulations of behavior elicited by bPAC and implied a requirement of synapsin for neuropeptidergic signaling.

### 3.1.4.2. Synapsin is required for neuropeptidergic signaling induced by bPAC photoactivation

To test if synapsin was required for neuropeptide secretion, NLP-21::Venus was expressed in the *snn-1(tm2557)* mutant background. Photoactivation of bPAC in this mutant could not induce secretion as in wt animals (figure 3.29 left). Similar to the phenotype in *unc-31(n1304)* mutant background, this deficiency was not due to reduced fluorescent puncta in the neuron of interest. Both, neuronal cell bodies and processes displayed a significantly increased fluorescence in the synapsin mutant, and, therefore, neuropeptide retention in the cholinergic neurons (figure 3.29 right).

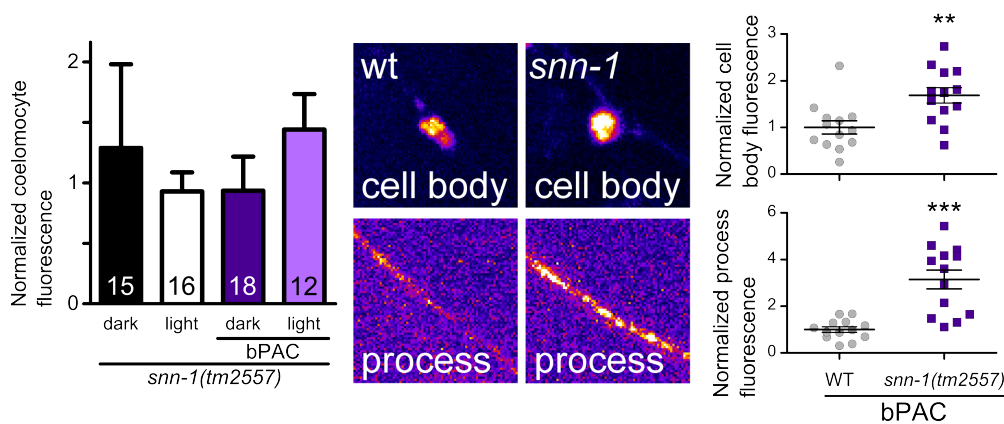


**Figure 3.29.: synapsin mutants were deficient in neuropeptide secretion upon bPAC photo-stimulation.**

NLP-21::Venus marker expressed in synapsin mutant *snn-1(tm2557)* did not change the observed normalized coelomocyte fluorescence (left, black and white bars). bPAC-induced neuropeptide release was impaired by the *snn-1(tm2557)* mutation, since no NLP-21::Venus endocytosis in coelomocytes could be observed (left, violet and light violet bars). This effect was not due to reduced expression of NLP-21::Venus in *snn-1(tm2557)* background, since fluorescence of neuronal cell bodies and processes was increased in the mutant (center: representative images, right: quantification).

$n_{\text{Cell Body and Process}} = 13$  and  $13$ . Mean  $\pm$  SEM. Normalized and compared to wild type without photostimulation (figure 3.13), Student's T-test. Nerve cord fluorescence: Mann-Whitney U Test. *ns* :  $p \geq 0.05$ ; \* :  $p \leq 0.05$ ; \*\* :  $p \leq 0.01$ ; \*\*\* :  $p \leq 0.001$ .

Due to the inability of the synapsin mutant to secrete neuropeptides upon bPAC photostimulation, we expected that these animals would also fail to increase mPSC amplitudes in BWB when photoactivated. To test this hypothesis, Dr. Jana F. Liewald

recorded voltage clamp data from *snn-1(tm2557)* animals that expressed bPAC in cholinergic neurons. As expected, these animals could not increase mPSC amplitude during photostimulation (figure 3.30 left). Furthermore, the rate of mPSCs was reduced compared to recording from wt animals (figure 3.30 right).

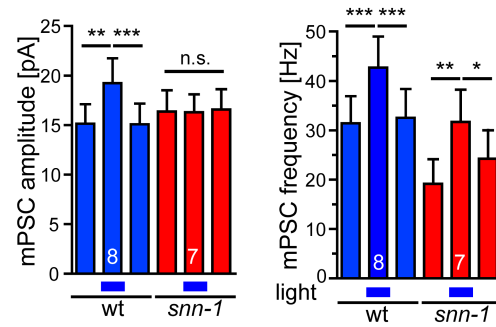


**Figure 3.30.: synapsin mutants were deficient in mPSC amplitude modulation upon bPAC photostimulation.**

bPAC-induced effect on mPSC amplitude was impaired by the *snn-1(tm2557)* mutation (left). Nevertheless, bPAC photoactivation increased the mPSC rate in *snn-1(tm2557)* background, though with reduced basal level (right).

Mean  $\pm$  SEM. Intra group = paired Student's T-Test, inter group = Student's T-test. *ns* :  $p \geq 0.05$ ; \* :  $p \leq 0.05$ ; \*\* :  $p \leq 0.01$ ; \*\*\* :  $p \leq 0.001$ . Measurement and analysis by Dr. Jana F. Liewald.

### 3.1.4.3. Defective vesicle mobilization in synapsin mutant synapses

The reduced mPSC rate observed in *snn-1(tm2557)* mutants is an indication of defective vesicle mobilization in the synapse of cholinergic neurons. In order to test this hypothesis, Dr. Szi-chieh Yu acquired images of cholinergic synapses with and without bPAC photostimulation for 30 s by HPF-EM. The ultrastructure and data analysis were performed by myself. The synapses in bPAC *snn-1(tm2557)* mutants without photostimulation were significantly smaller in perimeter and area than in the control group bPAC wt dark (figure 3.31 left and center, respectively). After photostimulation, there were no significant changes in either the area or the perimeter of bPAC wt 30 s compared to bPAC *snn-1(tm2557)* 30 s synapses. Nonetheless, the isoperimetric quotient of bPAC *snn-1(tm2557)* 30 s synapses was increased compared to bPAC wt 30 s synapses (figure 3.31 right). Therefore, also for these profiles, all measurements were normalized to the ideal area of 164 100 nm<sup>2</sup> and the ideal perimeter of 1548 nm.

We then analyzed the SV and docked SV counts in the *snn-1(tm2557)* mutant pro-



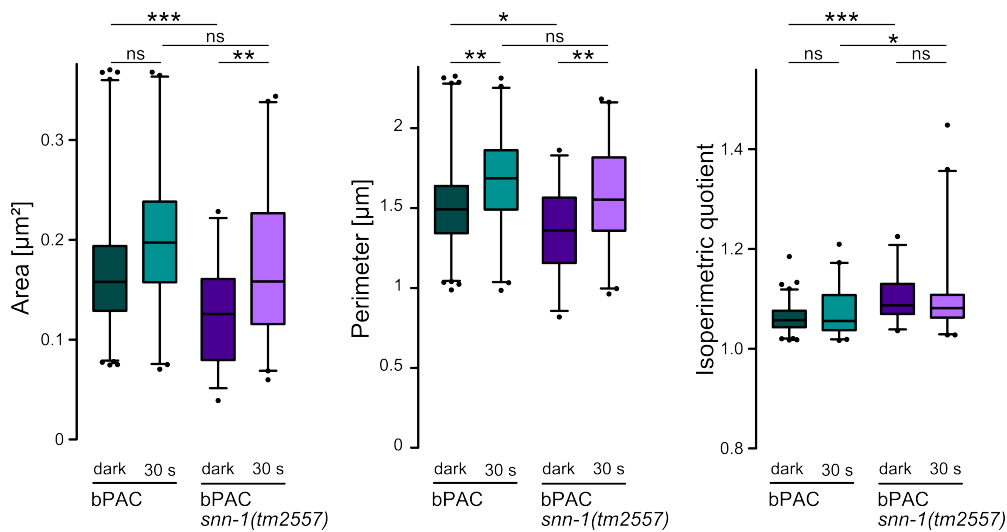


**Figure 3.31.: Perimeter, area and isoperimetric quotient of synapsin mutant profiles analyzed by HPF-EM.**

The perimeter and area of bPAC *snn-1(tm2557)* dark synapses were reduced compared to bPAC wt dark (left and center, respectively). Upon photostimulation, there was no distinction of these properties between wt and *snn-1(tm2557)* mutant synapses. The isoperimetric quotient was not changed in *snn-1(tm2557)* mutant synapses compare to wt in the dark condition, but it was increased in bPAC *snn-1(tm2557)* 30 s compared to bPAC wt 30 s synapses.

n = 168, 94, 78 and 82. Median, IQR, whiskers: 2.5 to 97.5. ANOVA, Tukey's HSD. ns :  $p \geq 0.05$ ; \* :  $p \leq 0.05$ ; \*\* :  $p \leq 0.01$ ; \*\*\* :  $p \leq 0.001$

files. Upon photostimulation of bPAC, we observed a reduction of docked SVs that was comparable to the reduction present in bPAC wt synapses after 30 s bPAC stimulation (figure 3.32 left). In contrast to the wt synapses, bPAC photostimulation in the *snn-1(tm2557)* mutant background did not reduce the count of SVs (figure 3.32 right). There was a tendency to reduce counts of LVs in both *snn-1(tm2557)* mutant groups (bPAC wt dark:  $0.44 \pm 0.06$ ; bPAC wt 30 s:  $0.71 \pm 0.10$ ; bPAC *snn-1(tm2557)* dark:  $0.45 \pm 0.10$ ; bPAC *snn-1(tm2557)* 30 s:  $0.47 \pm 0.11$ ; n = 168, 94, 78 and 82, Mean  $\pm$  SEM. ANOVA, Tukey's HSD, all ns). This is in line with synapsin mutation effects in *D. melanogaster* [398].

The aforementioned lack of SV reduction in the bPAC *snn-1(tm2557)* 30 s group could be due to a deficient targeting of the SVs to the release sites next to the DP. Hence, we analyzed the sum linear distance of SVs to the DP per normalized profile area in all profiles containing a DP (figure 3.33 pictogram left). There was no

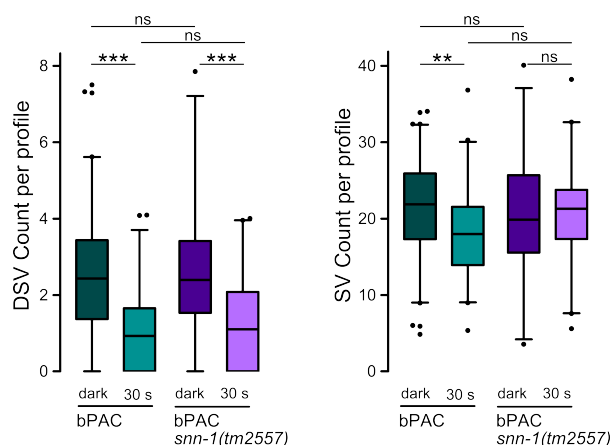


**Figure 3.32.: synapsin mutation impaired bPAC-induced SV recruitment from the reserve pool.**

bPAC photoactivation in *snn-1(tm2557)* mutant background reduced the number of docked SVs as in the wt control group (left). In contrast to bPAC photoactivation in wt animals, though, *snn-1(tm2557)* mutant synapses did not show reduced numbers of SVs (right).

n = 168, 94, 78 and 82. Median, IQR, whiskers: 2.5 to 97.5. ANOVA, Tukey's HSD. ns :  $p \geq 0.05$ ; \* :  $p \leq 0.05$ ; \*\* :  $p \leq 0.01$ ; \*\*\* :  $p \leq 0.001$

difference between both unstimulated groups (figure 3.33 left). Upon bPAC photoactivation for 30 s, bPAC wt SVs showed a reduced distance to the DP, while bPAC *snn-1(tm2557)* SVs were located at longer distances from the DP (figure 3.33 left). This effect is not dependent on the increased isoperimetric quotient found in bPAC photostimulated synapses, since bPAC 300 s synapses had their SVs nearest to the DP (figure 3.33 right).

In addition to the effect in SV availability, we expected bPAC *snn-1(tm2557)* synapses to be deficient in DCV localization, since these animals were impaired in bPAC-induced neuropeptidergic signaling. Although NLP-21::Venus fluorescence showed an increased signal in processes of cholinergic neurons in bPAC *snn-1(tm2557)* animals, we observed a reduced number of DCVs per profile in these mutants by HPF-EM (figure 3.34, left). Furthermore, the distribution of the DCVs in respect to the DP was shifted towards longer distances in bPAC *snn-1(tm2557)* synapses (figure 3.34 right, single distances normalized to profile area).

Importantly, the reduced number of DCVs in both bPAC *snn-1(tm2557)* groups is not an artifact of the area normalization. The absolute number of DCVs per profile in both groups is also lower than in the bPAC wt dark group (bPAC dark:  $2.3 \pm 2.3$

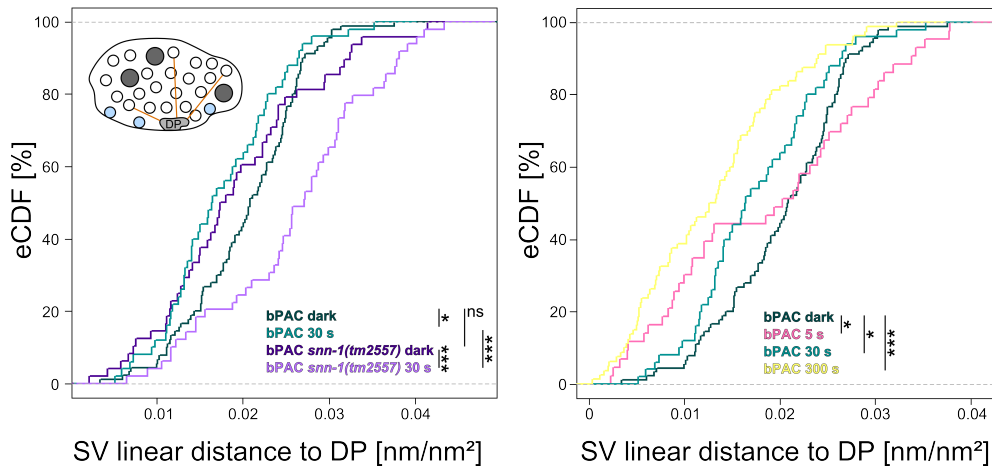


**Figure 3.33.: bPAC-induced SV mobilization deficiency in synapsin mutant synapses.**

Both dark control groups show no change in distribution of SVs, but upon photoactivation bPAC *snn-1(tm2557)* 30 s displayed longer distances, contrary to bPAC wt 30 s (left). This effect is not dependent on the isoperimetric quotient increase observed in bPAC *snn-1(tm2557)* 30 s synapses, since the lowest distances were observed in bPAC 300 s synapses (right), the latter with the highest isoperimetric quotient in the tested groups.

Pictogram of analysis procedure, calculation:  $\frac{\sum SV \text{ to } DP \text{ distance}}{Area}$  (inset, exemplary distances in orange).  $n_{left} = 90, 50, 48$  and  $49$ ,  $n_{right} = 90, 43, 50$  and  $80$ . empirical cumulative distribution function. Kolmogorov-Smirnov Test. *ns* :  $p \geq 0.05$ ; \* :  $p \leq 0.05$ ; \*\* :  $p \leq 0.01$ ; \*\*\* :  $p \leq 0.001$

vs.  $1.0 \pm 1.1$  and  $1.1 \pm 1.3$ , bPAC *snn-1(tm2557)* dark and 30 s, respectively. Mean  $\pm$  SD). Dr. Szi-chieh Yu therefore searched for DCVs up to 240 nm flanking the DP (6 sections). Likewise, in the sections flanking the DP, *snn-1(tm2557)* synapses displayed a reduced count of DCVs (figure 3.35).

In combination to the observed effect in the fluorescent imaging of NLP-21::Venus in *snn-1(tm2557)* animals, the data above implies that synapsin was required for DCV localization in the synapse and its vicinity. Since DCVs did not accumulate in the synapse, they enriched in the processes and cell bodies of the neurons and could not be released as in wt neurons. Hence, we expected that bPAC photoactivation in synapsin mutants would not induce SV size enlargement (figure 3.36).

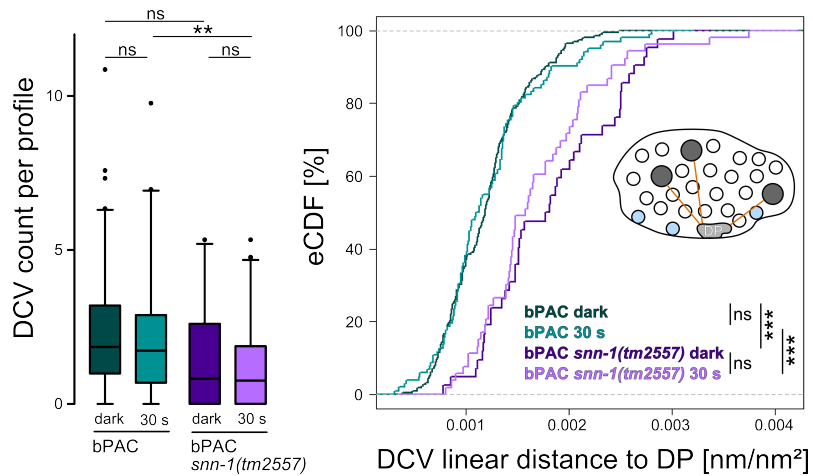


**Figure 3.34.: Synapsin mutant synapses had abnormal DCV localization.**

Synapsin mutation displayed a reduced count of DCVs compared to wt synapses (left). The distribution of the DCVs relative to the DP was impaired in *snn-1(tm2557)* synapses (right).

Pictogram of analysis procedure, calculation:  $\frac{DCV\ to\ DP\ distance}{Area \times 164100}$  (inset, distances in orange)  $n_{left} = 168, 91, 78$  and  $82$ ,  $n_{right} = 226, 102, 42$  and  $53$ . Left: Median, IQR, whiskers: 2.5 to 97.5, right: empirical cumulative distribution function. Left: ANOVA, Tukey's HSD, right: Kolmogorov-Smirnov Test. *ns* :  $p \geq 0.05$ ; \* :  $p \leq 0.05$ ; \*\* :  $p \leq 0.01$ ; \*\*\* :  $p \leq 0.001$

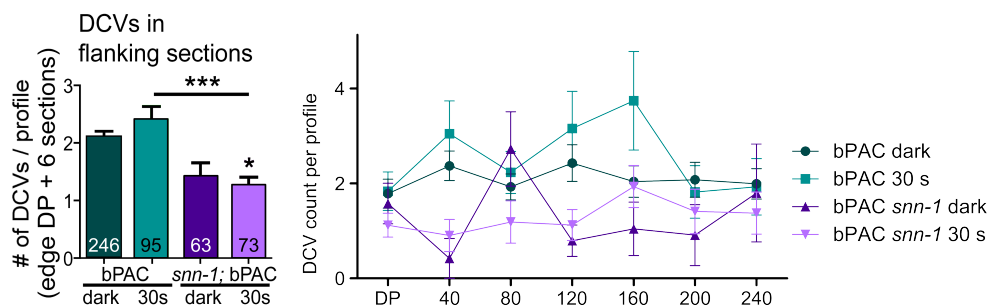


**Figure 3.35.: Synapsin mutant synapses had reduced number of DCVs in flanking sections.**

Total count of DCVs in flanking sections to the DP were reduced in synapsin mutant synapses (left). Nonetheless, the distribution of these DCVs was homogeneous across the synaptic profiles in all tested groups (right).

Mean  $\pm$  SEM. ANOVA, Tukey's HSD. *ns* :  $p \geq 0.05$ ; \* :  $p \leq 0.05$ ; \*\* :  $p \leq 0.01$ ; \*\*\* :  $p \leq 0.001$ . Data acquisition and analysis by Dr. Szi-chieh Yu

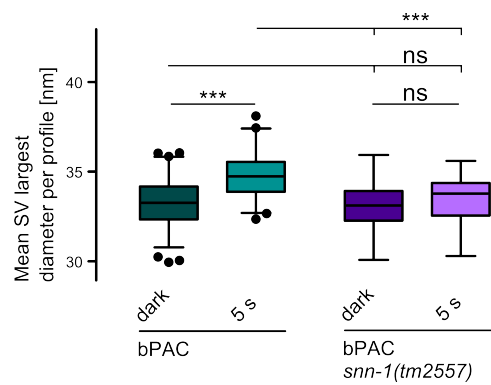


**Figure 3.36.: SV size unaffected in synapsin mutants after bPAC photoactivation.**

bPAC photoactivation did increase the mean SV Feret's diameter per profile for profiles with at least 10 SVs in synapsin mutants.

n = 159, 87, 68 and 72 profiles. Median, IQR, whiskers: 2.5 to 97.5. Kruskal-Wallis test, Dunn's Multiple Comparison Test. ns :  $p \geq 0.05$ ; \* :  $p \leq 0.05$ ; \*\* :  $p \leq 0.01$ ; \*\*\* :  $p \leq 0.001$

#### 3.1.4.4. Analysis of the SNN-1B(S9A) PKA phosphorylation site mutant

These results suggest a previously unknown function of synapsin in *C. elegans* in the regulation of DCV localization and subsequent release. Thus, synapsin phosphorylation by PKA might be the regulatory mechanism for vesicle availability, including DCVs. As described in the introduction, *C. elegans* expresses two isoforms of synapsin and both are homologous to the mammalian synapsins. Human synapsin II has a known PKA phosphorylation site at S10, the homologous site in *C. elegans* is present in isoform SNN-1B(S9). We thus obtained a SNN-1B(S9A) variation generated by CRISPR/Cas9 genomic mutation, from a commercial provider (section A.1, p. 225).

bPAC photoactivation in SNN-1B(S9A) mutant animals increased speed and mean bending angles (figure 3.37 left and right, respectively). Interestingly, the point mutant moved significantly faster than wt animals also after light was turned off. Although SNN-1B(S9A) phosphorylation mutant animals displayed a tendency for decreased mean bending angles during photoactivation, this behavior was not significantly different from the response of bPAC wt animals. Nonetheless, after light was turned off, bPAC SNN-1B(S9A) animals could not sustain the increased bending angles as bPAC wt animals. In comparison, bPAC *snn-1(tm2557)* background did not increase mean bending angles, while it permanently increased speed during photoactivation (section 3.1.4.1, p. 107).

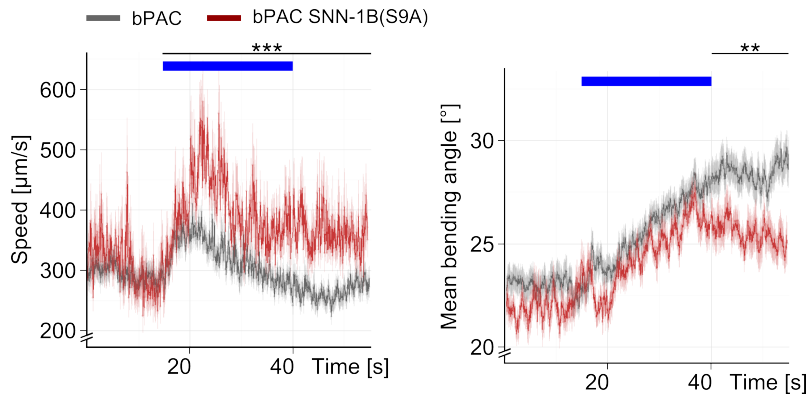


**Figure 3.37.: bPAC-induced effect partially dependent on synapsin SNN-1B(S9A) phosphorylation site.**

Synapsin phosphorylation mutant SNN-1B(S9A) had an enhanced speed compared to bPAC in wt background during and after photostimulation (left). Further, the phosphorylation mutant was not capable of maintaining the increased bending angles after photostimulation (right).

$n = \geq 20$ . Mean  $\pm$  SEM. ANOVA, Bonferroni correction. *ns* :  $p \geq 0.05$ ; \* :  $p \leq 0.05$ ; \*\* :  $p \leq 0.01$ ; \*\*\* :  $p \leq 0.001$ , significance region with at least 95 % of data points meeting p-value description.

#### 3.1.4.5. NLP-21 deficiency affected cAMP-induced behavior as observed in SNN-1B(S9A) animals

Since neuropeptidergic signaling was required for bPAC-induced modulation of behavior, bPAC was expressed in cholinergic neurons of *nlp-21(tm2569)* mutant animals. Upon photoactivation of bPAC in *nlp-21(tm2569)*, speed and mean bending angles were increased as in the synapsin phosphorylation mutant SNN-1B(S9A) described above (figure 3.38).

The reaction to bPAC photostimulation in these mutants is clustered together and similar to the effect of bPAC photoactivation in *unc-31(n1304)* mutants, lacking neuropeptidergic signaling (figure 3.39). Nonetheless, the difference between the effects of bPAC photostimulation across these mutants were very variable, as observed by the increased distance in the dendrogram. This is an indication that NLP-21 is one of the neuropeptides involved in the bPAC elicited behavior modulation.

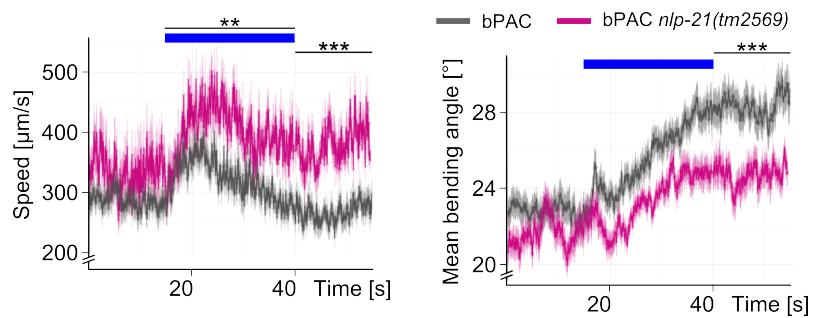


**Figure 3.38.: bPAC-induced effect partially dependent on NLP-21 neuropeptides.**

Animals expressing bPAC in *nlp-21(tm2569)* mutants had an enhanced speed compared to bPAC in wt background during and after photostimulation (left). Further, the neuropeptidergic mutant was not capable of maintaining the increased bending angles after photostimulation (right).

$n = \geq 20$ . Mean  $\pm$  SEM. ANOVA, Bonferroni correction. *ns* :  $p \geq 0.05$ ; \* :  $p \leq 0.05$ ; \*\* :  $p \leq 0.01$ ; \*\*\* :  $p \leq 0.001$ , significance region with at least 95% of data points meeting p-value description.

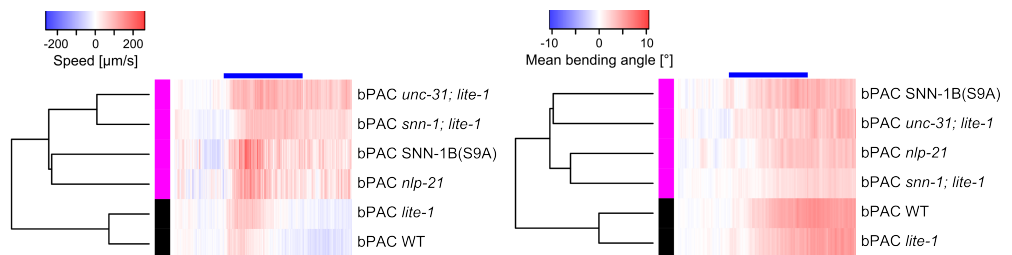


**Figure 3.39.: NLP-21 required for bPAC-induced effect on behavior.**

Cluster analysis of bPAC-induced effects in the *nlp-21(tm2569)* background was similar to the effects elicited in the synapsin phosphorylation mutant SNN-1B(S9A) (speed left, mean bending angle right). Although the difference between phenotypes was high, these mutants clustered to the canonical mutants *unc-31(n1304)* and *snn-1(tm2557)*.

Photoactivation denoted by blue bar. Similarity calculated by DTW and clustered by hierarchical clustering.  $n \geq 20$ .



### 3.1.5. Brief conclusion

In conclusion, bPAC photoactivation in cholinergic neurons induced neuropeptidergic signaling and increased the probability of SV release. Thus, bPAC can be used to further modulate neuronal output in addition to rhodopsin control of neuronal depolarization state. Further, cAMP signal transduction analysis revealed a new function of synapsin in the control of DCV release, although not all pathways of signal transduction could be characterized during this work. Nevertheless, bPAC and rhodopsin based tools allow complementary optogenetic analysis and both systems were thus applied in the following characterization of the interneuron RIS.

## 3.2. Characterization of the interneuron RIS

The second part of this work delineates the analysis of the GABAergic neuron RIS with hitherto unknown function in the behavior of adult *C. elegans*. RIS was shown to be a peptidergic neuron, since it requires neuropeptidergic signaling for behavior modulation during larval molts. Here, characterization and modulation of RIS output in adult animals through the optogenetic tools described and established during this thesis were performed.

### 3.2.1. Single cell expression system

For optogenetic analysis of RIS, a specific promoter had to be found. Unfortunately, to the date of writing, no known single promoter expresses in RIS alone. Therefore, a combinatorial system was required to specifically express in RIS.

#### 3.2.1.1. Cre/LoxP based expression system

From the available methods for combinatorial expression, the Cre/LoxP system was selected for the higher compatibility with previous work performed in the laboratory of Prof. Alexander Gottschalk (figure 3.40 schematic). Two promoter pairs tested had mutual expression solely in RIS: the promoters of *ggr-1* & *ggr-2* and the promoters of *ntr-2* & *ggr-2*.

The promoter pair *ggr-1* and *ggr-2* drove expression in about 90 % of the transgenic animals in RIS when cultivated at 20 °C (figure 3.41). Further, below 1 % of the animals displayed expression in another, unidentified neuron (data from 128 animals).

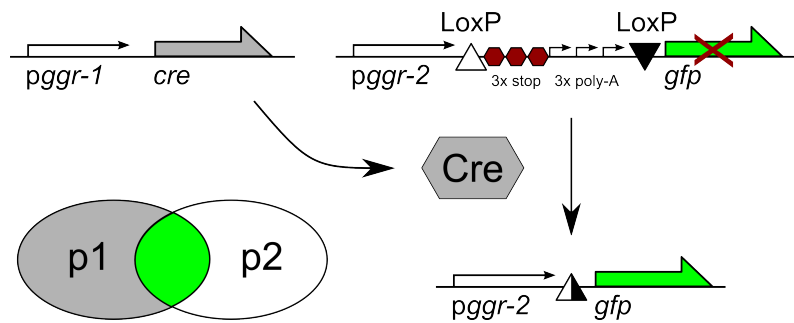


**Figure 3.40.: Cre/LoxP scheme for single cell expression in RIS.**

Single cell expression in RIS was achieved with the promoters of *ggr-1* and *ggr-2*, driving the expression of the Cre recombinase and the gene of interest, respectively. In this scheme, the second promoter drove the expression of GFP upon excision of the stop cassette by the Cre recombinase. The stop cassette is a DNA sequence flanked by LoxP sites containing 3 stop codons followed by 3 polyadenylation sequences. Only cells expressing both promoters will express the gene of interest (bottom left overlap of p1 and p2)

The transgenic animals without expression in RIS were due to mosaicism of the extrachromosomal array, since their progeny had the same distribution of expression in RIS (data from 5 animals). Following integration of the extrachromosomal array, all animals expressed in RIS (data from 1 integrated strain). When cultivated at 25 °C, the promoters drove expression in ventral motor neurons in about 25 % of the animals, thus all experiments were conducted at 20 °C (data from 30 animals).

I also characterized, the promoter pair *ntr-2* and *ggr-2*: This combination drove expression in RIS in only about 75 % of the transgenic animals when cultivated at 20 °C (data from 45 animals). This combination displayed an increased mosaicism rate, as well as variable promoter expression pattern, since about 20 % of the animals drove expression in an additional neuron in the head. Moreover, about 5 % of the animals showed expression in amphid neurons while further 5 % drove expression in ventral motor neurons. Therefore, this promoter pair was not used for further experiments.

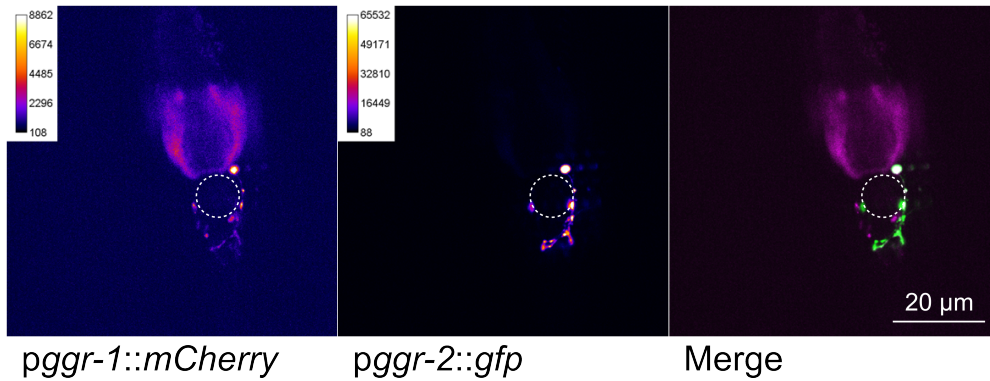


**Figure 3.41.: Promoter pair characterized for single cell expression in RIS.**

Co-expression of two fluorophores without the Cre/LoxP system for analysis of the expression overlap of both promoters (left *ggr-1* mCherry, center *ggr-2* GFP driven expression). Overlap of expression in only one cell, namely RIS (right merged channels, white neuron).

Promoter denoted with prefix “p”. Maximum intensity projection. Left and center – false colored; right – magenta: mCherry, green: GFP, white: promoter overlap. Scale bar 20  $\mu\text{m}$ .

### 3.2.1.2. Expression on a further cell in male animals

Although the system was reliable for sole expression of the proteins of interest in the RIS neuron of hermaphrodite animals, male animals displayed expression in a further neuron. The male specific neuron that showed protein expression is probably PDC (figure 3.42). In spite of the structured illumination tracker used for data acquisition during this thesis capability of selectively illuminating this neuron, it was not part of this work and remains to be analyzed in the future.

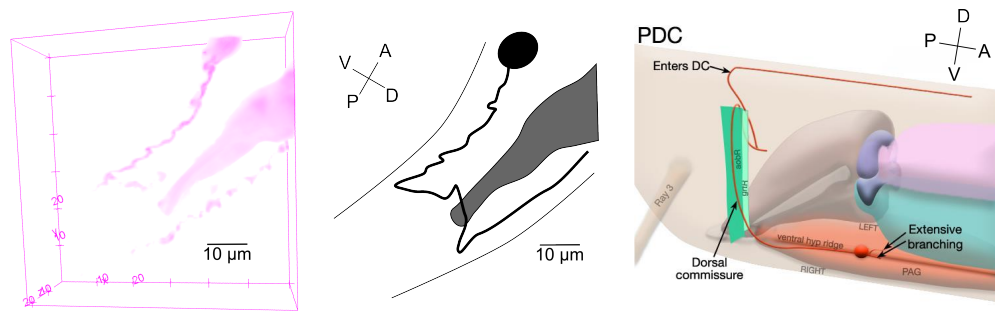


**Figure 3.42.: Promoter pair specific for RIS also drove expression in the male specific tale neuron.**

3D reconstruction of GFP expression driven in a male specific neuron by the RIS specific promoter pair (left). Schematic position of the neuron in the tail of the animal, black: neuron, gray: gut, lines: body outline (center). The neuron is probably the male specific neuron PDC (right, adapted from wormatlas.org [260]). Scale bar 10  $\mu\text{m}$ .

### 3.2.2. Acute RIS photoactivation induces locomotion pause behavior in adult animals

In order to characterize the function of RIS in adult hermaphrodites during behavior, ChR2(H134R) was expressed in RIS with the Cre/LoxP system described above. Since no function for RIS in adult behavior was known, the transgene was generated in the *lite-1(ce314)* background. As discussed for bPAC, this background is deficient in the intrinsic photophobic response to blue and violet light (section 3.1.1.2.3, p. 84). Hence, photostimulation of ChR2(H134R) in RIS would not be occluded by the photophobic response, should the latter inhibit the behavior modulation output of the former. Throughout the text the strain expressing ChR2(H134R) in RIS in the background *lite-1(ce314)* is further referenced as RIS::ChR2 for simplicity.

#### 3.2.2.1. Transgenic animals cease swimming behavior

Analogous to the first bPAC experiment, analysis of swimming behavior is a sensitive experiment for behavioral modulation due to optogenetic manipulation. Thus, it was also the first experiment performed with RIS::ChR2 animals. Upon photoactivation of RIS::ChR2 with the co-factor ATR, animals ceased swimming behavior (figure 3.43). This effect was reverted once the photoactivation light was turned off. Without the co-factor, however, there was no measurable change in the animals' swimming

rate.

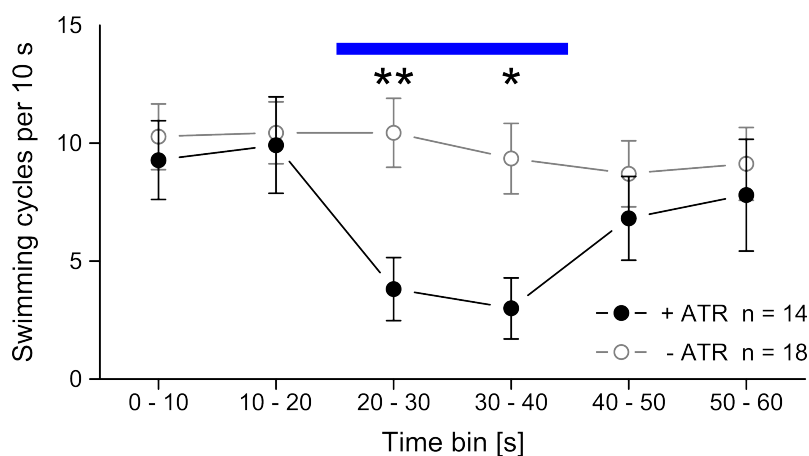


**Figure 3.43.: Acute RIS depolarization inhibited swimming behavior.**

Upon photoactivation of RIS::ChR2 animals raised in the presence of the ChR2 co-factor ATR, animals ceased swimming behavior (black, +ATR). This effect was reverted once the photoactivation light was turned off. Photoactivation of RIS::ChR2 without ATR did not change the swimming behavior of the animals (gray, -ATR)

Photoactivation denoted by blue bar. Mean  $\pm$  SEM. ANOVA, Bonferroni correction. *ns* :  $p \geq 0.05$ ; \* :  $p \leq 0.05$ ; \*\* :  $p \leq 0.01$ ; \*\*\* :  $p \leq 0.001$ .

### 3.2.2.2. Motility inhibition on solid substrate

Since swimming was inhibited, we analyzed if photostimulation of RIS::ChR2 could also inhibit crawling behavior on solid substrate. Moreover, solid substrate experiments allow analysis of more behavior parameters in comparison to swimming assays

Upon RIS::ChR2 photostimulation, animals stopped locomotion (figure 3.44). Irrespective of previous directionality, RIS::ChR2 led to motility inhibition in the first seconds of photoactivation. Importantly, this stop phenotype was stable for as long as the photoactivation light was kept on. Long periods of photoactivation could be achieved, but animals suffered from phototoxicity of the continuous blue light exposure (4 h, 20 adult hermaphrodites). Therefore, all data further analyzed was acquired with photoactivation for up to 5 min.

Further, no habituation to this stop phenotype could be observed. Multiple photoactivation cycles led to inhibition of movement in all cases (figure 3.45). Therefore,

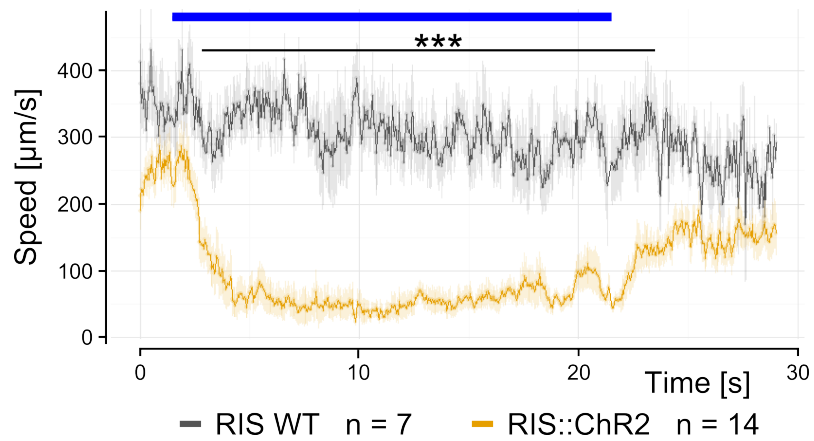


**Figure 3.44.: RIS depolarization led to immobility on solid substrate.**

RIS::ChR2 photoactivation led to motility stop in the first seconds of light application that remained for as long as the photoactivation light was on. This effect was reverted a few seconds after the photoactivation light was turned off.

Photoactivation denoted by blue bar. Mean  $\pm$  SEM. ANOVA, Tukey's HSD. *ns* :  $p \geq 0.05$ ; \* :  $p \leq 0.05$ ; \*\* :  $p \leq 0.01$ ; \*\*\* :  $p \leq 0.001$ , significance region with at least 95 % of data points meeting p-value description.

RIS' role in the neuronal network of *C. elegans* is unlikely subjected to downstream modulation.

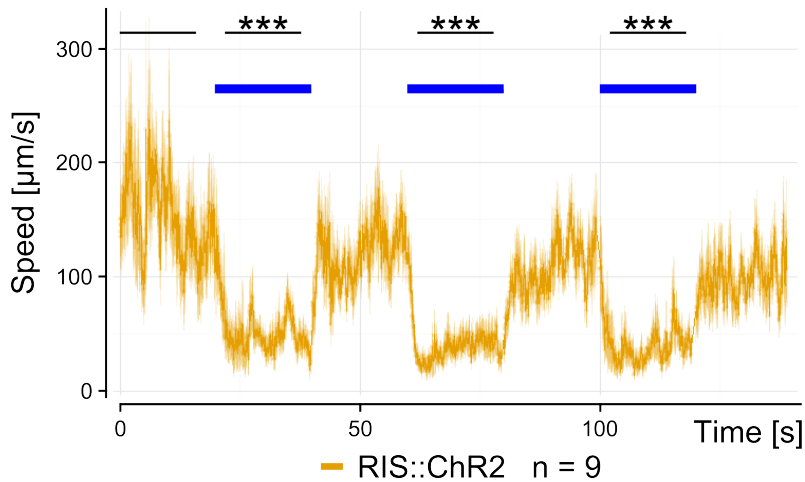


**Figure 3.45.: No habituation to multiple RIS::ChR2 photostimulation.**

The locomotion of RIS::ChR2 animals on solid substrate was inhibited at each photostimulation time frame and no habituation to the photostimulation could be detected.

Photoactivation denoted by blue bar. Mean  $\pm$  SEM. ANOVA, Bonferroni correction to first denoted period. *ns* :  $p \geq 0.05$ ; \* :  $p \leq 0.05$ ; \*\* :  $p \leq 0.01$ ; \*\*\* :  $p \leq 0.001$ , significance region with at least 95% of data points meeting p-value description.

### 3.2.2.3. Body elongation during RIS depolarization

Interestingly, the RIS::ChR2-evoked stop phenotype is coupled to a small body elongation of about 2% (figure 3.46). This effect was further analyzed in the master thesis of Caspar-Elias Glock, for which I provided the transgenic animals. By marking the cuticle of RIS::ChR2 animals, Caspar-Elias Glock could measure an elongation of about 10% in the head region of the animal upon photostimulation. Thus, the head is solely responsible for the body elongation observed.

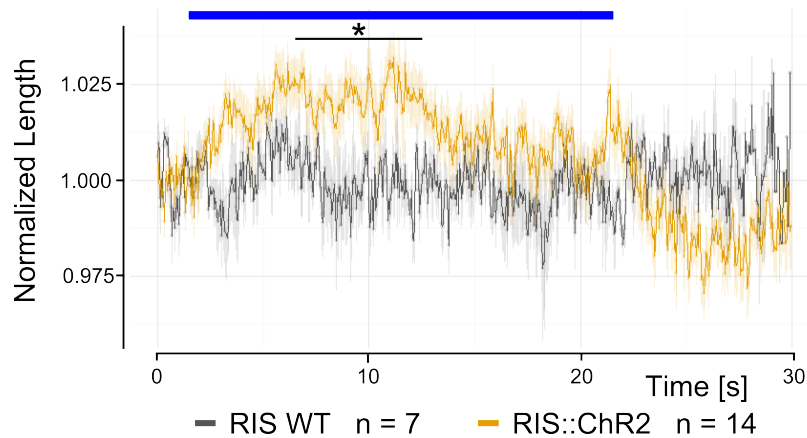


**Figure 3.46.: Small body elongation upon RIS::ChR2 photostimulation.**

The mean normalized length of RIS::ChR2 animals was increased by about 2% upon photostimulation. The animal body length reverted to the size prior to illumination after the light was turned off.

Photoactivation denoted by blue bar. Mean  $\pm$  SEM. ANOVA, Tukey's HSD. *ns* :  $p \geq 0.05$ ; \* :  $p \leq 0.05$ ; \*\* :  $p \leq 0.01$ ; \*\*\* :  $p \leq 0.001$ , significance region with at least 95% of data points meeting p-value description.

#### 3.2.2.4. High light dosage additionally inhibited pharynx pumping

These effects in behavior and body posture were observed with light dosages of about  $250 \mu\text{W mm}^{-2}$  and a wavelength of 470 nm, where more than half of RIS::ChR2 animals reacted to photoactivation with locomotion inhibition. Caspar-Elias Glock further analyzed the effect of increased photoactivation light intensity. It led to a further behavioral effect at about  $1 \text{ mW mm}^{-2}$ , where over 50% of the animals observed ceased pharynx pumping. At  $2.1 \text{ mW mm}^{-2}$ , 65% of the animals did not pump during photostimulation and the remaining 35% of the animals significantly reduced the pumping frequency (figure 3.47 left). Importantly, these high intensities are about one order of magnitude below the recently reported intensities that inhibit pharyngeal pumping in wt animals [399]. In addition, our RIS::ChR2 strain carries the *lite-1(ce314)* mutation (section 3.2.2, p. 122). This mutation was shown to be detrimental to wt pharyngeal pumping stop response to light [399].

The effect on pharyngeal pumping was confirmed by electropharyngeogram (EPG) measurements performed by Dr. Christina Schöler on animals provided by myself. She applied serotonin to induce pharyngeal pumping in cut head preparations, where the head of the animal is cut at about one third of the full body length. This cut



was performed to increase serotonin diffusion into the body cavity and to exclude swimming and therefore facilitate patch acquisition and maintenance. Upon photoactivation of RIS::ChR2 in presence of the co-factor ATR, pharyngeal depolarization were strongly inhibited (figure 3.47 center and right). Pharyngeal pumping inhibition did neither occur without ATR, nor was it sustained after photoactivation light was turned off, irrespective of whole animal or cut head preparation. The latter might be due to the serotonin application in the bath solution.

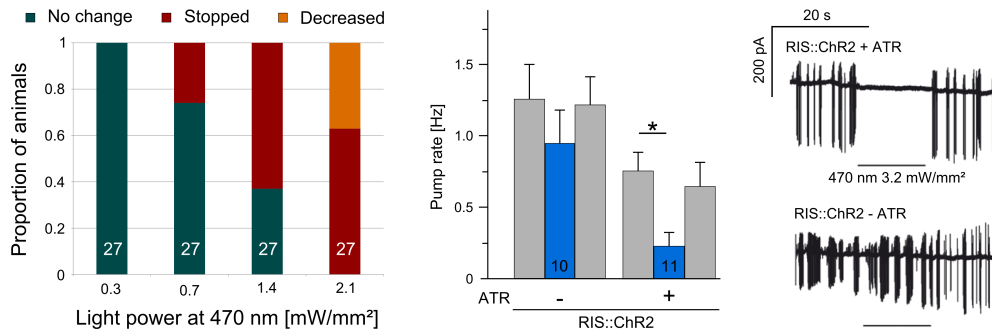


**Figure 3.47.: High light intensity photoactivation of RIS::ChR2 inhibited pharyngeal pumping.**

Light dosage increase to 2.1 mW mm<sup>-2</sup> impaired observable pharynx pumping rhythm in intact animals (left). EPG measurements of cut head preparations confirmed RIS::ChR2-mediated impairment of pharyngeal pumping. Strongly reduced pharyngeal activity was observed during RIS depolarization (center). Representative original traces from RIS::ChR2 with and without the co-factor ATR (right).

Center: Mean ± SEM. ANOVA, Bonferroni correction. *ns* :  $p \geq 0.05$ ; \* :  $p \leq 0.05$ ; \*\* :  $p \leq 0.01$ ; \*\*\* :  $p \leq 0.001$ . Measurement and analysis performed by Caspar-Elias Glock (left) and Dr. Christina Schöler (center, right).

These experiments further confirmed the acute behavior modulation of RIS, as well as the fast recovery once the neuron is hyperpolarized. In addition, the cut head preparations indicate that RIS likely modulating pharyngeal pumping through signal transduction in the nerve ring. Otherwise, we could expect a reduced effect due to the increased dilution of neurotransmitters next to the end of the pharynx (and RIS cell body), where the cut preparation interacts with the buffer.

### 3.2.2.5. RIS induced phenotypes are bypassed by mechanosensory stimuli

Nonetheless, the above mentioned inhibition of locomotion during RIS::ChR2 photostimulation is not a complete animal paralysis. Upon aversive stimulation, for in-

stance touching the head or the tail of the animal during photo-depolarization of RIS, the animal resumed locomotion for a brief time frame (figure 3.48). The distance moved during photostimulation was restricted to about one body length and animals stopped locomotion anew. Animals did not display a reduced reaction to mechanical stimulation after the photostimulation light was turned off.

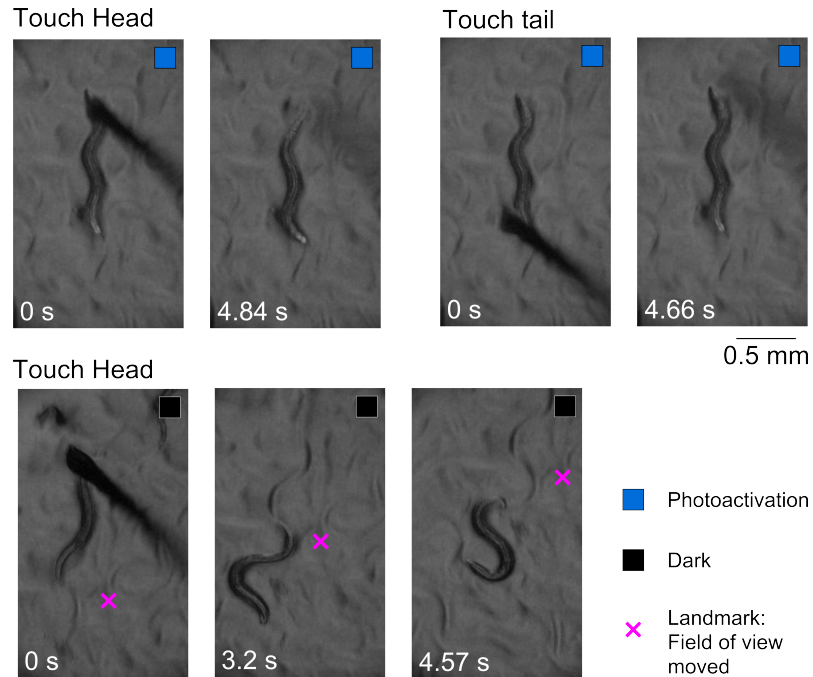


**Figure 3.48.: Aversive stimuli inhibited RIS::ChR2-induced locomotion pause.**

Mechanical stimulation of the head of an animal with locomotion inhibited by RIS::ChR2 depolarization led to directed locomotion away from the touch stimulus (top left). Further, mechanical stimulation of the tail during RIS::ChR2 photostimulation induced forward movement (top right). The locomotion amplitude was reduced in comparison to unstimulated animals, with a mean displacement below one body length. After photoactivation light was turned off, RIS::ChR2 animals reacted as non-transgenic wt animals with increased displacement and directionality change (bottom, cross demarcates a landmark, to indicate movement of the field of view).

Representative movie frames with time stamps. Blue and black boxes indicate presence or absence of photoactivation light. Scale bar 0.5 mm.

In conclusion, the RIS::ChR2-induced locomotion stop phenotype is not observed in normal behavior of well fed adult animals, especially when transferred to a plate without bacteria. In this condition, well fed animal behavior is a mixture between

long runs and foraging. The former described by long forward motion with low directionality change while the latter is a local search for food with high incidence of reversals and high directionality change.

#### **3.2.2.6. No inhibition of behavior during RIS hyperpolarization**

Interestingly, hyperpolarization of RIS during unrestrained locomotion on solid substrate did not lead to observable effects in behavior. Animals with Arch, an outward proton pump, or HisCl, a histamine gated chloride channel, expressed in RIS did not have impaired intrinsic locomotion pauses. Thus, RIS might rather have a very low probability of activation during crawling on solid substrate.

#### **3.2.3. Identification of signaling pathways within or involving RIS**

Although the RIS::ChR2-induced phenotype was not reminiscent of normal behavior, it could be used to elucidate the signaling mechanism from and to RIS in *C. elegans*. To further understand the genetic requirements for RIS function in the network, three methods were applied. First, RIS::ChR2 was expressed in candidate mutant backgrounds, affecting possible RIS signaling components, and their reaction to photoactivation were analyzed. Second, a forward genetic screen was performed to find a mutant capable of suppressing the RIS::ChR2-induced stop phenotype. Third, dissociation and culture of RIS neurons in media were established for cell specific RNA sequencing to explore and characterize the RIS transcriptome.

##### **3.2.3.1. Canonical mutant analysis shows neuropeptidergic signal requirement**

First, RIS::ChR2 was expressed in several canonical mutants to test the dependency to certain sub-circuits in the downstream neuronal network as well as if the phenotype was caused by GABAergic or neuropeptidergic signaling from RIS. Although RIS does express dopamine and serotonin receptors, *dop-1* and *ser-4* respectively, these were not selected for the initial screen, since these pathways probably serve a modulatory role in RIS function. The mutant *unc-25(e156)*, coding for the glutamic acid decarboxylase required for GABA production, was tested to address the requirement for GABAergic signaling. The mutant *unc-47(e307)*, coding for the vesicular GABA transporter, was tested since *unc-25(e156)* animals still filled GABAergic SVs with glycine. This was required, since *C. elegans* expresses 3 GABA/Glycine Receptor

family proteins (*ggr-1*, *ggr-2* and *ggr-3*; RIS itself expresses the first two genes). Then, the mutant *unc-9(e101)*, an innexin expressed in RIS, was used to test the requirement of gap junctions for RIS function. Further, the *unc-31(n1304)* mutant was tested, as CAPS/UNC-31 protein is partially required for neuropeptidergic signaling. Furthermore, the mutant *tdc-1(n3419)*, a tyrosine decarboxylase, was tested to address the requirement of tyramine signaling from the neuron RIM in the effect of RIS::ChR2 photostimulation, since both neuron types are in a feedback synaptic loop.

The analysis of the aforementioned strains were performed by Anke Hermann, Marlene Steiner and Caspar-Elias Glock during their laboratory rotation under my supervision. Their results are summarized in table 3.1.

**Table 3.1.:** Summary of RIS::ChR2-induced effect on several canonical mutants.

Genetic background	RIS::ChR2-induced stop	Notes
<i>tdc-1(n3419)</i>	Stop	
<i>unc-9(e101)</i>	Stop	
<i>unc-25(e156)</i>	Stop	Reduced probability of locomotion inhibition.
<i>unc-31(n1304)</i>	Stop	Mobility recovered during photostimulation.
<i>unc-47(e307)</i>	Stop	Increased body elongation during photostimulation.

In summary, none of the canonical mutations tested completely disrupted the RIS::ChR2-induced locomotion stop. Albeit GABAergic signaling mutants have shown a lower propensity for locomotion inhibition upon RIS::ChR2 photoactivation, RIS photodepolarization could still inhibit movement. Interestingly, RIS::ChR2 photoactivation in *unc-47(e307)* background led to an increase in the normalized body length. This could be due to the changed connectivity between RIS and RIM. RIM is a tyraminergetic neuron that inhibits muscle contraction in the head of the animal, specifically during escape behavior [267,400]. RIS and RIM are normally connected by both, chemical and electrical synapses [257,401]. In the absence of GABA, RIS photodepolarization could have led to an increased depolarization of RIM through gap junctions and therefore to an increased body elongation.

Further, although CAPS/UNC-31 mutants stopped during RIS::ChR2 photostimulation, locomotion was partially recovered during the photoactivation period. Thus, these experiments indicate a neuropeptidergic signaling requirement for RIS::ChR2-induced locomotion stop. Since *C. elegans* expresses over 100 neuropeptide genes and

canonical mutants are not available for all genes, other methods were explored: a forward genetic screen and the analysis of the RIS transcriptome.

### 3.2.3.2. The LIM-6 transcription factor is required for RIS::ChR2 induced phenotypes in adult animals

In order to characterize the neuropeptides required for RIS function, a forward genetic screen was performed in RIS::ChR2 animals. The EMS mutagenesis was performed in duplicate with help from Caspar-Elias Glock. The experiment was then further performed by myself, where 28 putative strains in which the parental animal did not stop during RIS::ChR2 photostimulation were isolated. From these, only up to 9 strains had independent mutations. The most represented mutation was a dominant locus in the X chromosome. This mutant as well as an additional strain were selected for chromosomal and subsequent interval mapping. These strains were then sent for WGS in the group of Dr. Baris Tursun. I analyzed the raw WGS data and characterized a new mutation in the *lim-6* gene (*lim-6(zx1)*, figure 3.49). *lim-6* is a gene coding for a transcription factor required for RIS function but not differentiation [347]. Unfortunately, the second sequenced strain could not be unambiguously traced to a single mutation and therefore will not be further described in this thesis.

The *lim-6(zx1)* expresses a mutated version of the protein, LIM-6(A239T). This point mutation is in the DNA-binding homeobox domain of both isoforms of the transcription factor [402, 403]. To further characterize if this mutation could change the sequence specificity of the transcription factor, the protein sequence was used as template for a model search in the protein model portal [404]. Two independent software packages were selected for modeling the structure of the homeobox domain, SWISS-MODEL and M4T [405–408]. Both software aligned the homeobox domain of LIM-6 to the POU protein:DNA complex from *Mus musculus* POU domain, class 5, transcription factor 1 protein [409] (sequence alignment in figure 3.50 top left). The quality of the alignment was assessed by the ProSA plot of residue scores, where negative energy indicate good quality of fit (figure 3.50 middle left) [363, 364]. Further, the calculated B-factor for the main chain showed significant loss of quality in the region outside of the homeobox. The homeobox itself had B-factors ranging from  $22 \text{ \AA}^2$  to  $180 \text{ \AA}^2$ , with the highest uncertainty in the loop region and the lowest in the DNA-recognition sites to which Alanine 239 was modeled to (figure 3.50 center, cartoon with A239 as stick representation). The model for LIM-6 was further improved with the electrostatic shell calculated by the Adaptive Poisson-Boltzmann Solver [351]

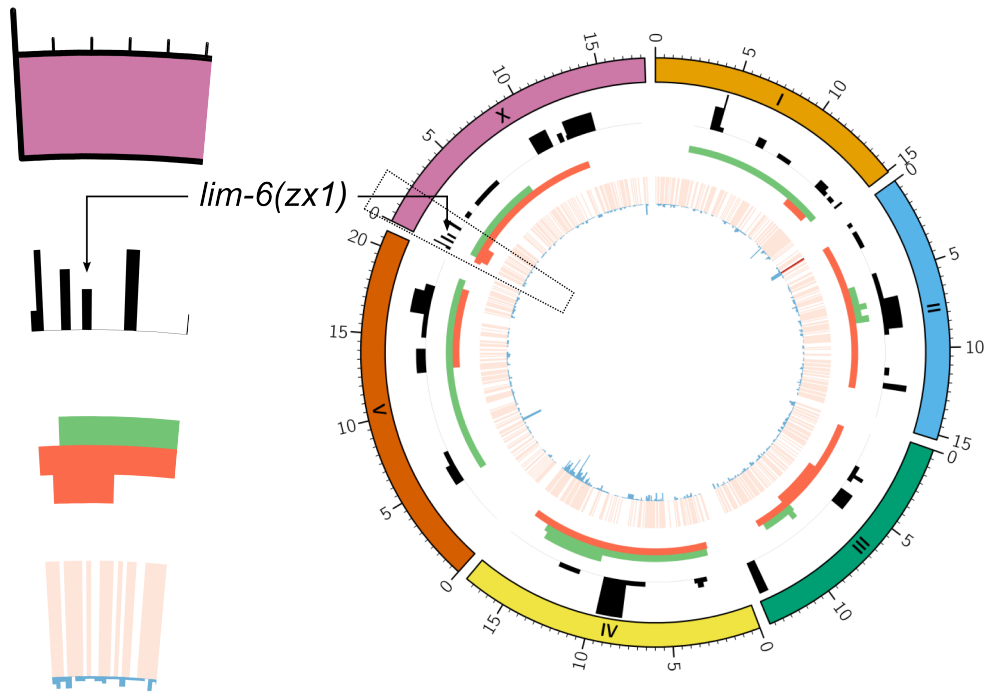


**Figure 3.49.: WGS of *lim-6* mutant responsible for RIS::Chr2-phenotype disruption.**  
 The strain with a dominant locus in the chromosome X was analyzed by WGS. The WGS summary with mutations is depicted by, outwards: Uncovered regions (blue), heat map of uncovered bases (red), deletions (red), insertions (green), SNPs/variations (black). The mutation in the genomic locus that was in accordance to the interval mapping was in *lim-6(zx1)*.

with a PQR file generated with PARSE force field and a pH of 7 [361,362] (figure 3.50 top right). The model showed that the point mutation is in the last amino acid of the C-terminal- $\alpha$ -Helix in the homeobox domain, the last amino acid that binds to the major groove of the DNA. The change in the recognition site is depicted by the virtual mutagenesis and electrostatic shell recalculation of the homeobox domain in LIM-6(A239T). The DNA-recognition motif was changed to a neutral charge with added sterical hindrance by the enlarged side-chain of Threonine.

In addition, an analysis of LIM-6 wt specific DNA base contacts was performed in the Conserved Domains and Protein Classification suite [410] based on a transcription factor DNA interaction study [411]. The 317 similar sequences found by BLAST to LIM-6 wt were analyzed. There, 31.5% of the sequences displayed an Alanine and

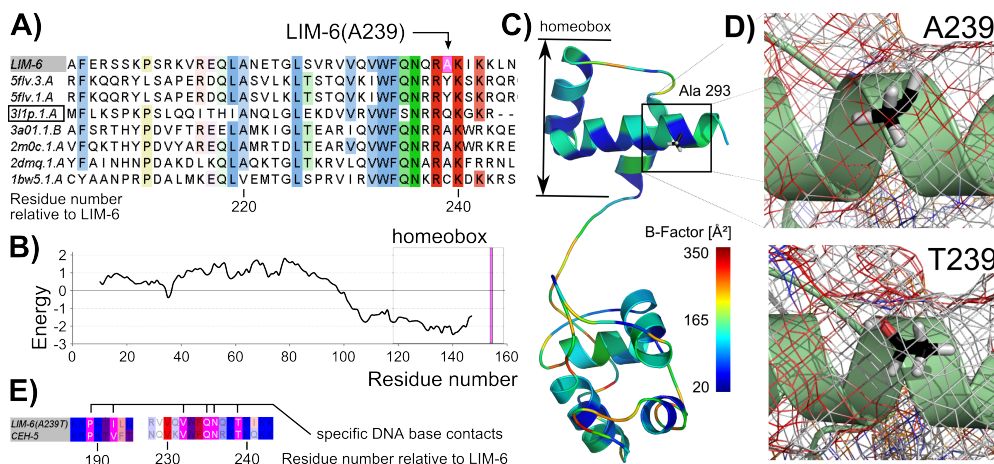


**Figure 3.50.: LIM-6(A239T) mutation disrupts DNA-recognition motif.**

**A)** BLAST search by two independent providers returned the POU domain, class 5, transcription factor 1 from *M. musculus* as matching the homeobox domain of LIM-6 (sequence alignment top left, box, PDB). **B)** The model structure had a good quality of fit for the homeobox domain according to the ProSA plot of residue scores for the homeobox domain. Because ProSA used a sliding window of 10 amino acids, A239 quality of fit is not displayed (middle left, magenta). **C)** Further, the range of the calculated B-factor showed low model quality distal to the homeobox. **D)** The model for LIM-6 homeobox domain was enriched by a calculated electrostatic shell. Virtual mutagenesis of LIM-6(A239T) and recalculation of the electrostatic shell showed two effects of the mutation to the DNA-recognition motif: Increased sterical hindrance and a shift to neutral charge (red to white shift of the mesh). **E)** The *C. elegans* homeobox transcription factor most similar to LIM-6(A239T), concerning the specific DNA base contacts, is CEH-5 (magenta: specific DNA contacts).

Top right: A239. Bottom right: T239. Representation: A/T 239 as sticks, backbone as cartoon. Electrostatic shell with blue: negative; white: neutral; red: positive.

6.0% displayed a Threonine in the equivalent position to LIM-6(A239). This third sequence alignment confirmed Alanine 239 as a DNA-binding amino acid. Analysis of the further DNA-binding amino acids within LIM-6(A239T) showed that the *C. elegans* transcription factor CEH-5 had the most similar specific DNA base contacts, with only one variation in an amino acid contacting the DNA minor groove (figure 3.50 bottom left). Thus, the DNA-motif recognized by LIM-6(A239T), is significantly different from the LIM-6 wt transcription factor and not identical to other known homeobox transcription factors.

Furthermore, *lim-6* is also expressed in other cells [403]. Hence, it cannot be excluded that the inability of LIM-6(A239T) animals to stop during RIS::Chr2 photoac-

tivation was due to a deficit of protein expression in these cells. Further analysis is required to ensure miss-expression in RIS as the sole cause for the LIM-6(A239T) mutant phenotype. Development of RIS assessed by its morphology in the adult animal as well as expression of RIS::ChR2 are not affected by *lim-6(zx1)*, as these were constraints for mutant isolation.

### 3.2.3.3. Cell specific RNA sequencing revealed putative neuropeptides required for RIS function

The second method for the characterization of neuropeptide requirement in RIS was the analysis of the RIS transcriptome. Therefore, two RIS reporter strains were generated for RIS cell extraction and subsequent RNA sequencing. The first reporter strain expressed GFP specifically in RIS while the second did not make use of the combinatorial Cre/LoxP expression system but rather relied on a two-fluorophore-sorting mechanism. The second strain was required since the GFP fluorescence of the first strain was insufficient for the automatic sorting process.

Preliminary cell dissociation studies with RIS::GFP strain showed that RIS could be dissociated from L4 larvae grown at 20 °C. Further, after two days of incubation in liquid media, neurons partially grew processes in the cell culture (figure 3.51). The RIS cell body *in vitro* had a maximum diameter of about 3.5 µm, somewhat more than the mean size *in vivo* of about 2 µm to 3 µm [412]. I estimated the RIS cell count from the dilution analyzed to an amount of 30 000 ± 5000 extracted live neurons, which amounts to about 0.05 % of the total RIS cells before extraction. At least 20 000 cells were required for subsequent RNA-Seq. Hence, although with very low efficiency, cell specific RNA extraction and sequencing were possible. These were then performed by the group of David M. Miller, III. and the results provided as a cooperation (extraction procedure performed by myself explained in section 2.2.2.5, p. 67, while extraction, RNA-Seq and constraints of the data analysis are explained in section A.5, p. 228).

The list of transcripts in RIS with at least two fold over-expression compared to non-RIS cells contains 556 genes. These genes were first analyzed for known RIS-markers by David M. Miller, III.. Table 3.2 summarizes the RIS marker genes in the RIS enriched data set sorted for their false discovery rate (FDR) corrected p-values. Since all known RIS marker genes were found to be over-expressed in the RNA-Seq data, it validated its usage for analysis of further RIS enriched genes.



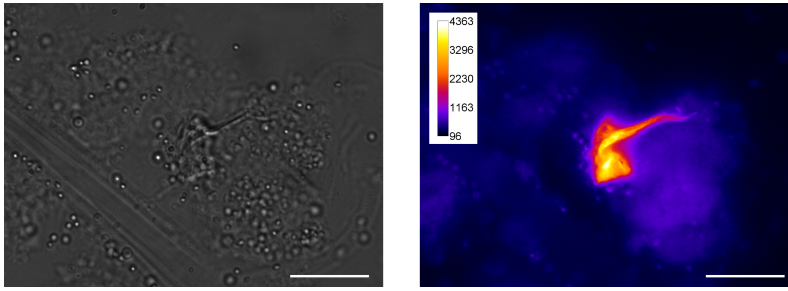


**Figure 3.51.: Preliminary RIS::GFP cell dissociation and cultivation.**

L4 larvae were dissociated and their cells cultivated for 2 days. RIS::GFP showed partial neurite re-growth after cell dissociation (left transmission light, right false colored GFP channel). Further, RIS cell count was estimated from the dilution analyzed to about  $30\,000 \pm 5000$  extracted cells. This trial confirmed the feasibility of cell extraction for a subsequent RNA sequencing experiment.

Scale bar 5  $\mu$ m

**Table 3.2.:** RIS marker genes present in RNA-Seq dataset sorted by p-value.

Gene	Enrichment	FDR corr. p- value	Description	Reference
<i>nhr-67</i>	125	0.000 085	Encodes a nuclear receptor.	[413]
<i>aptf-1</i>	122	0.001	Encodes one of four <i>C. elegans</i> AP-2-like transcription factors.	[335]
<i>ser-4</i>	18.4	0.001	Encodes an ortholog of mammalian 5-HT1 metabotropic serotonin receptors.	[347]
<i>zig-5</i>	68	0.002	Encodes a predicted secreted protein that is a member of the immunoglobulin superfamily of proteins.	[347]
<i>lim-6</i>	23	0.014	Encodes a LIM class homeodomain protein.	[403]
<i>unc-9</i>	18.3	0.017	Encodes an innexin, an integral transmembrane channel protein that is a structural component of invertebrate gap junctions.	[414]
<i>unc-47</i>	26	0.022	Encodes a transmembrane vesicular GABA transporter.	[415]
<i>dop-1</i>	20	0.031	Encodes a D1-like dopamine receptor required for regulation of locomotion.	[347]
<i>unc-25</i>	12	0.033	Encodes the <i>C. elegans</i> ortholog of the GABA neurotransmitter biosynthetic enzyme, glutamic acid decarboxylase.	[415]
<i>cam-1</i>	12.5	0.036	Encodes a receptor tyrosine kinase of the immunoglobulin superfamily.	[416]

**Table 3.2.:** (continued)

Gene	Enrichment	FDR corr. p- value	Description	Reference
<i>sng-1</i>	18.6	0.04	Encodes the <i>C. elegans</i> synaptogyrin ortholog, a synaptic vesicle integral membrane protein.	[417]

The list of genes in the RIS data set was enriched by GO term and analyzed for their occurrence. Figure 3.52 shows the 14 groups of GO terms found for biological processes. These are further subdivided into 209 subgroups, from which the name of the term with the highest incidence is used to name the group (unnamed groups: yellow – establishment or maintenance of epithelial cell apical/basal polarity, cyan – homophilic cell adhesion via plasma membrane adhesion molecules, green – glucose metabolism, red – asymmetric cell division). The GO term visualization summarized the main biological processes to which RIS-enriched genes partake in. These revolve around locomotion as well as the requirement for neuropeptidergic and GABAergic signaling. Since the canonical mutant analysis showed that GABAergic signaling did not inhibit RIS::Chr2-induced stop of locomotion, an in depth analysis of the neuropeptidergic signaling tagged molecules was performed to specify further putative genes for behavioral analysis.

About 12% of the up-regulated genes in RIS were marked by GO terms as taking part in neuropeptidergic signaling. The subset of these genes that had both, their false discovery rate (FDR) corrected p-value as well as the fold change in expression, increased to the upper quartile were selected and displayed in a partial volcano plot (figure 3.53). This subset contains 6 neuropeptides, including *flp-11*, and 3 neuropeptide receptor expressing genes. Analyses of these genes were not part of this thesis but of follow-up work performed by Petrus Van der Auwera (section 4.2.1, p. 156 for a discussion of preliminary results).

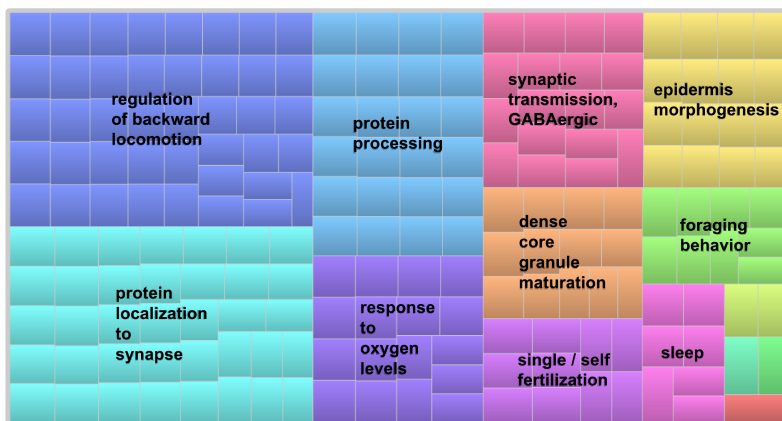


**Figure 3.52.: RIS up-regulated biological process gene ontology.**

TreeMap of 1273 GO terms for biological processes from the RIS up-regulated genes discovered by RNA sequencing. The grouped GO terms correspond to semantic similar biological processes and the term with highest incidence in a group is displayed (unnamed groups, see text). In summary, the set of up-regulated genes in RIS correlates with GO terms for behavior modulation as well as neuropeptidergic and GABAergic signaling. GO terms grouped and displayed by REViGO.

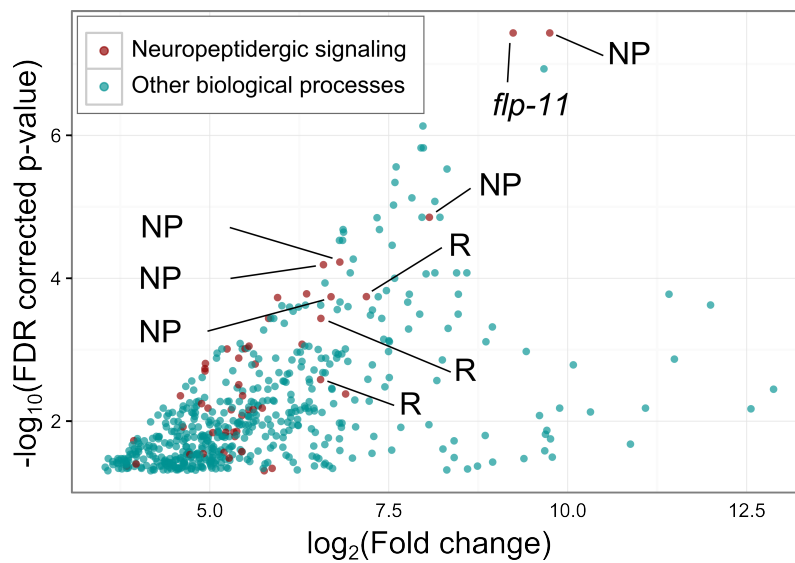


**Figure 3.53.: Volcano plot of RIS up-regulated genes.**

About 12% of the RIS up-regulated genes are described as taking part in neuropeptidergic signaling (red). The neuropeptide related genes pertaining to the upper quartile in both, fold change and FDR corrected p-values, contain *flp-11* and 5 further neuropeptides (NP), as well as 3 neuropeptide receptors (R). These genes were selected as the best candidates for subsequent behavioral analysis.

### 3.2.4. Analysis of the intrinsic activity of RIS

Both sections above analyzed the effect of acute RIS depolarization as well as putative genes required for RIS function (section 3.2.2, p. 122 and 3.2.3, respectively). Nonetheless, the full locomotion stop observed during RIS::Chr2 photoactivation was not reminiscent of *C. elegans* behavior in the environmental conditions applied during this work. Hence, analysis of RIS intrinsic activity would allow to better characterize the function of RIS in *C. elegans* neuronal network function and thus in its behavior. Therefore, Caspar-Elias Glock generated animals expressing GCaMP6 in RIS with the Cre/LoxP system described herein, henceforth referenced as RIS::GCaMP6 animals.

The first RIS::GCaMP6 analysis of freely behaving animals was a collaboration between Caspar-Elias Glock, Dr. Sebastian Wabnig and myself. This effort was required, since no automatic neuronal process tracking system was established at that time. Due to the manual tracking, no correlation to quantified velocities could be calculated, although behavior could be described in three general states: forward and backward locomotion as well as locomotion halt.

Multiple movies of different animals were acquired where RIS activity was observed during locomotion stop, irrespective of a subsequent directionality change in the movement of the animal. Due to the manual analysis required, only one representative frame set is depicted here. The analysis of the obtained movie showed that RIS had a calcium wave during locomotion stop in the nerve ring region (figure 3.54). In addition, the RIS region with the process branch showed an increased calcium concentration during backwards movement. The calcium signal increase observed during the reversal in the RIS cell body is likely an artifact due to the high intestine fluorescence in combination with the posterior localization of the cell body during reversals. The latter due to a contraction of the body during backwards movement.

Further, the calcium signal change had a higher magnitude in the process of RIS. This effect could be caused by either or a combination of the following reasons:

1. Lower volume to area ratio of the process compared to cell body led to increased change of calcium concentration at the same calcium intake.
2. Higher calcium buffering capacity of the cell body compared to the process.
3. Distinct expression or modulation of calcium channels in the cell body compared to the process.
4. Localized calcium dynamics due to localized upstream neuronal signaling.

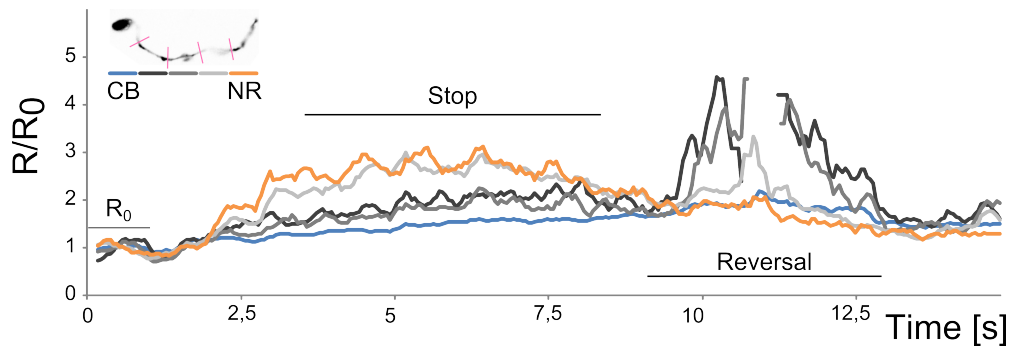


**Figure 3.54.: RIS activity during free locomotion monitored by calcium imaging.**

RIS::GCaMP6 animals were manually tracked during unrestricted locomotion on solid substrate. A calcium signal was observed during locomotion stop in the nerve ring region of the process (NR, orange). During backward locomotion, an increase in the  $\text{Ca}^{2+}$  signal occurred in the region where the branch is situated in. Furthermore, there was almost no change in the signal from the cell body during locomotion stop (CB, blue).

Strain provided by Caspar-Elias Glock, tracking performed with Caspar-Elias Glock and Dr. Sebastian Wabnig. Inset, color coded RIS regions. Data normalized to first second ( $R_0$ ). Moving average of 250 ms. Missing data points due to periods where the structure was out of focus.

#### 5. Irregular distribution of GCaMP6 in cell body versus process.

Thus, an automated system capable of tracking not only the cell body but also the process of RIS in freely behaving animals on solid substrate was required. To the time of writing, creation of such a tracking device and analysis of RIS activity during unrestrained locomotion was part of the PhD thesis of Petrus Van der Auwera (section 4.2.1, p. 155 for confirmatory data provided by Petrus Van der Auwera).

### 3.2.5. bPAC photoactivation in RIS led to increased locomotion stop probability

Since RIS is neuropeptidergic, I speculated whether cAMP signaling in RIS could modulate behavior. This would be in line with the likely opposite effects of serotonin and dopamine in RIS extrapolated from the receptor expression pattern. Dopamine could act through DOP-1, a D1-like dopamine receptor expressed in RIS, and  $G_{\alpha S}$  coupled [418, 419], while serotonin could reduce cAMP effects through SER-4 receptor [349]. Therefore, bPAC was expressed specifically in RIS with the Cre/LoxP system described above. In addition, expression was driven in *lite-1(ce314)* background

mutation to exclude photophobic responses during analysis. The resulting strain is henceforth referenced as RIS::bPAC.

#### **3.2.5.1. No acute locomotion inhibition upon RIS::bPAC photostimulation**

Intrinsic RIS activity was, as monitored by calcium imaging, highest during locomotion inhibition. Thus, I expected a higher propensity for RIS::bPAC animals to stop during photoactivation. However, bPAC did not induce acute locomotion inhibition during photoactivation, in contrast to the effect observed during depolarization in the RIS::ChR2 strain (figure 3.55).

Further, bPAC did not induce body elongation during photoactivation. Hence, RIS depolarization, but not stimulatory cAMP signaling, was required for acute locomotion inhibition. In the context of the findings in the first half of the thesis, this indicated cell-type specific differences in the mechanisms controlling neurotransmitter and neuropeptide release in cholinergic neurons versus RIS. In accordance, RIS::ChR2 led to neuropeptidergic signaling while cholinergic expression of ChR2 variant did not. Hence, there is a difference in regulation of neuronal output between neurons that mainly transmit signals through small chemical neurotransmitters versus those that transmit signals through neuropeptidergic signaling.

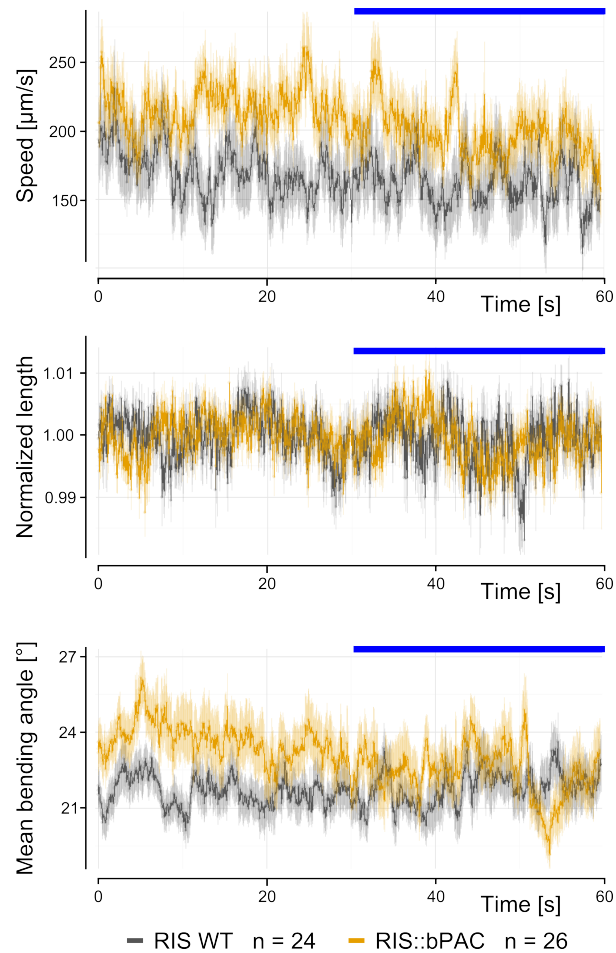


**Figure 3.55.: RIS::bPAC photoactivation did not modulate behavior drastically.**

Photoactivation of bPAC in RIS did neither acutely inhibit locomotion (top), nor induced a body elongation (center) as observed in RIS::Chr2 photostimulation. Further, RIS::bPAC photoactivation did not change body bending (bottom). Photoactivation denoted by blue bar. Mean  $\pm$  SEM. ANOVA, Bonferroni correction. All time points *ns* :  $p \geq 0.05$ .



### 3.2.5.2. Probability of stop increased during RIS::bPAC photostimulation

Since bPAC did not acutely induce stops, we analyzed if the probability of short stops was increased upon RIS::bPAC photostimulation. Therefore, the proportion of frames in a movie with locomotion stopped before and during photoactivation of bPAC in RIS were calculated. The mean count of stop frames was increased in RIS::bPAC animals during photostimulation, in contrast to the increased reversals observed in animals without bPAC expression. Further, the duration of these short stops (0.2 s to 5 s) were in the same range as the short stops observed during intrinsic activity measurements.

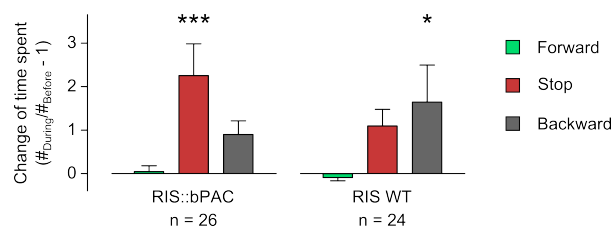


**Figure 3.56.: RIS::bPAC photoactivation increased probability of short locomotion pauses.**

Relative change of frames counted with movement grouped to either forward, stop or backward locomotion, before and during photoactivation. Positive change indicated higher count during stimulus. There was a higher probability of stopped locomotion in RIS::bPAC animals during photoactivation, while worms without bPAC expression had an increased tendency for reversal movement. Importantly, RIS::bPAC photoactivation did not increase the probability of reversals. Mean  $\pm$  SEM. ANOVA, Bonferroni correction, versus no change. *ns* :  $p \geq 0.05$ ; \* :  $p \leq 0.05$ ; \*\* :  $p \leq 0.01$ ; \*\*\* :  $p \leq 0.001$ .

Thus, RIS::bPAC photoactivation increased the probability of animals stopping their locomotion throughout the photoactivation period. In contrast to RIS::Chr2 though, the locomotion stops were not synchronized and had a lower probability of occurrence. This result further indicates the different regulation mechanism between RIS and the cholinergic motoneurons described in the first part of this work.

### 3.2.6. Brief conclusion

The interneuron RIS modulated behavior by induction of locomotion stop when depolarized through neuropeptidergic signaling. GABAergic signaling mutants did not disrupt the stop phenotype when RIS::Chr2 animals were photoactivated. Further,

optogenetic manipulation of cAMP levels in RIS led to an increased probability of short stops, but indicated a different regulation mechanism compared to cholinergic motoneurons regarding neuropeptidergic signaling.

## 4. Discussion

### 4.1. Modulation of cholinergic neurons function by light-evoked activity of bPAC/cAMP generation

The results presented herein showed that bPAC photostimulation in cholinergic motoneurons of *C. elegans* augmented their output through two distinct pathways. First, bPAC increased the probability of SV release, an effect also observed during light-evoked depolarization of these neurons with ChR2. Second, bPAC induced neuropeptidergic signaling from cholinergic neurons, an effect not observed during ChR2 mediated depolarization of the same neurons. These neuropeptides led to increased SV filling in cholinergic motoneurons, an effect dependent on the modulation of the vAChT. In addition, a new regulatory role of Synapsin in DCV signaling was observed.

#### 4.1.1. bPAC's low dark activity may still modulate behavior

The reduced bending angle observed in bPAC expressing animals might be due to the intrinsic dark activity of the enzyme. bPAC's dark activity has been quantified by Ryu and colleagues [207] and cAMP production during dark activity may be estimated to about  $1.0\% \pm 0.9\%$  of the cAMP production during photoactivation. Thus, bPAC expression alone will likely generate cAMP in the neurons of *C. elegans*. This may lead to compensatory effects, such as induction of the  $G_{\alpha i}$  pathway. This would be in agreement with the phenotype of animals with activated  $G_{\alpha i}$  pathway. These animals have shallow bending angles and reduced locomotion rate [420]. Nevertheless, the effects observed here are not as detrimental as the effects observed in the studies with EuPAC $\alpha$  [204]. Lower expression levels of bPAC could further reduce dark effects while still preserving the strong cAMP induction in the light.

#### 4.1.2. A new model for cholinergic SV quantal size regulation

The SV quantal size modulation due to bPAC photostimulation in cholinergic motoneurons is dependent on neuropeptidergic signaling, as shown by electrophysiological (section 3.1.2, p. 93) and ultrastructural (section 3.1.3.2, p. 104) analysis. In addition, bPAC photostimulation induced DCV release from cholinergic neurons (section 3.1.2, p. 92). Further, the SV quantal size increase was inhibited by Vesamicol, a vAChT blocker (section 3.1.3.3, p. 106). Hence, a new model of pre-synaptic SV quantal size modulation is suggested, in which neuropeptides secreted by a cholinergic neuron act on the cholinergic motoneuron pre-synapse to increase SV loading by modulation of vAChT (figure 4.1).

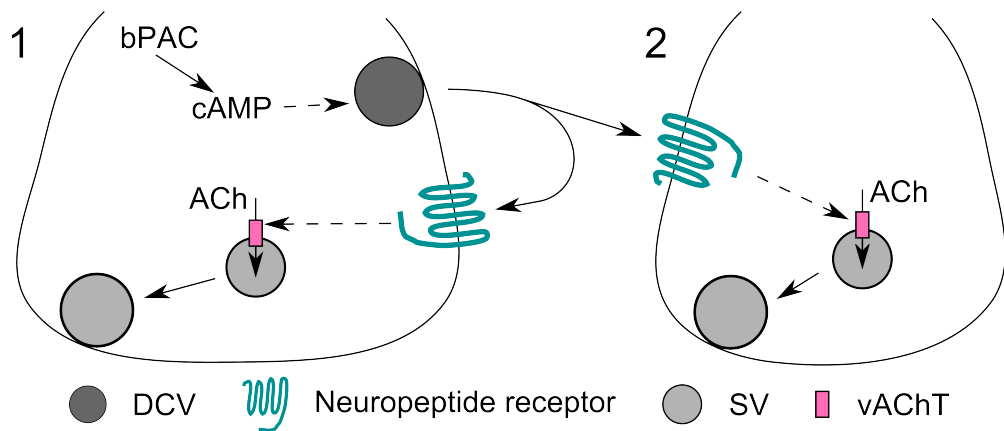


**Figure 4.1.: Proposed model of cholinergic SV quantal size modulation.**

bPAC photostimulation increases cAMP concentration in cholinergic neurons, which leads to neuropeptidergic signaling. The neuropeptide is either sensed by auto-receptors (1) or acts on downstream cholinergic motoneurons (2). Activation of a non-cAMP dependent signal transduction pathway leads to increased SV loading with ACh by modulation of vAChT, ultimately leading to SV size increase (exaggerated).

A similar model has been suggested in the example of the mammalian parasympathetic ciliary ganglion neurons. There, co-localization and release of ACh with the neuropeptide pituitary adenylate cyclase-activating polypeptide (PACAP) leads to a modulation of the pre-synapse, ultimately increasing SV quantal content [421]. In contrast to the model presented here, PACAP functions through NO signaling [421]. Since the *C. elegans* genome does not contain a gene coding for NO synthases [422], the mechanism of modulation, if at all, diverged during evolution. Nonetheless,

PACAP belong, together with vasoactive intestinal peptides (VIPs), to a superfamily of neuropeptides with high sequence conservation in vertebrates [423]. This has been proposed to be due to a co-evolution of both neuropeptides after a gene duplication and their specific receptors can, to some extent, be activated by the remaining neuropeptide [424]. Interestingly, analysis of *C. elegans*, teleost fish and human genomes by Cardoso *et al.* suggested conserved synteny in the region of VIP/PACAP receptor-coding genes [425]. An independent study identified a secretin-like receptor in the genome of *C. elegans* in the same chromosome location as suggested by Cardoso *et al.* [426]. This receptor, SEB-3, was identified to enhance locomotion and behavioral arousal implicated in stress response, albeit the mechanism has not been elucidated [427]. SEB-3 is expressed predominantly in neurons, albeit without further specification [427]. Since *seb-3* gain of function mutations lead to increased locomotion speed on solid substrate [427], this receptor might be involved in the mechanism described here.

Further candidate receptors can be obtained by comparing gene expression patterns in cholinergic motoneurons [428] with the *C. elegans* behavior database [240]. For example, *npr-20* is expressed in cholinergic motoneurons and deletion mutants of this receptor are slower and have reduced bending angles compared to wt animals. Since neither information on NPR-20 ligand, nor its signal transduction pathway have been reported, BLAST analysis of homology to other model organisms could be used to infer its function [429]<sup>1</sup>. The highest homology to *D. melanogaster* proteome is to the Trissin receptor, which leads to increased intracellular calcium levels upon activation [430]. This would result in a promising candidate for the neuropeptide receptor for the model presented here, should NPR-20 be coupled to increased intracellular calcium concentration.

Intriguingly, high amplitude mPSCs were shown to require neuronal RyR/UNC-68 expression [284], but analysis of bPAC photostimulation effect in the deletion mutant *unc-68(r1162)* performed during this thesis was not impaired (the increased response in bending angles compared to wt is due to the reduced intrinsic basal bending angles of the mutant, figure 3.28). Hence, the effects observed after bPAC photostimulation are not dependent on internal calcium stores, but likely PM localized calcium increase due to the neuropeptidergic signal.

The model can be thus further specified with micro domain specific signal transduction (figure 4.2). Without any optogenetic manipulation, intrinsic activation of adeny-

---

<sup>1</sup>WormBase web site, <http://www.wormbase.org>, release WS256, date 16/12/2016.

lyl cyclases (ACs) lead to localized PKA/KIN-1 signaling. This is mainly achieved by AKAP organization of PKA/KIN-1 regulatory domain [431, 432] and possibly phosphodiesterase (PDE) [433] in the vicinity of AC [434]. This architecture may be required for the reported PKA/KIN-1 control of calcium channels in GABAergic motoneurons of *C. elegans* (UNC-2 and EGL-19) [435]. The calcium channel UNC-2 is localized in the active zone of the pre-synapse [436] and also expressed in cholinergic motoneurons [428]. Thus, PKA/KIN-1 signaling might increase SV release probability also through increased intra-cellular calcium concentration (figure 4.2 top left, one SV depicted). In turn, RyR/UNC-68 activation may lead to higher cytoplasmic calcium concentrations that lead to the observed high amplitude mPSCs [284] and supposedly increased SV size ((figure 4.2 top right, exaggerated SV size). bPAC photostimulation disrupted localized cAMP signaling as well as induced DCV release. The neuropeptidergic signal transduction is likely coupled to cytoplasmic calcium increase and not to activation of  $G_q$  alpha subunit ( $G_{\alpha q}$ ) pathway, since the latter requires RyR/UNC-68 activation for calcium release into the cytosol [437]. The calcium increase likely activates calcium-calmodulin-dependent kinase II (CaMKII/UNC-43) [438] and this might lead to vAChT activity stimulation and thus SV filling state modulation. Since CaMKII/UNC-43 mutations have diverse abnormal phenotypes [438] and the kinase is required to maintain DCV localization [439], analysis of vAChT putative phosphorylation sites is likely more informative. Albeit unconvincing, vAChT has three predicted CaMKII/UNC-43 phosphorylation sites, out of which one is in the regulatory C-terminal cytoplasmic domain [355, 402]. A more plausible possibility is regulation of the membrane-bound choline acetyltransferase (MChAT) found in SVs. CaMKII/UNC-43 was shown to induce MChAT function and newly synthesized ACh was preferentially transported by vAChT in a mammalian synaptosome *in vitro* assay [440]. Further, these effects were also inhibited by Vesamicol application [440], in a similar pattern to the results presented in this thesis. Hence, the modulation of SV filling state may be conserved through diverse species and neuropeptides might allow for the specific control of this mechanism.

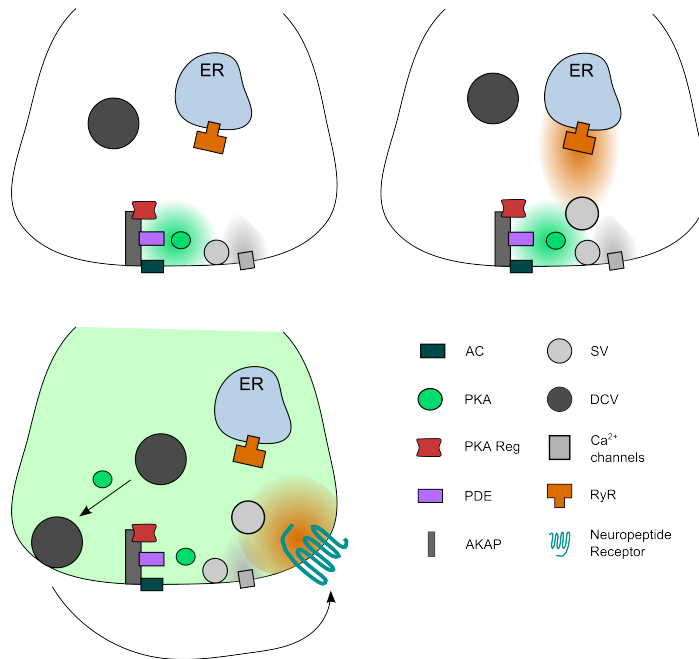


**Figure 4.2.: Model of cAMP and calcium distribution leading to bPAC induced effects.**

cAMP/PKA likely enhances SV release probability through activation of calcium channels (top left). Increased intra-cellular calcium concentration through RyR/UNC-68 activity might lead to increased SV filling (top right). bPAC photostimulation disrupts the micro domain architecture of cAMP signaling, leading to cAMP/PKA dependent DCV release, neuropeptide receptor activation and intracellular calcium increase, by-passing RyR/UNC-68 function on SV filling modulation (bottom left).

Not shown: high AC stimulation may induce DCV release in an activity dependent manner, likely paired to RyR/UNC-68 signaling.

Green background - cAMP signal. Orange background - high calcium concentration. Gray background - calcium channel localized signal.

### 4.1.3. Possible role of Synapsin in neuropeptidergic signaling

The behavior elicited by bPAC photoactivation in the *snn-1(tm2557)* deletion mutant was different than the effect observed in the SNN-1B(S9A) phosphorylation site point mutant. The former completely disrupted the bPAC effect on bending angles while the latter only reduced it. Further, the transient character of bPAC elicited speed increase was partially present in the phosphorylation mutant, but not on the deletion mutant. Although electrophysiological and ultrastructural data were not yet acquired for the phosphorylation mutant, the behavior response supports a role of Synapsin in DCV and SV turnover. The latter has been extensively described in the literature and synapsins have a conserved role across species [60,65]. The additional effects on DCV release indicates a new role of Synapsin in neuropeptidergic signaling.

One difference between both mutants is that the phosphorylation mutant is only present in the Synapsin SNN-1B isoform. The SNN-1A isoform does not include the domain A, where S9 is conserved (figure 4.3). In contrast, all mammalian Synapsin isoforms contain the A domain [441]. The site S9 (figure 4.3 bottom, 1) is targeted by PKA/KIN-1 and calcium-calmodulin-dependent kinase (CaMK) and phosphorylation specifically disrupts the affinity to negatively charged lipids up to the B domain, increasing SV release probability [292,442].

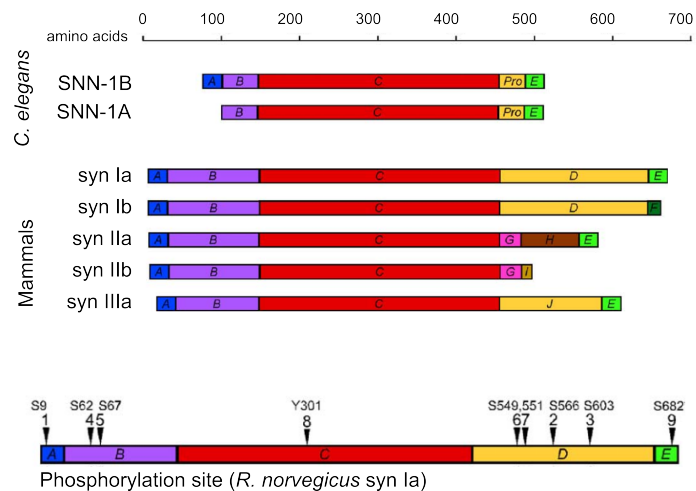


**Figure 4.3.: Comparison of Synapsin domains and phosphorylation sites.** Domain organization of *C. elegans* and mammalian Synapsins (top). Phosphorylation sites based on rat syn Ia (bottom). Adapted from [441].



In *M. musculus* neuronal cell culture, the induction of neuronal activity with either the depolarizer KCl or the PKA/KIN-1 activator Forskolin led to Synapsin S9 phosphorylation [63, 443, 444]. Interestingly, the phosphorylation of the S9 site itself was not sufficient to detach Synapsin from the SVs [63]. During sustained activity, a further signaling cascade leads to, presumably, additional phosphorylation in other residues of Synapsin and ultimately detaching the Synapsins from the SVs. In mammalian neurons, this process is not only activity dependent, but also dependent on the frequency of activation, where CaMK is required for low stimulus frequency and mitogen-activated protein kinase (MAPK) for both, low and high stimulus frequencies [445]. Synapsin has at least four phosphorylation sites for MAPK (figure 4.3 bottom, 4 to 7) [445, 446]. Disruption of these phosphorylation sites led mainly to synaptic development malfunction, but also to reduced short-term plasticity [447]. Synapsin itself also enhances SV associated c-Src kinase activity (SRC-1 in *C. elegans* [448]), leading to phosphorylation of site 8 (figure 4.3 bottom, 8) [449, 450]. Homozygous *src-1* mutants as well as animals grown in RNAi targeted to this gene have severe gonad morphogenesis and neuronal growth cone path-finding defects [451]. Therefore, an analysis of its role in vesicle release in the synapse regarding synapsin phosphorylation may be elucidated by the same CRISPR/Cas9 mediated phosphorylation site mutation technique applied for S9. Such an effort could reveal a further function of SRC-1 in *C. elegans*, since activation of c-Src kinase reduces neurotransmitter release, independent of the phosphorylation state of S9 [450, 452]. The c-Src phosphorylation site is in direct vicinity to the ATP binding site [453]. These might be contradictory signals, as ATP binding is essential for SV recruitment and facilitates phosphorylation of S9 [453]. Hence our SNN-1B(S9A) mutant may have increased affinity to vesicles with imbalanced regulation by cytosolic kinases. The deletion mutant abolished the increase in mean bending angles as well as the increase in mPSC amplitude. Thus, the effects observed in the S9A mutant argue for reduced neuropeptidergic signaling and require further analysis. It is conceivable that S9A specifically reduces the probability of DCV recruitment, possibly by preferentially tethering DCVs to the cytoskeleton, a theory that requires further analysis.

Interestingly, the *nlp-21(tm2569)* behavior results resembled SNN-1B(S9A). Although further analysis is still required, this phenotype indicates that NLP-21 is one of the bPAC effector neuropeptides. NLP-21 is expressed, among others, in the cholinergic AS neurons [454]. Although the function of these neurons is not yet clearly described, it is possible that AS neurons inhibit GABAergic motoneurons through neuropeptidergic signaling. This scenario could lead to the phenotype observed in wt animals:

bPAC photoactivation in cholinergic neurons induces increased SV and DCV release. The former leads to excitation of GABAergic motoneurons through the feed forward mechanism (section 1.3.1.2, p. 28). Hence, no over-excitation of muscle cells is observable in the first seconds of bPAC photoactivation. The neuropeptidergic signal leads to increased SV filling in cholinergic neurons, adding to the increased frequency of release a higher mPSC amplitude. In parallel, a further neuropeptidergic signal, presumably from AS neurons, leads to a delayed inhibition of GABAergic motoneurons. BWM cells hyper contract to the observed levels and bending angles are increased. Upon termination of photoactivation, the cholinergic neurons reduce SV filling and cease DCV release, ultimately reaching pre-stimulus phenotype.

#### **4.1.4. bPAC as an enhancer of rhodopsin based optogenetic tools**

bPAC could be used to enhance the muscle contraction caused by C1V1 depolarization in cholinergic neurons (section 3.1.1.2.5, p. 86). Since C1V1 has a broad, red-shifted absorption spectrum, contraction caused by blue light is possibly due to partial photoactivation of C1V1. Nonetheless, these results indicate that bPAC could be used to enhance the cholinergic output upon photostimulation of other rhodopsin tools. The co-expression and co-photoactivation of bPAC with ChR2(C128S) in cholinergic neurons, at the expense of no spectral differentiation, was performed by Dr. Sebastian Wabnig. He had previously established a strain expressing RCaMP in BWM cells combined with ChR2(C128S) expression in cholinergic neurons. Effects evoked by cholinergic neuron stimulation were read out as the fluorescence of RCaMP, a proxy for calcium concentration in BWM cells and therefore an indicator of cholinergic neuron activity [455]. Co-photoactivation of bPAC with ChR2(C128S) in this system showed an increase in RCaMP fluorescence augmenting the signal produced by photostimulation of ChR2(C128S) alone (figure 4.4).

This experiment confirms the behavioral, electrophysiological and ultrastructural results presented in this thesis. Photoactivation of bPAC increased the ChR2(C128S) mediated cholinergic neuron signaling by, likely, modulating the SV quantal size. Furthermore, this experiment is a primer for further dissection of the cAMP pathway triggered by bPAC and the search for the neuropeptide and its cognate receptor. The expression of two supplementary optogenetic tools in this system might pose a detriment to wide screenings based on crossing to canonical mutations, though. Another option is to use feeding RNAi to test putative targets without the need for genetic mutations, as also implemented by Dr. Sebastian Wabnig in his previous work [455].

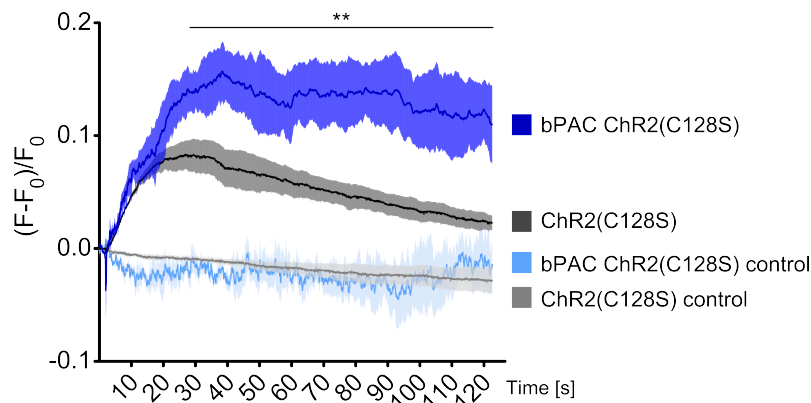


**Figure 4.4.:** RCaMP relative fluorescence in body wall muscle cells. ChR2(C128S) in cholinergic neurons causes neuronal depolarization that lead to increased calcium in body wall muscle cells. Co-photostimulation of bPAC and ChR2(C128S) further increase the calcium concentration in the cytosol of body wall muscle cells. Mean  $\pm$  SEM, ANOVA, Tukey correction, \*\*:  $p \leq 0.01$ . Significance region with at least 95 % of data points meeting p-value description shown for bPAC ChR2(C128S) versus ChR2(C128S) strains. Animals, experiment and analysis by Dr. Sebastian Wabnig.

As a benefit, such reverse genetic screen is more accessible to automated scoring than any other method applied to bPAC animals during this thesis.

#### 4.1.5. bPAC long time photostimulation induced necrosis

A neuronal toxicity assay was performed with bPAC expressing animals to test if long, constant activation of cAMP pathway might lead to cell death. This effect was observed after 24 h of uninterrupted stimuli (figure 4.5). The swelling of cholinergic neurons observed during this thesis is reminiscent of neuronal cell death induced by  $G_{\alpha S}$  gain of function mutations [390,456], both in phenotype as well as time domain. This phenotype is unlikely due to prolonged activation of cAMP response element-binding protein (CREB) and transcription, since a constitutive active version of CREB does not lead to necrosis, at least in mammalian cells [457]. Cell death is thus likely an effect of increased neuronal activity induced by bPAC photoactivation. Prolonged neuronal depolarization with a hyperactive mechanosensory channel (MEC-4(d)) has been shown to cause necrotic-like cell death [458]. The toxicity of MEC-4(d) is due to a cytosolic overload with calcium ions that ultimately activate calpain, a calcium dependent protease, in a non localized manner [459]. Recently, depolarization by

sodium ions was also shown to induce necrotic-like cell death, albeit the process yet remains to be described [460]. Therefore, it is conceivable that prolonged constant depolarization of neurons with ChR2(C128S) will also lead to necrotic-like cell death.

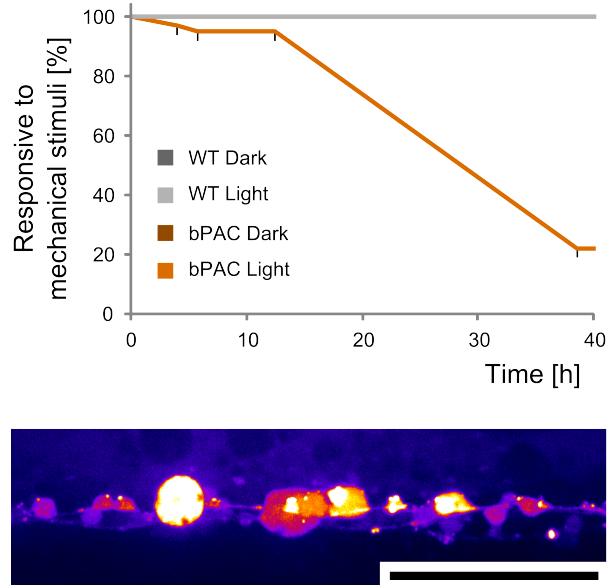


**Figure 4.5.: Uninterrupted bPAC photostimulation for 24 h led to cholinergic cell death.** Animals were exposed to uninterrupted blue light and tested for cholinergic activity with a mechanical stimulus. Animals were considered to have dead cholinergic neurons if no behavior response was observed after three consecutive mechanical stimuli to the posterior region at specific time points (ticks). Animals were considered alive if pharyngeal pumping could be observed during the assay (top). False colored YFP signal in the VNC after 24 h of bPAC photostimulation (bottom). Scale bar 10  $\mu\text{m}$ .

## 4.2. Possible roles of RIS in the neuronal network of *C. elegans*

The results presented herein propose a role of the interneuron RIS in the neuronal network of the adult animal in locomotion. Photoactivation of ChR2 in RIS led to an acute behavioral stop coupled to inhibition of pharyngeal pumping. Analysis of the RIS::ChR2 induced phenotype in diverse signal transduction mutants led to the inference, that RIS modulates behavior through neuropeptidergic signaling. Additionally,

intrinsic RIS depolarizations measured by calcium signal were correlated with short behavioral stops. The observed calcium dynamics suggested that RIS has compartmentalized signal transduction volumes with two main sites at the nerve ring and the short branch sent to the VNC. Further, bPAC photostimulation in RIS increased short pause probability that displayed the same duration as the intrinsic activity induced short stops observed during calcium imaging.

#### 4.2.1. RIS activity correlates with locomotion stop

The data presented in this work could only show a correlation between RIS activity and locomotion stop, due to the manual tracking procedure. Thus, an automated system for validation of the results obtained as well as further analysis of the causal relationship between both signals was required. The tracker devised by Petrus Van der Auwera is able to image the neuronal process of RIS, allowing the analysis of the cross-correlation between RIS activity and locomotion in freely behaving animals. The analysis of calcium imaging data confirmed the intrinsic activity of RIS during locomotion stop, although a subset of reversals had no detectable RIS activity. As observed in the manual tracking of RIS activity presented in this thesis, the automated tracking also confirmed that RIS activity precedes a change in locomotion speed. Further, RIS activity in the nerve ring is a predictor of locomotion stop with a time lag of about 50 ms. This is in agreement to the recently described intrinsic RIS activity between larval molts, where lethargus is induced by neuropeptidergic as well as GABAergic signaling from RIS [336].

To confirm the hypothesis that RIS uses neuropeptidergic signaling in adult animals, further tests were required. Neuropeptides originate from propeptides that are cleaved by proprotein convertases at specific residues. *C. elegans* has four genes that code for proprotein convertases, of which *egl-3* is the major neuronal convertase [461, 462] and required in RIS for its activity during larval lethargus [335]. The cleaved proteins are further processed by carboxypeptidases. In the case of EGL-3 cut peptides, the basic amino acid in the C-terminus is cleaved by the carboxypeptidase EGL-21 [463]. *C. elegans* has two further carboxypeptidase coding genes [464]. FLPs are further amidated in their C-terminus to increase peptide stability and induce function [465, 466], although the enzymes encoded by *pamn-1* and *pgal-1* were found by homology to *D. melanogaster* proteins, they have not yet been enzymatically confirmed [467]. An additional analysis performed by Petrus Van der Auwera confirmed the requirement of neuropeptidergic signaling for function of RIS. He observed that

EGL-3 is required for the RIS::ChR2 photoactivation induced locomotion stop. Further, he confirmed the requirement for the neuropeptide FLP-11 to induce stop in the adult animal.

Since EGL-3 and FLP-11 were shown to be required for larval lethargus [335,336], the same pathway is used during adult locomotion. However, *flp-11* gene has three alternative transcripts resulting in different neuropeptide subsets. These encode in total four FLP peptides and a putative, non FLP peptide [468, p. 68]. Thus, it remains to be analyzed which of the FLP-11 neuropeptides are expressed and required for the behavior modulation induced by RIS::ChR2 photoactivation. Moreover, the RNA-Seq data suggest that RIS expresses 27 additional neuropeptide associated genes and these require further analysis on their role in RIS::ChR2 photo-depolarization induced locomotion stops. Interestingly, the lack of long quiescent phases during adult locomotion paired with the observed intrinsic activity of RIS during short stops argues for a change in pathway modulation after the last larval molt. Thus, it might be possible that RIS expresses a different set of FLP-11 isoforms during larval and adult states.

#### **4.2.2. Serotonin reduced RIS activity, as monitored by calcium imaging**

One of the RIS marker genes, *ser-4* [347], encodes a metabotropic serotonin receptor that attenuates adenylyl cyclase function in *C. elegans* [349]. Thus, serotonin may reduce vesicle fusion probability in RIS, especially in view of the cAMP dependence of neuropeptidergic signaling described in this thesis. Further experiments are required to analyze this possibility, but it would be in line with diverse neuronal networks where a serotonergic neuron's activity positively correlates with behavior arousal [469,470]. However, SER-4, in combination with the serotonin gated chloride channel channel MOD-1, is required for locomotion attenuation through serotonin signaling [471]. Therefore, RIS probably does not mediate the serotonin induced reduction of locomotion speed. Importantly, this phenotype is not a full inhibition of movement and *ser-4* mutants alone are hyperactive compared to wt animals [471–473]. Thus, serotonin could have a negative effect on RIS activity.

In order to test this hypothesis, RIS::GCaMP6 animals were incubated with 50 mM serotonin, one order of magnitude higher than the required concentration for serotonin induced locomotion attenuation in wt [471,474,475]. Incubation of well fed animals with serotonin for 30 min led to a reduction of the measured calcium sig-

nal in RIS (figure 4.6). Thus, the serotonin induced locomotion attenuation is likely not mediated by RIS and this result is in accordance to SER-4 activation and reduced cAMP signaling in RIS.

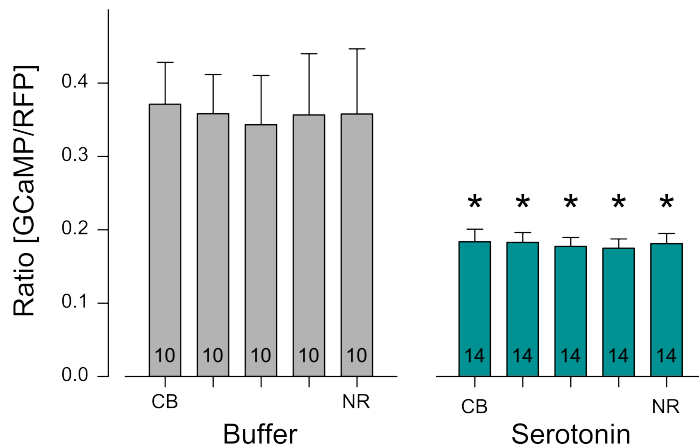


**Figure 4.6.: RIS activity decreased with exogenous serotonin application as monitored by calcium imaging.**

Animals were incubated for 30 min with 50 mM serotonin to induce serotonin mediated locomotion attenuation. Analysis of the ratio of GCaMP6 to RFP signal in five equidistant segments from cell body to nerve ring (CB and NR, respectively). Calcium imaging showed a reduction in RIS activity due to incubation with serotonin.

Mean  $\pm$  SEM. ANOVA, Bonferroni correction. ns :  $p \geq 0.05$ ; \* :  $p \leq 0.05$ ; \*\* :  $p \leq 0.01$ ; \*\*\* :  $p \leq 0.001$ .

Strain provided by Caspar-Elias Glock.

A caveat of long serotonin exposure is that response of the neuronal network to sharp steps in the serotonin concentration are not accounted for. Thus, RIS might still modulate behavior in presence of fast serotonin concentration changes not tested yet. This is possibly due to the low affinity of SER-4 for serotonin [349], as well as the local dynamics of serotonin signaling. In line with this acute effect, serotonin was shown to mediate exploitative behavior upon food encounter, abruptly reducing the speed of the animal [476].

An additional acute effect on locomotion is the response to aversive stimuli. For instance, cupric ions are toxic for *C. elegans* and the dopamine receptor DOP-1 mediates the aversive stimulus by regulating neuropeptidergic signaling [477,478]. Hence, RIS may be involved in this acute response to serotonin and dopamine, allowing the animal to modulate locomotion output through an acute inhibition of movement. It

remains open for further analysis if RIS mediates this abrupt locomotion stop.

### 4.2.3. RIS inhibition did not modulate behavior

Although serotonin application could reduce RIS activity as monitored by calcium imaging in movement restrained animals, applied methods for neuronal inactivation did not change behavior.

The cell specific expression of the proton pump Arch in RIS was achieved with the same promoter combination as for ChR2. The photoactivation of Arch did not modulate behavior: manual counting of movement reversals per time frame showed no change in presence versus absence of the Arch co-factor ATR. Since the extrachromosomal array led to expression in other neuronal cells, this strain was not quantitatively analyzed (figure 4.7).

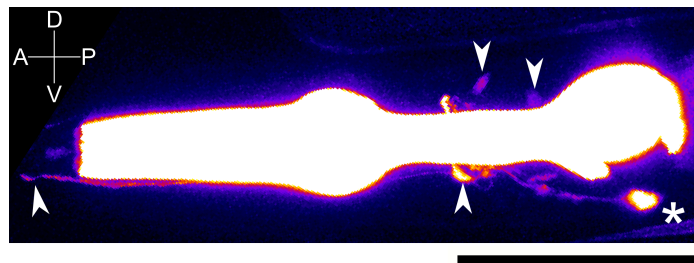


**Figure 4.7.: High unspecific expression in addition to expected Arch in RIS.**

Arch expression in RIS (asterisk) was accompanied by unspecific expression in uncharacterized neuronal cell bodies and processes (arrow heads). Maximum projection, false color, scale bar 50  $\mu\text{m}$ .

RIS optogenetic inhibition will require further optimizations not performed during this work. Otherwise, optogenetic cell ablation to characterize the behavior effects of loss of RIS function was pursued instead. Therefore, RIS specific cell ablation with miniSOG was explored by Caspar-Elias Glock during his master thesis. Although expression of miniSOG in RIS was possible, photoactivation did not lead to cell ablation as expected. Recently, membrane targeted miniSOG was shown to be at least two fold faster to induce neuronal cell ablation in *C. elegans* than the original mitochondrial targeted version of miniSOG used in our work [479]. Thus, further experiments to induce RIS cell ablation could be performed with the new targeting sequence that could lead to the desired effect of RIS loss of function.

Since none of the above methods efficiently inhibited the function of RIS in the



neuronal network of the adult *C. elegans*, I expressed HisCl1 in RIS to allow pharmacological inhibition of the neuron, henceforth described as RIS::HisCl1. Incubation of RIS::HisCl1 animals in NGM plates supplemented with 10 mM histamine did not reduce reversal probability compared to animals without histamine (figure 4.8).

Hence, inhibition of RIS during adult locomotion on solid substrate does not lead to profound behavior changes, which is in accordance to RIS inactivity during larval motile phases [335].

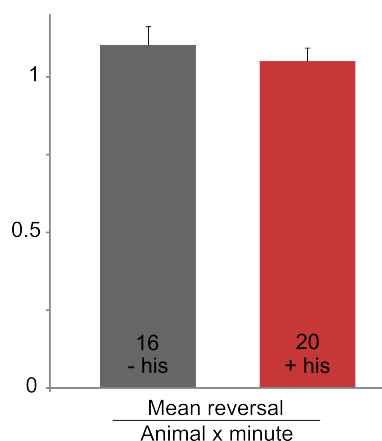


**Figure 4.8: RIS::HisCl1 histamine inhibition did not reduce reversal frequency.** RIS::HisCl1 animals in presence of histamine (red) did not display reduced reversal probability compared to control animals without histamine (grey). Mean  $\pm$  SEM. Student's T-Test: *ns*.

#### 4.2.4. Possible auto-regulatory mechanism of RIS inactivation

The single cell expression system for RIS characterized in this work uses the promoter of two GABA/glycine receptors: GGR-1 and GGR-2. The former driving lower expression levels than the latter, as quantified by fluorescent probes (section 3.2.1.1, p. 119). The up-regulated expression of *ggr-2* in RIS was further confirmed by RNA-Seq, where *ggr-2* transcription had a 71.7 fold increase compared to non-RIS cells with a FDR corrected p-value of 0.00029. *ggr-1*, in contrast, was confirmed with no increase expression in RIS versus non-RIS cells. The expression of GGR-2, specially, may be linked with an auto-inhibitory RIS activity. In addition, our RNA-Seq profile indicates over-expression of the GABA<sub>A</sub>  $\beta$ -like receptor subunit, GAB-1 (33.76 fold change, 0.040 FDR corrected p-value). Since no GABA<sub>A</sub>  $\alpha$  subunit was over-expressed, this is possibly not functional or a false positive. Alternatively, the expression of the GABA<sub>A</sub>  $\alpha$  subunit is tightly controlled and could not be found by analyzing only the transcriptome with increased count in RIS vs non-RIS cells. In addition, the RNA-Seq data shows over-expression of the excitatory GABA recep-

tor LGC-35 (34.18 fold change, 0.011 FDR corrected p-value). LGC-35 is a proposed GABA spill over receptor, mainly inducing feed-back from GABAergic to cholinergic motoneuron regulation of body wave propagation [480].

Nonetheless, there is no evidence for an autaptic (time-delayed self-feedback) connection in RIS, as has been shown in diverse vertebrate systems [481–483]. Thus, GGR-2 and LGC-35 may only be sensors for GABAergic volume transmission from RIS (see section 4.2.5, p. 160 for further possibilities). Interestingly, the RNA-Seq data showed an up-regulation of the gene *frpr-3* in RIS versus non-RIS cells (69.2 fold change, 0.0021 FDR corrected p-value). As introduced, FRPR-3 is an FLP-11 receptor with medium affinity [337]. Hence, RIS might be auto-regulated. If so, auto-regulation would probably be missed in the analysis of the RIS::ChR2 strain, since the intrinsic neuronal activity would be decoupled from vesicle release by the photo-induced depolarization. Although preliminary, analysis of RIS::bPAC strain could allow to infer an auto-regulatory mechanism in RIS. bPAC Photostimulation increased the probability of short stops, arguing for facilitated neuropeptidergic RIS signaling. In contrast to the effect of bPAC in cholinergic motoneurons, neuropeptidergic release from RIS seemed to be stochastic and not continuous throughout the illumination period. This could be due to the mentioned differential regulation of neuropeptidergic release in the unrelated cell classes. An alternative hypothesis is that regulation of DCV release is identical to cholinergic motoneurons concerning bPAC photoactivation, but an auto-regulatory effect of FRPR-3 activation leads to intermittent behavioral effects. Arguing against this hypothesis is the lack of concerted behavioral stop at the first seconds of bPAC photostimulation in RIS. Nonetheless, the intrinsic RIS activity recently observed on onset of lethargus in larval animals is a short period of high activity followed by long period of low activity throughout the duration of lethargus [336]. It may thus be possible, that the initial peak in activity reflects the onset of auto-regulatory mechanism in RIS. However, localization and specific knock-down or knock-out studies of these receptors in combination with monitoring intrinsic RIS activity are required to further probe this hypothesis.

#### **4.2.5. Possible RIS role in the neuronal network of *C. elegans***

RIS has been located into the interneuron layer responsible for locomotion by White *et al.* [257]. Neither RIS laser ablation studies [316], nor my own experiments with optogenetic or pharmacological hyperpolarization of RIS, could confirm its role in locomotion. Nonetheless, optogenetic induced neuronal depolarization in RIS::ChR2

led to acute stop of movement during light application, confirming the requirement of RIS in modulation of behavior. The work performed by Caspar-Elias Glock and Petrus Van der Auwera and the work presented herein confirmed that although GABA-ergic, RIS modulates behavior through neuropeptidergic signaling. The information processing leading to behavior modulation performed by RIS can thus be discussed in three roughly self-contained parts (scheme in figure 4.9).

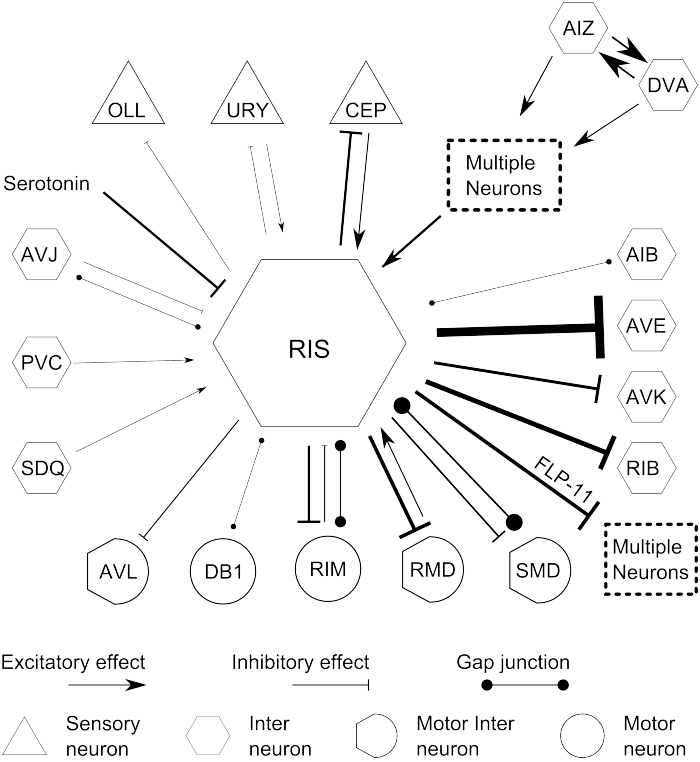


**Figure 4.9.: Information processing and role of RIS in the *C. elegans* neuronal network controlling behavior.**

Schematic of RIS information processing leading to behavioral modulation. Neuron classes and connections, as well as probable modulators, are depicted without distinction of their site of action.

Data for graph from [260,429]

**4.2.5.1. Information input on RIS**

RIS has few chemical synaptic inputs, mainly from SDQ and PVC neurons [257] (figure 4.9). The former is an aerotaxis-promoting sensory neuron, specifically sens-

ing oxygen. Aerotaxis is achieved with the signal of additional sensory neurons in absence of food while the SDQ output is dampened in presence of food [484]. The latter functions in the forward locomotion neuronal network, modulating the response to posterior harsh touch sensed by the mechanosensory neuron PVD [485,486]. Further noteworthy presynaptic partners are the dopaminergic CEP neurons [487]. CEPs are mechanosensory and, redundantly with two further neuronal classes, mediate the sensation of the presence of bacteria, ultimately reducing locomotion speed in presence of food [475,488].

In addition to chemical synapses, RIS has gap junctions to five neuronal classes. The interneurons AIB and AVJ, the motoneurons DB1 and RIM and the moto-interneurons SMD. AIB integrates sensory information [489] and promotes locomotion turns and local search behavior [312]. AVJ is a neuron of yet unknown function that recently was shown to be GABAergic, albeit with low anti-GABA staining compared to other GABAergic neurons that was further reduced during adulthood [264]. Hence, the RIS expressed GABA receptors might also be located in the post-synapse to the few additional chemical synapses between RIS and AVJ. DB1 is the anterior motoneuron of its class. It expresses proprioceptive mechanosensors that are likely localize to the anterior part of its process [303]. The proprioceptive signal is propagated through gap junctions, thus possibly also to RIS [303]. RIM is a tyramineric neuron with a function in locomotion reversal modulation [490]. RIM also has additional chemical synapses to RIS and thus could induce RIS hyperpolarization through tyramineric signaling. Indeed, RIM inhibition by optogenetic modulation led to increased reversal frequency [491]. Further, SMD are also connected by chemical synapses from RIS. These neurons define the amplitude of  $\Omega$ -turns, a behavior where after a reversal the head and tail of the animal come to close proximity and directionality of forward movement is changed by about  $180^\circ$ . This behavior was named by the posture of the animal during the turn, that resembles the greek letter  $\Omega$ . It is interesting to note, that chemical synapses and gap junctions formed to the same neuron are mostly not in the same location, but rather at different sites of their processes (figure 1.22, [257]).

Further, RIS expresses at least four innexins (INX-6, INX-7, UNC-7 and UNC-9) [414, 492]. From these, UNC-7 and UNC-9 can create a heterotypic channel [492] depending on the expression pattern of the postsynaptic cell. In addition, UNC-9 hemichannel state is modulated by a stomatin-like protein, UNC-1, and both proteins are required in neurons for proper locomotion [493]. Hence, not only may RIS generate selective gap junctions with different postsynaptic cells, these may themselves be

modulated depending on neuronal network state.

Furthermore, our RNA-Seq data suggests the expression of at least 50 additional, mostly uncharacterized, receptors. Among those more than 15 sequences code for neuropeptide receptors. Thus, although synaptic connectivity might be of low number, RIS may be a hub for information processing of humoral signals.

#### 4.2.5.2. Processing in RIS

The structure of RIS allows for localized calcium dynamics, specifically in the short branch and the varicosities present in the nerve ring region (figure 1.22). Compartmentalized calcium dynamics may be an overall adaptation to the reduced number of neurons in the neuronal network, thus enabling multiple signals to be independently evaluated or processed with a time delay, as shown in another neuronal cell class in *C. elegans* [494]. Indeed, activity in the nerve ring was increased during locomotion stop, while the branch showed increased calcium dynamics during backward movement (section 3.2.4, p. 139). In addition to the localized calcium dynamics, the RIS receptor expression profile obtained by RNA-Seq argues for multiple signal transduction pathways that could modulate vesicle release probability. This was tested and validated by the expression and photoactivation of bPAC in RIS (section 3.2.5.2, p. 143), where the probability of spontaneous stops was increased.

#### 4.2.5.3. RIS output and modulation of behavior

RIS behavior modulation requires neuropeptidergic signaling via FLP-11 in larvae [336] and adult animals. Nonetheless, RIS expresses additional neuropeptides that could modulate behavior in more subtle ways. Apart from locomotion and pharynx inhibition, adult animals also relax their neck musculature upon RIS::ChR2 photostimulation (Master thesis, Caspar-Elias Glock), a behavior that requires neuropeptidergic signaling in larvae [495]. In addition, GABAergic signaling from RIS may also modulate behavior in a subtle manner.

In addition, second layer synaptic connections analysis may help place RIS in the neuronal network of *C. elegans*. A recent computational study on the neuronal information transmission based on the connectome highlights connected pair of neurons with their mutual neighbors [496]. There, RIS appears in the following triads, where the first two neurons are directly connected to each other and the third neuron is a second layer connection both previous neurons: AIZ, DVA, RIS and RIS, AVK,

RIP. The former triad might be a further indication to the role of RIS in locomotion stop and directionality change [312, 497]. Interestingly, RIP is the sole connection between somatic and pharyngeal neuronal networks and required to inhibit pharyngeal pumping after mechanosensory stimulus to the head [311, 498, 499]. Hence, the latter triad suggest an additional mode of pharyngeal pumping modulation. Since RIS::ChR2 inhibition of pharyngeal pumping was dependent on increased photoactivation power, this might be an indication that this effect required an increased inhibition of the neuronal network and not a direct neuropeptidergic effect from RIS to the pharyngeal neuronal network or musculature. Nonetheless, recent revision of RIP ablation experiments showed no effect on pharyngeal pumping, arguing for a humoral effect [500].

#### 4.2.6. Comparison of RIS to similar modules in neuronal networks of species

The parasitic nematode *Ascaris suum* nervous system contains 298 neurons and is similar to *C. elegans* [257, 501]. *A. suum* has a RIS neuron (figure 4.10) and it expresses the *afp-6* gene, the homologue to *C. elegans flp-11* [502]. The coded neuropeptides also induce behavioral stop in *A. suum*, but are more broadly expressed than in *C. elegans*. Further, *afp-6* neuropeptides also displayed an excitatory function in the ovijector leading to increased contraction frequency [503]. Interestingly, these neuropeptides significantly reduced cAMP concentration, while FLP-11c also decreased cyclic guanosine monophosphate (cGMP) concentration [504]. In addition, these peptides induce muscle hyperpolarization and relaxation [504], an effect also observed in RIS::ChR2 studies performed by Caspar-Elias Glock.

In fact, a recent study on the gene product of *flp-11* showed that it is conserved in nematoda, together with *flp-32*. Both genes code for the analogous neuropeptides AMRN(A/S)LVRFamide, with FLP-11 displaying specific and confined expression patterns while FLP-32 being broadly expressed [506]. Further, FLP-11 inhibits motor function in different nematode species while FLP-32 role remains to be elucidated [506]. Noteworthy, *A. suum* does not code a known *flp-32* gene homologue but *afp-6* expresses a neuropeptide homologous to FLP-32 [506].

Although motoneuron anatomy and development across nematode species is not conserved [507], it may be possible for RIS to be subjected to the same evolutionary pressure as FLP-11 neuropeptides. This has been proposed for the transcription

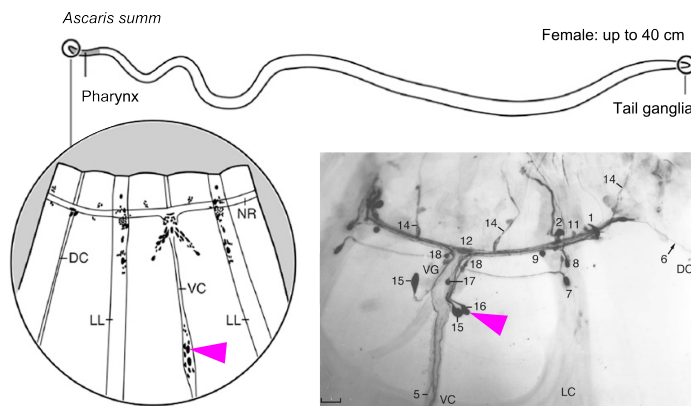


**Figure 4.10.: RIS counterpart in *Ascaris suum*.**

Schematic of *A. suum* nervous system in the head with the *C. elegans* RIS counterpart marked (left, arrowhead). Immunoreactivity with anti-NGAPQFPVRamide which matches FLP-11.

Figure adapted from [505], scale bar 100  $\mu$ m.

factor driving *flp-11* expression in RIS, APTF-1, a conserved homologue of AP2 transcription factor [335]. Mutation of the human homologue TFAP2B may lead to abnormal behavior during sleep [335, 508]. Despite the similarities, RIS::ChR2 photoactivation did not hyperpolarize BWM cells (Master Thesis Caspar-Elias Glock). Hence, in mammals the inhibition of locomotion as well as sleep and sleep-like states might be controlled by separated modules. The latter are based on the introduced galaninergic and orexin/hypocretin system (section 1.3.1.5, p. 36). This feed-back regulated network controls sleep where muscle relaxation is present [339–342]. In addition, mammals possess a second network of interneurons in the brainstem, that upon activation lead to behavior locomotion stop [509]. Importantly, this phenotype is neither coupled to muscle relaxation nor to freezing, but to a specific posture, allowing for a fast of locomotion restart [509].

Gene duplications, as described above for neuropeptidergic effect in cholinergic motoneurons, led to the VIP/PACAP set of genes in vertebrates. Thus, sleep and locomotion stop might have been separated from a common ancestor behavior originally regulated by a single process. Hence, RIS could represent an archetypical module in neuronal networks defined by the low synaptic input and a hub for humoral signaling, with high activation threshold and the capability of acutely inhibiting multiple aspects of behavior.





## 5. Outlook

Three main results were presented in this thesis and some of the possible continuative analysis are summarized herein. Common to all below is, that automation of laboratory techniques would increase output. Despite the increased lack of flexibility and the cost of automation, the current state in micro fluidic devices for *C. elegans* handling and analysis would empower the many of the proposed investigations.

### 5.1. Auto regulatory, neuropeptidergic signaling in cholinergic motoneurons

The bPAC induced neuropeptide release from cholinergic neurons requires further analysis in respect to both, the signal and the signal transduction pathway. Analysis of mutant genes coding for diverse neuropeptides could lead a further required transducer. It is likely a combination of multiple neuropeptides that lead to the observed effects, since deletion of *nlp-21* did neither fully impair the bPAC induced effect on behavior nor fully resembled the phenotype of *unc-31* mutants. Such analysis could also be performed with a RNAi sensitive strain in cholinergic neurons, thereby increasing throughput as well as reducing off-target effects due to a full deletion strain. In fact, an adaptation of the strain generate by Dr. Sebastian Wabnig, expressing ChR2(C128) and RCaMP in addition to bPAC would allow an all optical analysis of RNAi experiments, further increasing screenig speed.

The same strain can be used to analyze the signal transduction pathway activated by these neuropeptides. Since bPAC enhanced the effect of ChR2(C128S) in cholinergic motoneurons, disturbance of signal transduction would lead to inhibition of enhanced response to photostimulation.

Both analysis benefit from extensive literature on the transcriptome of cholinergic neurons and their subgroups, thereby allowing to test promising candidates first. Further, the  $G_{\alpha S}$  pathway was already excluded by the work presented herein.

## 5.2. Synapsin requirement for neuropeptidergic signaling

Analogously to the pathways mentioned above, the effect of synapsin on DCV release can be analyzed by the same method. Nonetheless, one could first test if the SNN-1B(S9A) mutation impairs DCV release, as did the deletion mutant. This could readily be performed by generating a SNN-1B(S9A) mutant strain containing an NLP-21::Venus marker, followed by analysis of coelomocyte fluorescence after bPAC photostimulation. A challenging, subsequent analysis would be to observe the DCV transport in cholinergic motoneurons. Thereby one could infer if the SNN-1B(S9A) mutation might destabilize DCV organization in synaptic puncta. DCV transport analysis could also be used to infer the mechanism by which the deletion mutant of synapsin impairs neuropeptidergic signaling. Synapsin might be required to tether DCVs in the vicinity to release sites, and thus its deletion would impair DCV priming. These analysis may require sub-diffraction-limited imaging techniques, though.

## 5.3. RIS role in behavior regulation

Part of the project involving the analysis of RIS function in the adult *C. elegans* are constituents of the PhD thesis from Petrus Van der Auwera. His main work is based on the calcium imaging in RIS in freely behaving animals. His current data confirms the initial analysis performed by myself with Caspar-Elias Glock and Dr. Sebastian Wabnig on the intrinsic activity of RIS during locomotion. In addition, his work also encompasses the characterization of candidate genes retrieved from the RNA-Seq analysis.

In view of the neuropeptidergic release elicited by RIS::Chr2 depolarization and the behavioral effect elicited by RIS::bPAC photostimulation, analysis of the DCV secretion pathway could lead to further insights into the different regulation mechanisms compared to the cholinergic neurons mentioned above. First, a neuropeptide marker strain for RIS should be generated. This could be done with heterologous expression of the NLP-21::Venus marker using the recombination system described herein. Second, a coelomocyte marker-uptake experiment could be used to infer the relative proportion of DCV secretion dependent on depolarization and cAMP signaling. It is expected that depolarization will lead to highly increased coelomocyte fluorescence while cAMP pathway activation might be dependent on intrinsic signaling, as was the case in the behavior experiments shown here. Although behavior

phenotype is easily scored, that is locomotion stop, a screening based solely on this phenotype might miss more subtle RIS functions. Hence, an additional method for scoring RIS activity would be desired.

In this line, the current progress in voltage indicators could allow to image intrinsic voltage variations in RIS. This is likely a better reporter for RIS information processing, since calcium imaging relies on the assumption that voltage variations are accurately transduced into calcium concentration variations. As shown, RIS has gap junctions to one third of its synaptic partners. In the case that these ground RIS voltage, voltage variations could be measured by voltage imaging before these are dissipated, while calcium imaging would not report a variation.

In addition, the mutagenesis performed with the help of Caspar-Elias Glock yielded eight further mutants that were not yet characterized. From these, three have had their chromosomal location outlined and require an interval mapping before whole genome sequencing could be indicative of the mutation in question. Although labor intensive, this analysis is based on robust methods and should hence deliver putative new mutations to the *C. elegans* community. In this respect, the characterized mutation in the LIM-6 transcription factor could be of interest for developmental biologist and geneticists, as this mutation does not impair morphology of RIS, but its function. Since *lim-6* is expressed in further neurons, the impact of this mutation is likely lower to development than the canonical deletion mutant.

Last, the developmental change from a lethargus inducing neuron to a neuron participating in the locomotion control of adult animals could be indicative of a conserved mechanism. As discussed, conservation of molecular pathways, from transcription through neuropeptide up to the neuron itself, the latter at least among nematodes, is striking. Hence, sleep and sleep-like behaviors might be further interconnected to wakefulness than previously thought. Comparative analysis with other model organisms could allow a better understanding of processes leading to homeostatic control of sleep and wakefulness.



# Bibliography

- [1] S. Ramón y Cajal, *Histologie du système nerveux de l'homme & des vertébrés*. Paris: Maloine, 1909. (Cited on pages 1 and 2.)
- [2] P. Fatt and B. Katz, "Spontaneous subthreshold activity at motor nerve endings," *The Journal of physiology*, vol. 117, no. 1, pp. 109–128, 1952. (Cited on page 1.)
- [3] Y. Tabuse, "Protein kinase C isotypes in *C. elegans*," *Journal of biochemistry*, vol. 132, no. 4, pp. 519–522, 2002. (Cited on page 2.)
- [4] S. R. y. Cajal, *Neuron Theory Or Reticular Theory?: Objective Evidence of the Anatomical Unity of Nerve Cells*. Trabajos del Instituto Ramón y Cajal, Consejo Superior de Investigaciones Científicas, Instituto Ramón y Cajal, 1954. (Cited on page 2.)
- [5] C. Nielsen, *Animal Evolution: Interrelationships of the Living Phyla: Interrelationships of the Living Phyla*. OUP Oxford, 2001. (Cited on page 2.)
- [6] J. F. Ryan, "Did the ctenophore nervous system evolve independently?," *Zoology (Jena, Germany)*, vol. 117, no. 4, pp. 225–226, 2014. (Cited on page 2.)
- [7] S. P. Leys, "Elements of a 'nervous system' in sponges," *The Journal of experimental biology*, vol. 218, no. Pt 4, pp. 581–591, 2015. (Cited on page 2.)
- [8] E. R. Kandel, J. H. Schwartz, and T. M. Jessell, eds., *Principles of neural science*. New York, NY: McGraw-Hill Health Professions Division, 4. ed. ed., 2000. (Cited on pages 3 and 5.)
- [9] M. Vander Laan Bennett and D. C. Spray, *Gap junctions*. Cold Spring Harbor Laboratory, 1985. (Cited on page 3.)
- [10] E. J. FURSHPAN and D. D. POTTER, "Transmission at the giant motor synapses of the crayfish," *The Journal of physiology*, vol. 145, no. 2, pp. 289–325, 1959. (Cited on page 3.)
- [11] A. A. Auerbach and M. Vander Laan Bennett, "A Rectifying Electrotonic Synapse in the Central Nervous System of a Vertebrate," *The Journal of General Physiology*, vol. 53, no. 2, pp. 211–237, 1969. (Cited on page 3.)
- [12] K. R. Norman and A. V. Maricq, "Innexin function: minding the gap junction," *Current biology : CB*, vol. 17, no. 18, pp. R812–4, 2007. (Cited on page 3.)
- [13] C. I. Bargmann, "Neurobiology of the *Caenorhabditis elegans* genome," *Science*, vol. 282, no. 5396, pp. 2028–2033, 1998. (Cited on page 3.)
- [14] R. Feil and T. Kleppisch, "NO/cGMP-dependent modulation of synaptic transmission," *Handbook of experimental pharmacology*, no. 184, pp. 529–560, 2008. (Cited on page 4.)
- [15] M. Zoli, C. Torri, R. Ferrari, A. Jansson, I. Zini, K. Fuxe, and L. F. Agnati, "The emergence of the volume transmission concept1Published on the World Wide Web on 12 January 1998.1," *Brain Research Reviews*, vol. 26, no. 2-3, pp. 136–147, 1998. (Cited on page 4.)
- [16] S. Olah, M. Fule, G. Komlosi, C. Varga, R. Baldi, P. Barzo, and G. Tamas, "Regulation of cortical microcircuits by unitary GABA-mediated volume transmission," *Nature*, vol. 461, no. 7268, pp. 1278–1281, 2009.

(Cited on page 4.)

- [17] N. K. Charlie, M. A. Schade, A. M. Thormure, and K. G. Miller, "Presynaptic UNC-31 (CAPS) is required to activate the G alpha(s) pathway of the *Caenorhabditis elegans* synaptic signaling network," *Genetics*, vol. 172, no. 2, pp. 943–961, 2006. (Cited on page 4.)
- [18] X.-G. Lin, M. Ming, M.-R. Chen, W.-p. Niu, Y.-D. Zhang, B. Liu, Y.-M. Jiu, J.-W. Yu, T. Xu, and Z.-X. Wu, "UNC-31/CAPS docks and primes dense core vesicles in *C. elegans* neurons," *Biochemical and Biophysical Research Communications*, vol. 397, no. 3, pp. 526–531, 2010. (Cited on pages 4 and 11.)
- [19] C. Salio, L. Lossi, F. Ferrini, and A. Merighi, "Neuropeptides as synaptic transmitters," *Cell and tissue research*, vol. 326, no. 2, pp. 583–598, 2006. (Cited on page 4.)
- [20] C. I. Maeder, A. San-Miguel, E. Y. Wu, H. Lu, and K. Shen, "In vivo neuron-wide analysis of synaptic vesicle precursor trafficking," *Traffic (Copenhagen, Denmark)*, vol. 15, no. 3, pp. 273–291, 2014. (Cited on page 4.)
- [21] B. Ceccarelli and W. P. Hurlbut, "Vesicle hypothesis of the release of quanta of acetylcholine," *Physiological reviews*, vol. 60, no. 2, pp. 396–441, 1980. (Cited on page 4.)
- [22] P. J. Morin, N. G. Liu, R. J. Johnson, S. E. Lee-man, and R. E. Fine, "Isolation and characterization of rapid transport vesicle subtypes from rabbit optic nerve," *Journal of Neurochemistry*, vol. 56, no. 2, pp. 415–427, 1991. (Cited on page 4.)
- [23] O. Loewi, "Über humorale übertragbarkeit der Herznervenwirkung," *Pflügers Archiv für die Gesamte Physiologie des Menschen und der Tiere*, vol. 189, no. 1, pp. 239–242, 1921. (Cited on page 4.)
- [24] L. E. Eiden, "The cholinergic gene locus," *Journal of Neurochemistry*, vol. 70, no. 6, pp. 2227–2240, 1998. (Cited on page 4.)
- [25] T. Kitamoto, W. Wang, and P. M. Salvaterra, "Structure and organization of the *Drosophila* cholinergic locus," *The Journal of biological chemistry*, vol. 273, no. 5, pp. 2706–2713, 1998. (Cited on page 4.)
- [26] S. Sulieman, "Does GABA increase the efficiency of symbiotic N<sub>2</sub> fixation in legumes?," *Plant signaling & behavior*, vol. 6, no. 1, pp. 32–36, 2011. (Cited on page 4.)
- [27] B. G. Forde and P. J. Lea, "Glutamate in plants: metabolism, regulation, and signalling," *Journal of experimental botany*, vol. 58, no. 9, pp. 2339–2358, 2007. (Cited on page 4.)
- [28] L. A. E. Erland, S. J. Murch, R. J. Reiter, and P. K. Saxena, "A new balancing act: The many roles of melatonin and serotonin in plant growth and development," *Plant signaling & behavior*, vol. 10, no. 11, p. e1096469, 2015. (Cited on page 4.)
- [29] S. Takamori, M. Holt, K. Stenius, E. A. Lemke, M. Gronborg, D. Riedel, H. Urlaub, S. Schenck, B. Brugger, P. Ringler, S. A. Muller, B. Rammner, F. Gräter, J. S. Hub, B. L. de Groot, G. Mieskes, Y. Moriyama, J. Klingauf, H. Grubmüller, J. Heuser, F. Wieland, and R. Jahn, "Molecular anatomy of a trafficking organelle," *Cell*, vol. 127, no. 4, pp. 831–846, 2006. (Cited on pages 5 and 6.)
- [30] J. Zhao, S. Benlekbir, and J. L. Rubinstein, "Electron cryomicroscopy observation of rotational states in a eukaryotic V-ATPase," *Nature*, vol. 521, no. 7551, pp. 241–245, 2015. (Cited on page 5.)
- [31] J. Zhao, S. Benlekbir, and J. L. Rubinstein, *Yeast V-ATPase state 1*. 2015. (Cited on page 5.)
- [32] S. Poëa-Guyon, M. R. Ammar, M. Erard, M. Amar, A. W. Moreau, P. Fossier, V. Gleize, N. Vitale, and N. Morel, "The V-ATPase membrane domain is a sensor of granular pH that controls the exocytotic machinery," *The Journal of Cell Biology*, vol. 203, no. 2, pp. 283–298, 2013. (Cited on page 5.)
- [33] B. J. Bowman, M. E. McCall, R. Baertsch, and E. J. Bowman, "A model for the proteolipid ring and bafilomycin/concanamycin-

- binding site in the vacuolar ATPase of *Neurospora crassa*," *The Journal of biological chemistry*, vol. 281, no. 42, pp. 31885–31893, 2006. (Cited on page 5.)
- [34] R. Maron, Y. Stern, B. I. Kanner, and S. Schuldiner, "Functional asymmetry of the amine transporter from chromaffin granules," *The Journal of biological chemistry*, vol. 258, no. 19, pp. 11476–11481, 1983. (Cited on page 5.)
- [35] G. G. Ernstrom, R. Weimer, D. R. L. Pawar, S. Watanabe, R. J. Hobson, D. Greenstein, and E. M. Jorgensen, "V-ATPase V1 sector is required for corpse clearance and neurotransmission in *Caenorhabditis elegans*," *Genetics*, vol. 191, no. 2, pp. 461–475, 2012. (Cited on page 5.)
- [36] D. Wang and P. R. Hiesinger, "The vesicular ATPase: a missing link between acidification and exocytosis," *The Journal of Cell Biology*, vol. 203, no. 2, pp. 171–173, 2013. (Cited on page 5.)
- [37] R. W. Daniels, C. A. Collins, K. Chen, M. V. Gelfand, D. E. Featherstone, and A. DiAntonio, "A single vesicular glutamate transporter is sufficient to fill a synaptic vesicle," *Neuron*, vol. 49, no. 1, pp. 11–16, 2006. (Cited on page 5.)
- [38] T. L. Colliver, S. J. Pyott, M. Achalabun, and A. G. Ewing, "VMAT-Mediated changes in quantal size and vesicular volume," *The Journal of neuroscience : the official journal of the Society for Neuroscience*, vol. 20, no. 14, pp. 5276–5282, 2000. (Cited on page 5.)
- [39] K. L. Budzinski, R. W. Allen, B. S. Fujimoto, P. Kensel-Hammes, D. M. Belnap, S. M. Bajjalieh, and D. T. Chiu, "Large structural change in isolated synaptic vesicles upon loading with neurotransmitter," *Biophysical journal*, vol. 97, no. 9, pp. 2577–2584, 2009. (Cited on pages 5 and 28.)
- [40] M. Frerking, S. Borges, and M. Wilson, "Variation in GABA mini amplitude is the consequence of variation in transmitter concentration," *Neuron*, vol. 15, no. 4, pp. 885–895, 1995. (Cited on page 6.)
- [41] X. Wang, Y. Li, K. L. Engisch, S. T. Nakanishi, S. E. Dodson, G. W. Miller, T. C. Cope, M. J. Pinter, and M. M. Rich, "Activity-dependent presynaptic regulation of quantal size at the mammalian neuromuscular junction in vivo," *The Journal of neuroscience : the official journal of the Society for Neuroscience*, vol. 25, no. 2, pp. 343–351, 2005. (Cited on page 6.)
- [42] V. Riazanski, L. V. Deriy, P. D. Shevchenko, B. Le, E. A. Gomez, and D. J. Nelson, "Presynaptic CLC-3 determines quantal size of inhibitory transmission in the hippocampus," *Nature neuroscience*, vol. 14, no. 4, pp. 487–494, 2011. (Cited on page 6.)
- [43] S. Schenck, S. M. Wojcik, N. Brose, and S. Takamori, "A chloride conductance in VG-LUT1 underlies maximal glutamate loading into synaptic vesicles," *Nature neuroscience*, vol. 12, no. 2, pp. 156–162, 2009. (Cited on page 6.)
- [44] G. Ahnert-Hilger, B. Nurnberg, T. Exner, T. Schafer, and R. Jahn, "The heterotrimeric G protein Go2 regulates catecholamine uptake by secretory vesicles," *The EMBO journal*, vol. 17, no. 2, pp. 406–413, 1998. (Cited on page 6.)
- [45] B. A. Bahr and S. M. Parsons, "Acetylcholine transport and drug inhibition kinetics in Torpedo synaptic vesicles," *Journal of Neurochemistry*, vol. 46, no. 4, pp. 1214–1218, 1986. (Cited on page 6.)
- [46] R. Jahn and T. C. Sudhof, "Synaptic vesicle traffic: rush hour in the nerve terminal," *Journal of Neurochemistry*, vol. 61, no. 1, pp. 12–21, 1993. (Cited on page 6.)
- [47] M. L. Nguyen, G. D. Cox, and S. M. Parsons, "Kinetic parameters for the vesicular acetylcholine transporter: two protons are exchanged for one acetylcholine," *Biochemistry*, vol. 37, no. 38, pp. 13400–13410, 1998. (Cited on page 6.)

- [48] H. Varoqui and J. D. Erickson, "Active transport of acetylcholine by the human vesicular acetylcholine transporter," *The Journal of biological chemistry*, vol. 271, no. 44, pp. 27229–27232, 1996. (Cited on page 6.)
- [49] F. Cash, S. W. Vernon, P. Phelan, J. Goodchild, and R. A. Baines, "Central cholinergic synaptic vesicle loading obeys the set-point model in *Drosophila*," *Journal of Neurophysiology*, vol. 115, no. 2, pp. 843–850, 2016. (Cited on pages 6 and 7.)
- [50] G. A. Rogers and S. M. Parsons, "Inhibition of acetylcholine storage by acetylcholine analogs in vitro," *Molecular pharmacology*, vol. 36, no. 2, pp. 333–341, 1989. (Cited on page 6.)
- [51] P. Khare, A. Mulakaluri, and S. M. Parsons, "Search for the acetylcholine and vesamicol binding sites in vesicular acetylcholine transporter: the region around the luminal end of the transport channel," *Journal of Neurochemistry*, vol. 115, no. 4, pp. 984–993, 2010. (Cited on page 6.)
- [52] Y. Wang, Z. Zhou, T. Leylek, H. Tan, Y. Sun, F. E. Parkinson, and J.-F. Wang, "Protein cysteine S-nitrosylation inhibits vesicular uptake of neurotransmitters," *Neuroscience*, vol. 311, pp. 374–381, 2015. (Cited on pages 6 and 7.)
- [53] L. T. Ferreira, M. S. Santos, N. G. Kolmakova, J. Koenen, J. Barbosa, JR, M. V. Gomez, C. Guatimosim, X. Zhang, S. M. Parsons, V. F. Prado, and M. A. M. Prado, "Structural requirements for steady-state localization of the vesicular acetylcholine transporter," *Journal of Neurochemistry*, vol. 94, no. 4, pp. 957–969, 2005. (Cited on page 7.)
- [54] H. O. Lawal and D. E. Krantz, "SLC18: Vesicular neurotransmitter transporters for monoamines and acetylcholine," *Molecular aspects of medicine*, vol. 34, no. 2-3, pp. 360–372, 2013. (Cited on page 7.)
- [55] A. Alfonso, K. Grundahl, J. S. Duerr, H. P. Han, and J. B. Rand, "The *Caenorhabditis elegans* unc-17 gene: a putative vesicular acetylcholine transporter," *Science*, vol. 261, no. 5121, pp. 617–619, 1993. (Cited on page 7.)
- [56] C. Shaw, "Neuropeptides and their evolution," *Parasitology*, vol. 113 Suppl, pp. S35–45, 1996. (Cited on page 7.)
- [57] G. J. Siegel, ed., *Basic neurochemistry: Molecular, cellular and medical aspects*. Philadelphia PA u.a.: Lippincott Williams & Wilkins, 6. ed. ed., 1999. (Cited on page 7.)
- [58] A. Münster-Wandowski, J.-F. Zander, K. Richter, and G. Ahnert-Hilger, "Co-existence of Functionally Different Vesicular Neurotransmitter Transporters," *Frontiers in synaptic neuroscience*, vol. 8, p. 4, 2016. (Cited on page 7.)
- [59] S. R. Neves, P. T. Ram, and R. Iyengar, "G protein pathways," *Science (New York, N.Y.)*, vol. 296, no. 5573, pp. 1636–1639, 2002. (Cited on page 7.)
- [60] A. Denker, K. Krohnert, J. Buckers, E. Neher, and S. O. Rizzoli, "The reserve pool of synaptic vesicles acts as a buffer for proteins involved in synaptic vesicle recycling," *Proceedings of the National Academy of Sciences of the United States of America*, vol. 108, no. 41, pp. 17183–17188, 2011. (Cited on pages 7 and 150.)
- [61] D. Gitler, Q. Cheng, P. Greengard, and G. J. Augustine, "Synapsin IIa controls the reserve pool of glutamatergic synaptic vesicles," *The Journal of neuroscience : the official journal of the Society for Neuroscience*, vol. 28, no. 43, pp. 10835–10843, 2008. (Cited on pages 7 and 28.)
- [62] M. Bykhovskaia, "Synapsin regulation of vesicle organization and functional pools," *Seminars in Cell & Developmental Biology*, vol. 22, no. 4, pp. 387–392, 2011. (Cited on page 7.)
- [63] A. Orenbuch, Y. Shulman, N. Lipstein, A. Bechar, Y. Lavy, E. Brumer, M. Vasileva, J. Kahn, L. Barki-Harrington, T. Kuner, and D. Gitler, "Inhibition of exocytosis or endocytosis blocks activity-dependent redistribu-



- tion of synapsin," *Journal of Neurochemistry*, vol. 120, no. 2, pp. 248–258, 2012. (Cited on pages 8 and 151.)
- [64] S. O. Rizzoli and W. J. Betz, "Synaptic vesicle pools," *Nature reviews. Neuroscience*, vol. 6, no. 1, pp. 57–69, 2005. (Cited on page 8.)
- [65] A. Denker, I. Bethani, K. Krohnert, C. Korber, H. Horstmann, B. G. Wilhelm, S. V. Barysch, T. Kuner, E. Neher, and S. O. Rizzoli, "A small pool of vesicles maintains synaptic activity in vivo," *Proceedings of the National Academy of Sciences*, vol. 108, no. 41, pp. 17177–17182, 2011. (Cited on pages 8 and 150.)
- [66] M. Muller, K. S. Y. Liu, S. J. Sigrist, and G. W. Davis, "RIM controls homeostatic plasticity through modulation of the readily-releasable vesicle pool," *The Journal of neuroscience : the official journal of the Society for Neuroscience*, vol. 32, no. 47, pp. 16574–16585, 2012. (Cited on page 8.)
- [67] J. W. Hammond, S.-M. Lu, and H. A. Gelbard, "Platelet Activating Factor Enhances Synaptic Vesicle Exocytosis Via PKC, Elevated Intracellular Calcium, and Modulation of Synapsin 1 Dynamics and Phosphorylation," *Frontiers in cellular neuroscience*, vol. 9, p. 505, 2015. (Cited on page 8.)
- [68] O. A. T. Afuwape, C. R. Wasser, T. Schikorski, and E. T. Kavalali, "Synaptic vesicle pool specific modification of neurotransmitter release by intravesicular free radical generation," *The Journal of physiology*, 2016. (Cited on page 8.)
- [69] A. Denker and S. O. Rizzoli, "Synaptic vesicle pools: an update," *Frontiers in synaptic neuroscience*, vol. 2, p. 135, 2010. (Cited on page 8.)
- [70] J. E. Heuser and T. S. Reese, "Evidence for recycling of synaptic vesicle membrane during transmitter release at the frog neuromuscular junction," *The Journal of Cell Biology*, vol. 57, no. 2, pp. 315–344, 1973. (Cited on page 8.)
- [71] T. W. Scranton, M. Iwata, and S. S. Carlson, "The SV2 protein of synaptic vesicles is a keratan sulfate proteoglycan," *Journal of Neurochemistry*, vol. 61, no. 1, pp. 29–44, 1993. (Cited on pages 8 and 27.)
- [72] R. Janz, Y. Goda, M. Geppert, M. Missler, and T. C. Südhof, "SV2A and SV2B Function as Redundant Ca<sup>2+</sup> Regulators in Neurotransmitter Release," *Neuron*, vol. 24, no. 4, pp. 1003–1016, 1999. (Cited on page 8.)
- [73] J. Vautrin, "SV2 frustrating exocytosis at the semi-diffusor synapse," *Synapse (New York, N.Y.)*, vol. 63, no. 4, pp. 319–338, 2009. (Cited on pages 8 and 9.)
- [74] N. C. Harata, A. M. Aravanis, and R. W. Tsien, "Kiss-and-run and full-collapse fusion as modes of exo-endocytosis in neurosecretion," *Journal of Neurochemistry*, vol. 97, no. 6, pp. 1546–1570, 2006. (Cited on page 8.)
- [75] A. A. Alabi and R. W. Tsien, "Perspectives on Kiss-and-Run: Role in Exocytosis, Endocytosis, and Neurotransmission," *Annual Review of Physiology*, vol. 75, no. 1, pp. 393–422, 2013. (Cited on pages 8, 9, 10, and 13.)
- [76] C. R. Wasser, M. Ertunc, X. Liu, and E. T. Kavalali, "Cholesterol-dependent balance between evoked and spontaneous synaptic vesicle recycling," *The Journal of physiology*, vol. 579, no. Pt 2, pp. 413–429, 2007. (Cited on page 9.)
- [77] R. M. Weimer, E. O. Gracheva, O. Meyrignac, K. G. Miller, J. E. Richmond, and J.-L. Bessereau, "UNC-13 and UNC-10/rim localize synaptic vesicles to specific membrane domains," *The Journal of neuroscience : the official journal of the Society for Neuroscience*, vol. 26, no. 31, pp. 8040–8047, 2006. (Cited on page 9.)
- [78] H. Hibino, R. Pironkova, O. Onwumere, M. Vologodskaja, A. J. Hudspeth, and F. Lesage, "RIM binding proteins (RBPs) couple Rab3-interacting molecules (RIMs) to voltage-gated Ca(2+) channels," *Neuron*, vol. 34, no. 3, pp. 411–423, 2002. (Cited on page 9.)
- [79] J. M. Henley, T. J. Craig, and K. A. Wilkinson, "Neuronal SUMOylation: mechanisms, physiology, and roles in neuronal dysfunction,"

- tion," *Physiological reviews*, vol. 94, no. 4, pp. 1249–1285, 2014. (Cited on page 9.)
- [80] E. O. Gracheva, G. Hadwiger, M. L. Nonet, and J. E. Richmond, "Direct interactions between *C. elegans* RAB-3 and Rim provide a mechanism to target vesicles to the presynaptic density," *Neuroscience letters*, vol. 444, no. 2, pp. 137–142, 2008. (Cited on page 9.)
- [81] I. Dulubova, X. Lou, J. Lu, I. Huryeva, A. Alam, R. Schneggenburger, T. C. Südhof, and J. Rizo, "A Munc13/RIM/Rab3 tripartite complex: from priming to plasticity?," *The EMBO journal*, vol. 24, no. 16, pp. 2839–2850, 2005. (Cited on page 9.)
- [82] K. Zhou, T. M. Stawicki, A. Goncharov, and Y. Jin, "Position of UNC-13 in the active zone regulates synaptic vesicle release probability and release kinetics," *eLife*, vol. 2, p. e01180, 2013. (Cited on page 9.)
- [83] Z. Hu, X.-J. Tong, and J. M. Kaplan, "UNC-13L, UNC-13S, and Tomosyn form a protein code for fast and slow neurotransmitter release in *Caenorhabditis elegans*," *eLife*, vol. 2, p. e00967, 2013. (Cited on page 10.)
- [84] T. Baba, T. Sakisaka, S. Mochida, and Y. Takai, "PKA-catalyzed phosphorylation of tomosyn and its implication in Ca<sup>2+</sup>-dependent exocytosis of neurotransmitter," *The Journal of cell biology*, vol. 170, no. 7, pp. 1113–1125, 2005. (Cited on page 10.)
- [85] E. O. Gracheva, E. B. Maryon, M. Berthelot-Grosjean, and J. E. Richmond, "Differential Regulation of Synaptic Vesicle Tethering and Docking by UNC-18 and TOM-1," *Frontiers in synaptic neuroscience*, vol. 2, p. 141, 2010. (Cited on page 10.)
- [86] R. F. G. Toonen, K. J. de Vries, R. Zalm, T. C. Südhof, and M. Verhage, "Munc18-1 stabilizes syntaxin 1, but is not essential for syntaxin 1 targeting and SNARE complex formation," *Journal of Neurochemistry*, vol. 93, no. 6, pp. 1393–1400, 2005. (Cited on page 10.)
- [87] Y. A. Chen and R. H. Scheller, "SNARE-mediated membrane fusion," *Nature reviews. Molecular cell biology*, vol. 2, no. 2, pp. 98–106, 2001. (Cited on page 10.)
- [88] R. Heidelberger and G. Matthews, "Vesicle Priming and Depriming," *Neuron*, vol. 41, no. 3, pp. 311–313, 2004. (Cited on page 10.)
- [89] G. Nagy, K. Reim, U. Matti, N. Brose, T. Binz, J. Rettig, E. Neher, and J. B. Sørensen, "Regulation of releasable vesicle pool sizes by protein kinase A-dependent phosphorylation of SNAP-25," *Neuron*, vol. 41, no. 3, pp. 417–429, 2004. (Cited on page 10.)
- [90] J. Gao, M. Hirata, A. Mizokami, J. Zhao, I. Takahashi, H. Takeuchi, and M. Hirata, "Differential role of SNAP-25 phosphorylation by protein kinases A and C in the regulation of SNARE complex formation and exocytosis in PC12 cells," *Cellular signalling*, vol. 28, no. 5, pp. 425–437, 2015. (Cited on page 10.)
- [91] J. M. Madison, S. Nurrish, and J. M. Kaplan, "UNC-13 interaction with syntaxin is required for synaptic transmission," *Current biology : CB*, vol. 15, no. 24, pp. 2236–2242, 2005. (Cited on page 10.)
- [92] R. T. Wragg, D. Snead, Y. Dong, T. F. Ramlall, I. Menon, J. Bai, D. Eliezer, and J. S. Dittman, "Synaptic vesicles position complexin to block spontaneous fusion," *Neuron*, vol. 77, no. 2, pp. 323–334, 2013. (Cited on page 10.)
- [93] A. Maximov, J. Tang, X. Yang, Z. P. Pang, and T. C. Südhof, "Complexin controls the force transfer from SNARE complexes to membranes in fusion," *Science (New York, N.Y.)*, vol. 323, no. 5913, pp. 516–521, 2009. (Cited on page 10.)
- [94] Q. Zhou, Y. Lai, T. Bacaj, M. Zhao, A. Y. Lyubimov, M. Uervirojnangkoorn, O. B. Zeldin, A. S. Brewster, N. K. Sauter, A. E. Cohen, S. M. Soltis, R. Alonso-Mori, M. Chollet, H. T. Lemke, R. A. Pfuetzner, U. B. Choi, W. I. Weis, J. Diao, T. C. Südhof, and A. T. Brunger, "Architecture of the synaptotagmin-SNARE machinery for neuronal exocytosis," *Nature*, vol. 525, no. 7567, pp. 62–67, 2015. (Cited on page 10.)

- page 10.)
- [95] R. W. Cho, L. K. Buhl, D. Volfson, A. Tran, F. Li, Y. Akbergenova, and J. T. Littleton, "Phosphorylation of Complexin by PKA Regulates Activity-Dependent Spontaneous Neurotransmitter Release and Structural Synaptic Plasticity," *Neuron*, vol. 88, no. 4, pp. 749–761, 2015. (Cited on page 10.)
- [96] P. J. Wen, S. Grenklo, G. Arpino, X. Tan, H.-S. Liao, J. Heureaux, S.-Y. Peng, H.-C. Chiang, E. Hamid, W.-D. Zhao, W. Shin, T. Nareoja, E. Evergren, Y. Jin, R. Karlsson, S. N. Ebert, A. Jin, A. P. Liu, O. Shupliakov, and L.-G. Wu, "Actin dynamics provides membrane tension to merge fusing vesicles into the plasma membrane," *Nature communications*, vol. 7, p. 12604, 2016. (Cited on page 10.)
- [97] P. S. Kaeser, L. Deng, Y. Wang, I. Dulubova, X. Liu, J. Rizo, and T. C. Sudhof, "RIM proteins tether Ca<sup>2+</sup> channels to presynaptic active zones via a direct PDZ-domain interaction," *Cell*, vol. 144, no. 2, pp. 282–295, 2011. (Cited on page 11.)
- [98] J. Rizo and J. Xu, "The Synaptic Vesicle Release Machinery," *Annual review of biophysics*, vol. 44, pp. 339–367, 2015. (Cited on page 11.)
- [99] S. Hilfiker, V. A. Pieribone, C. Nordstedt, P. Greengard, and A. J. Czernik, "Regulation of synaptotagmin I phosphorylation by multiple protein kinases," *Journal of Neurochemistry*, vol. 73, no. 3, pp. 921–932, 1999. (Cited on page 10.)
- [100] G. J. O. Evans and A. Morgan, "Phosphorylation-dependent interaction of the synaptic vesicle proteins cysteine string protein and synaptotagmin I," *The Biochemical journal*, vol. 364, no. Pt 2, pp. 343–347, 2002. (Cited on page 10.)
- [101] G. J. Evans, M. C. Wilkinson, M. E. Graham, K. M. Turner, L. H. Chamberlain, R. D. Burgoyne, and A. Morgan, "Phosphorylation of cysteine string protein by protein kinase A. Implications for the modulation of exocytosis," *The Journal of biological chemistry*, vol. 276, no. 51, pp. 47877–47885, 2001. (Cited on page 10.)
- [102] L. H. Chamberlain and R. D. Burgoyne, "Cysteine-string protein: the chaperone at the synapse," *Journal of Neurochemistry*, vol. 74, no. 5, pp. 1781–1789, 2000. (Cited on page 10.)
- [103] M. G. Chheda, U. Ashery, P. Thakur, J. Rettig, and Z. H. Sheng, "Phosphorylation of Snapin by PKA modulates its interaction with the SNARE complex," *Nature cell biology*, vol. 3, no. 4, pp. 331–338, 2001. (Cited on page 10.)
- [104] S.-C. Yu, S. M. Klosterman, A. A. Martin, E. O. Gracheva, and J. E. Richmond, "Differential roles for snapin and synaptotagmin in the synaptic vesicle cycle," *PLoS One*, vol. 8, no. 2, p. e57842, 2013. (Cited on page 10.)
- [105] P. Thakur, D. R. Stevens, Z.-H. Sheng, and J. Rettig, "Effects of PKA-mediated phosphorylation of Snapin on synaptic transmission in cultured hippocampal neurons," *The Journal of neuroscience : the official journal of the Society for Neuroscience*, vol. 24, no. 29, pp. 6476–6481, 2004. (Cited on page 10.)
- [106] T. Schmidt, C. Schirra, U. Matti, D. R. Stevens, and J. Rettig, "Snapin accelerates exocytosis at low intracellular calcium concentration in mouse chromaffin cells," *Cell calcium*, vol. 54, no. 2, pp. 105–110, 2013. (Cited on page 10.)
- [107] Y. Hua and R. H. Scheller, "Three SNARE complexes cooperate to mediate membrane fusion," *Proceedings of the National Academy of Sciences of the United States of America*, vol. 98, no. 14, pp. 8065–8070, 2001. (Cited on page 10.)
- [108] X. Han, C.-T. Wang, J. Bai, E. R. Chapman, and M. B. Jackson, "Transmembrane segments of syntaxin line the fusion pore of Ca<sup>2+</sup>-triggered exocytosis," *Science (New York, N.Y.)*, vol. 304, no. 5668, pp. 289–292, 2004. (Cited on page 10.)
- [109] J. E. Keller and E. A. Neale, "The role of the synaptic protein snap-25 in the potency of botulinum neurotoxin type A," *The Journal of bi-*

- ological chemistry*, vol. 276, no. 16, pp. 13476–13482, 2001. (Cited on page 10.)
- [110] J. E. Keller, F. Cai, and E. A. Neale, "Uptake of botulinum neurotoxin into cultured neurons," *Biochemistry*, vol. 43, no. 2, pp. 526–532, 2004. (Cited on page 10.)
- [111] L. Shi, Q.-T. Shen, A. Kiel, J. Wang, H.-W. Wang, T. J. Melia, J. E. Rothman, and F. Pincet, "SNARE proteins: one to fuse and three to keep the nascent fusion pore open," *Science (New York, N.Y.)*, vol. 335, no. 6074, pp. 1355–1359, 2012. (Cited on page 11.)
- [112] L. L. G. Schwenen, R. Hubrich, D. Milovanovic, B. Geil, J. Yang, A. Kros, R. Jahn, and C. Steinem, "Resolving single membrane fusion events on planar pore-spanning membranes," *Scientific reports*, vol. 5, p. 12006, 2015. (Cited on page 11.)
- [113] J. E. Richmond, W. S. Davis, and E. M. Jorgensen, "UNC-13 is required for synaptic vesicle fusion in *C. elegans*," *Nature neuroscience*, vol. 2, no. 11, pp. 959–964, 1999. (Cited on page 11.)
- [114] S. Speese, M. Petrie, K. Schuske, M. Ailion, K. Ann, K. Iwasaki, E. M. Jorgensen, and T. F. J. Martin, "UNC-31 (CAPS) is required for dense-core vesicle but not synaptic vesicle exocytosis in *Caenorhabditis elegans*," *The Journal of neuroscience : the official journal of the Society for Neuroscience*, vol. 27, no. 23, pp. 6150–6162, 2007. (Cited on page 11.)
- [115] M. Hammarlund, S. Watanabe, K. Schuske, and E. M. Jorgensen, "CAPS and syntaxin dock dense core vesicles to the plasma membrane in neurons," *The Journal of Cell Biology*, vol. 180, no. 3, pp. 483–491, 2008. (Cited on page 11.)
- [116] G. Kabachinski, D. M. Kielar-Grevstad, X. Zhang, D. J. James, and T. F. J. Martin, "Resident CAPS on dense-core vesicles docks and primes vesicles for fusion," *Molecular Biology of the Cell*, vol. 27, no. 4, pp. 654–668, 2016. (Cited on page 11.)
- [117] X.-Q. Dai, G. Plummer, M. Casimir, Y. Kang, C. Hajmrle, H. Y. Gaisano, J. E. Manning Fox, and P. E. MacDonald, "SUMOylation Regulates Insulin Exocytosis Downstream of Secretory Granule Docking in Rodents and Humans," *Diabetes*, vol. 60, no. 3, pp. 838–847, 2011. (Cited on page 11.)
- [118] T. Sollner, M. K. Bennett, S. W. Whiteheart, R. H. Scheller, and J. E. Rothman, "A protein assembly-disassembly pathway in vitro that may correspond to sequential steps of synaptic vesicle docking, activation, and fusion," *Cell*, vol. 75, no. 3, pp. 409–418, 1993. (Cited on page 12.)
- [119] M. K. Bennett, "SNAREs and the specificity of transport vesicle targeting," *Current Opinion in Cell Biology*, vol. 7, no. 4, pp. 581–586, 1995. (Cited on page 12.)
- [120] J. T. Littleton, R. J. Barnard, S. A. Titus, J. Slind, E. R. Chapman, and B. Ganetzky, "SNARE-complex disassembly by NSF follows synaptic-vesicle fusion," *Proceedings of the National Academy of Sciences of the United States of America*, vol. 98, no. 21, pp. 12233–12238, 2001. (Cited on page 12.)
- [121] A. Petrelli, G. F. Gilestro, S. Lanzardo, P. M. Comoglio, N. Migone, and S. Giordano, "The endophilin-CIN85-Cbl complex mediates ligand-dependent downregulation of c-Met," *Nature*, vol. 416, no. 6877, pp. 187–190, 2002. (Cited on page 12.)
- [122] A. Elhamdani, F. Azizi, E. Solomaha, H. C. Palfrey, and C. R. Artalejo, "Two mechanistically distinct forms of endocytosis in adrenal chromaffin cells: Differential effects of SH3 domains and amphiphysin antagonism," *FEBS letters*, vol. 580, no. 13, pp. 3263–3269, 2006. (Cited on page 12.)
- [123] A. Roux, K. Uyhazi, A. Frost, and P. de Camilli, "GTP-dependent twisting of dynamin implicates constriction and tension in membrane fission," *Nature*, vol. 441, no. 7092, pp. 528–531, 2006. (Cited on page 12.)
- [124] A. J. Newton, T. Kirchhausen, and V. N.

- Murthy, "Inhibition of dynamin completely blocks compensatory synaptic vesicle endocytosis," *Proceedings of the National Academy of Sciences of the United States of America*, vol. 103, no. 47, pp. 17955–17960, 2006. (Cited on page 12.)
- [125] K. E. Poskanzer, K. W. Marek, S. T. Sweeney, and G. W. Davis, "Synaptotagmin I is necessary for compensatory synaptic vesicle endocytosis in vivo," *Nature*, vol. 426, no. 6966, pp. 559–563, 2003. (Cited on page 12.)
- [126] T. Soykan, T. Maritzen, and V. Haucke, "Modes and mechanisms of synaptic vesicle recycling," *Current Opinion in Neurobiology*, vol. 39, pp. 17–23, 2016. (Cited on page 12.)
- [127] S. Watanabe, B. R. Rost, M. Camacho-Perez, M. W. Davis, B. Sohl-Kielczynski, C. Rosenmund, and E. M. Jorgensen, "Ultrafast endocytosis at mouse hippocampal synapses," *Nature*, vol. 504, no. 7479, pp. 242–247, 2013. (Cited on page 13.)
- [128] S. Watanabe, Q. Liu, M. W. Davis, G. Hollopeter, N. Thomas, N. B. Jorgensen, and E. M. Jorgensen, "Ultrafast endocytosis at *Caenorhabditis elegans* neuromuscular junctions," *eLife*, vol. 2, p. e00723, 2013. (Cited on page 13.)
- [129] S. Watanabe, T. Trimbuch, M. Camacho-Pérez, B. R. Rost, B. Brokowsky, B. Söhl-Kielczynski, A. Felies, M. W. Davis, C. Rosenmund, and E. M. Jorgensen, "Clathrin regenerates synaptic vesicles from endosomes," *Nature*, vol. 515, no. 7526, pp. 228–233, 2014. (Cited on page 13.)
- [130] I. Delvendahl, N. P. Vyleta, H. von Gersdorff, and S. Hallermann, "Fast, Temperature-Sensitive and Clathrin-Independent Endocytosis at Central Synapses," *Neuron*, vol. 90, no. 3, pp. 492–498, 2016. (Cited on page 13.)
- [131] M. A. Cousin, "Activity-dependent bulk synaptic vesicle endocytosis—a fast, high capacity membrane retrieval mechanism," *Molecular neurobiology*, vol. 39, no. 3, pp. 185–189, 2009. (Cited on page 13.)
- [132] G. Cheung and M. A. Cousin, "Synaptic vesicle generation from activity-dependent bulk endosomes requires calcium and calcineurin," *The Journal of neuroscience : the official journal of the Society for Neuroscience*, vol. 33, no. 8, pp. 3370–3379, 2013. (Cited on page 13.)
- [133] M. L. Nonet, A. M. Holgado, F. Brewer, C. J. Serpe, B. A. Norbeck, J. Holleran, L. Wei, E. Hartwig, E. M. Jorgensen, and A. Alfonso, "UNC-11, a *Caenorhabditis elegans* AP180 homologue, regulates the size and protein composition of synaptic vesicles," *Molecular Biology of the Cell*, vol. 10, no. 7, pp. 2343–2360, 1999. (Cited on page 13.)
- [134] Y. Saheki and P. de Camilli, "Synaptic vesicle endocytosis," *Cold Spring Harbor perspectives in biology*, vol. 4, no. 9, p. a005645, 2012. (Cited on page 13.)
- [135] I. Pelassa, C. Zhao, M. Pasche, B. Odermatt, and L. Lagnado, "Synaptic vesicles are "primed" for fast clathrin-mediated endocytosis at the ribbon synapse," *Frontiers in molecular neuroscience*, vol. 7, p. 91, 2014. (Cited on page 13.)
- [136] L. He, X.-S. Wu, R. Mohan, and L.-G. Wu, "Two modes of fusion pore opening revealed by cell-attached recordings at a synapse," *Nature*, vol. 444, no. 7115, pp. 102–105, 2006. (Cited on page 13.)
- [137] S. P. Gandhi and C. F. Stevens, "Three modes of synaptic vesicular recycling revealed by single-vesicle imaging," *Nature*, vol. 423, no. 6940, pp. 607–613, 2003. (Cited on page 13.)
- [138] D. Dupuy, N. Bertin, C. A. Hidalgo, K. Venkatesan, D. Tu, D. Lee, J. Rosenberg, N. Svrzikapa, A. Blanc, A. Carnec, A.-R. Carvunis, R. Pulak, J. Shingles, J. Reece-Hoyes, R. Hunt-Newbury, R. Viveiros, W. A. Mohler, M. Tasan, F. P. Roth, C. Le Peuch, I. A. Hope, R. Johnsen, D. G. Moerman, A.-L. Barabási, D. Baillie, and M. Vidal, "Genome-scale analysis of in vivo spatiotem-

- poral promoter activity in *Caenorhabditis elegans*," *Nature biotechnology*, vol. 25, no. 6, pp. 663–668, 2007. (Cited on page 13.)
- [139] R. N. Day and M. W. Davidson, "The fluorescent protein palette: tools for cellular imaging," *Chemical Society reviews*, vol. 38, no. 10, pp. 2887–2921, 2009. (Cited on page 13.)
- [140] C. Schmitt, C. Schultheis, N. Pokala, S. J. Husson, J. F. Liewald, C. I. Bargmann, and A. Gottschalk, "Specific expression of channelrhodopsin-2 in single neurons of *Caenorhabditis elegans*," *PLoS one*, vol. 7, no. 8, p. e43164, 2012. (Cited on page 13.)
- [141] E. J. A. Hubbard, "FLP/FRT and Cre/lox recombination technology in *C. elegans*," *Methods (San Diego, Calif.)*, vol. 68, no. 3, pp. 417–424, 2014. (Cited on page 13.)
- [142] C. C. Mello, J. M. Kramer, D. Stinchcomb, and V. Ambros, "Efficient gene transfer in *C. elegans*: extrachromosomal maintenance and integration of transforming sequences," *EMBO J*, vol. 10, no. 12, pp. 3959–3970, 1991. (Cited on pages 14, 23, and 65.)
- [143] V. J. P. Robert and J.-L. Bessereau, "Manipulating the *Caenorhabditis elegans* genome using mariner transposons," *Genetica*, vol. 138, no. 5, pp. 541–549, 2010. (Cited on page 14.)
- [144] T. Bacaj and S. Shaham, "Temporal control of cell-specific transgene expression in *Caenorhabditis elegans*," *Genetics*, vol. 176, no. 4, pp. 2651–2655, 2007. (Cited on page 14.)
- [145] V. Praitis, E. Casey, D. Collar, and J. Austin, "Creation of low-copy integrated transgenic lines in *Caenorhabditis elegans*," *Genetics*, vol. 157, no. 3, pp. 1217–1226, 2001. (Cited on page 14.)
- [146] E. Kage-Nakadai, H. Kobuna, O. Funatsu, M. Otori, K. Gengyo-Ando, S. Yoshina, S. Hori, and S. Mitani, "Single/low-copy integration of transgenes in *Caenorhabditis elegans* using an ultraviolet trimethylpsoralen method," *BMC Biotechnology*, vol. 12, no. 1, p. 1, 2012. (Cited on page 14.)
- [147] Susana Q Lima and Gero Miesenböck, "Remote control of behavior through genetically targeted photostimulation of neurons," *Cell*, vol. 121, no. 1, pp. 141–152, 2005. (Cited on page 14.)
- [148] Stephanie Szobota, Pau Gorostiza, Filippo Del Bene, Claire Wyart, Doris L Fortin, Kathleen D Kolstad, Orapim Tulyathan and Matthew Volgraf, Rika Numano, Holly L Aaron, Ethan K Scott, Richard H Kramer, John Flannery, Herwig Baier and Dirk Trauner, and Ehud Y Isacoff, "Remote control of neuronal activity with a light-gated glutamate receptor," *Neuron*, vol. 54, no. 4, pp. 535–545, 2007. (Cited on page 14.)
- [149] T. Fehrentz, M. Schönberger, and D. Trauner, "Optochemical Genetics," *Angewandte Chemie International Edition*, p. n/a, 2011. (Cited on page 14.)
- [150] A. Mourot, T. Fehrentz, Y. Le Feuvre, C. M. Smith, C. Herold, D. Dalkara, F. Nagy, D. Trauner, and R. H. Kramer, "Rapid optical control of nociception with an ion-channel photoswitch," *Nature Methods*, 2012. (Cited on page 14.)
- [151] J. A. Frank, D. A. Yushchenko, D. J. Hodson, N. Lipstein, J. Nagpal, G. A. Rutter, J.-S. Rhee, A. Gottschalk, N. Brose, C. Schultz, and D. Trauner, "Photoswitchable diacylglycerols enable optical control of protein kinase C," *Nature chemical biology*, 2016. (Cited on page 14.)
- [152] Georg Nagel, Doris Ollig, Markus Fuhrmann, Suneel Kateriya, Anna Maria Musti, Ernst Bamberg, and Peter Hegemann, "Channelrhodopsin-1: a light-gated proton channel in green algae," *Science*, vol. 296, no. 5577, pp. 2395–2398, 2002. (Cited on page 14.)
- [153] Georg Nagel, Tanjef Szellas, Wolfram Huhn, Suneel Kateriya, Nona Adeishvili, Peter Berthold, Doris Ollig, Peter Hegemann, and Ernst Bamberg, "Channelrhodopsin-2, a directly light-gated cation-selective membrane

- channel," *Proceedings of the National Academy of Sciences of the United States of America*, vol. 100, no. 24, pp. 13940–13945, 2003. (Cited on page 14.)
- [154] O. A. Sineshchekov, K.-H. Jung, and J. L. Spudich, "Two rhodopsins mediate phototaxis to low- and high-intensity light in *Chlamydomonas reinhardtii*," *Proceedings of the National Academy of Sciences of the United States of America*, vol. 99, no. 13, pp. 8689–8694, 2002. (Cited on page 14.)
- [155] T. Suzuki, K. Yamasaki, S. Fujita, K. Oda, M. Iseki, K. Yoshida, M. Watanabe, H. Daiyasu, H. Toh, E. Asamizu, S. Tabata, K. Miura, H. Fukuzawa, S. Nakamura, and T. Takahashi, "Archaeal-type rhodopsins in *Chlamydomonas*: Model structure and intracellular localization," *Biochemical and Biophysical Research Communications*, vol. 301, no. 3, pp. 711–717, 2003. (Cited on page 14.)
- [156] G. Nagel, M. Brauner, J. F. Liewald, N. Adeishvili, E. Bamberg, and A. Gottschalk, "Light activation of channelrhodopsin-2 in excitable cells of *Caenorhabditis elegans* triggers rapid behavioral responses," *Curr Biol*, vol. 15, no. 24, pp. 2279–2284, 2005. (Cited on pages 14, 15, 17, 23, and 63.)
- [157] C. Bamann, T. Kirsch, G. Nagel, and E. Bamberg, "Spectral characteristics of the photocycle of channelrhodopsin-2 and its implication for channel function," *Journal of Molecular Biology*, vol. 375, no. 3, pp. 686–694, 2008. (Cited on page 14.)
- [158] E. Ritter, K. Stehfest, A. Berndt, P. Hegemann, and F. J. Bartl, "Monitoring light-induced structural changes of Channelrhodopsin-2 by UV-visible and Fourier transform infrared spectroscopy," *The Journal of biological chemistry*, vol. 283, no. 50, pp. 35033–35041, 2008. (Cited on pages 14 and 15.)
- [159] A. Berndt, O. Yizhar, L. A. Gunaydin, P. Hegemann, and K. Deisseroth, "Bi-stable neural state switches," *Nature neuroscience*, vol. 12, no. 2, pp. 229–234, 2009. (Cited on pages 15 and 17.)
- [160] H. E. Kato, F. Zhang, O. Yizhar, C. Ramakrishnan, T. Nishizawa, K. Hirata, J. Ito, Y. Aita, T. Tsukazaki, S. Hayashi, P. Hegemann, A. D. Maturana, R. Ishitani, K. Deisseroth, and O. Nureki, "Crystal structure of the channelrhodopsin light-gated cation channel," *Nature*, 2012. (Cited on page 15.)
- [161] A. Berndt, S. Y. Lee, C. Ramakrishnan, and K. Deisseroth, "Structure-Guided Transformation of Channelrhodopsin into a Light-Activated Chloride Channel," *Science*, vol. 344, no. 6182, pp. 420–424, 2014. (Cited on page 15.)
- [162] F. Schneider, C. Grimm, and P. Hegemann, "Biophysics of Channelrhodopsin," *Annual review of biophysics*, vol. 44, pp. 167–186, 2015. (Cited on page 15.)
- [163] E. G. Govorunova, E. N. Spudich, C. E. Lane, O. A. Sineshchekov, and J. L. Spudich, "New channelrhodopsin with a red-shifted spectrum and rapid kinetics from *Mesostigma viride*," *mBio*, vol. 2, no. 3, pp. e00115–11, 2011. (Cited on page 15.)
- [164] S.-Y. Hou, E. G. Govorunova, M. Ntefidou, C. E. Lane, E. N. Spudich, O. A. Sineshchekov, and J. L. Spudich, "Diversity of *Chlamydomonas* channelrhodopsins," *Photochemistry and photobiology*, vol. 88, no. 1, pp. 119–128, 2012. (Cited on page 15.)
- [165] E. G. Govorunova, O. A. Sineshchekov, H. Li, R. Janz, and J. L. Spudich, "Characterization of a highly efficient blue-shifted channelrhodopsin from the marine alga *Platymonas subcordiformis*," *The Journal of biological chemistry*, vol. 288, no. 41, pp. 29911–29922, 2013. (Cited on page 15.)
- [166] N. C. Klapoetke, Y. Murata, S. S. Kim, S. R. Pulver, A. Birdsey-Benson, Y. K. Cho, T. K. Morimoto, A. S. Chuong, E. J. Carpenter, Z. Tian, J. Wang, Y. Xie, Z. Yan, Y. Zhang, B. Y. Chow, B. Surek, M. Melkonian, V. Jayaraman, M. Constantine-Paton, G. K.-S. Wong, and E. S. Boyden, "Independent optical ex-

- citation of distinct neural populations," *Nature Methods*, vol. 11, no. 3, pp. 338–346, 2014. (Cited on pages 15 and 16.)
- [167] J. Wietek, M. Broser, B. S. Krause, and P. Hegemann, "Identification of a Natural Green Light Absorbing Chloride Conducting Channelrhodopsin from *Proteomonas sulcata*," *The Journal of biological chemistry*, vol. 291, no. 8, pp. 4121–4127, 2016. (Cited on page 15.)
- [168] O. Yizhar, L. E. Fenno, M. Prigge, F. Schneider, T. J. Davidson, D. J. O'Shea, V. S. Sohal, I. Goshen, J. Finkelstein, J. T. Paz, K. Stehfest, R. Fudim, C. Ramakrishnan, J. R. Huguenard, P. Hegemann, and K. Deisseroth, "Neocortical excitation/inhibition balance in information processing and social dysfunction," *Nature*, vol. 477, no. 7363, pp. 171–178, 2011. (Cited on pages 15 and 17.)
- [169] K. Erbguth, M. Prigge, F. Schneider, P. Hegemann, and A. Gottschalk, "Bimodal activation of different neuron classes with the spectrally red-shifted channelrhodopsin chimera C1V1 in *Caenorhabditis elegans*," *PloS one*, vol. 7, no. 10, p. e46827, 2012. (Cited on pages 16 and 17.)
- [170] L. C. Schild and D. A. Glauser, "Dual Color Neural Activation and Behavior Control with Chrimson and CoChR in *Caenorhabditis elegans*," *Genetics*, vol. 200, no. 4, pp. 1029–1034, 2015. (Cited on page 16.)
- [171] M. Sato, M. Kubo, T. Aizawa, N. Kamo, T. Kikukawa, K. Nitta, and M. Demura, "Role of putative anion-binding sites in cytoplasmic and extracellular channels of *Natronomonas pharaonis* halorhodopsin," *Biochemistry*, vol. 44, no. 12, pp. 4775–4784, 2005. (Cited on pages 16 and 17.)
- [172] F. Zhang, L.-P. Wang, M. Brauner, J. F. Liewald, K. Kay, N. Watzke, P. G. Wood, E. Bamberg, G. Nagel, A. Gottschalk, and K. Deisseroth, "Multimodal fast optical interrogation of neural circuitry," *Nature*, vol. 446, no. 7136, pp. 633–639, 2007. (Cited on pages 16 and 17.)
- [173] S. A. Waschuk, A. G. Bezerra, JR, L. Shi, and L. S. Brown, "Leptosphaeria rhodopsin: bacteriorhodopsin-like proton pump from a eukaryote," *Proceedings of the National Academy of Sciences of the United States of America*, vol. 102, no. 19, pp. 6879–6883, 2005. (Cited on pages 16 and 17.)
- [174] B. Y. Chow, X. Han, A. S. Dobry, X. Qian, A. S. Chuong, M. Li, M. A. Henninger, G. M. Belfort, Y. Lin, P. E. Monahan, and E. S. Boyden, "High-performance genetically targetable optical neural silencing by light-driven proton pumps," *Nature*, vol. 463, no. 7277, pp. 98–102, 2010. (Cited on pages 16 and 17.)
- [175] X. Han, B. Y. Chow, H. Zhou, N. C. Klapoetke, A. Chuong, R. Rajimehr, A. Yang, M. V. Baratta, J. Winkle, R. Desimone, and E. S. Boyden, "A High-Light Sensitivity Optical Neural Silencer: Development and Application to Optogenetic Control of Non-Human Primate Cortex," *Frontiers in Systems Neuroscience*, vol. 5, 2011. (Cited on page 16.)
- [176] J. N. Stirman, M. M. Crane, S. J. Husson, S. Wabnig, C. Schultheis, A. Gottschalk, and H. Lu, "Real-time multimodal optical control of neurons and muscles in freely behaving *Caenorhabditis elegans*," *Nature methods*, vol. 8, no. 2, pp. 153–158, 2011. (Cited on pages 16, 69, 70, 81, 229, and 237.)
- [177] S. J. Husson, J. F. Liewald, C. Schultheis, J. N. Stirman, H. Lu, and A. Gottschalk, "Microbial light-activatable proton pumps as neuronal inhibitors to functionally dissect neuronal networks in *C. elegans*," *PLoS One*, vol. 7, no. 7, p. e40937, 2012. (Cited on page 16.)
- [178] A. Okazaki, Y. Sudo, and S. Takagi, "Optical Silencing of *C. elegans* Cells with Arch Proton Pump," *PloS one*, vol. 7, no. 5, p. e35370, 2012. (Cited on page 16.)
- [179] J. V. Raimondo, L. Kay, T. J. Ellender, and C. J. Akerman, "Optogenetic silencing strate-



- gies differ in their effects on inhibitory synaptic transmission," *Nature neuroscience*, vol. 15, no. 8, pp. 1102–1104, 2012. (Cited on page 16.)
- [180] M. Mahn, M. Prigge, S. Ron, R. Levy, and O. Yizhar, "Biophysical constraints of optogenetic inhibition at presynaptic terminals," *Nature neuroscience*, vol. 19, no. 4, pp. 554–556, 2016. (Cited on page 17.)
- [181] Y.-H. Chen, M.-L. Wu, and W.-M. Fu, "Regulation of Presynaptic NMDA Responses by External and Intracellular pH Changes at Developing Neuromuscular Synapses," *Journal of Neuroscience*, vol. 18, no. 8, pp. 2982–2990, 1998. (Cited on page 17.)
- [182] C. Cosentino, L. Alberio, S. Gazzarrini, M. Aquila, E. Romano, S. Cermenati, P. Zuccolini, J. Petersen, M. Beltrame, J. L. van Etten, J. M. Christie, G. Thiel, and A. Moroni, "Optogenetics. Engineering of a light-gated potassium channel," *Science (New York, N.Y.)*, vol. 348, no. 6235, pp. 707–710, 2015. (Cited on page 17.)
- [183] J. Y. Lin, M. Z. Lin, P. Steinbach, and R. Y. Tsien, "Characterization of engineered channelrhodopsin variants with improved properties and kinetics," *Biophys J*, vol. 96, no. 5, pp. 1803–1814, 2009. (Cited on page 17.)
- [184] S. Kleinlogel, K. Feldbauer, R. E. Dempski, H. Fotis, P. G. Wood, C. Bamann, and E. Bamberg, "Ultra light-sensitive and fast neuronal activation with the Ca<sup>2+</sup>-permeable channelrhodopsin CatCh," *Nature neuroscience*, vol. 14, no. 4, pp. 513–518, 2011. (Cited on page 17.)
- [185] A. Berndt, P. Schoenenberger, J. Mattis, K. M. Tye, K. Deisseroth, P. Hegemann, and T. G. Oertner, "High-efficiency channelrhodopsins for fast neuronal stimulation at low light levels," *Proceedings of the National Academy of Sciences of the United States of America*, vol. 108, no. 18, pp. 7595–7600, 2011. (Cited on page 17.)
- [186] S. Ullrich, R. Gueta, and G. Nagel, "Degradation of channelopsin-2 in the absence of retinal and degradation resistance in certain mutants," *Biological chemistry*, vol. 394, no. 2, pp. 271–280, 2013. (Cited on page 17.)
- [187] M. Gomelsky and G. Klug, "BLUF: a novel FAD-binding domain involved in sensory transduction in microorganisms," *Trends in biochemical sciences*, vol. 27, no. 10, pp. 497–500, 2002. (Cited on pages 17, 19, and 20.)
- [188] Y. Han, "A eukaryotic BLUF domain mediates light-dependent gene expression in the purple bacterium *Rhodobacter sphaeroides* 2.4.1," *Proceedings of the National Academy of Sciences of the United States of America*, vol. 101, no. 33, pp. 12306–12311, 2004. (Cited on page 17.)
- [189] J. M. Christie, J. Gawthorne, G. Young, N. J. Fraser, and A. J. Roe, "LOV to BLUF: Flavoprotein Contributions to the Optogenetic Toolkit," *Molecular Plant*, vol. 5, no. 3, pp. 533–544, 2012. (Cited on page 17.)
- [190] A. Kita, K. Okajima, Y. Morimoto, M. Ikeuchi, and K. Miki, "Structure of a cyanobacterial BLUF protein, Tll0078, containing a novel FAD-binding blue light sensor domain," *Journal of molecular biology*, vol. 349, no. 1, pp. 1–9, 2005. (Cited on page 17.)
- [191] A. Jung, T. Domratcheva, M. Tarutina, Q. Wu, W.-H. Ko, R. L. Shoeman, M. Gomelsky, K. H. Gardner, and I. Schlichting, "Structure of a bacterial BLUF photoreceptor: insights into blue light-mediated signal transduction," *Proceedings of the National Academy of Sciences of the United States of America*, vol. 102, no. 35, pp. 12350–12355, 2005. (Cited on pages 17 and 18.)
- [192] S. Anderson, V. Dragnea, S. Masuda, J. Ybe, K. Moffat, and C. Bauer, "Structure of a novel photoreceptor, the BLUF domain of AppA from *Rhodobacter sphaeroides*," *Biochemistry*, vol. 44, no. 22, pp. 7998–8005, 2005. (Cited on page 17.)
- [193] T. Domratcheva, B. L. Grigorenko, I. Schlichting, and A. V. Nemukhin, "Molecular models predict light-induced glutamine tautomer-

- ization in BLUF photoreceptors," *Biophysical journal*, vol. 94, no. 10, pp. 3872–3879, 2008. (Cited on page 17.)
- [194] T. Domratcheva, E. Hartmann, I. Schlichting, and T. Kottke, "Evidence for Tautomerisation of Glutamine in BLUF Blue Light Receptors by Vibrational Spectroscopy and Computational Chemistry," *Scientific reports*, vol. 6, p. 22669, 2016. (Cited on pages 17 and 18.)
- [195] S. Masuda, Y. Tomida, H. Ohta, and K.-I. Takamiya, "The critical role of a hydrogen bond between Gln63 and Trp104 in the blue-light sensing BLUF domain that controls AppA activity," *Journal of Molecular Biology*, vol. 368, no. 5, pp. 1223–1230, 2007. (Cited on page 18.)
- [196] S. Masuda, K. Hasegawa, H. Ohta, and T.-a. Ono, "Crucial role in light signal transduction for the conserved Met93 of the BLUF protein PixD/Slr1694," *Plant & cell physiology*, vol. 49, no. 10, pp. 1600–1606, 2008. (Cited on page 18.)
- [197] J. T. M. Kennis and T. Mathes, "Molecular eyes: proteins that transform light into biological information," *Interface focus*, vol. 3, no. 5, p. 20130005, 2013. (Cited on page 18.)
- [198] A. A. Gil, A. Haigney, S. P. Laptinok, R. Brust, A. Lukacs, J. N. Iuliano, J. Jeng, E. H. Melief, R.-K. Zhao, E. Yoon, I. P. Clark, M. Towrie, G. M. Greetham, A. Ng, J. J. Truglio, J. B. French, S. R. Meech, and P. J. Tonge, "Mechanism of the AppABLUF Photocycle Probed by Site-Specific Incorporation of Fluorotyrosine Residues: Effect of the Y21 pKa on the Forward and Reverse Ground-State Reactions," *Journal of the American Chemical Society*, vol. 138, no. 3, pp. 926–935, 2016. (Cited on page 18.)
- [199] M. Tanwar, S. Nahar, S. Gulati, S. K. Veetil, and S. Kateriya, "Molecular determinant modulates thermal recovery kinetics and structural integrity of the bacterial BLUF photoreceptor," *FEBS letters*, vol. 590, no. 14, pp. 2146–2157, 2016. (Cited on page 19.)
- [200] M. Iseki, S. Matsunaga, A. Murakami, K. Ohno, K. Shiga, K. Yoshida, M. Sugai, T. Takahashi, T. Hori, and M. Watanabe, "A blue-light-activated adenylyl cyclase mediates photoavoidance in *Euglena gracilis*," *Nature*, vol. 415, no. 6875, pp. 1047–1051, 2002. (Cited on page 19.)
- [201] Saskia Schröder-Lang, Martin Schwärzel, Reinhard Seifert, Timo Strünker, Suneel Kateriya, Jens Looser, Masakatsu Watanabe and U. Benjamin Kaupp, Peter Hegemann, and Georg Nagel, "Fast manipulation of cellular cAMP level by light in vivo," *Nat Methods*, vol. 4, no. 1, pp. 39–42, 2007. (Cited on page 19.)
- [202] M. Stierl, P. Stumpf, D. Udvari, R. Gueta, R. Hagedorn, A. Losi, W. Gärtner, L. Peterreit, M. Efetova, M. Schwarzel, T. G. Oertner, G. Nagel, and P. Hegemann, "Light-modulation of cellular cAMP by a small bacterial photoactivated adenylyl cyclase, bPAC, of the soil bacterium *beggiatoa*," *The Journal of biological chemistry*, 2010. (Cited on pages 19 and 84.)
- [203] T. Nagahama, T. Suzuki, S. Yoshikawa, and M. Iseki, "Functional transplant of photoactivated adenylyl cyclase (PAC) into *Aplysia* sensory neurons," *Neuroscience research*, vol. 59, no. 1, pp. 81–88, 2007. (Cited on page 19.)
- [204] S. Weissenberger, C. Schultheis, J. F. Liewald, K. Erbguth, G. Nagel, and A. Gottschalk, "PACa- an optogenetic tool for in vivo manipulation of cellular cAMP levels, neurotransmitter release, and behavior in *Caenorhabditis elegans*," *Journal of Neurochemistry*, vol. 116, no. 4, pp. 616–625, 2011. (Cited on pages 19, 20, 27, and 145.)
- [205] M. A. Schade, N. K. Reynolds, C. M. Dollins, and K. G. Miller, "Mutations that rescue the paralysis of *Caenorhabditis elegans* ric-8 (synembryon) mutants activate the G alpha(s) pathway and define a third major branch of the synaptic signaling network," *Genetics*,

- vol. 169, no. 2, pp. 631–649, 2005. (Cited on pages 19 and 88.)
- [206] J. F. Liewald, B. Brauner, G. J. Stephens, M. Bouhours, C. Schultheis, M. Zhen, and A. Gottschalk, "Optogenetic analysis of synaptic function," *Nat Methods*, vol. 5, no. 10, pp. 895–902, 2008. (Cited on pages 19, 63, and 225.)
- [207] M.-H. Ryu, O. V. Moskvin, J. Siltberg-Liberles, and M. Gomelsky, "Natural and engineered photoactivated nucleotidyl cyclases for optogenetic applications," *The Journal of biological chemistry*, 2010. (Cited on pages 19 and 145.)
- [208] B. Berse and J. K. Blusztajn, "Coordinated Up-regulation of Choline Acetyltransferase and Vesicular Acetylcholine Transporter Gene Expression by the Retinoic Acid Receptor , cAMP, and Leukemia Inhibitory Factor/Ciliary Neurotrophic Factor Signaling Pathways in a Murine Septal Cell Line," *Journal of Biological Chemistry*, vol. 270, no. 38, pp. 22101–22104, 1995. (Cited on page 20.)
- [209] M. Shimojo, D. Wu, and L. B. Hersh, "The cholinergic gene locus is coordinately regulated by protein kinase A II in PC12 cells," *Journal of Neurochemistry*, vol. 71, no. 3, pp. 1118–1126, 1998. (Cited on page 20.)
- [210] X. Castell, N. Cheviron, J.-V. Barnier, and M.-F. Diebler, "Exploring the regulation of the expression of ChAT and VAcHT genes in NG108-15 cells: implication of PKA and PI3K signaling pathways," *Neurochemical research*, vol. 28, no. 3-4, pp. 557–564, 2003. (Cited on page 20.)
- [211] J. Nakai, M. Ohkura, and K. Imoto, "A high signal-to-noise Ca(2+) probe composed of a single green fluorescent protein," *Nature biotechnology*, vol. 19, no. 2, pp. 137–141, 2001. (Cited on page 21.)
- [212] J. Akerboom, T.-W. Chen, T. J. Wardill, L. Tian, J. S. Marvin, S. Mutlu, N. C. Calderon, F. Esposti, B. G. Borghuis, X. R. Sun, A. Gordus, M. B. Orger, R. Portugues, F. Engert, J. J. Macklin, A. Filosa, A. Aggarwal, R. A. Kerr, R. Takagi, S. Kracun, E. Shigetomi, B. S. Khakh, H. Baier, L. Lagnado, S. S.-H. Wang, C. I. Bargmann, B. E. Kimmel, V. Jayaraman, K. Svoboda, D. S. Kim, E. R. Schreiter, and L. L. Looger, "Optimization of a GCaMP calcium indicator for neural activity imaging," *The Journal of neuroscience : the official journal of the Society for Neuroscience*, vol. 32, no. 40, pp. 13819–13840, 2012. (Cited on page 21.)
- [213] Y. Yamada and K. MIKOSHIBA, "Quantitative comparison of novel GCaMP-type genetically encoded Ca(2+) indicators in mammalian neurons," *Frontiers in cellular neuroscience*, vol. 6, p. 41, 2012. (Cited on page 21.)
- [214] T.-W. Chen, T. J. Wardill, Y. Sun, S. R. Pulver, S. L. Renninger, A. Baohan, E. R. Schreiter, R. A. Kerr, M. B. Orger, V. Jayaraman, L. L. Looger, K. Svoboda, and D. S. Kim, "Ultrasensitive fluorescent proteins for imaging neuronal activity," *Nature*, vol. 499, no. 7458, pp. 295–300, 2013. (Cited on page 21.)
- [215] A. Miyawaki, J. Llopis, R. Heim, J. M. McCaffery, J. A. Adams, M. Ikura, and R. Y. Tsien, "Fluorescent indicators for Ca<sup>2+</sup> based on green fluorescent proteins and calmodulin," *Nature*, vol. 388, no. 6645, pp. 882–887, 1997. (Cited on page 21.)
- [216] N. Heim and O. Griesbeck, "Genetically encoded indicators of cellular calcium dynamics based on troponin C and green fluorescent protein," *The Journal of biological chemistry*, vol. 279, no. 14, pp. 14280–14286, 2004. (Cited on page 21.)
- [217] K. Horikawa, Y. Yamada, T. Matsuda, K. Kobayashi, M. Hashimoto, T. Matsu-ura, A. Miyawaki, T. Michikawa, K. MIKOSHIBA, and T. Nagai, "Spontaneous network activity visualized by ultrasensitive Ca(2+) indicators, yellow Cameleon-Nano," *Nature methods*, vol. 7, no. 9, pp. 729–732, 2010. (Cited on page 21.)
- [218] J. E. McCombs and A. E. Palmer, "Measuring calcium dynamics in living cells with geneti-

- cally encodable calcium indicators," *Methods (San Diego, Calif.)*, vol. 46, no. 3, pp. 152–159, 2008. (Cited on page 21.)
- [219] F. S. Pavone, ed., *Laser Imaging and Manipulation in Cell Biology*. Weinheim, Germany: Wiley-VCH Verlag GmbH & Co. KGaA, 2010. (Cited on page 21.)
- [220] S. Pletnev, N. G. Gurskaya, N. V. Pletneva, K. A. Lukyanov, D. M. Chudakov, V. I. Martynov, V. O. Popov, M. V. Kovalchuk, A. Wlodawer, Z. Dauter, and V. Pletnev, "Structural basis for phototoxicity of the genetically encoded photosensitizer KillerRed," *The Journal of biological chemistry*, vol. 284, no. 46, pp. 32028–32039, 2009. (Cited on page 21.)
- [221] L. Avery and H. Horvitz, "A cell that dies during wild-type *C. elegans* development can function as a neuron in a *ced-3* mutant," *Cell*, vol. 51, no. 6, pp. 1071–1078, 1987. (Cited on page 21.)
- [222] J. Kobayashi, H. Shidara, Y. Morisawa, M. Kawakami, Y. Tanahashi, K. Hotta, and K. Oka, "A method for selective ablation of neurons in *C. elegans* using the phototoxic fluorescent protein, KillerRed," *Neuroscience letters*, vol. 548, pp. 261–264, 2013. (Cited on page 21.)
- [223] K. Takemoto, T. Matsuda, N. Sakai, D. Fu, M. Noda, S. Uchiyama, I. Kotera, Y. Arai, M. Horiuchi, K. Fukui, T. Ayabe, F. Inagaki, H. Suzuki, and T. Nagai, "SuperNova, a monomeric photosensitizing fluorescent protein for chromophore-assisted light inactivation," *Scientific reports*, vol. 3, p. 2629, 2013. (Cited on page 21.)
- [224] X. Shu, V. Lev-Ram, T. J. Deerinck, Y. Qi, E. B. Ramko, M. W. Davidson, Y. Jin, M. H. Ellisman, and R. Y. Tsien, "A genetically encoded tag for correlated light and electron microscopy of intact cells, tissues, and organisms," *PLoS biology*, vol. 9, no. 4, p. e1001041, 2011. (Cited on page 22.)
- [225] Y. B. Qi, E. J. Garren, X. Shu, R. Y. Tsien, and Y. Jin, "Photo-inducible cell ablation in *Caenorhabditis elegans* using the genetically encoded singlet oxygen generating protein miniSOG," *Proceedings of the National Academy of Sciences of the United States of America*, vol. 109, no. 19, pp. 7499–7504, 2012. (Cited on page 22.)
- [226] J. Yuan, S. Shaham, S. Ledoux, H. M. Ellis, and H. R. Horvitz, "The *C. elegans* cell death gene *ced-3* encodes a protein similar to mammalian interleukin-1 beta-converting enzyme," *Cell*, vol. 75, no. 4, pp. 641–652, 1993. (Cited on page 22.)
- [227] M. Enari, H. Hug, and S. Nagata, "Involvement of an ICE-like protease in Fas-mediated apoptosis," *Nature*, vol. 375, no. 6526, pp. 78–81, 1995. (Cited on page 22.)
- [228] M. Los, M. van de Craen, L. C. Penning, H. Schenk, M. Westendorp, P. A. Baeuerle, W. Droge, P. H. Kramer, W. Fiers, and K. Schulze-Osthoff, "Requirement of an ICE/CED-3 protease for Fas/APO-1-mediated apoptosis," *Nature*, vol. 375, no. 6526, pp. 81–83, 1995. (Cited on page 22.)
- [229] J. Yuan, "Genetic control of cellular suicide," *Reproductive toxicology (Elmsford, N)*, vol. 11, no. 2-3, pp. 377–384, 1997. (Cited on page 22.)
- [230] J. E. Sulston and H. R. Horvitz, "Post-embryonic cell lineages of the nematode, *Caenorhabditis elegans*," *Developmental Biology*, vol. 56, no. 1, pp. 110–156, 1977. (Cited on page 23.)
- [231] J. Sulston, E. Schierenberg, J. G. White, and J. Thomson, "The embryonic cell lineage of the nematode *Caenorhabditis elegans*," *Developmental Biology*, vol. 100, no. 1, pp. 64–119, 1983. (Cited on pages 23 and 33.)
- [232] G. Schiavo, F. Benfenati, B. Poulain, O. Rossetto, P. Polverino de Laureto, B. R. DasGupta, and C. Montecucco, "Tetanus and botulinum-B neurotoxins block neurotransmitter release by proteolytic cleavage of synaptobrevin," *Nature*, vol. 359, no. 6398, pp. 832–835, 1992. (Cited on page 23.)
- [233] G. Schiavo, B. Poulain, O. Rossetto, F. Benfe-

- nati, L. Tauc, and C. Montecucco, "Tetanus toxin is a zinc protein and its inhibition of neurotransmitter release and protease activity depend on zinc," *The EMBO journal*, vol. 11, no. 10, pp. 3577–3583, 1992. (Cited on page 23.)
- [234] S. T. Sweeney, K. Broadie, J. Keane, H. Niemann, and C. J. O'Kane, "Targeted expression of tetanus toxin light chain in *Drosophila* specifically eliminates synaptic transmission and causes behavioral defects," *Neuron*, vol. 14, no. 2, pp. 341–351, 1995. (Cited on page 23.)
- [235] H. T. McMahon, Y. A. Ushkaryov, L. Edelman, E. Link, T. Binz, H. Niemann, R. Jahn, and T. C. Sudhof, "Cellubrevin is a ubiquitous tetanus-toxin substrate homologous to a putative synaptic vesicle fusion protein," *Nature*, vol. 364, no. 6435, pp. 346–349, 1993. (Cited on page 23.)
- [236] E. Link, H. McMahon, G. Fischer von Mollard, S. Yamasaki, H. Niemann, T. C. Sudhof, and R. Jahn, "Cleavage of cellubrevin by tetanus toxin does not affect fusion of early endosomes," *The Journal of biological chemistry*, vol. 268, no. 25, pp. 18423–18426, 1993. (Cited on page 23.)
- [237] N. Pokala, Q. Liu, A. Gordus, and C. I. Bargmann, "Inducible and titratable silencing of *Caenorhabditis elegans* neurons in vivo with histamine-gated chloride channels," *Proceedings of the National Academy of Sciences of the United States of America*, vol. 111, no. 7, pp. 2770–2775, 2014. (Cited on pages 23 and 64.)
- [238] D. L. Chase and M. R. Koelle, "Biogenic amine neurotransmitters in *C. elegans*: WormBook," 20.02.2007. (Cited on page 23.)
- [239] L. R. Varshney, B. L. Chen, E. Paniagua, D. H. Hall, and D. B. Chklovskii, "Structural Properties of the *Caenorhabditis elegans* Neuronal Network," *PLoS Computational Biology*, vol. 7, no. 2, p. e1001066, 2011. (Cited on pages 24, 31, 32, and 33.)
- [240] E. Yemini, T. Jucikas, L. J. Grundy, A. E. X. Brown, and W. R. Schafer, "A database of *Caenorhabditis elegans* behavioral phenotypes," *Nature methods*, vol. 10, no. 9, pp. 877–879, 2013. (Cited on pages 24 and 147.)
- [241] C. Maximino, R. X. d. C. Silva, S. d. N. S. da Silva, L. d. S. D. S. Rodrigues, H. Barbosa, T. S. de Carvalho, L. K. D. R. Leao, M. G. Lima, K. R. M. Oliveira, and A. M. Herculanio, "Non-mammalian models in behavioral neuroscience: consequences for biological psychiatry," *Frontiers in behavioral neuroscience*, vol. 9, p. 233, 2015. (Cited on page 24.)
- [242] B. L. Aken, S. Ayling, D. Barrell, L. Clarke, V. Curwen, S. Fairley, J. Fernandez Banet, K. Billis, C. Garcia Giron, T. Hourlier, K. Howe, A. Kahari, F. Kokocinski, F. J. Martin, D. N. Murphy, R. Nag, M. Ruffier, M. Schuster, Y. A. Tang, J.-H. Vogel, S. White, A. Zadissa, P. Fliccek, and S. M. J. Searle, "The Ensembl gene annotation system," *Database : the journal of biological databases and curation*, vol. 2016, 2016. (Cited on page 24.)
- [243] D. Osumi-Sutherland, S. J. Marygold, G. H. Millburn, P. A. McQuilton, L. Ponting, R. Stefancsik, K. Falls, N. H. Brown, and G. V. Gkoutos, "The *Drosophila* phenotype ontology," *Journal of biomedical semantics*, vol. 4, no. 1, p. 30, 2013. (Cited on page 24.)
- [244] H. K. Inagaki, Y. Jung, E. D. Hoopfer, A. M. Wong, N. Mishra, J. Y. Lin, R. Y. Tsien, and D. J. Anderson, "Optogenetic control of *Drosophila* using a red-shifted channelrhodopsin reveals experience-dependent influences on courtship," *Nature methods*, vol. 11, no. 3, pp. 325–332, 2014. (Cited on page 24.)
- [245] J. B. Lack, J. D. Lange, A. D. Tang, R. B. Corbett-Detig, and J. E. Pool, "A Thousand Fly Genomes: An Expanded *Drosophila* Genome Nexus," *Molecular biology and evolution*, 2016. (Cited on page 24.)
- [246] K. Howe, M. D. Clark, C. F. Torroja, J. Torrance, C. Berthelot, M. Muffato,

- J. E. Collins, S. Humphray, K. McLaren, L. Matthews, S. McLaren, I. Sealy, M. Caccamo, C. Churcher, C. Scott, J. C. Barrett, R. Koch, G.-J. Rauch, S. White, W. Chow, B. Kilian, L. T. Quintais, J. A. Guerra-Assuncao, Y. Zhou, Y. Gu, J. Yen, J.-H. Vogel, T. Eyre, S. Redmond, R. Banerjee, J. Chi, B. Fu, E. Langley, S. F. Maguire, G. K. Laird, D. Lloyd, E. Kenyon, S. Donaldson, H. Sehra, J. Almeida-King, J. Loveland, S. Trevanion, M. Jones, M. Quail, D. Willey, A. Hunt, J. Burton, S. Sims, K. McLay, B. Plumb, J. Davis, C. Clee, K. Oliver, R. Clark, C. Riddle, D. Elliot, G. Threadgold, G. Harden, D. Ware, S. Begum, B. Mortimore, G. Kerry, P. Heath, B. Phillimore, A. Tracey, N. Corby, M. Dunn, C. Johnson, J. Wood, S. Clark, S. Pelan, G. Griffiths, M. Smith, R. Glithero, P. Howden, N. Barker, C. Lloyd, C. Stevens, J. Harley, K. Holt, G. Panagiotidis, J. Lovell, H. Beasley, C. Henderson, D. Gordon, K. Auger, D. Wright, J. Collins, C. Raisen, L. Dyer, K. Leung, L. Robertson, K. Ambridge, D. Leongamornlert, S. McGuire, R. Gilderthorp, C. Griffiths, D. Manthravadi, S. Nichol, G. Barker, S. Whitehead, M. Kay, J. Brown, C. Murnane, E. Gray, M. Humphries, N. Sycamore, D. Barker, D. Saunders, J. Wallis, A. Babbage, S. Hammond, M. Mashreghi-Mohammadi, L. Barr, S. Martin, P. Wray, A. Ellington, N. Matthews, M. Ellwood, R. Woodmansey, G. Clark, J. D. Cooper, A. Tromans, D. Grafham, C. Skuce, R. Pandian, R. Andrews, E. Harrison, A. Kimberley, J. Garnett, N. Fosker, R. Hall, P. Garner, D. Kelly, C. Bird, S. Palmer, I. Gehring, A. Berger, C. M. Dooley, Z. Ersan-Urun, C. Eser, H. Geiger, M. Geisler, L. Karotki, A. Kirn, J. Konantz, M. Konantz, M. Oberlander, S. Rudolph-Geiger, M. Teucke, C. Lanz, G. Raddatz, K. Osoegawa, B. Zhu, A. Rapp, S. Widaa, C. Langford, F. Yang, S. C. Schuster, N. P. Carter, J. Harrow, Z. Ning, J. Herrero, S. M. J. Searle, A. Enright, R. Geisler, R. H. A. Plasterk, C. Lee, M. Westerfield, P. J. de Jong, L. I. Zon, J. H. Postlethwait, C. Nusslein-Vollhard, T. J. P. Hubbard, H. Roest Crolius, J. Rogers, and D. L. Stemple, "The zebrafish reference genome sequence and its relationship to the human genome," *Nature*, vol. 496, no. 7446, pp. 498–503, 2013. (Cited on page 24.)
- [247] L. Johnston, R. E. Ball, S. Acuff, J. Gaudet, A. Sornborger, and J. D. Lauderdale, "Electrophysiological recording in the brain of intact adult zebrafish," *Journal of visualized experiments : JoVE*, no. 81, p. e51065, 2013. (Cited on page 24.)
- [248] A. V. Kalueff, M. Gebhardt, A. M. Stewart, J. M. Cachat, M. Brimmer, J. S. Chawla, C. Craddock, E. J. Kyzar, A. Roth, S. Landsman, S. Gaikwad, K. Robinson, E. Baatrup, K. Tierney, A. Shamchuk, W. Norton, N. Miller, T. Nicolson, O. Braubach, C. P. Gilman, J. Pittman, D. B. Rosemberg, R. Gerlai, D. Echevarria, E. Lamb, S. C. F. Neuhaus, W. Weng, L. Bally-Cuif, and H. Schneider, "Towards a comprehensive catalog of zebrafish behavior 1.0 and beyond," *Zebrafish*, vol. 10, no. 1, pp. 70–86, 2013. (Cited on page 24.)
- [249] D. Studer, S. Zhao, X. Chai, P. Jonas, W. Graber, S. Nestel, and M. Frotscher, "Capture of activity-induced ultrastructural changes at synapses by high-pressure freezing of brain tissue," *Nature protocols*, vol. 9, no. 6, pp. 1480–1495, 2014. (Cited on page 24.)
- [250] H. Shoji, K. Takao, S. Hattori, and T. Miyakawa, "Contextual and cued fear conditioning test using a video analyzing system in mice," *Journal of visualized experiments : JoVE*, no. 85, 2014. (Cited on page 24.)
- [251] J. Kimble and D. Hirsh, "The postembryonic cell lineages of the hermaphrodite and male gonads in *Caenorhabditis elegans*," *Developmental Biology*, vol. 70, no. 2, pp. 396–417, 1979. (Cited on page 23.)
- [252] S. Brenner, "The genetics of *Caenorhabditis*

- elegans," *Genetics*, vol. 77, no. 1, pp. 71–94, 1974. (Cited on pages 23 and 63.)
- [253] J. E. Sulston and S. Brenner, "The DNA of *Caenorhabditis elegans*," *Genetics*, vol. 77, no. 1, pp. 95–104, 1974. (Cited on page 23.)
- [254] L. Byerly, S. Scherer, and R. L. Russell, "The life cycle of the nematode *Caenorhabditis elegans*. II. A simplified method for mutant characterization," *Developmental Biology*, vol. 51, no. 1, pp. 34–48, 1976. (Cited on page 23.)
- [255] L. Byerly, R. C. Cassada, and R. L. Russell, "The life cycle of the nematode *Caenorhabditis elegans*. I. Wild-type growth and reproduction," *Developmental Biology*, vol. 51, no. 1, pp. 23–33, 1976. (Cited on page 23.)
- [256] J. G. White, E. Southgate, J. N. Thomson, and S. Brenner, "The structure of the ventral nerve cord of *Caenorhabditis elegans*," *Philos Trans R Soc Lond B Biol Sci*, vol. 275, no. 938, pp. 327–348, 1976. (Cited on page 23.)
- [257] J. G. White, E. Southgate, J. N. Thomson, and S. Brenner, "The Structure of the Nervous System of the Nematode *Caenorhabditis elegans*," *Philosophical Transactions of the Royal Society of London. Series B, Biological Sciences*, vol. 314, no. 1165, pp. 1–340, 1986. (Cited on pages 23, 25, 28, 30, 33, 34, 130, 160, 161, 162, and 164.)
- [258] G. A. Nelson, W. W. Schubert, T. M. Marshall, E. R. Benton, and E. V. Benton, "Radiation effects in *Caenorhabditis elegans*, mutagenesis by high and low LET ionizing radiation," *Mutation research*, vol. 212, no. 2, pp. 181–192, 1989. (Cited on page 23.)
- [259] D. M. Raizen and L. Avery, "Electrical activity and behavior in the pharynx of *Caenorhabditis elegans*," *Neuron*, vol. 12, no. 3, pp. 483–495, 1994. (Cited on pages 23 and 227.)
- [260] "WormAtlas," 2002–2016. (Cited on pages 24, 29, 122, and 161.)
- [261] B. Szigeti, P. Gleeson, M. Vella, S. Khayrulin, A. Palyanov, J. Hokanson, M. Currie, M. Cantarelli, G. Idili, and S. Larson, "OpenWorm: an open-science approach to modeling *Caenorhabditis elegans*," *Frontiers in computational neuroscience*, vol. 8, p. 137, 2014. (Cited on page 25.)
- [262] E. Serrano-Saiz, R. J. Poole, T. Felton, F. Zhang, E. D. de La Cruz, and O. Hobert, "Modular control of glutamatergic neuronal identity in *C. elegans* by distinct homeodomain proteins," *Cell*, vol. 155, no. 3, pp. 659–673, 2013. (Cited on page 25.)
- [263] L. Pereira, P. Kratsios, E. Serrano-Saiz, H. Sheftel, A. E. Mayo, D. H. Hall, J. G. White, B. LeBoeuf, L. R. Garcia, U. Alon, and O. Hobert, "A cellular and regulatory map of the cholinergic nervous system of *C. elegans*," *eLife*, vol. 4, 2015. (Cited on page 25.)
- [264] M. Gendrel, E. G. Atlas, and O. Hobert, "A cellular and regulatory map of the GABAergic nervous system of *C. elegans*," *eLife*, vol. 5, 2016. (Cited on pages 25, 26, 33, and 162.)
- [265] N. Flames and O. Hobert, "Gene regulatory logic of dopamine neuron differentiation," *Nature*, vol. 458, no. 7240, pp. 885–889, 2009. (Cited on page 25.)
- [266] E. E. Hare and C. M. Loer, "Function and evolution of the serotonin-synthetic bas-1 gene and other aromatic amino acid decarboxylase genes in *Caenorhabditis*," *BMC evolutionary biology*, vol. 4, p. 24, 2004. (Cited on page 25.)
- [267] M. J. Alkema, M. Hunter-Ensor, N. Ringstad, and H. R. Horvitz, "Tyramine Functions independently of octopamine in the *Caenorhabditis elegans* nervous system," *Neuron*, vol. 46, no. 2, pp. 247–260, 2005. (Cited on pages 25 and 130.)
- [268] J. S. Duerr, D. L. Frisby, J. Gaskin, A. Duke, K. Asermely, D. Huddleston, L. E. Eiden, and J. B. Rand, "The *cat-1* gene of *Caenorhabditis elegans* encodes a vesicular monoamine transporter required for specific monoamine-dependent behaviors," *The Journal of neuroscience : the official journal of the Society for Neu-*

- rosience*, vol. 19, no. 1, pp. 72–84, 1999. (Cited on page 25.)
- [269] R. Pocock and O. Hobert, “Hypoxia activates a latent circuit for processing gustatory information in *C. elegans*,” *Nature neuroscience*, vol. 13, no. 5, pp. 610–614, 2010. (Cited on page 25.)
- [270] D. Tanaka, K. Furusawa, K. Kameyama, H. Okamoto, and M. Doi, “Melatonin signaling regulates locomotion behavior and homeostatic states through distinct receptor pathways in *Caenorhabditis elegans*,” *Neuropharmacology*, vol. 53, no. 1, pp. 157–168, 2007. (Cited on page 26.)
- [271] M. L. Migliori, A. Romanowski, S. H. Simonetta, D. Valdez, M. Guido, and D. A. Golombek, “Daily variation in melatonin synthesis and arylalkylamine N-acetyltransferase activity in the nematode *Caenorhabditis elegans*,” *Journal of pineal research*, vol. 53, no. 1, pp. 38–46, 2012. (Cited on page 26.)
- [272] L. S. Nelson, M. L. Rosoff, and C. Li, “Disruption of a neuropeptide gene, *flp-1*, causes multiple behavioral defects in *Caenorhabditis elegans*,” *Science*, vol. 281, no. 5383, pp. 1686–1690, 1998. (Cited on page 26.)
- [273] I. Hums, J. Riedl, F. Mende, S. Kato, H. S. Kaplan, R. Latham, M. Sonntag, L. Traunmüller, and M. Zimmer, “Regulation of two motor patterns enables the gradual adjustment of locomotion strategy in *Caenorhabditis elegans*,” *eLife*, vol. 5, 2016. (Cited on page 26.)
- [274] M. A. Lim, J. Chitturi, V. Laskova, J. Meng, D. Findeis, A. Wiekenberg, B. Mulcahy, L. Luo, Y. Li, Y. Lu, W. Hung, Y. Qu, C.-Y. Ho, D. Holmyard, N. Ji, R. McWhirter, A. D. Samuel, D. M. Miller, R. Schnabel, J. A. Calarco, and M. Zhen, “Neuroendocrine modulation sustains the *C. elegans* forward motor state,” *eLife*, vol. 5, 2016. (Cited on page 26.)
- [275] F. M. Gregoire, N. Chomiki, D. Kachinskas, and C. H. Warden, “Cloning and developmental regulation of a novel member of the insulin-like gene family in *Caenorhabditis elegans*,” *Biochemical and Biophysical Research Communications*, vol. 249, no. 2, pp. 385–390, 1998. (Cited on page 26.)
- [276] C. Li, L. S. Nelson, K. Kim, A. Nathoo, and A. C. Hart, “Neuropeptide gene families in the nematode *Caenorhabditis elegans*,” *Annals of the New York Academy of Sciences*, vol. 897, pp. 239–252, 1999. (Cited on page 26.)
- [277] A. N. Nathoo, R. A. Moeller, B. A. Westlund, and A. C. Hart, “Identification of neuropeptide-like protein gene families in *Caenorhabditiselegans* and other species,” *Proceedings of the National Academy of Sciences of the United States of America*, vol. 98, no. 24, pp. 14000–14005, 2001. (Cited on page 26.)
- [278] S. B. Pierce, M. Costa, R. Wisotzkey, S. Devadhar, S. A. Homburger, A. R. Buchman, K. C. Ferguson, J. Heller, D. M. Platt, A. A. Pasquinelli, L. X. Liu, S. K. Doberstein, and G. Ruvkun, “Regulation of DAF-2 receptor signaling by human insulin and *ins-1*, a member of the unusually large and diverse *C. elegans* insulin gene family,” *Genes & Development*, vol. 15, no. 6, pp. 672–686, 2001. (Cited on page 26.)
- [279] C. Li and K. Kim, “Family of FLP Peptides in *Caenorhabditis elegans* and Related Nematodes,” *Frontiers in endocrinology*, vol. 5, p. 150, 2014. (Cited on page 26.)
- [280] K. Kim and C. Li, “Expression and regulation of an FMRFamide-related neuropeptide gene family in *Caenorhabditis elegans*,” *The Journal of comparative neurology*, vol. 475, no. 4, pp. 540–550, 2004. (Cited on page 26.)
- [281] J. E. Mellem, P. J. Brockie, D. M. Madsen, and A. V. Maricq, “Action potentials contribute to neuronal signaling in *C. elegans*,” *Nature neuroscience*, vol. 11, no. 8, pp. 865–867, 2008. (Cited on page 27.)
- [282] S. R. Lockery, M. B. Goodman, and S. Fau-



- mont, "First report of action potentials in a *C. elegans* neuron is premature," *Nature neuroscience*, vol. 12, no. 4, pp. 365–6; author reply 366, 2009. (Cited on page 27.)
- [283] Z.-W. Wang, "Origin of quantal size variation and high-frequency miniature postsynaptic currents at the *Caenorhabditis elegans* neuromuscular junction," *Journal of neuroscience research*, vol. 88, no. 16, pp. 3425–3432, 2010. (Cited on page 27.)
- [284] Q. Liu, B. Chen, M. Yankova, D. K. Morrest, E. Maryon, A. R. Hand, M. L. Nonet, and Z.-W. Wang, "Presynaptic ryanodine receptors are required for normal quantal size at the *Caenorhabditis elegans* neuromuscular junction," *The Journal of neuroscience : the official journal of the Society for Neuroscience*, vol. 25, no. 29, pp. 6745–6754, 2005. (Cited on pages 27, 147, and 148.)
- [285] R. Janz, K. Hofmann, and T. C. Südhof, "SVOP, an evolutionarily conserved synaptic vesicle protein, suggests novel transport functions of synaptic vesicles," *The Journal of neuroscience : the official journal of the Society for Neuroscience*, vol. 18, no. 22, pp. 9269–9281, 1998. (Cited on page 27.)
- [286] D. Reigada, I. Díez-Pérez, P. Gorostiza, A. Verdaguier, Gómez de Aranda, Inmaculada, O. Pineda, J. Vilarrasa, J. Marsal, J. Blasi, J. Aleu, and C. Solsona, "Control of neurotransmitter release by an internal gel matrix in synaptic vesicles," *Proceedings of the National Academy of Sciences of the United States of America*, vol. 100, no. 6, pp. 3485–3490, 2003. (Cited on page 27.)
- [287] P. de Camilli, R. Cameron, and P. Greengard, "Synapsin I (protein I), a nerve terminal-specific phosphoprotein. I. Its general distribution in synapses of the central and peripheral nervous system demonstrated by immunofluorescence in frozen and plastic sections," *The Journal of Cell Biology*, vol. 96, no. 5, pp. 1337–1354, 1983. (Cited on page 28.)
- [288] O. Bloom, E. Evergren, N. Tomilin, O. Kjaerulff, P. Low, L. Brodin, V. A. Pieribone, P. Greengard, and O. Shupliakov, "Colocalization of synapsin and actin during synaptic vesicle recycling," *The Journal of Cell Biology*, vol. 161, no. 4, pp. 737–747, 2003. (Cited on page 28.)
- [289] H. T. Kao, B. Porton, S. Hilfiker, G. Stefani, V. A. Pieribone, R. DeSalle, and P. Greengard, "Molecular evolution of the synapsin gene family," *The Journal of experimental zoology*, vol. 285, no. 4, pp. 360–377, 1999. (Cited on page 28.)
- [290] Q. Ch'ng, D. Sieburth, J. M. Kaplan, and S. K. Kim, "Profiling Synaptic Proteins Identifies Regulators of Insulin Secretion and Lifespan," *PLoS Genetics*, vol. 4, no. 11, p. e1000283, 2008. (Cited on page 28.)
- [291] Y. Akbergenova and M. Bykhovskaia, "Synapsin maintains the reserve vesicle pool and spatial segregation of the recycling pool in *Drosophila* presynaptic boutons," *Brain Research*, vol. 1178, pp. 52–64, 2007. (Cited on page 28.)
- [292] M. Hosaka, R. E. Hammer, and T. C. Südhof, "A phospho-switch controls the dynamic association of synapsins with synaptic vesicles," *Neuron*, vol. 24, no. 2, pp. 377–387, 1999. (Cited on pages 28 and 150.)
- [293] J. N. Jovanovic, A. J. Czernik, A. A. Fienberg, P. Greengard, and T. S. Sihra, "Synapsins as mediators of BDNF-enhanced neurotransmitter release," *Nature neuroscience*, vol. 3, no. 4, pp. 323–329, 2000. (Cited on page 28.)
- [294] M. Borrell-Pages, J. M. Canals, F. P. Cordeliers, J. A. Parker, J. R. Pineda, G. Grange, E. A. Bryson, M. Guillermier, E. Hirsch, P. Hantraye, M. E. Cheetham, C. Neri, J. Alberch, E. Brouillet, F. Saudou, and S. Humbert, "Cystamine and cysteamine increase brain levels of BDNF in Huntington disease via HS1b and transglutaminase," *The Journal of clinical investigation*, vol. 116, no. 5, pp. 1410–1424, 2006. (Cited on page 28.)
- [295] P. Petrova, A. Raibekas, J. Pevsner, N. Vigo,

- M. Anafi, M. K. Moore, A. E. Peaire, V. Shridhar, D. I. Smith, J. Kelly, Y. Durocher, and J. W. Commissiong, "MANF: a new mesencephalic, astrocyte-derived neurotrophic factor with selectivity for dopaminergic neurons," *Journal of molecular neuroscience : MN*, vol. 20, no. 2, pp. 173–188, 2003. (Cited on page 28.)
- [296] S. J. Dixon and P. J. Roy, "Muscle arm development in *Caenorhabditis elegans*," *Development (Cambridge, England)*, vol. 132, no. 13, pp. 3079–3092, 2005. (Cited on page 28.)
- [297] J. M. Kramer, "Basement membranes: Worm-Book," 01.09.2005. (Cited on page 28.)
- [298] H. Hutter, B. E. Vogel, J. D. Plenefisch, C. R. Norris, R. B. Proenca, J. Spieth, C. Guo, S. Mastwal, X. Zhu, J. Scheel, and E. M. Hedgecock, "Conservation and novelty in the evolution of cell adhesion and extracellular matrix genes," *Science (New York, N.Y.)*, vol. 287, no. 5455, pp. 989–994, 2000. (Cited on page 28.)
- [299] B. D. Ackley, S. H. Kang, J. R. Crew, C. Suh, Y. Jin, and J. M. Kramer, "The basement membrane components nidogen and type XVIII collagen regulate organization of neuromuscular junctions in *Caenorhabditis elegans*," *The Journal of neuroscience : the official journal of the Society for Neuroscience*, vol. 23, no. 9, pp. 3577–3587, 2003. (Cited on page 28.)
- [300] W. C. Spencer, G. Zeller, J. D. Watson, S. R. Henz, K. L. Watkins, R. D. McWhirter, S. Petersen, V. T. Sreedharan, C. Widmer, J. Jo, V. Reinke, L. Petrella, S. Strome, S. E. von Stetina, M. Katz, S. Shaham, G. Rätsch, and D. M. Miller III, "A spatial and temporal map of *C. elegans* gene expression," *Genome research*, vol. 21, no. 2, pp. 325–341, 2011. (Cited on page 28.)
- [301] M. D. Nelson, T. Janssen, N. York, K. H. Lee, L. Schoofs, and D. M. Raizen, "FRPR-4 Is a G-Protein Coupled Neuropeptide Receptor That Regulates Behavioral Quiescence and Posture in *Caenorhabditis elegans*," *PLoS One*, vol. 10, no. 11, p. e0142938, 2015. (Cited on page 29.)
- [302] T. M. Barnes and S. Hekimi, "The *Caenorhabditis elegans* avermectin resistance and anesthetic response gene *unc-9* encodes a member of a protein family implicated in electrical coupling of excitable cells," *Journal of Neurochemistry*, vol. 69, no. 6, pp. 2251–2260, 1997. (Cited on page 29.)
- [303] Q. Wen, M. D. Po, E. Hulme, S. Chen, X. Liu, S. W. Kwok, M. Gershow, A. M. Leifer, V. Butler, C. Fang-Yen, T. Kawano, W. R. Schafer, G. Whitesides, M. Wyart, D. B. Chklovskii, M. Zhen, and A. D. T. Samuel, "Proprioceptive coupling within motor neurons drives *C. elegans* forward locomotion," *Neuron*, vol. 76, no. 4, pp. 750–761, 2012. (Cited on pages 29, 30, and 162.)
- [304] S. L. McIntire, E. Jorgensen, J. Kaplan, and H. R. Horvitz, "The GABAergic nervous system of *Caenorhabditis elegans*," *Nature*, vol. 364, no. 6435, pp. 337–341, 1993. (Cited on pages 29 and 30.)
- [305] M. Jospin, Y. B. Qi, T. M. Stawicki, T. Boulin, K. R. Schuske, H. R. Horvitz, J.-L. Bessereau, E. M. Jorgensen, and Y. Jin, "A neuronal acetylcholine receptor regulates the balance of muscle excitation and inhibition in *Caenorhabditis elegans*," *PLoS biology*, vol. 7, no. 12, p. e1000265, 2009. (Cited on pages 29 and 88.)
- [306] G. Safdie, J. F. Liewald, S. Kagan, E. Battat, A. Gottschalk, and M. Treinin, "RIC-3 phosphorylation enables dual regulation of excitation and inhibition of *Caenorhabditis elegans* muscle," *Molecular Biology of the Cell*, vol. 27, no. 19, pp. 2994–3003, 2016. (Cited on page 29.)
- [307] K. Schuske, A. A. Beg, and E. M. Jorgensen, "The GABA nervous system in *C. elegans*," *Trends in Neurosciences*, vol. 27, no. 7, pp. 407–414, 2004. (Cited on page 30.)
- [308] L. E. Waggoner, G. Zhou, R. W. Schafer, and W. R. Schafer, "Control of Alternative Behavioral States by Serotonin in *Caenorhabditis*

- elegans," *Neuron*, vol. 21, no. 1, pp. 203–214, 1998. (Cited on page 30.)
- [309] J. S. Duerr, H.-P. Han, S. D. Fields, and J. B. Rand, "Identification of major classes of cholinergic neurons in the nematode *Caenorhabditis elegans*," *The Journal of comparative neurology*, vol. 506, no. 3, pp. 398–408, 2008. (Cited on page 30.)
- [310] G. Haspel and M. J. O'Donovan, "A perimotor framework reveals functional segmentation in the motoneuronal network controlling locomotion in *Caenorhabditis elegans*," *The Journal of neuroscience : the official journal of the Society for Neuroscience*, vol. 31, no. 41, pp. 14611–14623, 2011. (Cited on page 30.)
- [311] M. Chalfie, J. E. Sulston, J. G. White, E. Southgate, J. N. Thomson, and S. Brenner, "The neural circuit for touch sensitivity in *Caenorhabditis elegans*," *The Journal of neuroscience : the official journal of the Society for Neuroscience*, vol. 5, no. 4, pp. 956–964, 1985. (Cited on pages 30 and 164.)
- [312] J. M. Gray, J. J. Hill, and C. I. Bargmann, "A circuit for navigation in *Caenorhabditis elegans*," *Proceedings of the National Academy of Sciences of the United States of America*, vol. 102, no. 9, pp. 3184–3191, 2005. (Cited on pages 31, 32, 33, 162, and 164.)
- [313] S. W. Flavell, N. Pokala, E. Z. Macosko, D. R. Albrecht, J. Larsch, and C. I. Bargmann, "Serotonin and the Neuropeptide PDF Initiate and Extend Opposing Behavioral States in *C. elegans*," *Cell*, vol. 154, no. 5, pp. 1023–1035, 2013. (Cited on page 31.)
- [314] B. Bentley, R. Branicky, C. L. Barnes, E. T. Bullmore, P. E. Vértés, and W. R. Schafer, "The multilayer connectome of *Caenorhabditis elegans*." (Cited on page 31.)
- [315] C. Eastman, H. R. Horvitz, and Y. Jin, "Coordinated transcriptional regulation of the unc-25 glutamic acid decarboxylase and the unc-47 GABA vesicular transporter by the *Caenorhabditis elegans* UNC-30 homeodomain protein," *The Journal of neuroscience : the official journal of the Society for Neuroscience*, vol. 19, no. 15, pp. 6225–6234, 1999. (Cited on page 33.)
- [316] E. L. Tsalik and O. Hobert, "Functional mapping of neurons that control locomotory behavior in *Caenorhabditis elegans*," *Journal of neurobiology*, vol. 56, no. 2, pp. 178–197, 2003. (Cited on pages 33 and 160.)
- [317] P. McNamara, I. Capellini, E. Harris, C. L. Nunn, R. A. Barton, and B. Preston, "The Phylogeny of Sleep Database: A New Resource for Sleep Scientists," *The open sleep journal*, vol. 1, pp. 11–14, 2008. (Cited on page 35.)
- [318] F. Strumwasser, "The cellular basis of behavior in *Aplysia*," *Journal of psychiatric research*, vol. 8, no. 3, pp. 237–257, 1971. (Cited on page 35.)
- [319] E. R. Brown, S. Piscopo, R. de Stefano, and A. Giuditta, "Brain and behavioural evidence for rest-activity cycles in *Octopus vulgaris*," *Behavioural brain research*, vol. 172, no. 2, pp. 355–359, 2006. (Cited on page 35.)
- [320] K. Mendoza-Angeles, A. Cabrera, J. Hernandez-Falcon, and F. Ramon, "Slow waves during sleep in crayfish: a time-frequency analysis," *Journal of Neuroscience Methods*, vol. 162, no. 1-2, pp. 264–271, 2007. (Cited on page 35.)
- [321] J. C. Hendricks, A. Sehgal, and A. I. Pack, "The need for a simple animal model to understand sleep," *Progress in Neurobiology*, vol. 61, no. 4, pp. 339–351, 2000. (Cited on page 35.)
- [322] C. Liu, P. R. Haynes, N. C. Donelson, S. Aharon, and L. C. Griffith, "Sleep in Populations of *Drosophila Melanogaster* (1,2,3)," *eNeuro*, vol. 2, no. 4, 2015. (Cited on page 35.)
- [323] I. V. Zhdanova, S. Y. Wang, O. U. Leclair, and N. P. Danilova, "Melatonin promotes sleep-like state in zebrafish," *Brain Research*, vol. 903, no. 1-2, pp. 263–268, 2001. (Cited on page 35.)

- [324] W. F. Flanigan, JR, C. P. Knight, K. M. Hartse, and A. Rechtschaffen, "Sleep and wakefulness in chelonian reptiles. I. The box turtle, *Terrapene carolina*," *Archives italiennes de biologie*, vol. 112, no. 3, pp. 227–252, 1974. (Cited on page 35.)
- [325] W. F. Flanigan, JR, "Sleep and wakefulness in chelonian reptiles. II. The red-footed tortoise, *Geochelone carbonaria*," *Archives italiennes de biologie*, vol. 112, no. 3, pp. 253–277, 1974. (Cited on page 35.)
- [326] J. A. Hobson, "Electrographic correlates of behavior in the frog with special reference to sleep," *Electroencephalography and clinical neurophysiology*, vol. 22, no. 2, pp. 113–121, 1967. (Cited on page 35.)
- [327] T. C. n. Roth, J. A. Lesku, C. J. Amlaner, and S. L. Lima, "A phylogenetic analysis of the correlates of sleep in birds," *Journal of sleep research*, vol. 15, no. 4, pp. 395–402, 2006. (Cited on page 35.)
- [328] T. Allison and D. V. Cicchetti, "Sleep in mammals: ecological and constitutional correlates," *Science (New York, N.Y.)*, vol. 194, no. 4266, pp. 732–734, 1976. (Cited on page 35.)
- [329] D. Martinez-Gonzalez, J. A. Lesku, and N. C. Rattenborg, "Increased EEG spectral power density during sleep following short-term sleep deprivation in pigeons (*Columba livia*): evidence for avian sleep homeostasis," *Journal of sleep research*, vol. 17, no. 2, pp. 140–153, 2008. (Cited on page 35.)
- [330] D. M. Raizen, J. E. Zimmerman, M. H. Maycock, U. D. Ta, Y.-j. You, M. V. Sundaram, and A. I. Pack, "Lethargus is a *Caenorhabditis elegans* sleep-like state," *Nature*, vol. 451, no. 7178, pp. 569–572, 2008. (Cited on page 35.)
- [331] A. J. Hill, R. Mansfield, Lopez, Jessie M. N. G., D. M. Raizen, and C. van Buskirk, "Cellular stress induces a protective sleep-like state in *C. elegans*," *Current biology : CB*, vol. 24, no. 20, pp. 2399–2405, 2014. (Cited on page 35.)
- [332] S. Iwanir, N. Tramm, S. Nagy, C. Wright, D. Ish, and D. Biron, "The microarchitecture of *C. elegans* behavior during lethargus: homeostatic bout dynamics, a typical body posture, and regulation by a central neuron," *Sleep*, vol. 36, no. 3, pp. 385–395, 2013. (Cited on page 35.)
- [333] M. Nelson, N. Trojanowski, J. George-Raizen, C. Smith, C.-C. Yu, C. Fang-Yen, and D. Raizen, "The neuropeptide NLP-22 regulates a sleep-like state in *Caenorhabditis elegans*," *Nature Communications*, vol. 4, 2013. (Cited on page 35.)
- [334] I. Mertens, I. Clinckspoor, T. Janssen, R. Nachman, and L. Schoofs, "FMR-Famide related peptide ligands activate the *Caenorhabditis elegans* orphan GPCR Y59H11AL.1," *Peptides*, vol. 27, no. 6, pp. 1291–1296, 2006. (Cited on page 35.)
- [335] M. Turek, I. Lewandrowski, and H. Bringmann, "An AP2 Transcription Factor Is Required for a Sleep-Active Neuron to Induce Sleep-like Quiescence in *C. elegans*," *Current Biology*, 2013. (Cited on pages 35, 135, 155, 156, 159, and 165.)
- [336] M. Turek, J. Besseling, J.-P. Spies, S. König, and H. Bringmann, "Sleep-active neuron specification and sleep induction require FLP-11 neuropeptides to systemically induce sleep," *eLife*, vol. 5, 2016. (Cited on pages 35, 36, 155, 156, 160, and 163.)
- [337] I. Mertens, A. Vandingenen, T. Meeusen, T. Janssen, W. Luyten, R. J. Nachman, A. de Loof, and L. Schoofs, "Functional characterization of the putative orphan neuropeptide G-protein coupled receptor C26F1.6 in *Caenorhabditis elegans*," *FEBS letters*, vol. 573, no. 1-3, pp. 55–60, 2004. (Cited on pages 35 and 160.)
- [338] D. E. Lowery, T. G. Geary, T. M. Kubiak, and J. Larsch, 2003. (Cited on page 35.)
- [339] L. Appelbaum, G. X. Wang, G. S. Maro, R. Mori, A. Tovin, W. Marin, T. Yoko-

- gawa, K. Kawakami, S. J. Smith, Y. Gothilf, E. Mignot, and P. Mourrain, "Sleep-wake regulation and hypocretin-melatonin interaction in zebrafish," *Proceedings of the National Academy of Sciences of the United States of America*, vol. 106, no. 51, pp. 21942–21947, 2009. (Cited on pages 35 and 165.)
- [340] K. S. Eriksson, O. A. Sergeeva, H. L. Haas, and O. Selbach, "Orexins/hypocretins and aminergic systems," *Acta physiologica (Oxford, England)*, vol. 198, no. 3, pp. 263–275, 2010. (Cited on pages 35 and 165.)
- [341] C. B. Saper, T. C. Chou, and T. E. Scammell, "The sleep switch: hypothalamic control of sleep and wakefulness," *Trends in Neurosciences*, vol. 24, no. 12, pp. 726–731, 2001. (Cited on pages 35 and 165.)
- [342] S. E. Gaus, R. E. Strecker, B. A. Tate, R. A. Parker, and C. B. Saper, "Ventrolateral preoptic nucleus contains sleep-active, galaninergic neurons in multiple mammalian species," *Neuroscience*, vol. 115, no. 1, pp. 285–294, 2002. (Cited on pages 35 and 165.)
- [343] I. Gvilia, "Underlying Brain Mechanisms that Regulate Sleep–Wakefulness Cycles," in *Science of awakening* (A. Clow and L. Thorn, eds.), vol. 93 of *International Review of Neurobiology*, pp. 1–21, s.l.: Elsevier textbooks, 2010. (Cited on page 35.)
- [344] K. M. Parisky, J. Agosto, S. R. Pulver, Y. Shang, E. Kuklin, J. J. L. Hodge, K. Kang, X. Liu, P. A. Garrity, M. Rosbash, and L. C. Griffith, "PDF cells are a GABA-responsive wake-promoting component of the *Drosophila* sleep circuit," *Neuron*, vol. 60, no. 4, pp. 672–682, 2008. (Cited on page 36.)
- [345] S. Choi, M. Chatzigeorgiou, K. P. Taylor, W. R. Schafer, and J. M. Kaplan, "Analysis of NPR-1 reveals a circuit mechanism for behavioral quiescence in *C. elegans*," *Neuron*, vol. 78, no. 5, pp. 869–880, 2013. (Cited on page 36.)
- [346] D. Chen, K. P. Taylor, Q. Hall, and J. M. Kaplan, "The Neuropeptides FLP-2 and PDF-1 act in Concert to Arouse *Caenorhabditis elegans* Locomotion," *Genetics*, 2016. (Cited on page 36.)
- [347] E. L. Tsalik, T. Niacaris, A. S. Wenick, K. Pau, L. Avery, and O. Hobert, "LIM homeobox gene-dependent expression of biogenic amine receptors in restricted regions of the *C. elegans* nervous system," *Developmental biology*, vol. 263, no. 1, pp. 81–102, 2003. (Cited on pages 36, 131, 135, and 156.)
- [348] K. Singh, J. Y. Ju, M. B. Walsh, M. A. DiIorio, and A. C. Hart, "Deep conservation of genes required for both *Drosophila melanogaster* and *Caenorhabditis elegans* sleep includes a role for dopaminergic signaling," *Sleep*, vol. 37, no. 9, pp. 1439–1451, 2014. (Cited on page 36.)
- [349] B. Olde and W. R. McCombie, "Molecular cloning and functional expression of a serotonin receptor from *Caenorhabditis elegans*," *Journal of molecular neuroscience : MN*, vol. 8, no. 1, pp. 53–62, 1997. (Cited on pages 36, 140, 156, and 157.)
- [350] E. Hamid, E. Church, C. A. Wells, Z. Zurawski, H. E. Hamm, and S. Alford, "Modulation of neurotransmission by GPCRs is dependent upon the microarchitecture of the primed vesicle complex," *The Journal of neuroscience : the official journal of the Society for Neuroscience*, vol. 34, no. 1, pp. 260–274, 2014. (Cited on page 36.)
- [351] N. A. Baker, D. Sept, S. Joseph, M. J. Holst, and J. A. McCammon, "Electrostatics of nanosystems: application to microtubules and the ribosome," *Proceedings of the National Academy of Sciences of the United States of America*, vol. 98, no. 18, pp. 10037–10041, 2001. (Cited on pages 54 and 131.)
- [352] M. Krzywinski, J. Schein, I. Birol, J. Connors, R. Gascoyne, D. Horsman, S. J. Jones, and M. A. Marra, "Circos: an information aesthetic for comparative genomics," *Genome research*, vol. 19, no. 9, pp. 1639–1645, 2009. (Cited on pages 54 and 73.)
- [353] J. Schindelin, I. Arganda-Carreras, E. Frise,

- V. Kaynig, M. Longair, T. Pietzsch, S. Preibisch, C. Rueden, S. Saalfeld, B. Schmid, J.-Y. Tinevez, D. J. White, V. Hartenstein, K. Eliceiri, P. Tomancak, and A. Cardona, "Fiji: an open-source platform for biological-image analysis," *Nature methods*, vol. 9, no. 7, pp. 676–682, 2012. (Cited on page 54.)
- [354] E. Afgan, D. Baker, van den Beek, Marius, D. Blankenberg, D. Bouvier, M. Čech, J. Chilton, D. Clements, N. Coraor, C. Eberhard, B. Grüning, A. Guerler, J. Hillman-Jackson, G. von Kuster, E. Rasche, N. Soranzo, N. Turaga, J. Taylor, A. Nekrutenko, and J. Goecks, "The Galaxy platform for accessible, reproducible and collaborative biomedical analyses: 2016 update," *Nucleic acids research*, 2016. (Cited on pages 54 and 72.)
- [355] Y. Xue, J. Ren, X. Gao, C. Jin, L. Wen, and X. Yao, "GPS 2.0, a tool to predict kinase-specific phosphorylation sites in hierarchy," *Molecular & cellular proteomics : MCP*, vol. 7, no. 9, pp. 1598–1608, 2008. (Cited on pages 54 and 148.)
- [356] C. A. Schneider, W. S. Rasband, and K. W. Eliceiri, "NIH Image to ImageJ: 25 years of image analysis," *Nature methods*, vol. 9, no. 7, pp. 671–675, 2012. (Cited on page 54.)
- [357] J. T. Robinson, H. Thorvaldsdóttir, W. Winckler, M. Guttman, E. S. Lander, G. Getz, and J. P. Mesirov, "Integrative genomics viewer," *Nature biotechnology*, vol. 29, no. 1, pp. 24–26, 2011. (Cited on page 54.)
- [358] M. R. Berthold, N. Cebon, F. Dill, T. R. Gabriel, T. Kötter, T. Meinl, P. Ohl, C. Sieb, K. Thiel, and B. Wiswedel, "KNIME: The Konstanz Information Miner," in *Data Analysis, Machine Learning and Applications* (C. Preisach, H. Burkhardt, L. Schmidt-Thieme, and R. Decker, eds.), Studies in Classification, Data Analysis, and Knowledge Organization, pp. 319–326, Berlin and Heidelberg: Springer Berlin Heidelberg, 2008. (Cited on page 54.)
- [359] A. Edelstein, N. Amodaj, K. Hoover, R. Vale, and N. Stuurman, "Computer control of microscopes using microManager," *Current protocols in molecular biology*, vol. Chapter 14, p. Unit14.20, 2010. (Cited on page 54.)
- [360] J. Vivek, "Neuroptikon: a customizable tool for dynamic, multi-scale visualization of complex neural circuits," *Frontiers in Neuroscience*, vol. 4, 2010. (Cited on page 54.)
- [361] T. J. Dolinsky, J. E. Nielsen, J. A. McCammon, and N. A. Baker, "PDB2PQR: an automated pipeline for the setup of Poisson-Boltzmann electrostatics calculations," *Nucleic acids research*, vol. 32, no. Web Server issue, pp. W665–7, 2004. (Cited on pages 54 and 132.)
- [362] T. J. Dolinsky, P. Czodrowski, H. Li, J. E. Nielsen, J. H. Jensen, G. Klebe, and N. A. Baker, "PDB2PQR: expanding and upgrading automated preparation of biomolecular structures for molecular simulations," *Nucleic acids research*, vol. 35, no. Web Server issue, pp. W522–5, 2007. (Cited on pages 54 and 132.)
- [363] M. J. Sippl, "Recognition of errors in three-dimensional structures of proteins," *Proteins*, vol. 17, no. 4, pp. 355–362, 1993. (Cited on pages 54 and 131.)
- [364] M. Wiederstein and M. J. Sippl, "ProSA-web: interactive web service for the recognition of errors in three-dimensional structures of proteins," *Nucleic acids research*, vol. 35, no. Web Server issue, pp. W407–10, 2007. (Cited on pages 54 and 131.)
- [365] R. C. Team, "R: A Language and Environment for Statistical Computing," 2015. (Cited on page 54.)
- [366] J. Ahringer, "Reverse genetics: WormBook," 06.04.2006. (Cited on page 55.)
- [367] T. Stiernagle, "Maintenance of *C. elegans*: WormBook," 11.02.2006. (Cited on page 63.)
- [368] I. A. Hope, *C. elegans: A practical approach*,

- vol. PAS/213 of *The practical approach series*. Oxford and New York: Oxford University Press, 1999. (Cited on page 65.)
- [369] D. T. Stinchcomb, J. E. Shaw, S. H. Carr, and D. Hirsh, "Extrachromosomal DNA transformation of *Caenorhabditis elegans*," *Mol Cell Biol*, vol. 5, no. 12, pp. 3484–3496, 1985. (Cited on page 65.)
- [370] E. M. Jorgensen and S. E. Mango, "The art and design of genetic screens: *Caenorhabditis elegans*," *Nature Reviews Genetics*, vol. 3, no. 5, pp. 356–369, 2002. (Cited on page 67.)
- [371] S. Zhang, D. Banerjee, and J. R. Kuhn, "Isolation and culture of larval cells from *C. elegans*," *PLoS one*, vol. 6, no. 4, p. e19505, 2011. (Cited on page 67.)
- [372] S. Zhang and J. R. Kuhn, "Cell isolation and culture: WormBook," 21.02.2013. (Cited on page 67.)
- [373] R. S. Kamath, A. G. Fraser, Y. Dong, G. Poulin, R. Durbin, M. Gotta, A. Kanapin, N. Le Bot, S. Moreno, M. Sohrmann, D. P. Welchman, P. Zipperlen, and J. Ahringer, "Systematic functional analysis of the *Caenorhabditis elegans* genome using RNAi," *Nature*, vol. 421, no. 6920, pp. 231–237, 2003. (Cited on page 67.)
- [374] R. Ghosh and S. W. Emmons, "Episodic swimming behavior in the nematode *C. elegans*," *The Journal of experimental biology*, vol. 211, no. Pt 23, pp. 3703–3711, 2008. (Cited on page 69.)
- [375] J. N. Stirman, M. Crane, S. J. Husson, A. Gottschalk, and H. Lu, "A multispectral optical illumination system with precise spatiotemporal control for the manipulation of optogenetic reagents," *Nature protocols*, vol. 7, no. 2, pp. 207–220, 2012. (Cited on pages 69, 229, and 237.)
- [376] N. A. Swierczek, A. C. Giles, C. H. Rankin, and R. A. Kerr, "High-throughput behavioral analysis in *C. elegans*," *Nature Methods*, 2011. (Cited on page 70.)
- [377] S. Faumont, G. Rondeau, T. R. Thiele, K. J. Lawton, K. E. McCormick, M. Sottile, O. Griesbeck, E. S. Heckscher, W. M. Roberts, C. Q. Doe, and S. R. Lockery, "An Image-Free Opto-Mechanical System for Creating Virtual Environments and Imaging Neuronal Activity in Freely Moving *Caenorhabditis elegans*," *PLoS one*, vol. 6, no. 9, p. e24666, 2011. (Cited on page 70.)
- [378] T. Giorgino, "Computing and Visualizing Dynamic Time Warping Alignments in R: The dtw Package," *Journal of Statistical Software*, vol. 31, no. 7, 2009. (Cited on page 72.)
- [379] G. Minevich, D. S. Park, D. Blankenberg, R. J. Poole, and O. Hobert, "CloudMap: A Cloud-Based Pipeline for Analysis of Mutant Genome Sequences," *Genetics*, vol. 192, no. 4, pp. 1249–1269, 2012. (Cited on page 72.)
- [380] A. Kalderimis, R. Lyne, D. Butano, S. Contrino, M. Lyne, J. Heimbach, F. Hu, R. Smith, R. Stepan, J. Sullivan, and G. Micklem, "InterMine: extensive web services for modern biology," *Nucleic acids research*, vol. 42, no. Web Server issue, pp. W468–72, 2014. (Cited on page 73.)
- [381] F. Supek, M. Bosnjak, N. Skunca, and T. Smuc, "REVIGO summarizes and visualizes long lists of gene ontology terms," *PLoS One*, vol. 6, no. 7, p. e21800, 2011. (Cited on page 73.)
- [382] P. Resnik, "Semantic Similarity in a Taxonomy: An Information-Based Measure and its Application to Problems of Ambiguity in Natural Language," *ArXiv e-prints*, 2011. (Cited on page 73.)
- [383] A. Field, J. Miles, and Z. Field, *Discovering statistics using R*. Los Angeles, Calif.: Sage, reprint ed., 2013. (Cited on page 75.)
- [384] J. Cohen, *Statistical Power Analysis for the Behavioral Sciences*. Hoboken: Taylor and Francis, 2nd ed. ed., 1988. (Cited on page 77.)
- [385] G. Cumming and S. Finch, "A Primer on the Understanding, Use, and Calculation of Confidence Intervals that are Based on Central

- and Noncentral Distributions," *Educational and Psychological Measurement*, vol. 61, no. 4, pp. 532–574, 2001. (Cited on page 77.)
- [386] C. Li and K. Kim, "Neuropeptides: Worm-Book," 25.09.2008. (Cited on page 80.)
- [387] Greg J Stephens, Bethany Johnson-Kerner, William Bialek, and William S Ryu, "Dimensionality and dynamics in the behavior of *C. elegans*," *PLoS Computational Biology*, vol. 4, no. 4, p. e1000028, 2008. (Cited on page 81.)
- [388] S. L. Edwards, N. K. Charlie, M. C. Milfort, B. S. Brown, C. N. Gravlin, J. E. Knecht, and K. G. Miller, "A novel molecular solution for ultraviolet light detection in *Caenorhabditis elegans*," *PLoS biology*, vol. 6, no. 8, p. e198, 2008. (Cited on page 84.)
- [389] T. M. Stawicki, S. Takayanagi-Kiya, K. Zhou, and Y. Jin, "Neuropeptides function in a homeostatic manner to modulate excitation-inhibition imbalance in *C. elegans*," *PLoS genetics*, vol. 9, no. 5, p. e1003472, 2013. (Cited on pages 88 and 89.)
- [390] A. J. Berger, A. C. Hart, and J. M. Kaplan, "G alpha-induced neurodegeneration in *Caenorhabditis elegans*," *The Journal of neuroscience: the official journal of the Society for Neuroscience*, vol. 18, no. 8, pp. 2871–2880, 1998. (Cited on pages 89 and 153.)
- [391] M. Tabish, R. A. Clegg, H. H. Rees, and M. J. Fisher, "Organization and alternative splicing of the *Caenorhabditis elegans* cAMP-dependent protein kinase catalytic-subunit gene (*kin-1*)," *The Biochemical journal*, vol. 339 (Pt 1), pp. 209–216, 1999. (Cited on page 89.)
- [392] M. W. Pastok, M. C. Prescott, C. Dart, P. Murray, H. H. Rees, and M. J. Fisher, "Structural diversity of the cAMP-dependent protein kinase regulatory subunit in *Caenorhabditis elegans*," *Cellular signalling*, vol. 25, no. 1, pp. 168–177, 2013. (Cited on page 89.)
- [393] S. Herrgard, P. Jambeck, S. S. Taylor, and S. Subramaniam, "Domain architecture of a *Caenorhabditis elegans* AKAP suggests a novel AKAP function," *FEBS letters*, vol. 486, no. 2, pp. 107–111, 2000. (Cited on page 89.)
- [394] D. Sieburth, J. M. Madison, and J. M. Kaplan, "PKC-1 regulates secretion of neuropeptides," *Nature neuroscience*, vol. 10, no. 1, pp. 49–57, 2007. (Cited on page 92.)
- [395] D. Touroutine, R. M. Fox, S. E. von Stetina, A. Burdina, D. M. r. Miller, and J. E. Richmond, "*acr-16* encodes an essential subunit of the levamisole-resistant nicotinic receptor at the *Caenorhabditis elegans* neuromuscular junction," *The Journal of biological chemistry*, vol. 280, no. 29, pp. 27013–27021, 2005. (Cited on page 95.)
- [396] R. Bhattacharya, D. Touroutine, B. Barbagallo, J. Climer, C. M. Lambert, C. M. Clark, M. J. Alkema, M. M. Francis, and L. Schoofs, "A Conserved Dopamine-Cholecystokinin Signaling Pathway Shapes Context-Dependent *Caenorhabditis elegans* Behavior," *PLoS Genetics*, vol. 10, no. 8, p. e1004584, 2014. (Cited on page 95.)
- [397] M. Kittelmann, J. F. Liewald, J. Hegemann, C. Schultheis, M. Brauner, W. Steuer Costa, S. Wabnig, S. Eimer, and A. Gottschalk, "In vivo synaptic recovery following optogenetic hyperstimulation," *Proceedings of the National Academy of Sciences of the United States of America*, vol. 110, no. 32, pp. E3007–16, 2013. (Cited on pages 101 and 312.)
- [398] Y. Akbergenova and M. Bykhovskaia, "Synapsin regulates vesicle organization and activity-dependent recycling at *Drosophila* motor boutons," *Neuroscience*, vol. 170, no. 2, pp. 441–452, 2010. (Cited on page 111.)
- [399] N. Bhatla and H. R. Horvitz, "Light and hydrogen peroxide inhibit *C. elegans* Feeding through gustatory receptor orthologs and pharyngeal neurons," *Neuron*, vol. 85, no. 4, pp. 804–818, 2015. (Cited on page 126.)
- [400] J. K. Pirri, A. D. McPherson, J. L. Donnelly, M. M. Francis, and M. J. Alkema, "A Tyramine-Gated Chloride Channel Coordinates Distinct Motor Programs of a *Caenorhabditis elegans* Escape Response," *Neuron*,



- vol. 62, no. 4, pp. 526–538, 2009. (Cited on page 130.)
- [401] B. L. Chen, David H Hall, and Dmitri B Chklovskii, “Wiring optimization can relate neuronal structure and function,” *Proceedings of the National Academy of Sciences of the United States of America*, vol. 103, no. 12, pp. 4723–4728, 2006. (Cited on page 130.)
- [402] “UniProt: a hub for protein information,” *Nucleic acids research*, vol. 43, no. Database issue, pp. D204–12, 2015. (Cited on pages 131 and 148.)
- [403] O. Hobert, K. Tessmar, and G. Ruvkun, “The *Caenorhabditis elegans* lim-6 LIM homeobox gene regulates neurite outgrowth and function of particular GABAergic neurons,” *Development (Cambridge, England)*, vol. 126, no. 7, pp. 1547–1562, 1999. (Cited on pages 131, 133, and 135.)
- [404] J. Haas, S. Roth, K. Arnold, F. Kiefer, T. Schmidt, L. Bordoli, and T. Schwede, “The Protein Model Portal—a comprehensive resource for protein structure and model information,” *Database : the journal of biological databases and curation*, vol. 2013, p. bat031, 2013. (Cited on page 131.)
- [405] M. Biasini, S. Bienert, A. Waterhouse, K. Arnold, G. Studer, T. Schmidt, F. Kiefer, T. Gallo Cassarino, M. Bertoni, L. Bordoli, and T. Schwede, “SWISS-MODEL: modelling protein tertiary and quaternary structure using evolutionary information,” *Nucleic acids research*, vol. 42, no. Web Server issue, pp. W252–8, 2014. (Cited on page 131.)
- [406] N. Fernandez-Fuentes, C. J. Madrid-Aliste, B. K. Rai, J. E. Fajardo, and A. Fiser, “M4T: a comparative protein structure modeling server,” *Nucleic acids research*, vol. 35, no. Web Server issue, pp. W363–8, 2007. (Cited on page 131.)
- [407] N. Fernandez-Fuentes, B. K. Rai, C. J. Madrid-Aliste, J. E. Fajardo, and A. Fiser, “Comparative protein structure modeling by combining multiple templates and optimizing sequence-to-structure alignments,” *Bioinformatics (Oxford, England)*, vol. 23, no. 19, pp. 2558–2565, 2007. (Cited on page 131.)
- [408] D. Rykunov, E. Steinberger, C. J. Madrid-Aliste, and A. Fiser, “Improved scoring function for comparative modeling using the M4T method,” *Journal of structural and functional genomics*, vol. 10, no. 1, pp. 95–99, 2009. (Cited on page 131.)
- [409] J. Vahokoski, M. R. Groves, V. Pogenberg, and M. Wilmanns, *POU protein:DNA complex*. 2010. (Cited on page 131.)
- [410] A. Marchler-Bauer, M. K. Derbyshire, N. R. Gonzales, S. Lu, F. Chitsaz, L. Y. Geer, R. C. Geer, J. He, M. Gwadz, D. I. Hurwitz, C. J. Lanczycki, F. Lu, G. H. Marchler, J. S. Song, N. Thanki, Z. Wang, R. A. Yamashita, D. Zhang, C. Zheng, and S. H. Bryant, “CDD: NCBI’s conserved domain database,” *Nucleic acids research*, vol. 43, no. Database issue, pp. D222–6, 2015. (Cited on page 132.)
- [411] J. M. Gruschus, D. H. Tsao, L. H. Wang, M. Nirenberg, and J. A. Ferretti, “Interactions of the vnd/NK-2 homeodomain with DNA by nuclear magnetic resonance spectroscopy: basis of binding specificity,” *Biochemistry*, vol. 36, no. 18, pp. 5372–5380, 1997. (Cited on page 132.)
- [412] W. R. Schafer, “Neurophysiological methods in *C. elegans*: an introduction: WormBook,” 02.06.2006. (Cited on page 134.)
- [413] S. Sarin, C. Antonio, B. Tursun, and O. Hobert, “The *C. elegans* Tailless/TLX transcription factor nhr-67 controls neuronal identity and left/right asymmetric fate diversification,” *Development (Cambridge, England)*, vol. 136, no. 17, pp. 2933–2944, 2009. (Cited on page 135.)
- [414] Z. F. Altun, B. Chen, Z.-W. Wang, and D. H. Hall, “High resolution map of *Caenorhabditis elegans* gap junction proteins,” *Developmental Dynamics*, vol. 238, no. 8, pp. 1936–1950, 2009. (Cited on pages 135 and 162.)
- [415] S. L. McIntire, E. Jorgensen, and H. R.

- Horvitz, "Genes required for GABA function in *Caenorhabditis elegans*," *Nature*, vol. 364, no. 6435, pp. 334–337, 1993. (Cited on page 135.)
- [416] M. Koga, M. Take-uchi, T. Tameishi, and Y. Ohshima, "Control of DAF-7 TGF-(alpha) expression and neuronal process development by a receptor tyrosine kinase KIN-8 in *Caenorhabditis elegans*," *Development (Cambridge, England)*, vol. 126, no. 23, pp. 5387–5398, 1999. (Cited on page 135.)
- [417] C. Abraham, L. Bai, and R. E. Leube, "Synaptogyrin-dependent modulation of synaptic neurotransmission in *Caenorhabditis elegans*," *Neuroscience*, vol. 190, pp. 75–88, 2011. (Cited on page 136.)
- [418] S. Suo, N. Sasagawa, and S. Ishiura, "Identification of a dopamine receptor from *Caenorhabditis elegans*," *Neuroscience letters*, vol. 319, no. 1, pp. 13–16, 2002. (Cited on page 140.)
- [419] S. Sanyal, R. F. Wintle, K. S. Kindt, W. M. Nuttley, R. Arvan, P. Fitzmaurice, E. Bigras, D. C. Merz, T. E. Hebert, D. van der Kooy, W. R. Schafer, J. G. Culotti, and H. H. M. van Tol, "Dopamine modulates the plasticity of mechanosensory responses in *Caenorhabditis elegans*," *The EMBO journal*, vol. 23, no. 2, pp. 473–482, 2004. (Cited on page 140.)
- [420] J. Mendel, H. Korswagen, K. Liu, Y. Hajdu-Cronin, M. Simon, R. Plasterk, and P. Sternberg, "Participation of the protein Go in multiple aspects of behavior in *C. elegans*," *Science*, vol. 267, no. 5204, pp. 1652–1655, 1995. (Cited on page 145.)
- [421] P. C. Pugh, S. S. Jayakar, and J. F. Margiotta, "PACAP/PAC1R signaling modulates acetylcholine release at neuronal nicotinic synapses," *Molecular and cellular neurosciences*, vol. 43, no. 2, pp. 244–257, 2010. (Cited on page 146.)
- [422] I. Gusarov, L. Gautier, O. Smolentseva, I. Shamovsky, S. Eremina, A. Mironov, and E. Nudler, "Bacterial nitric oxide extends the lifespan of *C. elegans*," *Cell*, vol. 152, no. 4, pp. 818–830, 2013. (Cited on page 146.)
- [423] S. Y. L. Ng, B. K. C. Chow, J. Kasamatsu, M. Kasahara, and L. T. O. Lee, "Agnathan VIP, PACAP and their receptors: ancestral origins of today's highly diversified forms," *PLoS One*, vol. 7, no. 9, p. e44691, 2012. (Cited on page 147.)
- [424] S. Wu, G. J. Roch, L. A. Cervini, J. E. Rivier, and N. M. Sherwood, "Newly-identified receptors for peptide histidine-isoleucine and GHRH-like peptide in zebrafish help to elucidate the mammalian secretin superfamily," *Journal of molecular endocrinology*, vol. 41, no. 5, pp. 343–366, 2008. (Cited on page 147.)
- [425] J. C. R. Cardoso, "Duplicated receptors for VIP and PACAP (VPAC1R and PAC1R) in a teleost fish, *Fugu rubripes*," *Journal of molecular endocrinology*, vol. 33, no. 2, pp. 411–428, 2004. (Cited on page 147.)
- [426] J.-I. Hwang, M. J. Moon, S. Park, D.-K. Kim, E. B. Cho, N. Ha, G. H. Son, K. Kim, H. Vaudry, and J. Y. Seong, "Expansion of secretin-like G protein-coupled receptors and their peptide ligands via local duplications before and after two rounds of whole-genome duplication," *Molecular biology and evolution*, vol. 30, no. 5, pp. 1119–1130, 2013. (Cited on page 147.)
- [427] C. Jee, J. Lee, J. P. Lim, D. Parry, R. O. Messing, and S. L. McIntire, "SEB-3, a CRF receptor-like GPCR, regulates locomotor activity states, stress responses and ethanol tolerance in *Caenorhabditis elegans*," *Genes, brain, and behavior*, vol. 12, no. 2, pp. 250–262, 2013. (Cited on page 147.)
- [428] R. M. Fox, Von Stetina, Stephen E, S. J. Barlow, C. Shaffer, K. L. Olszewski, J. H. Moore, D. Dupuy, M. Vidal, and D. M. Miller III, "A gene expression fingerprint of *C. elegans* embryonic motor neurons," *BMC Genomics*, vol. 6, p. 42, 2005. (Cited on pages 147 and 148.)
- [429] K. L. Howe, B. J. Bolt, S. Cain, J. Chan, W. J.

- Chen, P. Davis, J. Done, T. Down, S. Gao, C. Grove, T. W. Harris, R. Kishore, R. Lee, J. Lomax, Y. Li, H.-M. Muller, C. Nakamura, P. Nuin, M. Paulini, D. Raciti, G. Schindelman, E. Stanley, M. A. Tuli, K. van Auken, D. Wang, X. Wang, G. Williams, A. Wright, K. Yook, M. Berriman, P. Kersey, T. Schedl, L. Stein, and P. W. Sternberg, "WormBase 2016: expanding to enable helminth genomic research," *Nucleic acids research*, vol. 44, no. D1, pp. D774–80, 2016. (Cited on pages 147 and 161.)
- [430] T. Ida, T. Takahashi, H. Tominaga, T. Sato, K. Kume, K. Yoshizawa-Kumagaye, H. Nishio, J. Kato, N. Murakami, M. Miyazato, K. Kangawa, and M. Kojima, "Identification of the endogenous cysteine-rich peptide trissin, a ligand for an orphan G protein-coupled receptor in *Drosophila*," *Biochemical and Biophysical Research Communications*, vol. 414, no. 1, pp. 44–48, 2011. (Cited on page 147.)
- [431] R. Angelo and C. S. Rubin, "Molecular Characterization of an Anchor Protein (AKAPCE) That Binds the RI Subunit (RCE) of Type I Protein Kinase A from *Caenorhabditis elegans*," *Journal of Biological Chemistry*, vol. 273, no. 23, pp. 14633–14643, 1998. (Cited on page 148.)
- [432] R. G. Angelo and C. S. Rubin, "Characterization of Structural Features That Mediate the Tethering of *Caenorhabditis elegans* Protein Kinase A to a Novel A Kinase Anchor Protein: INSIGHTS INTO THE ANCHORING OF PKAI ISOFORMS," *Journal of Biological Chemistry*, vol. 275, no. 6, pp. 4351–4362, 2000. (Cited on page 148.)
- [433] K. L. Dodge, S. Khouangsathiene, M. S. Kapiloff, R. Mouton, E. V. Hill, M. D. Houslay, L. K. Langeberg, and J. D. Scott, "mAKAP assembles a protein kinase A/PDE4 phosphodiesterase cAMP signaling module," *The EMBO journal*, vol. 20, no. 8, pp. 1921–1930, 2001. (Cited on page 148.)
- [434] C. W. Dessauer, "Adenylyl cyclase–A-kinase anchoring protein complexes: the next dimension in cAMP signaling," *Molecular pharmacology*, vol. 76, no. 5, pp. 935–941, 2009. (Cited on page 148.)
- [435] H. Wang, D. Sieburth, and M. B. Goodman, "PKA Controls Calcium Influx into Motor Neurons during a Rhythmic Behavior," *PLoS genetics*, vol. 9, no. 9, p. e1003831, 2013. (Cited on page 148.)
- [436] Y. Saheki and C. I. Bargmann, "Presynaptic CaV2 calcium channel traffic requires CALF-1 and the alpha(2)delta subunit UNC-36," *Nature neuroscience*, vol. 12, no. 10, pp. 1257–1265, 2009. (Cited on page 148.)
- [437] S. Ryglewski, H. J. Pflueger, and C. Duch, "Expanding the neuron's calcium signaling repertoire: intracellular calcium release via voltage-induced PLC and IP3R activation," *PLoS biology*, vol. 5, no. 4, p. e66, 2007. (Cited on page 148.)
- [438] D. J. Reiner, E. M. Newton, H. Tian, and J. H. Thomas, "Diverse behavioural defects caused by mutations in *Caenorhabditis elegans unc-43* CaM kinase II," *Nature*, vol. 402, no. 6758, pp. 199–203, 1999. (Cited on page 148.)
- [439] C. M. Hoover, S. L. Edwards, S.-c. Yu, M. Kittelmann, J. E. Richmond, S. Eimer, R. M. Yorks, and K. G. Miller, "A Novel CaM Kinase II Pathway Controls the Location of Neuropeptide Release from *Caenorhabditis elegans* Motor Neurons," *Genetics*, vol. 196, no. 3, pp. 745–765, 2014. (Cited on page 148.)
- [440] Di Sha, H. Jin, R. D. Kopke, and J.-Y. Wu, "Choline acetyltransferase: regulation and coupling with protein kinase and vesicular acetylcholine transporter on synaptic vesicles," *Neurochemical research*, vol. 29, no. 1, pp. 199–207, 2004. (Cited on page 148.)
- [441] F. Cesca, P. Baldelli, F. Valtorta, and F. Benfenati, "The synapsins: Key actors of synapse function and plasticity," *Progress in Neurobiology*, vol. 91, no. 4, pp. 313–348, 2010. (Cited on page 148.)

- on page 150.)
- [442] L. Krabben, A. Fassio, V. K. Bhatia, A. Pechstein, F. Onofri, M. Fadda, M. Messa, Y. Rao, O. Shupliakov, D. Stamou, F. Benfenati, and V. Haucke, "Synapsin I senses membrane curvature by an amphipathic lipid packing sensor motif," *The Journal of neuroscience : the official journal of the Society for Neuroscience*, vol. 31, no. 49, pp. 18149–18154, 2011. (Cited on page 150.)
- [443] W. Macias, R. Carlson, A. Rajadhyaksha, A. Barczak, and C. Konradi, "Potassium chloride depolarization mediates CREB phosphorylation in striatal neurons in an NMDA receptor-dependent manner," *Brain Research*, vol. 890, no. 2, pp. 222–232, 2001. (Cited on page 151.)
- [444] C. Chen and W. G. Regehr, "The mechanism of cAMP-mediated enhancement at a cerebellar synapse," *The Journal of neuroscience : the official journal of the Society for Neuroscience*, vol. 17, no. 22, pp. 8687–8694, 1997. (Cited on page 151.)
- [445] P. Chi, P. Greengard, and T. A. Ryan, "Synaptic vesicle mobilization is regulated by distinct synapsin I phosphorylation pathways at different frequencies," *Neuron*, vol. 38, no. 1, pp. 69–78, 2003. (Cited on page 151.)
- [446] P. Chi, P. Greengard, and T. A. Ryan, "Synapsin dispersion and recluster during synaptic activity," *Nature neuroscience*, vol. 4, no. 12, pp. 1187–1193, 2001. (Cited on page 151.)
- [447] C. N. G. Giachello, F. Fiumara, C. Giacomini, A. Corradi, C. Milanese, M. Ghirardi, F. Benfenati, and P. G. Montarolo, "MAPK/Erk-dependent phosphorylation of synapsin mediates formation of functional synapses and short-term homosynaptic plasticity," *Journal of Cell Science*, vol. 123, no. Pt 6, pp. 881–893, 2010. (Cited on page 151.)
- [448] Y. Bei, J. Hogan, L. A. Berkowitz, M. Soto, C. E. Rocheleau, K. M. Pang, J. Collins, and C. C. Mello, "SRC-1 and Wnt signaling act together to specify endoderm and to control cleavage orientation in early *C. elegans* embryos," *Developmental Cell*, vol. 3, no. 1, pp. 113–125, 2002. (Cited on page 151.)
- [449] F. Onofri, S. Giovedi, P. Vaccaro, A. J. Czernik, F. Valtorta, P. de Camilli, P. Greengard, and F. Benfenati, "Synapsin I interacts with c-Src and stimulates its tyrosine kinase activity," *Proceedings of the National Academy of Sciences of the United States of America*, vol. 94, no. 22, pp. 12168–12173, 1997. (Cited on page 151.)
- [450] F. Onofri, M. Messa, V. Matafora, G. Bonanno, A. Corradi, A. Bachi, F. Valtorta, and F. Benfenati, "Synapsin phosphorylation by SRC tyrosine kinase enhances SRC activity in synaptic vesicles," *The Journal of biological chemistry*, vol. 282, no. 21, pp. 15754–15767, 2007. (Cited on page 151.)
- [451] B. Itoh, T. Hirose, N. Takata, K. Nishiwaki, M. Koga, Y. Ohshima, and M. Okada, "SRC-1, a non-receptor type of protein tyrosine kinase, controls the direction of cell and growth cone migration in *C. elegans*," *Development (Cambridge, England)*, vol. 132, no. 23, pp. 5161–5172, 2005. (Cited on page 151.)
- [452] H. Ohnishi, S. Yamamori, K. Ono, K. Aoyagi, S. Kondo, and M. Takahashi, "A src family tyrosine kinase inhibits neurotransmitter release from neuronal cells," *Proceedings of the National Academy of Sciences of the United States of America*, vol. 98, no. 19, pp. 10930–10935, 2001. (Cited on page 151.)
- [453] Y. Shulman, A. Stavsky, T. Fedorova, D. Mikulincer, M. Atias, I. Radinsky, J. Kahn, I. Slutsky, and D. Gitler, "ATP Binding to Synapsin IIa Regulates Usage and Clustering of Vesicles in Terminals of Hippocampal Neurons," *Journal of Neuroscience*, vol. 35, no. 3, pp. 985–998, 2015. (Cited on page 151.)
- [454] P. Kratsios, A. Stolfi, M. Levine, and O. Hobert, "Coordinated regulation of cholinergic motor neuron traits through a conserved terminal selector gene," *Nature neuroscience*, vol. 15, no. 2, pp. 205–214, 2011.

(Cited on page 151.)

- [455] S. Wabnig, J. F. Liewald, S.-C. Yu, A. Gottschalk, and M. A. Cousin, "High-Throughput All-Optical Analysis of Synaptic Transmission and Synaptic Vesicle Recycling in *Caenorhabditis elegans*," *PLoS one*, vol. 10, no. 8, p. e0135584, 2015. (Cited on page 152.)
- [456] H. C. Korswagen, J. H. Park, Y. Ohshima, and R. H. Plasterk, "An activating mutation in a *Caenorhabditis elegans* Gs protein induces neural degeneration," *Genes & Development*, vol. 11, no. 12, pp. 1493–1503, 1997. (Cited on page 153.)
- [457] K. Du, H. Asahara, U. S. Jhala, B. L. Wagner, and M. Montminy, "Characterization of a CREB gain-of-function mutant with constitutive transcriptional activity in vivo," *Molecular and Cellular Biology*, vol. 20, no. 12, pp. 4320–4327, 2000. (Cited on page 153.)
- [458] S. Chung, T. L. Gumienny, M. O. Hengartner, and M. Driscoll, "A common set of engulfment genes mediates removal of both apoptotic and necrotic cell corpses in *C. elegans*," *Nature cell biology*, vol. 2, no. 12, pp. 931–937, 2000. (Cited on page 153.)
- [459] L. Bianchi, B. Gerstbrein, C. Frokjaer-Jensen, D. C. Royal, G. Mukherjee, M. A. Royal, J. Xue, W. R. Schafer, and M. Driscoll, "The neurotoxic MEC-4(d) DEG/ENaC sodium channel conducts calcium: implications for necrosis initiation," *Nature neuroscience*, vol. 7, no. 12, pp. 1337–1344, 2004. (Cited on page 153.)
- [460] C. Matthewman, T. W. Miller-Fleming, D. M. R. Miller, and L. Bianchi, "Ca<sup>2+</sup> permeability and Na<sup>+</sup> conductance in cellular toxicity caused by hyperactive DEG/ENaC channels," *American journal of physiology. Cell physiology*, vol. 311, no. 6, pp. C920–C930, 2016. (Cited on page 154.)
- [461] J. Kass, T. C. Jacob, P. Kim, and J. M. Kaplan, "The EGL-3 proprotein convertase regulates mechanosensory responses of *Caenorhabditis elegans*," *The Journal of neuroscience : the official journal of the Society for Neuroscience*, vol. 21, no. 23, pp. 9265–9272, 2001. (Cited on page 155.)
- [462] S. J. Husson, E. Clynen, G. Baggerman, T. Janssen, and L. Schoofs, "Defective processing of neuropeptide precursors in *Caenorhabditis elegans* lacking proprotein convertase 2 (KPC-2/EGL-3): mutant analysis by mass spectrometry," *Journal of Neurochemistry*, vol. 98, no. 6, pp. 1999–2012, 2006. (Cited on page 155.)
- [463] S. J. Husson, T. Janssen, G. Baggerman, B. Bogert, A. H. Kahn-Kirby, K. Ashrafi, and L. Schoofs, "Impaired processing of FLP and NLP peptides in carboxypeptidase E (EGL-21)-deficient *Caenorhabditis elegans* as analyzed by mass spectrometry," *Journal of Neurochemistry*, vol. 102, no. 1, pp. 246–260, 2007. (Cited on page 155.)
- [464] T. C. Jacob and J. M. Kaplan, "The EGL-21 carboxypeptidase E facilitates acetylcholine release at *Caenorhabditis elegans* neuromuscular junctions," *The Journal of neuroscience : the official journal of the Society for Neuroscience*, vol. 23, no. 6, pp. 2122–2130, 2003. (Cited on page 155.)
- [465] B. A. Eipper, S. N. Perkins, E. J. Husten, R. C. Johnson, H. T. Keutmann, and R. E. Mains, "Peptidyl-alpha-hydroxyglycine alpha-amidating lyase. Purification, characterization, and expression," *The Journal of biological chemistry*, vol. 266, no. 12, pp. 7827–7833, 1991. (Cited on page 155.)
- [466] B. A. Eipper, S. L. Milgram, E. J. Husten, H. Y. Yun, and R. E. Mains, "Peptidylglycine alpha-amidating monooxygenase: a multifunctional protein with catalytic, processing, and routing domains," *Protein science : a publication of the Protein Society*, vol. 2, no. 4, pp. 489–497, 1993. (Cited on page 155.)
- [467] M. Han, D. Park, P. J. Vanderzalm, R. E. Mains, B. A. Eipper, and P. H. Taghert, "Drosophila uses two distinct neuropeptide amidating enzymes, dPAL1 and dPAL2,"

- Journal of Neurochemistry*, vol. 90, no. 1, pp. 129–141, 2004. (Cited on page 155.)
- [468] S. Dufour, *A comparative survey of the RF-amide peptide superfamily*. s.l.: Frontiers Media SA, 2015. (Cited on page 156.)
- [469] I. Kupfermann and K. R. Weiss, “Activity of an identified serotonergic neuron in free moving *Aplysia* correlates with behavioral arousal,” *Brain Research*, vol. 241, no. 2, pp. 334–337, 1982. (Cited on page 156.)
- [470] J. Jing and R. Gillette, “Escape swim network interneurons have diverse roles in behavioral switching and putative arousal in *Pleurobranchaea*,” *Journal of Neurophysiology*, vol. 83, no. 3, pp. 1346–1355, 2000. (Cited on page 156.)
- [471] G. Gürel, M. A. Gustafson, J. S. Pepper, H. R. Horvitz, and M. R. Koelle, “Receptors and other signaling proteins required for serotonin control of locomotion in *Caenorhabditis elegans*,” *Genetics*, vol. 192, no. 4, pp. 1359–1371, 2012. (Cited on page 156.)
- [472] R. W. Komuniecki, R. J. Hobson, E. B. Rex, V. M. Hapiak, and P. R. Komuniecki, “Biogenic amine receptors in parasitic nematodes: what can be learned from *Caenorhabditis elegans*?,” *Molecular and biochemical parasitology*, vol. 137, no. 1, pp. 1–11, 2004. (Cited on page 156.)
- [473] M. Carre-Pierrat, D. Baillie, R. Johnsen, R. Hyde, A. Hart, L. Granger, and L. Ségalat, “Characterization of the *Caenorhabditis elegans* G protein-coupled serotonin receptors,” *Invertebrate neuroscience : IN*, vol. 6, no. 4, pp. 189–205, 2006. (Cited on page 156.)
- [474] L. Segalat, D. Elkes, and J. Kaplan, “Modulation of serotonin-controlled behaviors by Go in *Caenorhabditis elegans*,” *Science*, vol. 267, no. 5204, pp. 1648–1651, 1995. (Cited on page 156.)
- [475] E. R. Sawin, R. Ranganathan, and H. Horvitz, “*C. elegans* Locomotory Rate Is Modulated by the Environment through a Dopaminergic Pathway and by Experience through a Serotonergic Pathway,” *Neuron*, vol. 26, no. 3, pp. 619–631, 2000. (Cited on pages 156 and 162.)
- [476] S. Iwanir, A. S. Brown, S. Nagy, D. Najjar, A. Kazakov, K. S. Lee, A. Zaslaver, E. Levine, and D. Biron, “Serotonin promotes exploitation in complex environments by accelerating decision-making,” *BMC biology*, vol. 14, p. 9, 2016. (Cited on page 157.)
- [477] D. Wang, Y. Yu, Y. Li, Y. Wang, and D. Wang, “Dopamine Receptors Antagonistically Regulate Behavioral Choice between Conflicting Alternatives in *C. elegans*,” *PLoS one*, vol. 9, no. 12, p. e115985, 2014. (Cited on page 157.)
- [478] M. Ezcurra, D. S. Walker, I. Beets, P. Swoboda, and W. R. Schafer, “Neuropeptidergic Signaling and Active Feeding State Inhibit Nociception in *Caenorhabditis elegans*,” *The Journal of neuroscience : the official journal of the Society for Neuroscience*, vol. 36, no. 11, pp. 3157–3169, 2016. (Cited on page 157.)
- [479] S. Xu and A. D. Chisholm, “Highly efficient optogenetic cell ablation in *C. elegans* using membrane-targeted miniSOG,” *Scientific reports*, vol. 6, p. 21271, 2016. (Cited on page 158.)
- [480] M. A. Jobson, C. M. Valdez, J. Gardner, L. R. Garcia, E. M. Jorgensen, and A. A. Beg, “Spillover transmission is mediated by the excitatory GABA receptor LGC-35 in *C. elegans*,” *The Journal of neuroscience : the official journal of the Society for Neuroscience*, vol. 35, no. 6, pp. 2803–2816, 2015. (Cited on page 160.)
- [481] H. van der Loos and E. M. Glaser, “Autapses in neocortex cerebri: synapses between a pyramidal cell’s axon and its own dendrites,” *Brain Research*, vol. 48, pp. 355–360, 1972. (Cited on page 160.)
- [482] M. R. Park, J. W. Lighthall, and S. T. Kitai, “Recurrent inhibition in the rat neostriatum,” *Brain Research*, vol. 194, no. 2, pp. 359–369, 1980. (Cited on page 160.)
- [483] G. Tamas, E. H. Buhl, and P. Somogyi, “Mas-

- sive autaptic self-innervation of GABAergic neurons in cat visual cortex," *The Journal of neuroscience : the official journal of the Society for Neuroscience*, vol. 17, no. 16, pp. 6352–6364, 1997. (Cited on page 160.)
- [484] A. J. Chang, N. Chronis, D. S. Karow, M. A. Marletta, and C. I. Bargmann, "A Distributed Chemosensory Circuit for Oxygen Preference in *C. elegans*," *PLOS Biology*, vol. 4, no. 9, p. e274, 2006. (Cited on page 162.)
- [485] W. Li, L. Kang, B. J. Piggott, Z. Feng, and X. Z. S. Xu, "The neural circuits and sensory channels mediating harsh touch sensation in *Caenorhabditis elegans*," *Nature communications*, vol. 2, p. 315, 2011. (Cited on page 162.)
- [486] S. J. Husson, W. Steuer Costa, S. Wabnig, J. N. Stirman, J. D. Watson, W. C. Spencer, J. Akerboom, L. L. Looger, M. Treinin, D. M. Miller III, H. Lu, and A. Gottschalk, "Optogenetic Analysis of a Nociceptor Neuron and Network Reveals Ion Channels Acting Downstream of Primary Sensors," *Current Biology*, 2012. (Cited on pages 162 and 312.)
- [487] R. Lints and S. W. Emmons, "Patterning of dopaminergic neurotransmitter identity among *Caenorhabditis elegans* ray sensory neurons by a TGFbeta family signaling pathway and a Hox gene," *Development (Cambridge, England)*, vol. 126, no. 24, pp. 5819–5831, 1999. (Cited on page 162.)
- [488] L. Kang, J. Gao, W. R. Schafer, Z. Xie, and X. Z. S. Xu, "C. elegans TRP family protein TRP-4 is a pore-forming subunit of a native mechanotransduction channel," *Neuron*, vol. 67, no. 3, pp. 381–391, 2010. (Cited on page 162.)
- [489] T. Wakabayashi, I. Kitagawa, and R. Shingai, "Neurons regulating the duration of forward locomotion in *Caenorhabditis elegans*," *Neuroscience Research*, vol. 50, no. 1, pp. 103–111, 2004. (Cited on page 162.)
- [490] Z. V. Guo, A. C. Hart, and S. Ramanathan, "Optical interrogation of neural circuits in *Caenorhabditis elegans*," *Nature Methods*, vol. 6, no. 12, pp. 891–896, 2009. (Cited on page 162.)
- [491] B. J. Piggott, J. Liu, Z. Feng, S. A. Wescott, and X. Z. S. Xu, "The neural circuits and synaptic mechanisms underlying motor initiation in *C. elegans*," *Cell*, vol. 147, no. 4, pp. 922–933, 2011. (Cited on page 162.)
- [492] T. A. Starich, J. Xu, I. M. Skerrett, B. J. Nicholson, and J. E. Shaw, "Interactions between innexins UNC-7 and UNC-9 mediate electrical synapse specificity in the *Caenorhabditis elegans* locomotory nervous system," *Neural development*, vol. 4, p. 16, 2009. (Cited on page 162.)
- [493] B. Chen, Q. Liu, Q. Ge, J. Xie, and Z.-W. Wang, "UNC-1 Regulates Gap Junctions Important to Locomotion in *C. elegans*," *Current Biology*, vol. 17, no. 15, pp. 1334–1339, 2007. (Cited on page 162.)
- [494] M. Hendricks, H. Ha, N. Maffey, and Y. Zhang, "Compartmentalized calcium dynamics in a *C. elegans* interneuron encode head movement," *Nature*, 2012. (Cited on page 163.)
- [495] J. Schwarz, H. Bringmann, and A. C. Hart, "Reduced Sleep-Like Quiescence in Both Hyperactive and Hypoactive Mutants of the Galphaq Gene egl-30 during lethargus in *Caenorhabditis elegans*," *PLoS One*, vol. 8, no. 9, p. e75853, 2013. (Cited on page 163.)
- [496] A. Azulay, E. Itskovits, and A. Zaslaver, "The *C. elegans* Connectome Consists of Homogenous Circuits with Defined Functional Roles," *PLoS Computational Biology*, vol. 12, no. 9, p. e1005021, 2016. (Cited on page 163.)
- [497] M. de Bono and Andres Villu Maricq, "Neuronal substrates of complex behaviors in *C. elegans*," *Annu Rev Neurosci*, vol. 28, pp. 451–501, 2005. (Cited on page 164.)
- [498] D. G. Albertson and J. N. Thomson, "The pharynx of *Caenorhabditis elegans*," *Philosophical transactions of the Royal Society of London. Series B, Biological sciences*, vol. 275, no. 938, pp. 299–325, 1976. (Cited on

- page 164.)
- [499] D. L. Riddle, *C. elegans II*, vol. 33 of *Cold Spring Harbor monograph series*. Cold Spring Harbor NY: Cold Spring Harbor Laboratory Press, 1997. (Cited on page 164.)
- [500] N. Dalliere, N. Bhatla, Z. Luedtke, D. K. Ma, J. Woolman, R. J. Walker, L. Holden-Dye, and V. O'Connor, "Multiple excitatory and inhibitory neural signals converge to fine-tune *Caenorhabditis elegans* feeding to food availability," *FASEB journal : official publication of the Federation of American Societies for Experimental Biology*, vol. 30, no. 2, pp. 836–848, 2016. (Cited on page 164.)
- [501] C. Holland, *Ascaris*. Burlington: Elsevier Science, 2013. (Cited on page 164.)
- [502] J. Y. Yew, R. Davis, S. Dikler, J. Nanda, B. Reinders, and A. O. Stretton, "Peptide products of the *afp-6* gene of the nematode *Ascaris suum* have different biological actions," *The Journal of comparative neurology*, vol. 502, no. 5, pp. 872–882, 2007. (Cited on page 164.)
- [503] C. L. Moffett, Am Beckett, A. Mousley, T. G. Geary, N. J. Marks, D. W. Halton, D. P. Thompson, and A. G. Maule, "The ovijector of *Ascaris suum*: multiple response types revealed by *Caenorhabditis elegans* FMRFamide-related peptides," *International journal for parasitology*, vol. 33, no. 8, pp. 859–876, 2003. (Cited on page 164.)
- [504] C. A. Reinitz, A. E. Pleva, and A. O. Stretton, "Changes in Cyclic Nucleotides, Locomotory Behavior, and Body Length Produced by Novel Endogenous Neuropeptides in the Parasitic Nematode *Ascaris suum*," *Molecular and Biochemical Parasitology*, vol. 180, no. 1, pp. 27–34, 2011. (Cited on page 164.)
- [505] P. Sithigorngul, J. L. Jarecki, and A. O. W. Stretton, "A specific antibody to neuropeptide AF1 (KNEFIRFamide) recognizes a small subset of neurons in *Ascaris suum*: differences from *Caenorhabditis elegans*," *The Journal of comparative neurology*, vol. 519, no. 8, pp. 1546–1561, 2011. (Cited on page 165.)
- [506] L. E. Atkinson, I. R. Miskelly, C. L. Moffett, C. J. McCoy, A. G. Maule, N. J. Marks, and A. Mousley, "Unraveling *flp-11/flp-32* dichotomy in nematodes," *International journal for parasitology*, vol. 46, no. 11, pp. 723–736, 2016. (Cited on page 164.)
- [507] Z. Han, S. Boas, and N. E. Schroeder, "Unexpected Variation in Neuroanatomy among Diverse Nematode Species," *Frontiers in neuroanatomy*, vol. 9, p. 162, 2015. (Cited on page 164.)
- [508] A. Mani, J. Radhakrishnan, A. Farhi, K. S. Carew, C. A. Warnes, C. Nelson-Williams, R. W. Day, B. Pober, M. W. State, and R. P. Lifton, "Syndromic patent ductus arteriosus: evidence for haploinsufficient TFAP2B mutations and identification of a linked sleep disorder," *Proceedings of the National Academy of Sciences of the United States of America*, vol. 102, no. 8, pp. 2975–2979, 2005. (Cited on page 165.)
- [509] J. Bouvier, V. Caggiano, R. Leiras, V. Caldeira, C. Bellardita, K. Balueva, A. Fuchs, and O. Kiehn, "Descending Command Neurons in the Brainstem that Halt Locomotion," *Cell*, vol. 163, no. 5, pp. 1191–1203, 2015. (Cited on page 165.)
- [510] W. Steuer Costa, J. F. Liewald, and A. Gottschalk, "Photoactivated adenylyl cyclases as optogenetic modulators of neuronal activity," *Methods in molecular biology (Clifton, N.J.)*, vol. 1148, pp. 161–175, 2014. (Cited on pages 225, 226, and 312.)
- [511] L. Avery, D. Raizen, and S. Lockery, "Electrophysiological methods," *Methods in cell biology*, vol. 48, pp. 251–269, 1995. (Cited on page 227.)
- [512] C. Schüler, E. Fischer, L. Shaltiel, W. Steuer Costa, and A. Gottschalk, "Arrhythmogenic effects of mutated L-type Ca<sup>2+</sup>-channels on an optogenetically paced muscular pump in *Caenorhabditis elegans*," *Scientific reports*, vol. 5, p. 14427, 2015. (Cited on pages 227, 267, and 312.)



- [513] R. M. Weimer, "Preservation of *C. elegans* tissue via high-pressure freezing and freeze-substitution for ultrastructural analysis and immunocytochemistry," *Methods in molecular biology (Clifton, N.J.)*, vol. 351, pp. 203–221, 2006. (Cited on page 227.)
- [514] M. Riedmiller and H. Braun, "A Direct Adaptive Method for Faster Backpropagation Learning: The RPROP Algorithm," in *IEEE INTERNATIONAL CONFERENCE ON NEURAL NETWORKS*, pp. 586–591, 1993. (Cited on page 267.)
- [515] D. Ramot, B. E. Johnson, T. L. Berry, L. Carnell, and M. B. Goodman, "The Parallel Worm Tracker: a platform for measuring average speed and drug-induced paralysis in nematodes," *PloS one*, vol. 3, no. 5, p. e2208, 2008. (Cited on page 312.)
- [516] S. J. Husson, W. Steuer Costa, C. Schmitt, and A. Gottschalk, "Keeping track of worm trackers," *WormBook : the online review of C. elegans biology*, pp. 1–17, 2012. (Cited on page 312.)
- [517] A. Bazzone, W. Steuer Costa, M. Braner, O. CĂflinescu, L. Hatahet, and K. Fendler, "Introduction to solid supported membrane based electrophysiology," *Journal of visualized experiments : JoVE*, no. 75, p. e50230, 2013. (Cited on page 312.)
- [518] E. Cohen, M. Chatzigeorgiou, S. J. Husson, W. Steuer Costa, A. Gottschalk, W. R. Schafer, and M. Treinin, "Caenorhabditis elegans nicotinic acetylcholine receptors are required for nociception," *Molecular and cellular neurosciences*, vol. 59, pp. 85–96, 2014. (Cited on page 312.)

## List of Figures

1.1. The legacy of Santiago Ramón y Cajal and Bernard Katz . . . . .	1
1.2. Synaptic transmission types . . . . .	3
1.3. The V-ATPase control of SV loading and release . . . . .	5
1.4. Neurotransmitter loading as exemplified for ACh . . . . .	6
1.5. SV pools . . . . .	8
1.6. SV release modes . . . . .	9
1.7. SV release machinery . . . . .	11
1.8. SV endocytosis modes . . . . .	12
1.9. Suggested mechanism of ChR2 pore formation and the ChR2 photocycle	15
1.10. BLUF domain light induced tautomerization and photocycle . . . . .	18
1.11. Motility modulation by EuPAC $\alpha$ expression in cholinergic neurons of <i>C. elegans</i> . . . . .	20
1.12. The genetically encoded calcium indicator GCaMP . . . . .	21
1.13. Light induced ROS production with miniSOG . . . . .	22
1.14. Comparison of model organisms in neuroscience . . . . .	24
1.15. <i>Caenorhabditis elegans</i> life cycle . . . . .	24
1.16. Representation of <i>C. elegans</i> neurons along the body depicting the po- sition of RIS . . . . .	25
1.17. <i>C. elegans</i> neuronal cell bodies and neurotransmitters . . . . .	26
1.18. BWM cell recording and SV quantal size . . . . .	27
1.19. Schematic of body wall muscle organization . . . . .	29
1.20. Cholinergic to GABAergic motoneuron feed-forward network . . . . .	30
1.21. Neuronal network topology and signal flow . . . . .	32
1.22. Schematic location of RIS in the adult hermaphrodite . . . . .	34
2.1. bPAC C1V1 contraction assay light protocol. . . . .	71
2.2. EM quantitative image analysis . . . . .	74
2.3. Exemplary fit curves for mPSC kinetic analysis . . . . .	75

3.1. Expression of bPAC in cholinergic neurons . . . . .	80
3.2. bPAC photoactivation enhances swimming behavior . . . . .	81
3.3. Transient speed increase followed by stronger body bending during bPAC photostimulation . . . . .	82
3.4. Increase in bending angles observed up to half a minute after light de- activation . . . . .	83
3.5. bPAC elicits a small body contraction . . . . .	84
3.6. Modulation of behavior by bPAC is LITE-1 independent . . . . .	85
3.7. bPAC requires intrinsic depolarization to modulate behavior . . . . .	86
3.8. bPAC augments C1V1 induced depolarization . . . . .	87
3.9. Expression of PDE-4D <sub>gof</sub> impairs the effect of bPAC on behavior . . . . .	88
3.10. Adenylyl cyclase gain of function mutant . . . . .	89
3.11. Body wall muscle cell voltage clamp measurements for bPAC or ChR2 stimulation . . . . .	90
3.12. bPAC effect on mPSCs is not dependent on GABAergic feedback . . . . .	91
3.13. bPAC photostimulation led to neuropeptide secretion, as monitored by coelomocyte fluorescence . . . . .	92
3.15. <i>unc-31(n1304)</i> impaired bPAC-induced mPSC amplitude increase . . . . .	93
3.14. UNC-31 required for bPAC induced neuropeptide secretion . . . . .	94
3.16. EPSC amplitude was not altered by bPAC photostimulation and ago- nist puff application in BWM recording . . . . .	96
3.17. mPSC kinetic parameter analysis confirmed neuropeptidergic effect on the presynapse of the NMJ . . . . .	97
3.18. Representative thin section with ultrastructure of pre-synapse marked	98
3.19. Perimeter and area of profiles analyzed by HPF-EM . . . . .	99
3.20. Isoperimetric quotient of HPF-EM profiles . . . . .	99
3.21. bPAC and ChR2 photoactivation reduced the number of SVs . . . . .	100
3.22. bPAC reduced the number DCVs after long time photostimulation . . . . .	101
3.23. LVs with increased diameter present in bPAC long- and ChR2(C128S) photostimulation . . . . .	102
3.24. SV size increased after bPAC photoactivation . . . . .	103
3.25. bPAC effect on ultrastructure is UNC-31 dependent . . . . .	105
3.26. Neuropeptidergic signaling required for bPAC-induced increase of SV size . . . . .	106
3.27. Vesamicol inhibits bPAC-induced mPSC amplitude increase . . . . .	107

3.28. Analysis of behavioral response of several mutants to bPAC photostimulation . . . . .	108
3.29. synapsin required for bPAC-induced neuropeptide secretion . . . . .	109
3.30. synapsin required for bPAC-induced mPSC amplitude modulation . . . . .	110
3.31. Perimeter, area and IPQ of synapsin mutant profiles analyzed by HPF-EM . . . . .	111
3.32. synapsin mutation impaired bPAC-induced SV recruitment from the reserve pool . . . . .	112
3.33. bPAC-induced SV mobilization deficiency in synapsin mutant synapses . . . . .	113
3.34. Synapsin mutant synapses had abnormal DCV localization . . . . .	114
3.35. Synapsin mutant synapses had reduced number of DCVs in flanking sections . . . . .	114
3.36. SV size unaffected in synapsin mutants after bPAC photoactivation . . . . .	115
3.37. bPAC-induced effect partially dependent on synapsin phosphorylation site . . . . .	117
3.38. bPAC-induced effect partially dependent on NLP-21 neuropeptides . . . . .	118
3.39. NLP-21 required for bPAC-induced effect on behavior . . . . .	118
3.40. Cre/LoxP scheme for single cell expression in RIS . . . . .	120
3.41. Promoter pair characterized for single cell expression in RIS . . . . .	121
3.42. Promoter pair specific for RIS also drove expression in the male specific tale neuron . . . . .	122
3.43. Acute RIS depolarization inhibited swimming behavior . . . . .	123
3.44. RIS depolarization led to immobility on solid substrate . . . . .	124
3.45. No habituation to multiple RIS::ChR2 photostimulation . . . . .	125
3.46. Small body elongation upon RIS::ChR2 photostimulation . . . . .	126
3.47. High light intensity photoactivation of RIS::ChR2 inhibited pharyngeal pumping . . . . .	127
3.48. Aversive stimuli inhibited RIS::ChR2-induced locomotion pause . . . . .	128
3.49. WGS of <i>lim-6</i> mutant responsible for RIS::ChR2-phenotype disruption . . . . .	132
3.50. LIM-6(A239T) mutation disrupts DNA-recognition motif . . . . .	133
3.51. Preliminary RIS::GFP cell dissociation and cultivation . . . . .	135
3.52. RIS up-regulated biological process gene ontology . . . . .	137
3.53. Volcano plot of RIS up-regulated genes . . . . .	138
3.54. RIS activity during free locomotion monitored by calcium imaging . . . . .	140
3.55. RIS::bPAC photoactivation did not modulate behavior drastically . . . . .	142

3.56. RIS::bPAC photoactivation increased probability of short locomotion pauses . . . . .	143
4.1. Proposed model of cholinergic SV quantal size modulation . . . . .	146
4.2. Model of cAMP and calcium distribution leading to bPAC induced effects	149
4.3. Comparison of Synapsin domains and phosphorylation sites . . . . .	150
4.4. bPAC increases ChR2(C128S) cholinergic output as measured by RCaMP fluorescence in body wall muscle cells. . . . .	153
4.5. Uninterrupted bPAC photostimulation for 24 h led to cholinergic cell death . . . . .	154
4.6. RIS activity decreased with exogenous serotonin application as monitored by calcium imaging . . . . .	157
4.7. High unspecific expression in addition to expected Arch in RIS . . . . .	158
4.8. RIS::HisCl1 histamine inhibition did not reduce reversal frequency . . .	159
4.9. Information processing and role of RIS in the <i>C. elegans</i> neuronal network controlling behavior . . . . .	161
4.10. RIS counterpart in <i>Ascaris suum</i> . . . . .	165
A.1. SNN-1B(S9A) sequence . . . . .	225
A.2. Electrophysiology sample preparation . . . . .	226
A.3. Electrophysiology mPSC analysis . . . . .	227
A.4. High pressure freezer with LED for optical stimulation . . . . .	228
B.1. KNIME Multimodal illumination tracker data workflow . . . . .	234
B.2. KNIME Multimodal illumination tracker data Input meta node . . . . .	234
B.3. KNIME Multimodal illumination tracker data file iterator meta node . . . . .	235
B.4. KNIME Multimodal illumination tracker data filter meta node . . . . .	235
B.5. KNIME Multimodal illumination tracker data quality control meta node	235
B.6. KNIME Multimodal illumination tracker data case meta node . . . . .	236
B.7. KNIME Contraction workflow . . . . .	239
B.8. KNIME Choreography workflow . . . . .	241
B.9. KNIME Choreography analysis . . . . .	242
B.10. KNIME Circos workflow . . . . .	245
B.11. KNIME Circos workflow meta node internal . . . . .	246
B.12. KNIME EM workflow . . . . .	252
B.13. KNIME EM meta node Read images . . . . .	254
B.14. KNIME EM meta node Prepare file paths . . . . .	254

B.15. KNIME EM meta node Read ROI Results . . . . .	255
B.16. KNIME EM meta node Exclude calculated . . . . .	256
B.17. KNIME EM meta node Prepare file paths dist . . . . .	256
B.18. KNIME EM meta node Processing . . . . .	257
B.19. KNIME EM meta node Distance calculations . . . . .	257
B.20. KNIME EM meta node distance . . . . .	258
B.21. KNIME EM meta node Enrich . . . . .	259
B.22. KNIME EM meta node SavePath . . . . .	259
B.23. KNIME EM meta node Calculations . . . . .	259
B.24. KNIME EM meta node Pooling . . . . .	260
B.25. KNIME EM meta node Bin Feature by Distance . . . . .	261
B.26. KNIME EM meta node Add missing values . . . . .	261
B.27. KNIME EM meta node Create eCDF Table . . . . .	262
B.28. KNIME Image pre-processing workflow . . . . .	265
B.29. KNIME Image pre-processing Path meta node . . . . .	265
B.30. KNIME Image pre-processing Calculation meta node . . . . .	265
B.31. KNIME Image pre-processing Animal stage meta node . . . . .	266
B.32. KNIME Image pre-processing Save images meta node . . . . .	266
B.33. KNIME Kymograph analysis . . . . .	271
B.34. KNIME Kymograph Find new files metanode . . . . .	272
B.35. KNIME Kymograph Iterate list of files metanode . . . . .	272
B.36. KNIME Kymograph Prepare file paths metanode . . . . .	272
B.37. KNIME Kymograph Read Results metanode . . . . .	273
B.38. KNIME Kymograph Process results metanode . . . . .	273
B.39. KNIME Kymograph Tagger metanode . . . . .	274
B.40. KNIME Kymograph Data processing metanode . . . . .	274
B.41. KNIME Kymograph Index pumps metanode . . . . .	275
B.42. KNIME Kymograph Calculate Pump properties metanode . . . . .	275
B.43. KNIME Kymograph Clean and prepare data metanode . . . . .	276
B.44. KNIME Kymograph Frequency metanode . . . . .	276
B.45. KNIME synch mPSCs workflow . . . . .	280
B.46. KNIME synch mPSCs Variables meta node . . . . .	281
B.47. KNIME synch mPSCs List files meta node . . . . .	281
B.48. KNIME synch mPSCs R meta node . . . . .	281
B.49. KNIME mPSC calculate Tau workflow . . . . .	281
B.50. KNIME mPSC calculate Tau - Read meta node . . . . .	282

B.51. KNIME mPSC calculate Tau - Filter meta node . . . . .	282
B.52. KNIME mPSC calculate Tau - Rise decay filter meta node . . . . .	282
B.53. KNIME mPSC calculate Tau - Get period meta node . . . . .	283
B.54. KNIME mPSC calculate Tau - Fit meta node . . . . .	283
B.55. KNIME mPSC calculate Tau - Synch meta node . . . . .	283
B.56. KNIME mPSC calculate Tau - Quality control meta node . . . . .	283
B.57. KNIME plot mPSCs workflow . . . . .	284
B.58. KNIME plot mPSCs - Filter meta node . . . . .	284
C.1. pWSC13 plasmid chart . . . . .	300
C.2. pWSC14 plasmid chart . . . . .	300
C.3. pWSC15 plasmid chart . . . . .	301
C.4. pWSC16 plasmid chart . . . . .	301
C.5. pWSC17 plasmid chart . . . . .	302
C.6. pWSC18 plasmid chart . . . . .	302
C.7. pWSC19 plasmid chart . . . . .	303
C.8. pWSC20 plasmid chart . . . . .	303
C.9. pWSC21 plasmid chart . . . . .	304
C.10.pWSC22 plasmid chart . . . . .	304
C.11.pWSC23 plasmid chart . . . . .	305
C.12.pWSC24 plasmid chart . . . . .	305
C.13.pWSC25 plasmid chart . . . . .	306
C.14.pWSC26 plasmid chart . . . . .	306
C.15.pWSC27 plasmid chart . . . . .	307
C.16.pWSC28 plasmid chart . . . . .	307
C.17.pWSC29 plasmid chart . . . . .	308
C.18.pWSC34 plasmid chart . . . . .	308
C.19.pWSC37 plasmid chart . . . . .	309
C.20.pWSC38 plasmid chart . . . . .	309
C.21.pWSC42 plasmid chart . . . . .	310
C.22.pWSC43 plasmid chart . . . . .	310
C.23.pWSC44 plasmid chart . . . . .	311
C.24.pWSC45 plasmid chart . . . . .	311

## List of Tables

1.1. Opsins and their variants for optogenetics . . . . .	17
2.1. Reagents. . . . .	39
2.2. Buffers and Media specifications. . . . .	40
2.3. Used kits. . . . .	41
2.4. Equipment used . . . . .	42
2.5. Organisms . . . . .	44
2.6. Transgenic <i>C. elegans</i> strains. . . . .	44
2.7. Oligonucleotides . . . . .	48
2.8. Plasmids . . . . .	52
2.9. Miscellaneous materials . . . . .	53
2.10. Software . . . . .	54
2.11. Basic PCR reaction mix. . . . .	56
2.12. PCR reaction conditions using Taq polymerase. . . . .	57
2.13. PCR reactions condition using Phusion polymerase. . . . .	57
2.14. PCR reaction conditions using Extend long template DNA polymerase mix. . . . .	58
2.15. AP reaction condition. . . . .	61
2.16. Dephosphorylation conditions. . . . .	61
2.17. T4 ligation reaction condition. . . . .	62
2.18. Injection mix content. . . . .	65
2.19. Data type and statistical hypothesis test performed for when assump- tions of parametric tests were met. . . . .	76
2.20. Non-parametric statistics . . . . .	76
3.1. Summary of RIS::Chr2-induced effect on several canonical mutants. . .	130
3.2. RIS marker genes present in RNA-Seq dataset sortet by p-value. . . . .	135
B.1. KNIME Multimodal illumination tracker data analysis summary . . . .	229



B.2. KNIME Multimodal illumination tracker data analysis manual input .	230
B.3. KNIME Contraction assay analysis summary . . . . .	237
B.4. KNIME Choreography and MWT summary . . . . .	240
B.5. KNIME Circos summary . . . . .	243
B.6. KNIME EM analysis summary . . . . .	247
B.7. KNIME EM analysis manual input . . . . .	248
B.8. KNIME Image pre-processing summary . . . . .	263
B.9. KNIME Analysis of pump frequency through kymographs summary .	267
B.10. KNIME synchronization and analysis of mPSCs summary . . . . .	277
B.11. EM ROI linear distance summary . . . . .	285
B.12. EM ROI distance through plasma membrane summary . . . . .	287
B.13. Multimodal illumination tracker data visualization summary . . . . .	289
B.14. Multimodal illumination tracker data visualization manual input . . .	289
B.15. Behavioral data cluster analysis summary . . . . .	290
B.16. Multimodal illumination tracker data visualization manual input . . .	290
B.17. Synchronize mPSCs summary . . . . .	292
B.18. Synchronize mPSCs summary . . . . .	293
B.19. . . . .	295
B.20. ImageJ EM ROI quantification summary . . . . .	296
B.21. ROI descriptions . . . . .	297

# Acronyms

**AC** adenylyl cyclase

**AChR** acetylcholine receptor

**AKAP** a-kinase anchoring protein

**AP** antartic phosphatase

**AP180** AP180 / UNC-11

**a-SNAP** a soluble NSF attachment protein / SNAP-1

**ACh** acetylcholine

**ATR** all-trans-retinal

**Baf A1** Bafilomycin A1

**BDNF** brain-derived neurotrophic factor

**BLUF** sensors of blue-light using FAD

**bPAC** photoactivatable adenylyl cyclase from *Beggiatoa spp.*

**BSA** bovine serum albumin

**BWM** body wall muscle

**C. reinhardtii** Chlamydomonas reinhardtii

**C. elegans** Caenorhabditis elegans

**CALI** chromophore-assisted light inactivation

**CaMK** calcium-calmodulin-dependent kinase

**CaMKII/UNC-43** calcium-calmodulin-dependent kinase II

**cAMP** cyclic adenosine monophosphate

**CAPS/UNC-31** Ca<sup>2+</sup>-dependent activator protein for secretion / UNC-31

**CFP** cyan fluorescent protein

**CGC** Caenorhabditis Genetics Center

**CGL** cholinergic gene locus

**cGMP** cyclic guanosine monophosphate  
**ChAT/CHA-1** choline acetyltransferase  
**CHDK** canon hack development kit  
**ChR1** channelrhodopsin 1  
**ChR2** channelrhodopsin 2  
**CI** confidence interval  
**CPLX1/CPX-1** complexin  
**CREB** cAMP response element-binding protein  
**CSP** cystein-string protein

**D. rerio** Danio rerio  
**D. melanogaster** Drosophila melanogaster  
**DCV** dense core vesicle  
**DIC** differential interference contrast  
**DNA** deoxyribonucleic acid  
**dNTP** desoxy nucleotide triphosphate  
**docked DCV** docked dense core vesicle  
**docked SV** docked synaptic vesicle  
**DP** dense projection  
**DTS** developmentally timed sleep  
**DTW** dynamic time warping

**E. coli** Escherichia coli  
**E. gracilis** Euglena gracilis  
**eCDF** empirical cumulative distribution function  
**EDTA** ethylene-diamine-tetra-acetic acid  
**EMS** ethyl methanesulfonate  
**ENDO** endosome  
**EPAC** exchange protein activated by cyclic AMP  
**EPG** electropharyngeogram  
**EPSC** excitatory post synaptic current  
**EtBr** ethidium bromide

**EuPAC $\alpha$**  photoactivatable adenylyl cyclase  $\alpha$  from *E. gracilis*

**FACS** fluorescence-activated cell sorting

**FAD** flavin adenine dinucleotide

**FDR** false discovery rate

**FLP** FMRF-like peptide

**FMN** flavin mononucleotide

**FRET** Förster resonance energy transfer

**G $_{\alpha i}$**  G<sub>i</sub> alpha subunit

**G $_{\alpha q}$**  G<sub>q</sub> alpha subunit

**G $_{\alpha s}$**  G<sub>s</sub> alpha subunit

**GABA** gamma-aminobutyric acid

**GCaMP** G-CaMP

**GEC1** genetically encoded Ca<sup>2+</sup> indicator

**GFP** green fluorescent protein

**GO** gene ontology

**GPCR** G protein-coupled receptor

**GUI** graphical user interface

**HisCl1** histamine gated chloride channel 1

**HPF-EM** high pressure freezing followed by electron microscopy

**IBMX** 3-isobutyl-1-methylxanthine

**ICE** interleukin-1  $\beta$  converting enzyme

**INS** insulin-like peptide

**KNIME** Konstanz Information Miner

**LB** lysogeny broth

**LV** large vesicle

**M. musculus** *Mus musculus*

**MAPK** mitogen-activated protein kinase

**MChAT** membrane-bound choline acetyltransferase

**miniSOG** mini singlet oxygen generator  
**MLP** multilayer perceptron  
**mPSC** miniature post synaptic current  
**Munc13/UNC-13** mammalian unc13  
**MWT** Multi Worm Tracker

**NaClO** sodium hypochlorite  
**NaN** not available number  
**NaN<sub>3</sub>** sodium azide  
**NaOH** sodium hydroxide  
**NBRP** National Bioresource Project  
**NGM** nematode growth medium  
**NLP** neuropeptide-like protein  
**NMDA** N-methyl-D-aspartate  
**NMJ** neuromuscular junction  
**NO** nitric oxide  
**NSF** N-ethylmaleimide sensitive factor / NSF-1

**PACAP** pituitary adenylate cyclase-activating polypeptide  
**PCA** phenol chloroform isoamyl alcohol  
**PCR** polymerase chain reaction  
**PDE** phosphodiesterase  
**PDF** pigment dispersing factor  
**PEG** polyethylene glycol  
**PKA/KIN-1** protein kinase A  
**PKC** protein kinase C  
**PM** plasma membrane

**Rab3/RAB-3** Rab3  
**RFP** red fluorescent protein  
**RIM-BP/RIMB-1** RIM binding protein  
**RIM/UNC-10** Rab3-interacting molecule  
**RNAi** RNA Interference

**ROI** region of interest  
**ROS** reactive oxygen species  
**Rprop** resilient backpropagation  
**RRP** readily releasable pool  
**RyR/UNC-68** ryanodine receptor

**SEWLB** single egg/worm lysis bugffer  
**SEWLB** single egg worm lysis buffer  
**SIS** stress-induced sleep  
**SNAP-25/RIC-4** synaptosomal-associated protein 25  
**Snapin/SNPN-1** Snapin  
**SNARE** soluble NSF attachment protein receptor  
**SNB-1** synaptobrevin  
**SNN-1** Synapsin / SNN-1  
**STX1/UNC-64** syntaxin  
**STXBP1/UNC-18** syntaxin-binding protein 1  
**STXBP5/TOM-1** syntaxin-binding protein 5 / Tomosyn  
**SV** synaptic vesicle  
**SYT/SNT-1** synaptotagmin

**TAE** TRIS acetate EDTA  
**TeTX** tetanus toxin  
**TRIS** tris-(hydroxymethyl)-aminomethane

**TRIZOL**

**unknown-type-2** unknown feature type 2  
**unknown-type-1** unknown feature type 1

**v-ATPase** vacuolar-type H<sup>+</sup>-adenosine triphosphatase  
**vAChT** vesicular acetylcholine transporter  
**VIP** vasoactive intestinal peptide  
**VNC** ventral nerve cord

**WGS** whole genome sequencing

**wt** wild type

**X. laevis** *Xenopus laevis*

## List of contributors

- Dr. Jana F. Liewald** Laboratory colleague. Contributed Electrophysiology data on BWM cells. XVII, XVIII, XXI, XXII, XXIII, 74, 90, 91, 93, 95, 96, 97, 104, 106, 109, 110, 225, 226
- Dr. Szi-chieh Yu** Laboratory colleague. Contributed HPF-EM data. XVIII, XXII, XXIII, 44, 73, 97, 104, 110, 112, 113, 227
- Prof. Alexander Gottschalk** Principal investigator. 39, 52, 119, 228
- Dr. Sebastian Wabnig** Laboratory colleague. Contributed preliminary data on bPAC ChR2(C128S) co-photoactivation and RCaMP in BWM cells fluorescence measurement. 44, 52, 66, 139, 152, 167, 168
- Jatin Nagpal** Laboratory colleague. 44, 66
- Heike Fettermann** Laboratory technician. 63
- Mona Höret** Laboratory technician. 63
- Kerstin Zehl** Laboratory technician. 63
- Negin AzimiHashemi** Laboratory colleague. 63, 66
- Tim Phillip Waldow** Laboratory research assistant . 63
- Dr. Elisabeth Fischer** Laboratory colleague. 66, 267
- Dr. Christian Schultheis** Laboratory colleague. Contributed ImageJ and R code. 66, 72
- Dr. Christina Schüler** Laboratory colleague. Contributed Electropharyngeogram data on pharyngeal muscle cells. 126, 127, 227
- Petrus Van der Auwera** Laboratory colleague. PhD thesis with emphasis in RIS calcium dynamics in freely behaving animals. 136, 140, 155, 160, 168, 228
- Barbara János** Laboratory colleague. Helped freezing animals during HPF-EM acquisition. 227
- Caspar-Elias Glock** Master student (2013). Project related work on RIS signaling pathway, tested several canonical pathway mutants as well as body wall muscle



calcium imaging for analysis of motor output during RIS activity. 44, 70, 125, 126, 127, 130, 131, 139, 157, 158, 160, 163, 164, 168, 169

**Anke Hermann** Laboratory rotation student (2013). Project related work on single cell expression in SMD and RMD neurons, second promoter pair test for validation of RIS experiment, as well as RIS related swimming assays. 48, 63, 130

**Jonas Pascal Weil** Laboratory rotation student (2014). Project related work on RIS signaling to AVK, ChR2(C128S,H134R) expression and *lim-6* knock-out. 48

**Marlene Steiner** Laboratory rotation student (2013). Project related work on GFP expression for RIS cell culture and RIS GABA mutant analysis. 130

**Dr. Kenneth Miller** Genetic Models of Disease Program, Oklahoma Medical Research Foundation, 825 Northeast 13th Street, Oklahoma City, OK (USA) 44

**Hernan Jaramillo** Research Assistant, Prof. Cori Bargmann, The Rockefeller University, 1230 York Avenue, New York, NY (USA) 44

**Prof. Manuel Zimmer** Research Institute of Molecular Pathology, Dr. Bohr-Gasse 7, 1030 Vienna (AT) 44

**Dr. Anindya Ghosh Roy** Group leader, National Brain Research Center, Deemed University, NH-8, Nainwal Mode, Manesar-122051, Haryana (IN) 44

**Prof. Harald Hutter** Simon Fraser University, Dep. of Biological Sciences, 8888 University Drive, Burnaby, BC (CA) 48

**Emiliano Cohen** PhD candidate, Prof. Millet Treinin Group, The Hebrew University of Jerusalem, Medical Neurobiology, Room Number 09 bld4 floor 4, Jerusalem (IL) 48

**Prof. Mark Gomelsky** Department of Molecular Biology, University of Wyoming, Ag C Bldg., Room 6007, Laramie, WY 82071 (USA) 52

**Dr. Manuela Stierl** Former PhD candidate, Prof. Peter Hegemann, Institute of Biology, Experimental Biophysics, Humboldt University Berlin, Invalidenstr. 42, 10115 Berlin (DE) 52

**Prof. Andrew Fire** Stanford University School of Medicine, 291 Campus Drive, Li Ka Shing Building Stanford, CA (USA) 52

**Prof. Cori Bargmann** The Rockefeller University, 1230 York Avenue, New York, NY (USA) 52

**Dr. Baris Tursun** Max Delbrück Center, Berlin Institute for Medical Systems Biology, Robert-Rössle-Str. 10, Building 89, Room 019, 13125 Berlin (DE) 55, 131

**Rebecca D. McWhirter** Research Assistant, Prof. David M. Miller, III., 3120 Medical Research Building 3, Nashville, TN 37232 (USA) 67, 228

**Kalen J. Petersen** Graduate student, Prof. David M. Miller, III., 3120 Medical Research Building 3, Nashville, TN 37232 (USA) 67

**David M. Miller, III.** 3120 Medical Research Building 3, Nashville, TN 37232 (USA) 67, 134, 228

## A. Methods performed by colleagues

This section contains a short description on methods that were used for acquisition of data contributed by colleagues and presented in this thesis, as well as a disclosure on personal involvement during data acquisition.

### A.1. CRISPR/Cas9 genomic mutation

CRISPR/Cas9 genomic mutation SNN-1B(S9A) was designed and performed by Knudra Transgenics (5201 S Green St, ste 140, Murray, UT, 84123 USA). The silent mutations introduced were required to suppress further genome editing by the Cas9 endonuclease (figure A.1).



Figure A.1.: SNN-1B(S9A) sequence.

Genomic mutations introduced to obtain SNN-1B(S9A) sequenced by two primers depicted against the wt sequence (top, NC\_003282: *snn-1*, *snn-1*: forward primer, *snn-1 r*: reverse primer) Mutations highlighted and sequence clipped to the region of interest. The encoded protein has a single point mutation, S9A (bottom).

### A.2. Electrophysiology of body wall muscle cells

Electrophysiology of body wall muscle cells was performed by Dr. Jana F. Liewald as described [206, 510]. Optogenetic activation was performed with an LED lamp

(KSL-70, Rapp OptoElectronic, Hamburg, Germany; 470 nm, 8 mW mm<sup>-2</sup>) controlled by an EPC10 amplifier (with Patchmaster software, HEKA, Germany). Puff-application in electrophysiology was performed with a Parker Picospritzer III with a application time range of 80 ms. mPSC analysis was performed by Dr. Jana F. Liewald with Mini Analysis software (Synaptosoft, Decatur, GA, USA, version 6.0.7).

Shortly, animals were immobilized and the body pressure relieved by a puncture of the hypodermis. The body is then opened with a cut, followed by gut aspiration. The hypodermis and muscle flap is glued to the substrate, allowing for BWM cell patching next to the VNC (figure A.2).

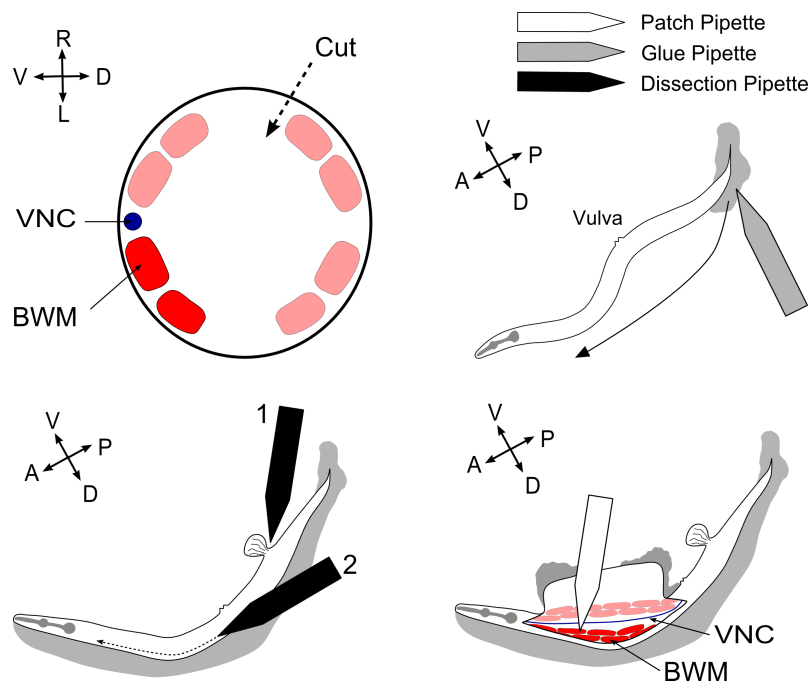


**Figure A.2.: Electrophysiology sample preparation.**

The BWM patched are next to the VNC (upper left). The animal is glued to the substrate (upper right) and a puncture at the tail releases the internal pressure (lower left). An posterior to anterior cut opens a hipodermis and BWM flap that is glued to the substrate (bottom left). Aspiration of the gut allows patching of a BWM next to the VNC (bottom right).

Figure from [510].

Voltage clamp recordings allow to investigate mPSCs (figure A.3 print screen during analysis).



**Figure A.3.: Electrophysiology mPSC analysis.**

Print screen during data analysis, mPSC calling performed by the software with manual quality control.

Figure provided by Dr. Jana F. Liewald.

### A.3. EPG Measurements

EPG of pharynx muscle cells was performed by Dr. Christina Schüler [259,511,512].

### A.4. High pressure freezing followed by electron microscopy (HPF-EM)

HPF-EM were performed by Dr. Szi-chieh Yu, with a subset of animals frozen by Barbara Jánosi and myself, as described in Weimer *et al.* [513]. Illumination by an LED lamp (KSL-70, Rapp OptoElectronic, Hamburg, Germany; 470 nm, 8 mW mm<sup>-2</sup>) and freezing were manually synchronized (figure A.4 depicts the high pressure freezer used). Thus, the minimal interval between end of illumination and high pressure freezing was 5 s. Freeze substitution, image acquisition and feature call were performed by Dr. Szi-chieh Yu. Image ROI tag were set by myself with help from Dr. Szi-chieh Yu (only PM and DP ROIs). Data analysis was performed by me with help from Dr. Szi-chieh Yu (section 2.2.7.5, p. 73).

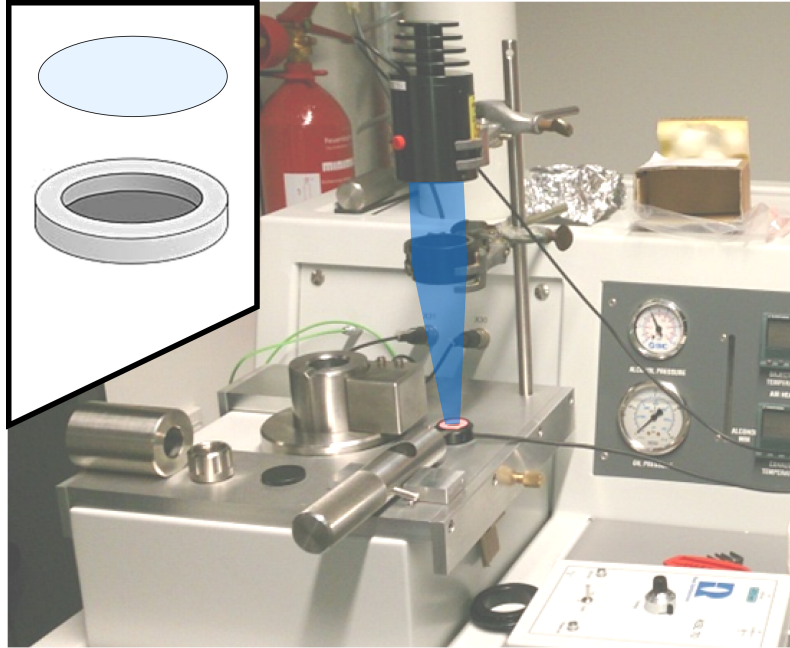


**Figure A.4.: High pressure freezer with LED for optical stimulation.**

Animals were optically stimulated with an LED and freezing were manually synchronized. Animals were frozen in a metallic planchet covered with a transparent sapphire disc (scheme in box).

Image provided by Dr. Szi-chieh Yu.

## **A.5. RIS isolation and RNA-Seq**

RIS cell dissociation, as performed by myself in the pilot RIS isolation, was conducted by Rebecca D. McWhirter. She further isolated the RIS cells with a fluorescence-activated cell sorting (FACS) system, where the constraints were expression of both fluorescent proteins, GFP and mCherry. The two fluorophore strain was required, since the Cre/LoxP driven RIS::GFP expression was not sufficiently bright for the sorting system. RNA extraction yielded about 5 ng per sample and library were amplified with Clontech SMARTer v3. The RNA-Seq produced about 60 million reads per sample. 556 genes were at least 2 times enriched in RIS with FDR-corrected p-value  $< 0.05$  (edgeR). This gene list was provided by David M. Miller, III. and further analyzed in this thesis by Petrus Van der Auwera, Prof. Alexander Gottschalk and myself. The RNA-Seq data presented in this work was acquired from 2 RIS and 2 internal control (all cells but RIS) groups from L4 larvae.

## B. Software

This chapter describes the software created during this thesis in detail. All software is included in the accompanying digital media.

### B.1. KNIME Workflows

The Konstanz Information Miner (KNIME) is an open platform software for data analysis pipelining and workflow automation. The following KNIME workflows were written during the course of this thesis. A table summarizes the required KNIME version, extensions, third-party software as well as file inputs and file outputs. Following, a description of the required files, the workflow automation as pseudo code and the workflow schematic is given.

#### B.1.1. KNIME Multimodal illumination tracker data analysis

The KNIME Multimodal illumination tracker data analysis workflow was written for analysis of data sets created by the multimodal illumination tracker [176,375]. The structure of the workflow is modular and hard coded, it requires many inputs from the user in different levels during the analysis process.

**Table B.1.:** KNIME Multimodal illumination tracker data analysis summary

Type	Description
KNIME version	2.12
KNIME Extensions	R
Third-party software	R
Input files	Table header, Folder with head encoded data from the Multimodal illumination tracker
Output files	Table of results, Optional visualization

The files for analysis are created by the Multimodal illumination tracker after head encoding and data analysis with 12 segments. Files for analysis are expected to be named as following: "GroupID worm XX-HEdata.txt", where GroupID is a string for the name of the group and XX is a string with two characters used for movie name deduplication in a folder. Movies with the same GroupID are binned in the same result group, irrespective of location in multiple folders.

Manual input is required in nodes listed in table B.2.

**Table B.2.:** KNIME Multimodal illumination tracker data analysis manual input

<b>Variable</b>	<b>Value</b>	<b>Description</b>
Max velocity	In $\mu\text{m s}^{-1}$	In Input variables. Velocities above this threshold are considered to be due to systemic error.
Min velocity	In $\mu\text{m s}^{-1}$	In Input variables. Velocities below this threshold are considered to be due to systemic error.
Allowed length variation	In %	In Input variables. Lengths below or above this threshold are considered to be due to systemic error.
End Time	In s	In Input variables. Movie time after this value are excluded from analysis.
Start Time	In s	In Input variables. Movie time before this value are excluded from analysis.
Moving average	Selection	In Input variables. Set to 0 no moving average is performed. Set to 1 a moving average with a center Gaussian of window 21 is applied to all data columns.



**Table B.2.:** (continued)

<b>Node</b>	<b>Value</b>	<b>Description</b>
Time to mean for length measurement	In s	In <code>Input variables</code> . Period length from <code>Start Time</code> in seconds for mean length measurement. The calculated mean length and the <code>Allowed length variation</code> define the threshold for length measurements, values beyond this region are considered to be due to systemic error.
List files	Selection	A list of folder for analysis.
Lookup table for heading	Input file	A file with column names for KNIME data table.
Norm. end time	In s	Period length from <code>Start Time</code> in seconds for mean data measurement. The calculated mean data define the value for data normalization.
Norm / Bin	Selection	Set to 0, data is passed without changes. Set to 1, data is normalized to the first seconds of the movie as defined by <code>Norm. end time</code> . Set to 2, time is binned into bins defined by <code>Time binner</code> .
Time binner	Set bins	In <code>Case for Norm.</code> Set amount and length of bins for the time domain.
Time Level	Set rules	In <code>Filter False Values</code> . Set rules for filtering data points acquired with wrong level.
To few data points	Input	In <code>Filter False Values</code> . Set a value from 0 to 1 for the amount of allowed exclusions before a whole movie is excluded from analysis. 0 does not allow any frame exclusion.
Filter group	Selection	Select the group for visualization.

**Table B.2.:** (continued)

<b>Node</b>	<b>Value</b>	<b>Description</b>
R Plot Mean+- SEM	Input	Change code for visualization of the feature of interest (see section B.2.2).
Save table	File path	Select file path to store results table.
Read saved table	File path	Select file path to previously stored results table.

**B.1.1.0.1. Pseudo code** The workflow in pseudo code is as follows:

1. If `Read saved table` set, read results table and go to `Filter GroupID` for visualization, else
2. Read input variables, `Lookup table` for heading and `List files`
3. Calculate movie length for analysis from variable input
4. Filter files with `HEdata.txt` in the name
5. For each file `HEdata.txt`, do
  - a) Read file
  - b) Add column header from `Lookup table` for heading
  - c) Crop time domain to variable start – end
  - d) Join mean length of the animal in start of movie
  - e) Exclude data points where column `Light` is set to 0
  - f) If `Moving average` set to 1, perform Gaussian moving average with 21 data points window
6. Add meta data to results table: `file path`, `GroupID`
7. Round time
8. Exclude data points where column `Level` is set to 0
9. Filter data points where `Time` and `Level` are not synchronized
10. Filter data points where column `Length variation` compared to mean length of start of movie is higher than `Allowed length variation`
11. Exclude movies with too many data points filtered out, as defined by `To few data points`
12. Calculate percent of filtered out data
13. Case `Norm / Bin`, do

- 1 - pass data
  - 2 - Normalize data columns to time range defined by `Norm. end time`
  - 3 - Bin time domain as defined in `Time binner & Set bins`
14. Calculate Speed as absolute velocity
  15. Calculate Mean, SD and N for each data column, grouped per `Time`, `GroupID` and `Level`
  16. Save results table
  17. Filter `GroupID` for visualization
  18. Plot results as defined in `R Plot Mean+-SEM B.2.2`

**B.1.1.0.2. Workflow scheme** The workflow schematic is depicted in figure B.1. The `Input variables` meta node defines the time range for analysis as well as the threshold filtering systematic errors (figure B.2). The `Iterate List of Files` meta node reads the result tables into KNIME, adds meta data based on the file name and crops the time column to the defined time range (figure B.3). The `Filter False Values` meta node filters data points acquired at wrong synchronization of image acquisition and light level output from the multimodal illumination tracker. It also excludes data points that do not meet the allowed length variation as well as completely excludes movies if the threshold of allowed wrong data points is reached (figure B.4). The `Quantify erroneous data points` meta node calculates the overall rate of data filtered out as a quality control for the user (figure B.5). The `Case for Norm` meta node selects how to further treat the data table dependent on the state of the variable `Norm / Bin`. It either does nothing, sends the data for normalization in the `Normalizer` meta node or bins the time domain (figure B.6).

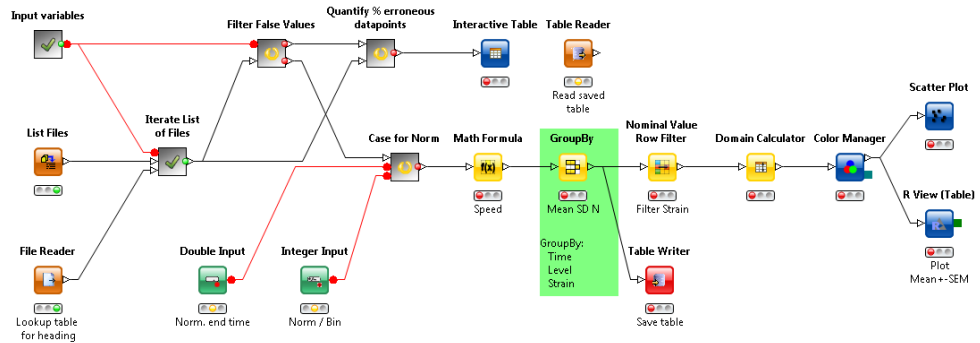


**Figure B.1.:** KNIME Multimodal illumination tracker data workflow. This workflow searches for data encoded by the Multimodal illumination tracker, filters data points wrongly assigned due to systematic errors and sends the table to R for results visualization.

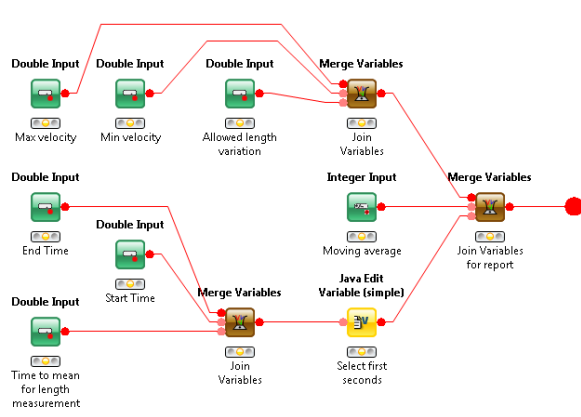


**Figure B.2.:** KNIME Multimodal illumination tracker data Input variables meta node internals. Variable input meta node for data quality control of tracker data output.

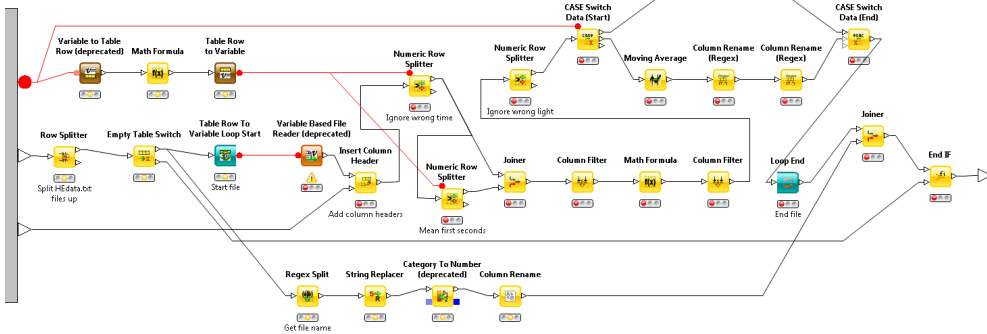


**Figure B.3:** KNIME Multimodal illumination tracker data *Iterate List of Files* meta node internal. This meta node reads the tracker output data and adds meta data. It also crops the movie length as selected for analysis. Optionally, a moving average on the data columns is performed.

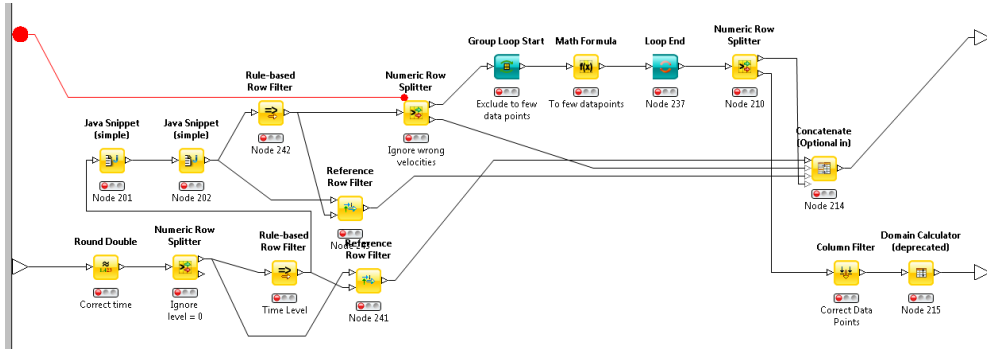


**Figure B.4:** KNIME Multimodal illumination tracker data *Filter False Values* meta node internal. This meta node filters the data table, excluding systematic errors from the tracker as defined by the user. Movies with too many entries filtered are excluded from analysis.

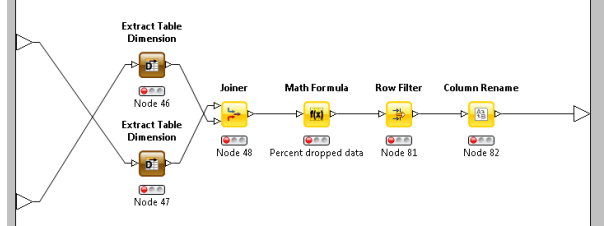


**Figure B.5:** KNIME Multimodal illumination tracker data *Quantify erroneous data points* meta node internal. This meta node calculates the percentage of data filtered out by the imposed constrains for quality control.

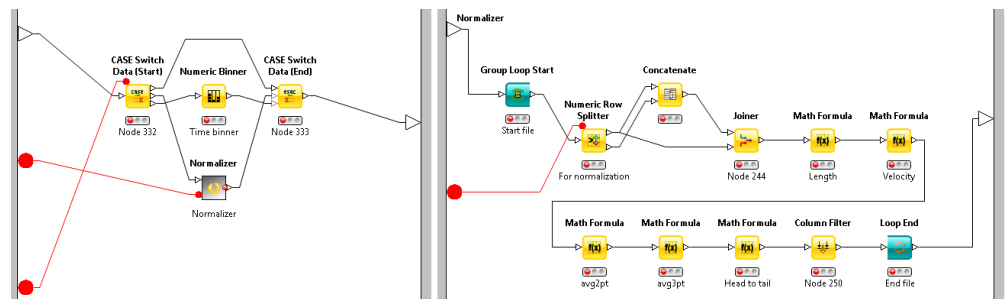


**Figure B.6:** KNIME Multimodal illumination tracker data Case for Norm meta node internal (left). This meta node processes the data table as defined by the variable Norm / Bin, i.e. pass or normalize data, or bin the time domain. Normalizer meta node internal (right). This node normalizes the data columns to the first seconds of the movie as defined by the the variable Norm. end time.

### B.1.2. KNIME Contraction assay analysis

The KNIME Contraction assay analysis workflow was written for analysis of data sets created by module adapted for contraction assays originated from the multi-modal illumination tracker [176,375]. There are hard coded variable values in this workflow, it requires therefore input from the user during the analysis process. The output is normalized animal's length grouped per genotype.

**Table B.3.:** KNIME Contraction assay analysis summary

Type	Description
KNIME version	2.12
KNIME Extensions	–
Third-party software	–
Input files	Folder with files for analysis
Output files	Optional analysis results

The files for analysis have three columns (Time (s), Illumination and Length (um)). The workflow expects file nomenclature to be “Group worm Number.txt”, where “Group” is the group identifier and “Number” is a suffix for deduplication of file names.

**B.1.2.0.3. Pseudo code** The workflow in pseudo code is as follows:

1. Read folder structure and search for files from type \* worm \*.txt
2. For each file in list do
  - a) Read file
  - b) Add Group identifier from file name Group
  - c) Define time domain for normalization
  - d) Calculate mean length of animal for this time domain
  - e) Define minimal and maximal allowed length of animal based on deviation from mean length
  - f) Replace all length values outside of the min max boundaries as not available number (NaN)
  - g) Recalculate mean length of animal for time domain
  - h) Normalize length to mean length

3. Group data by Group identifier and Time
4. Plot results

**B.1.2.0.4. Workflow scheme** The workflow schematic is depicted in figure B.7, the file reader meta node is expanded in the middle, while the normalizer meta node is expanded in the bottom of the figure. User input is required in the three nodes marked in red. The row filter defines the time domain for normalization. The two following math nodes define the minimal and maximal allowed variation in the length of the animal. Permissive values for these nodes are 0.6 and 1.3, allowing a contraction of 40 % and an elongation of 30 %, respectively.



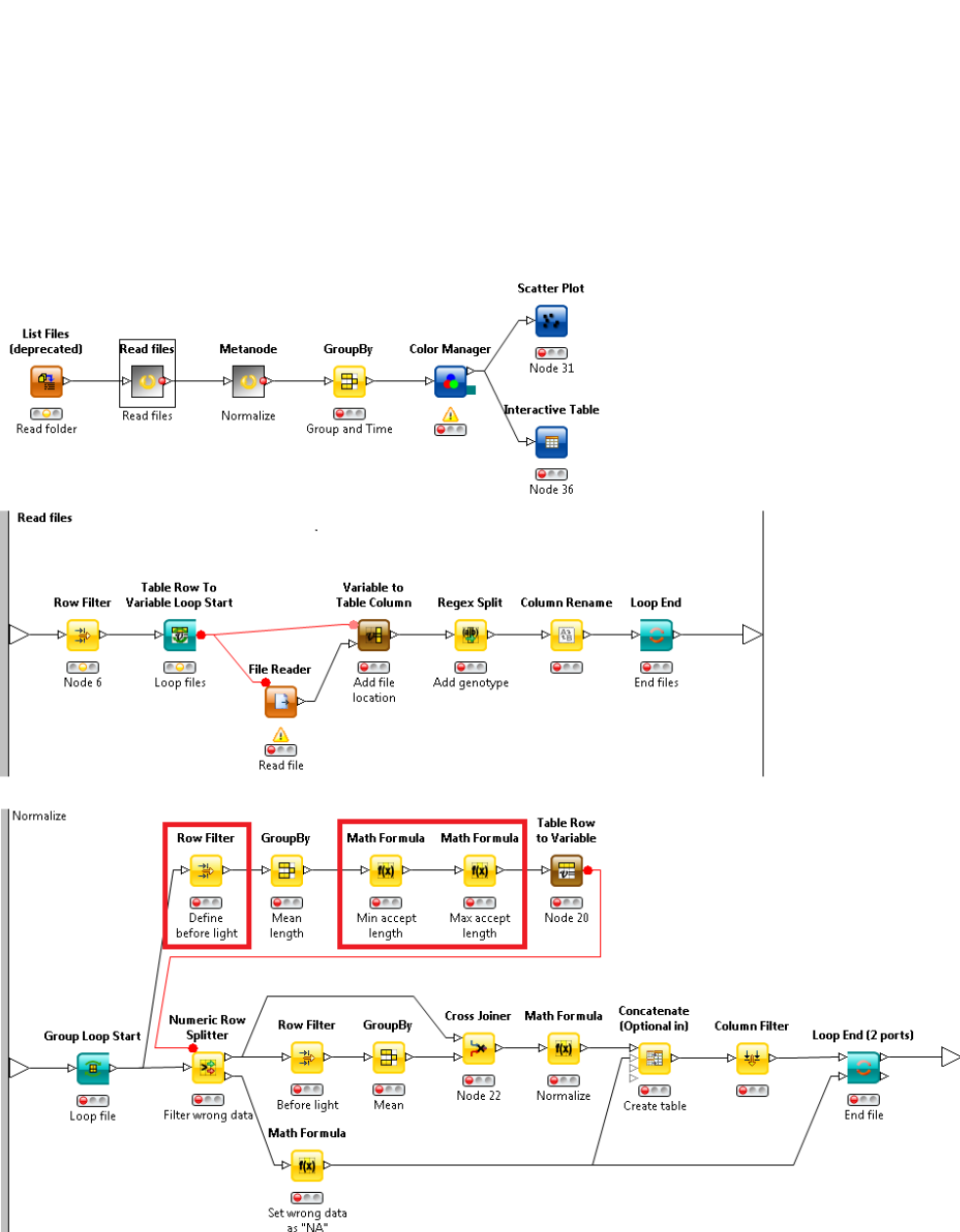


**Figure B.7:** KNIME Contraction assay analysis workflow. This workflow searches for all analyzed files from the contraction assay module of the multimodal illumination tracker and normalizes the length according to user input in the nodes marked in red.

### B.1.3. KNIME Choreography and MWT

This workflow automates the command line input required by Choreography. Furthermore, a simple visualization of Choreography's output and export through R (library ggplot2 required) is present.

**Table B.4.:** KNIME Choreography and MWT summary

Type	Description
KNIME version	2.12
KNIME Extensions	Next Generation Sequencing
Third-party software	bash, MWT Choreography, R
Input files	Chore_command.txt, Chore_header.txt, folder with files for analysis
Output files	Optional manual export after analysis

The required `Chore_command.txt` file contains the command to be sent for choreography with a semicolon as a place holder for the file location of the file to be analyzed by choreography. The required `Chore_header.txt` file contains two columns. The first column gives the name of unnamed columns in KNIME (viz. "Col0", "Col1", ...) and the name of columns from Choreography. `Chore_header.txt` is not required for choreography control, but for visualization of the data output from choreography. Furthermore, the folder organization where the Multi Worm Tracker (MWT) files are stored to requires the name of the genotype of interest to be the file name. Analysis will automatically group files with same name as independent measurements from the same genotype.

**B.1.3.0.5. Pseudo code** The workflow in pseudo code is as follows:

1. Read `Chore_command.txt`
2. Read folder structure and search for files from type `summary` and `dat`
3. Exclude folders that contain a `dat` file from analysis<sup>1</sup>
4. Create unique names for folders
5. Create the java command for Choreography
6. Send each command to Choreography

<sup>1</sup>This is for convenience only, should a folder be reanalyzed by Choreography, skip this action.

The analysis part of the workflow runs as follows:

1. Read folder structure and search for files from type dat
2. For each dat file listed do
  - a) Read dat file
  - b) Read Chore\_header.txt file
  - c) Insert correct column headers
  - d) Correct frame acquisition time to nearest possible time bin
3. Extract group name from file name
4. Join group name to the results table
5. Analyze features of interest grouped by group name and time
6. Plot results

**B.1.3.0.6. Workflow scheme** The workflow schematic is depicted in figure B.8 and the analysis scheme in figure B.9.

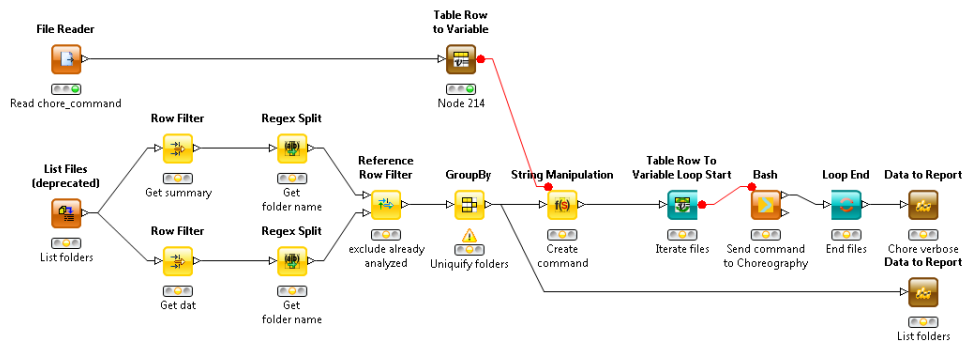


**Figure B.8:** KNIME Choreography workflow. This workflow searches for all yet not analyzed folders created with the MWT and creates a bash command for Choreography.

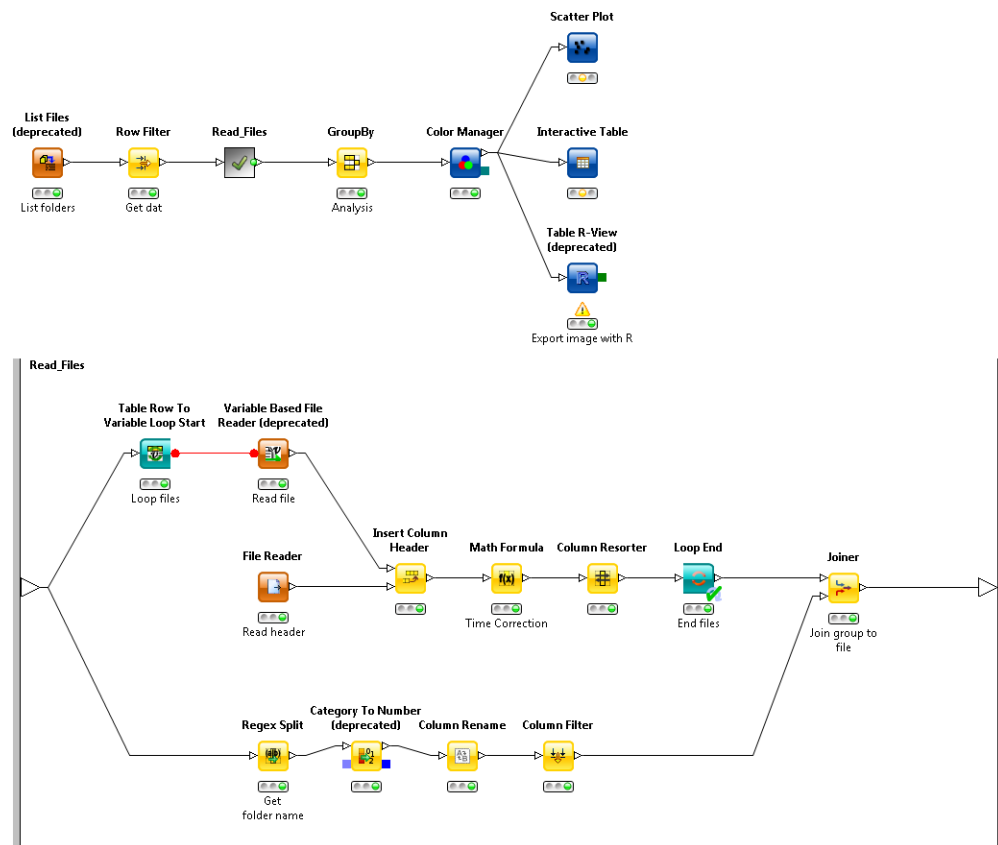


**Figure B.9.:** KNIME Choreography analysis. This workflow loads and groups the dat files generated by Choreography for analysis and plotting of the results. The file reader meta node is expanded in the lower part of the figure.

### B.1.4. KNIME Circos

The KNIME Circos workflow reads data output exported from the Galaxy Server and converts it into tables for Circos, a plotting program for chromosomal information.

**Table B.5.:** KNIME Circos summary

Type	Description
KNIME version	2.12
KNIME Extensions	–
Third-party software	–
Input files	5 files
Output files	5 files

The workflow requires five files, all in tab separated format without header or column names. The following list shows the content of each column and a small description.

- **Range** – Chromosome name; first base of range, last base of range. This range defines a bin for plotting in Circos. During this work, a range of about 100 000 was used.
- **INS** – Chromosome; start of insertion; end of insertion; bases inserted. This file lists the base insertions.
- **SNP** – Chromosome; start of insertion; end of insertion; base mutations. This file lists the positions for single nucleotide polymorphism, the base mutations column is usually 1.
- **DEL** – Chromosome; start of deletion; end of deletion; bases deleted. This file lists the bases deleted.
- **BED Uncovered bases** – Chromosome; start of uncovered region; end of uncovered region; amount of covered bases. This file lists the uncovered regions, the amount of covered bases column is usually 0.

**B.1.4.0.7. Pseudo code** The workflow in pseudo code is as follows:

1. Read all files
2. For INS, SNP, DEL and Uncovered bases file, do

- a) Rename chromosome names from Galaxy to Circos format
- b) Remove mitochondrial sequence information <sup>2</sup>
- c) Calculate length of each region
- d) For each chromosome, do
  - i. Filter Range file for processed chromosome
  - ii. Create a list of regions where an entry in each file is present
  - iii. For each region where an entry is present, do
    - A. Exclude all entries that are not in the range under process
    - B. Count the amount of features in this range
    - C. If BED uncovered bases: also count the amount of bases in this range
    - D. Write a table entry with chromosome name; region start; region end; amount of features in this range
    - E. If BED uncovered bases: also write a table entry with chromosome name; region start; region end; count of uncovered bases in this range
- e) Export a tab separated file without header or column names with the counts per region for each file as well as uncovered bases count per region. Column order and contents as above.

**B.1.4.0.8. Workflow scheme** The workflow schematic is depicted in figure B.10. All meta nodes have the same structure schematically drawn in figure B.11. Note that BED uncovered file process is split into two meta nodes. The second copy has a math node changed from counting the amount of features per region to counting the amount of uncovered bases per region (red highlight).

---

<sup>2</sup>Mutation was not in mtDNA, inferred from crossing for WGS

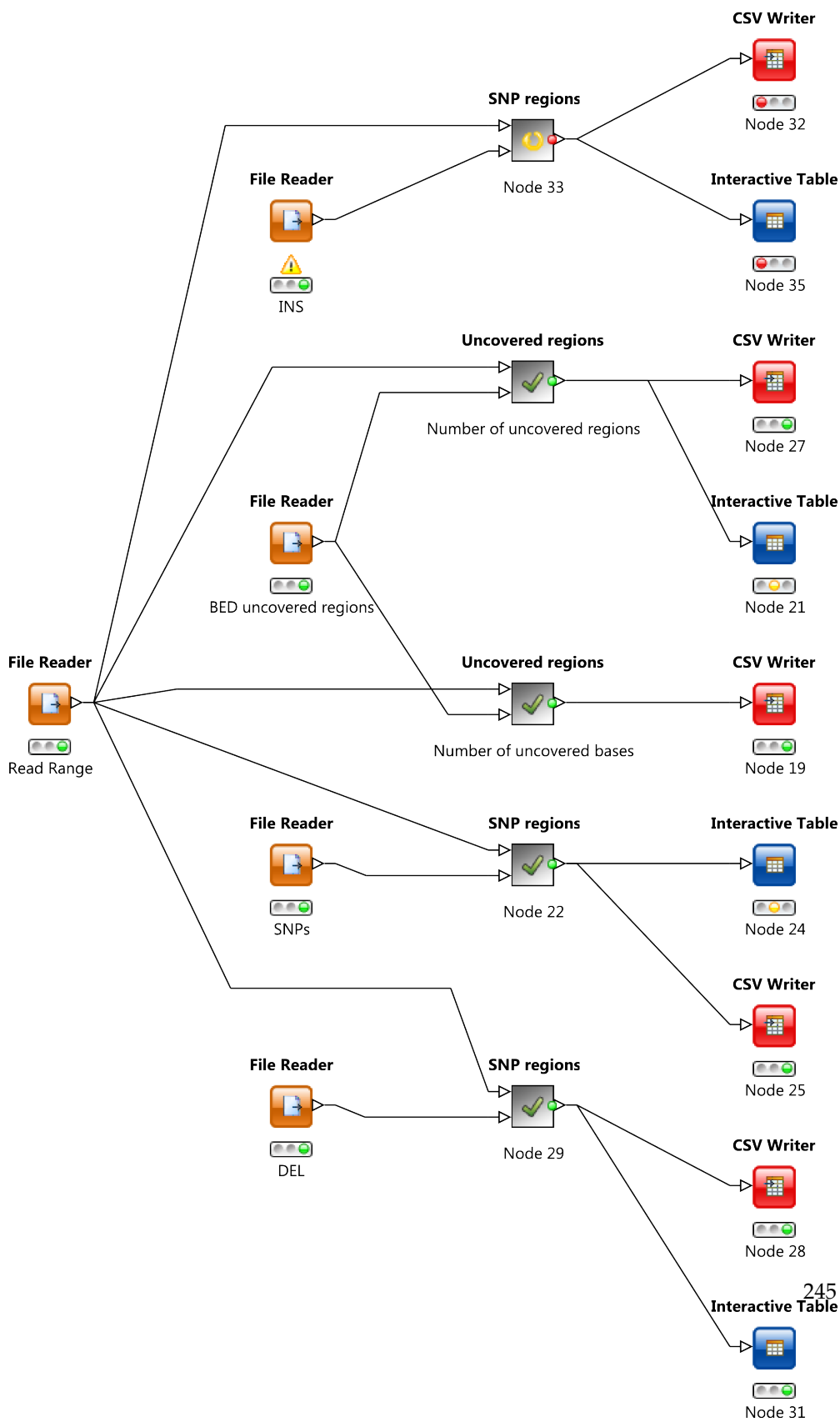


**Figure B.10.:** KNIME Circos workflow. This workflow converts the output from Galaxy Server into files with data binned into ranges, as required for plotting with Circos.

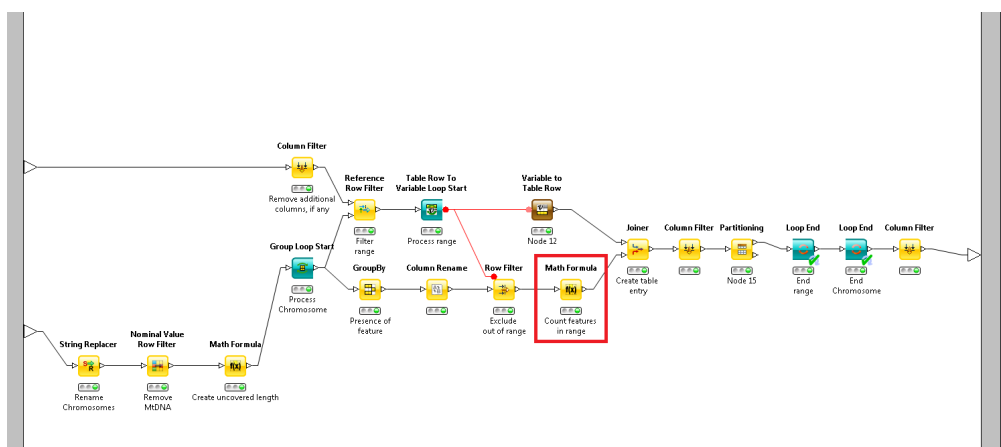


**Figure B.11.:** KNIME Circos workflow meta node internal. All meta nodes in this workflow have the same structure, apart from the math node highlighted in red for counting the amount of uncovered bases instead of the amount of uncovered regions.



### B.1.5. KNIME EM analysis

This workflow automates the analysis of the data output from ImageJ on the features of interest in EM images B.4.1. The structure of the workflow is modular and hard coded, it requires many inputs from the user in different levels during the analysis process.

**Table B.6.:** KNIME EM analysis summary

Type	Description
KNIME version	2.12
KNIME Extensions	
Third-party software	R
Input files	EM Images, ImageJ output B.4.1, CalculationHeader, Optional Distance tables
Output files	Distance tables, Result table, optional visualizations

This workflow requires data to be organized in a folder structure as follows: `.\GroupID\YYYY-MM-DD GroupID-Num\Contents`, where `GroupID` is an identification name for the experimental condition in the form of “AG” followed by a number, `YYYY-MM-DD` is the date of acquisition in Year (Y), Month (M) and Day (D), `Num` is a single numeral for deduplication and `Contents` is the image files, ROI zip files and output from ImageJ B.4.1. Further, this workflow expects images to be named as `AxSy-z`, where `A` is a letter and `x` is a numeral, both defining the grid position from where the image was acquired. `S` is a contraction for slice and `y` is a numeral defining the slice number from the grid depicted by the image. Multiple synapses analyzed in the same image are deduplicated by the addition of the suffix `-z` to the image name, where `z` is a numeral. This effectively copies the same image with a suffix in the name, as well as all ROI zip files use this suffix for link them to the correct synapse. Furthermore, images analyzed were also stored with a `scored-` prefix to the image name. The `scored-Image` was used to mark the features of interest to be tagged in ImageJ, as well as to search for scored images in this workflow.

Distance measurements in two dimensions are performed by an R script called by this workflow, see B.2.1. Manual input is required in nodes listed in table B.7.

**Table B.7.:** KNIME EM analysis manual input

<b>Variable</b>	<b>Value</b>	<b>Description</b>
Pixel size <sup>3</sup>	In nm px <sup>-1</sup>	Size in nm for a px
Select input for analysis <sup>4</sup>	0 or 1	Set to 0 for using a previously saved table or to 1 for using the computed table.
Perimeter factor	In nm	Normalization factor for feature count per perimeter of the plasma membrane.
Area Factor	In nm <sup>2</sup>	Normalization factor for feature count per area of the plasma membrane.
Bin size in nm <sup>5</sup>	In nm	Bin size for distance histogram of binned distance of feature to dense projection through the plasma membrane.
Select Dataset for eCDF	Selection	Select column for eCDF plot.
eCDF names <sup>6</sup>	Name of groups	Set the name of possible groups in the rule engine for table transformation to R format.
Groups for analysis	Selection	Select the groups for analysis.
Feature for analysis	Selection	Select the feature for analysis.
ROI type for analysis	Selection	Select the ROI type for analysis.
Freeze date	Date table	Freeze date in KNIME format, table input for each YYYY-MM-DD GroupID-Num folder.

<sup>3</sup>In meta node Calculation

<sup>4</sup>In meta node Pooling

<sup>5</sup>In meta node Bin Feature by Distance

<sup>6</sup>In meta node Create eCDF Table

**Table B.7.:** (continued)

<b>Node</b>	<b>Value</b>	<b>Description</b>
R eCDF	Group names	Input group names, add equivalent number of lines for the plot and select colors for plotting.
R Bee swarm	Characteristic	Select the ROI characteristic for plotting. Add folder path for image export. R requires libraries <code>beeswarm</code> and <code>gplots</code> .
R CountByArea	Color and file path	Select colors for all groups plotted. Add folder path for image export.
R CountByPerimeter	Color and file path	Select colors for all groups plotted. Add folder path for image export.
R Bar and error plot	Color and file path	Select colors for all groups plotted. Add folder path for image export.
R Count	Color and file path	Select colors for all groups plotted. Add folder path for image export.
ANOVA Count	Characteristic	Select the ROI characteristic for analysis.
ANOVA Count-ByArea	Characteristic	Select the ROI characteristic for analysis.
ANOVA Count-ByPerim	Characteristic	Select the ROI characteristic for analysis.
ANOVA	Characteristic	Select the ROI characteristic for analysis.

**B.1.5.0.9. Pseudo code** The workflow in pseudo code is as follows:

1. If `Select input for analysis` set to 1, do {
2. Read all folders
3. Search for `scored-` images
4. Filter original images that have been scored
5. For each image, do
  - a) Read all linked ROI results

- b) Add meta data to the image (file location, file name, file type, ROI name, ROI type, ROI old name<sup>7</sup>, grid position, slice number, GroupID, acquisition date
  - c) Add area and perimeter of plasma membrane to the pertaining ROIs
  - d) Calculate the area fraction as ROI area divided by plasma membrane ROI area
  - e) Calculate radius and diameter of a circle of area equal to ROI area
  - f) Search pre calculated ROI distance file
  - g) If ROI distances were calculated, do
    - i. Load calculated distances
  - h) else, do
    - i. Send ROI coordinates to R for distance calculations B.2.1
    - ii. Save table of calculated distances in Coordinates folder as ImageName\_results.table
  - i) Covert pixel to nm using Pixel size
6. Pool groups SV+DSV, DCV+UNKNOWN, CIS+UNKNOWN-Type-2, UNKNOWN+UNKNOWN-Type-2
  7. Join Freeze date table
  8. Save data table
  9. } else, if Select input for analysis set to 0, load data table
  10. In case analysis of counts, do
    - a) Select Groups for analysis
    - b) Add count of 0 for images without particular ROI types
    - c) Count each ROI type per image
    - d) Calculate the count per area by dividing count by area of plasma membrane times Area Factor
    - e) Calculate the count per perimeter by dividing count by perimeter of plasma membrane times Perimeter Factor
    - f) Select Feature for analysis
    - g) Analyze table in ANOVA Count, CountByArea, CountByPerim
    - h) Plot in R Count, CountByArea, CountByPerim
  11. In case analysis of ROI features, do
    - a) Select ROI type for analysis

---

<sup>7</sup>The name in the ROI zip file.

- b) Calculate mean ROI feature per image
  - c) Analyze in ANOVA
  - d) Plot in R Bee swarm, Bar and error plot
12. In case eCDF of ROI distances per area, do
- a) Select Dataset for eCDF
  - b) Sum distances per image
  - c) Divide summed distances by area of plasma membrane
  - d) Reorganize table for R, requires setting eCDF names
  - e) Plot data in R eCDF
13. In case histogram of ROI occurrence per distance, do
- a) Bin distances of ROI feature to Bin size in nm
  - b) Count occurrences per bin
  - c) Add bins with 0 features
  - d) Analyze data
  - e) Reorganize table for export
  - f) Export in Microsoft Excel xls format

**B.1.5.0.10. Workflow scheme** The workflow schematic is depicted in figure B.12. The colored background regions specify the overall function of the overlaying part of the workflow. From left to right: green, input; red, read ImageJ results; grey, distance calculation; lilac, save data table; dark, cyan count analysis; blue, ROI feature analysis; brown, eCDF analysis; yellow, export binned distances.

The following figures depict the internal structure of the meta nodes in the workflow.

Data input and calculation is performed through various meta nodes. The Read images meta node selects the images analyzed by searching for the scored- flagged images and use these as a reference for the original images (figure B.13). This allows one to store unscored images in the same folder without an effect on the analysis. The Prepare file paths meta node uses the absolute file path to a scored image to search for linked ImageJ result files (figure B.14). The Read ROI Results meta node reads all ROI result files associated to an image (figure B.15). It further extracts and adds meta data from the folder and file name. The internal meta node Add PM Area (expanded in the lower part of figure B.15) joins the corresponding plasma membrane

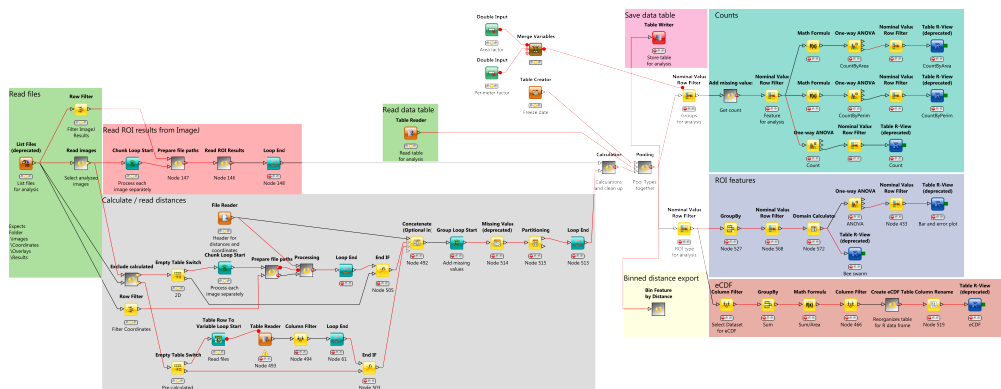


**Figure B.12.:** KNIME EM workflow overview. Color background for specific function: green, input; red, read ImageJ results; grey, distance calculation; lilac, save data table; dark, cyan count analysis; blue, ROI feature analysis; brown, eCDF analysis; yellow, export binned distances.

ROI area and perimeter to each ROI result. This allows for the calculation of the area fraction occupied by a ROI compared to the pertaining plasma membrane area. This node accepts synapses with a single defined plasma membrane ROI. Should a synapse have a second plasma membrane ROI defined, it will automatically sum the area of both ROIs. Cases with more than two plasma membrane ROIs defined ignore the further ROIs. There is no option to subtract one ROI from another. These cases, more than two plasma membrane ROIs or exclusion areas defined as a inner plasma membrane ROI, have to be calculated manually. The `Exclude` calculated meta node searches for precalculated 2D distance tables stored in a previous run of the workflow and excludes the pertaining ROI from distance measurements (figure B.16). It also sends the full file path of the precalculated distance tables to a table reader node. Should distances be recalculated, i.e. after changes made to the ROI coordinates, then the user has to manually discard the pertaining `ImageName_results.table` files from the `\Coordinates` folder. The `Prepare file paths for distance calculations` meta node adds a few nodes that check the amount of associated plasma membrane ROIs in an image to the already described `Prepare file paths` meta node (figure B.17). Only images with a single associated plasma membrane are sent for distance calculations. The `Processing` meta node sends only images with a single plasma membrane ROI for distance calculations (figure B.18). The internal `Distance calculations` meta node is depicted in figure B.19. It contains meta nodes for the distance calculations (first column of nodes), meta nodes for meta data addition (second

column) and a meta node to create the file name storage of the distance results table (right). Empty result tables are not stored by this meta node. The `Linear distance` and the `Path distance` meta nodes are similar (figure B.20), both send the coordinate file path to R for analysis. `Linear distance` uses the R script described in B.2.1.1, while `Path distance` uses the R script described in B.2.1.2. The latter additionally requires the coordinate file from the plasma membrane, passed to R in the beginning of the meta node. Both meta nodes contain a sequence of math nodes required to ensure proper data type after R calculation of distances. The concatenated results of all distances is passed further to the next meta node. The `Enrich` meta node adds meta data to the R output based on the full file path from the coordinate files (figure B.21). The concatenated results of all distance calculations are saved in a `table` file in the `Coordinates` folder for later reference. The `SavePath` meta node creates the full file path for table storage based on the coordinate file path (figure B.22). After distance calculations were performed, the missing distances are added as missing values. In the `Calculation` meta node, both data tables, ImageJ results and R distances, are joined to create one result table (figure B.23). Prior to the join process, ROI diameter and radius is added to the ImageJ result table. These calculations are performed in a circle of area equal to the ROI's area. After both tables are joined, the measurements are converted to nm based on the user input to the `Pixel size` node. This conversion is performed in the meta node `Pixel to nm` expanded in the bottom of the figure. The `Pooling` meta node pools different ROI types together (`SV+DSV`, `DCV+UNKNOWN`, `CIS+UNKNOWN-Type-2`, `UNKNOWN+UNKNOWN-Type-2`) and adds the **Freeze date** table to the results table (figure B.24). The results table sent for analysis depends on the state of the variable defined in the `Select input for analysis` node. The results table is sent for storage and analysis.

Analysis is performed by the user and depends on input to various nodes.

For analysis of synaptic vesicles distance to the dense projection in a binned distance manner, the user follows the `Bin Feature by Distance` meta node path in the workflow. This meta node selects images with a dense projection and bins the linear distance of synaptic vesicles to the dense projections according to the `Bin size in nm` variable (figure B.25). The binned distances are counted by bin and transformed into a table for export in a Microsoft Excel `xls` table for a histogram plot.

For ROI count analysis, the user selects `Group for analysis` follows the `Counts` path in the workflow. The data table is concatenated with 0 count rows for each type of ROI per image in the `Add missing values` meta node (figure B.26). This meta

node also calculates the ROI count divided by the area or perimeter of the pertaining plasma membrane. These are the count by area and count by perimeter values. A ROI feature of interest is then selected by the user and sent for analysis. Bypassing the math following math nodes allows to not scale the count by area or perimeter with, respectively, the values in the `Area factor` or `Perimeter factor`.

For ROI feature analysis, the user selects the ROI type of interest and follows the ROI features path in the workflow.

For eCDF plots of the linear distance of ROIs to the dense projection, the user selects the ROI type for analysis and follows the eCDF path in the workflow. It requires user input in the `Create eCDF Table` meta node, namely in the `Rule Engine` node. This meta node converts the result table into an appropriate R format (figure B.27).

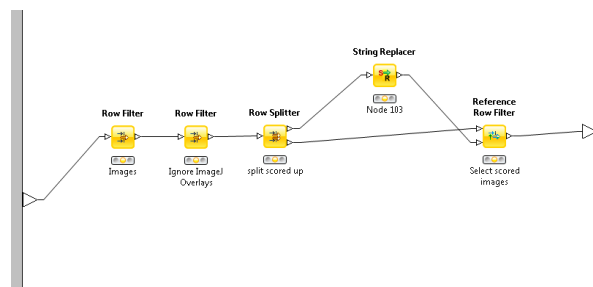


**Figure B.13.:** KNIME EM meta node `Read images` internal structure. This meta node searches for original images based on the scored- flag.

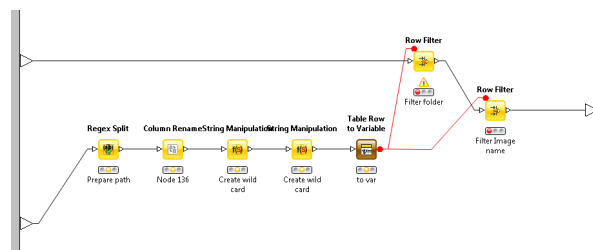


**Figure B.14.:** KNIME EM meta node `Prepare file paths` internal structure. This meta node uses the absolute file path of scored images to search for linked ImageJ result files.



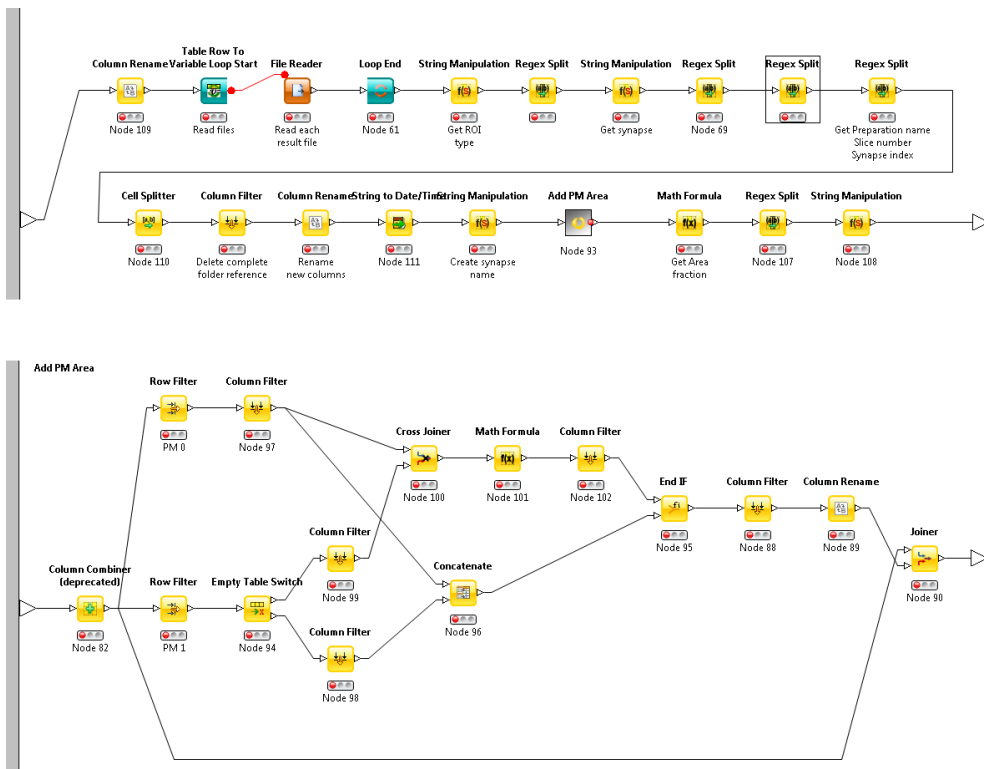


**Figure B.15.:** KNIME EM meta node Read ROI Results internal structure. This meta node reads all ROI result files linked to an image and adds meta data based on file name. It contains a meta node Add PM Area (expanded below) that joins the corresponding plasma membrane ROI area and perimeter to each ROI result. Area fraction is then calculated.

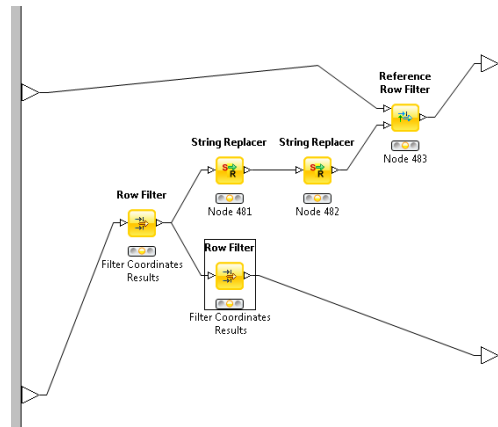


**Figure B.16.:** KNIME EM meta node `Exclude` calculated internal structure. This meta node searches for precalculated distance tables and excludes the pertaining ROI from a further calculation. It also sends the full path to the precalculated distance files for a table reader.

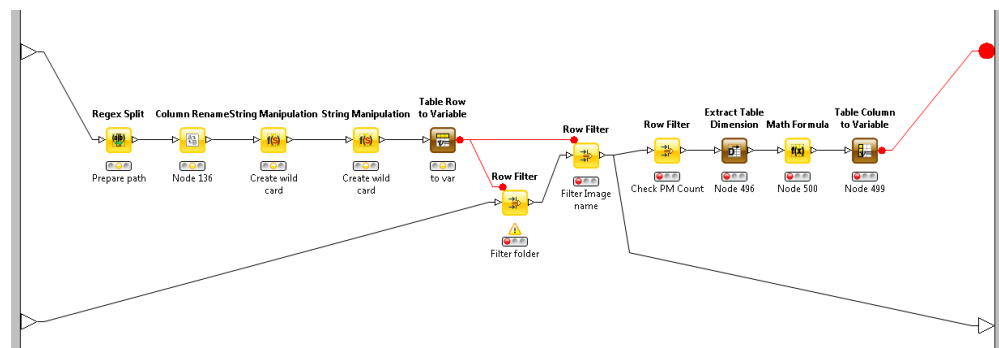


**Figure B.17.:** KNIME EM meta node `Prepare file paths for distances` internal structure. This meta node uses the absolute file path of scored images to search for linked ImageJ result files.

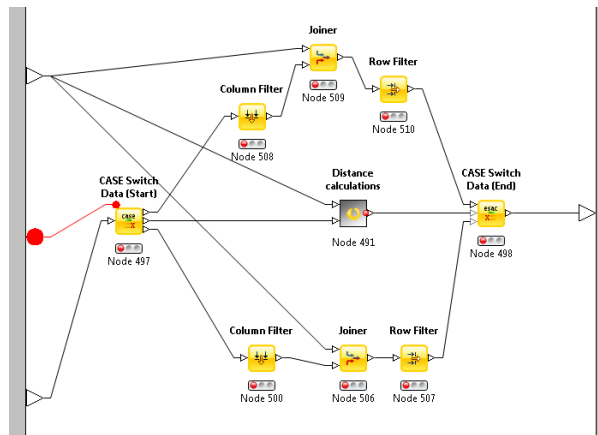


**Figure B.18.:** KNIME EM meta node Processing sends only images with a single associated plasma membrane ROI for distance calculations.

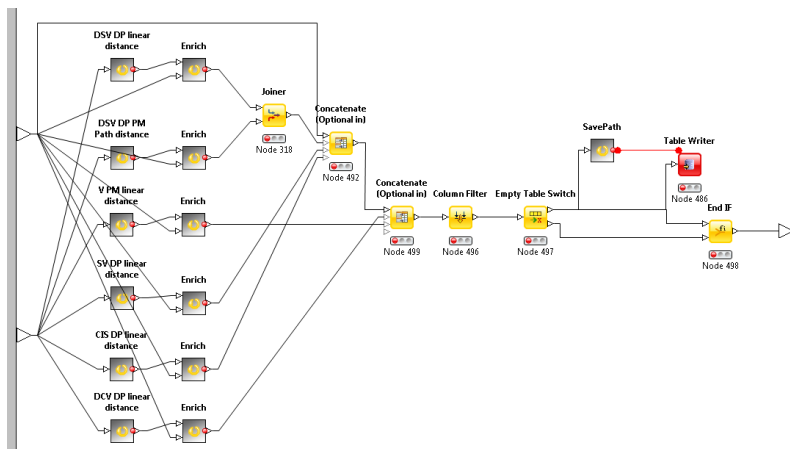


**Figure B.19.:** KNIME EM meta node Distance calculations itself is a collection of meta nodes for the actual distance calculations in R. It also contains a meta node for creation of the file name for storage of the distance results table.

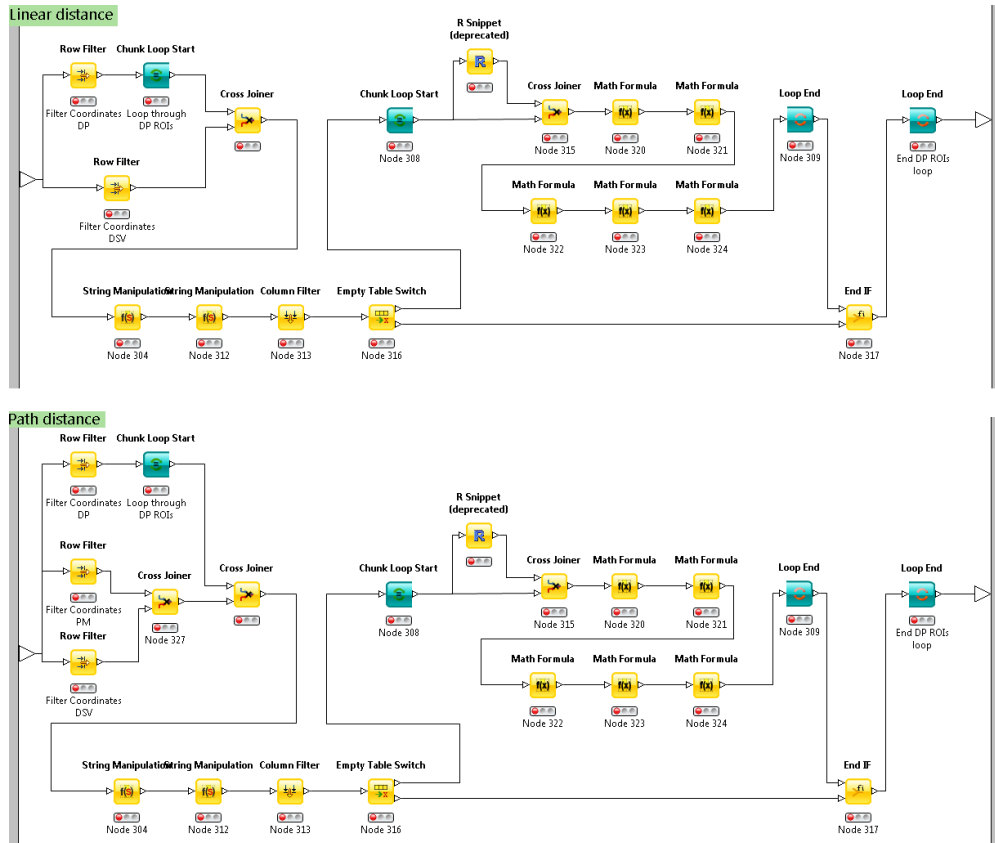


**Figure B.20.:** Top: KNIME EM meta node *Linear distance*. This meta node filters the ROI files for linear distance measurement and sends the file path of the coordinate files to R for distance calculation. Below: KNIME EM meta node *Path distance*. Function as above, but with addition of a filter for the plasma membrane ROI. Both: The file paths are sent sequentially to R, computed distance tables data type is ensured and sent for further processing.

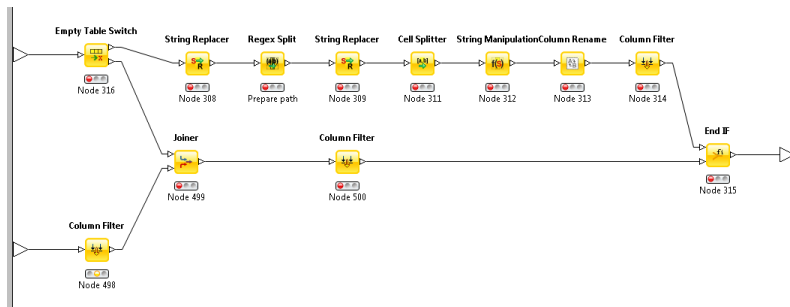


Figure B.21.: KNIME EM meta node Enrich. This meta node adds meta data to the R distance output.

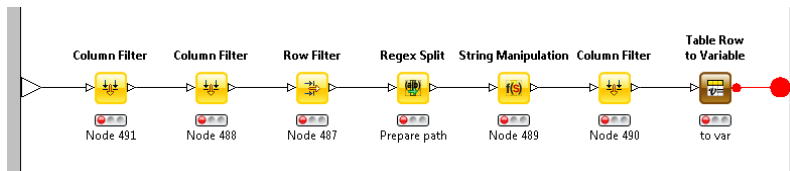


Figure B.22.: KNIME EM meta node SavePath. This meta node creates the file path for storage of the distance table.

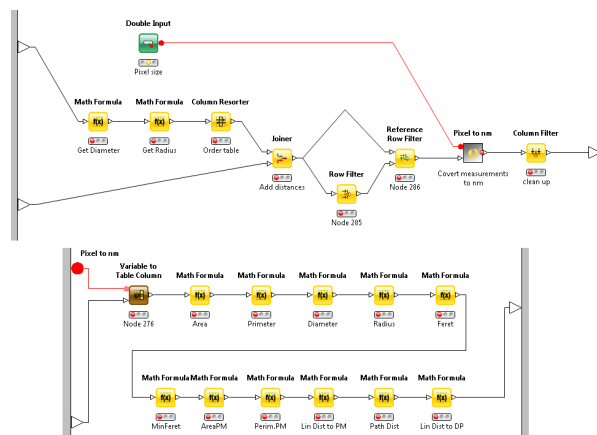


Figure B.23.: KNIME EM meta node Calculations. This meta node calculates radius and diameter of a circle of equal area to the ROI's area and joins the data from ImageJ and R output into one table. The values are converted to nm in the meta node Pixel to nm (expanded below).

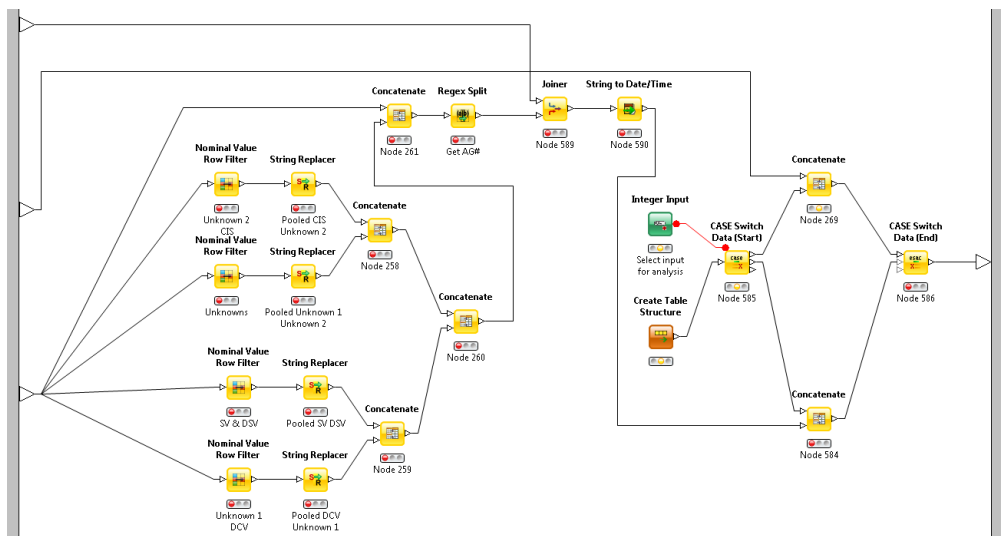
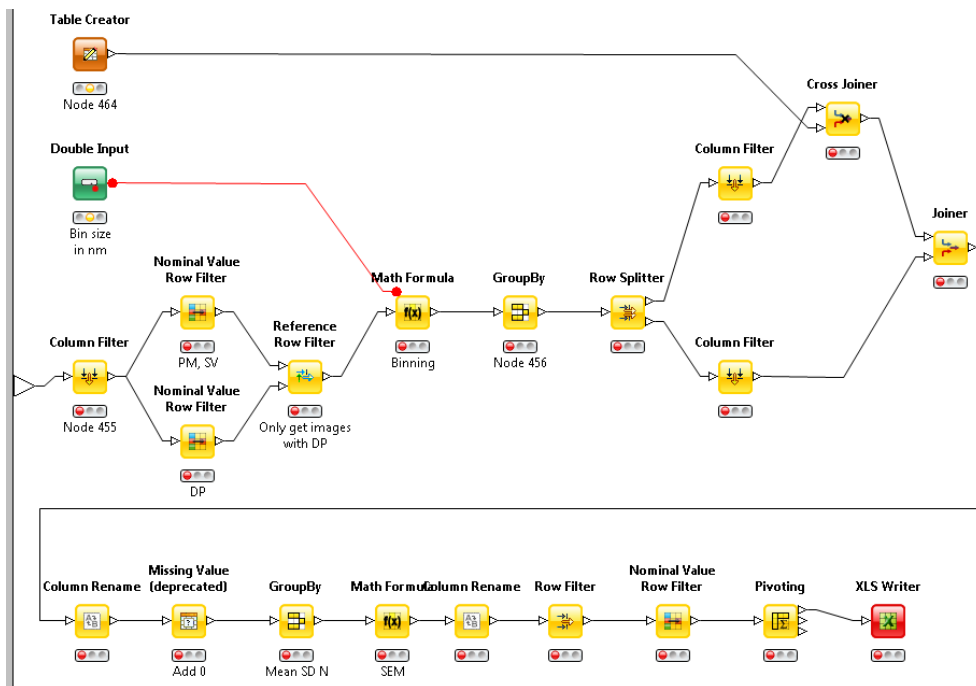
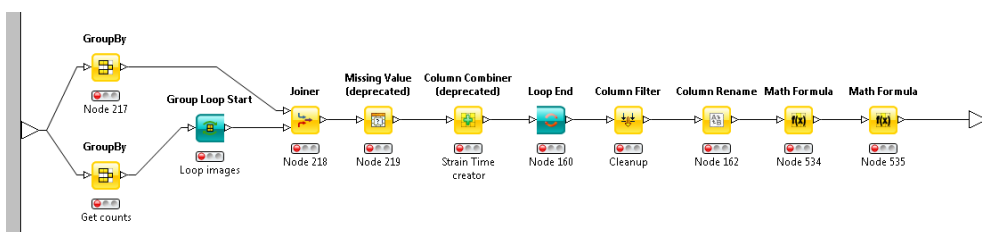


Figure B.24.: KNIME EM meta node Pooling. This meta node pools different ROI types together as described in the text and adds the freeze date table contents. Furthermore, a selection of the result table for analysis is performed by toggling the Select input for analysis variable.



**Figure B.25:** KNIME EM meta node Bin Feature by Distance. This meta node counts the occurrence of synaptic vesicles at binned distances from the dense projection and exports an Excel x1s file for a histogram plot.



**Figure B.26:** KNIME EM meta node Add missing values. This meta node pools adds rows to the result table with 0 counts for ROI types that are not present in a specific image. It also calculates the count by area and the count by perimeter values.

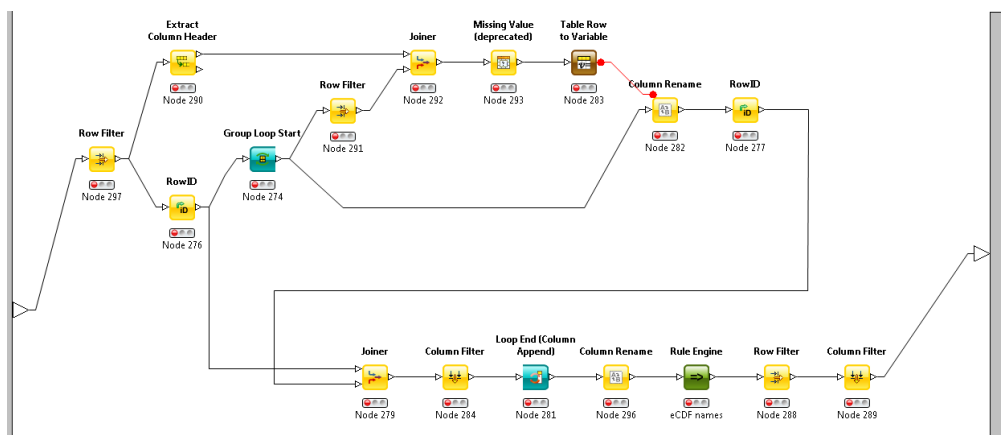


**Figure B.27.:** KNIME EM meta node Create eCDF Table. This meta node converts the result table into an R compatible format. It requires user input in the Rule Engine with the analyzed groups nomenclature.



### B.1.6. KNIME Image pre-processing

The KNIME Image pre-processing workflow improves image quality for automatic analysis of worm posture in threshold based trackers. Improvement is achieved in low contrast or low signal to noise conditions.

**Table B.8.:** KNIME Image pre-processing summary

Type	Description
KNIME version	2.12
KNIME Extensions	Image Processing, ImageJ macro
Third-party software	
Input files	jpeg images
Output files	jpg images

Movie files have to be converted into jpeg image sequences for compatibility with this workflow. The improved images are exported into a subfolder (*Enhanced*) with the same name as the original images. Improved images can be converted into movies for further processing, if required. The workflow also searches for already processed images and excludes the respective original images from processing. If variables are changed, the processed images have to be deleted prior to running this workflow.

**B.1.6.0.11. Pseudo code** The workflow in pseudo code is as follows:

1. List folder with images processing
2. Exclude original images (jpeg) if processed images (jpg) with same name are present
3. For each folder, process 50 images in batch mode as follows
  - a) Read images
  - b) Extract `file name` and create `enhanced file path` for storage
  - c) Convert images to grey scale
  - d) Background subtraction
  - e) Gaussian blur
  - f) Find threshold
  - g) If `Select animal stage` set to 1 (Adult), fill holes
  - h) Create overlay for manual quality control

- i) Convert image type
- j) Join meta data (file name, file path)
- k) Save enhanced image as jpg in file path

**B.1.6.0.12. Workflow scheme** The workflow schematic is depicted in figure B.28. Although only the variable selecting for animal life stage is set as variable input, it is recommended to adjust the image processing to the quality of the images in the first run of the workflow. Image processing nodes are found in the meta nodes Image calculation and Animal stage.

The Process path meta node compares files already processed to the list of original images. It excludes all processed original images from further image processing (figure B.29). Change the size in the Chunk loop start to increase or decrease the amount of images enhanced in parallel according to computer specifications (default 50). The Image calculation meta node converts the image to grey scale, then runs two ImageJ background subtractions with (rolling radius of 200 px and 20 px, respectively). The resulting images are added to the original image. Adjust these radii for optimal results, depending on the acquisition resolution. Following, a Gaussian blur with  $\sigma = 1$  despeckles the image at cost of blur (figure B.30). The Animal stage meta node may run an ImageJ command, depending on the value of the variable Select animal stage (figure B.31). This script iterates 7 times dilate – fill holes – erode macro, closing holes in the silhouette at cost of its width. An overlay image of the original image and the silhouette is generated for manual quality control. The Save images meta node iterates through all silhouette images and stores these in the Enhanced folder (figure B.32).

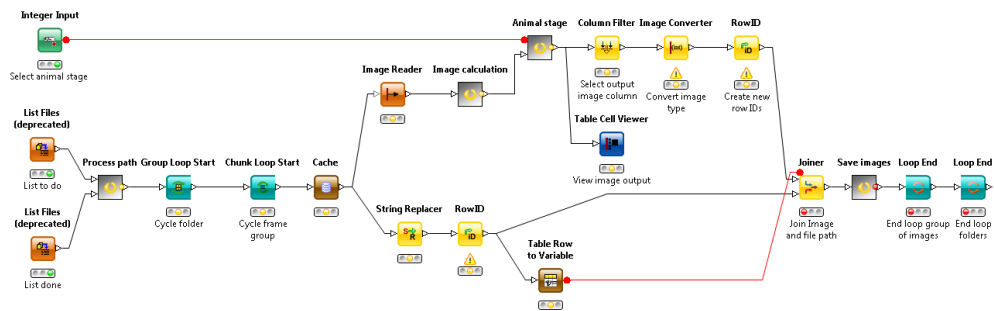


**Figure B.28.:** KNIME Image pre-processing workflow. This workflow enhances contrast and signal to noise ratio in images intended for automatic, threshold based, behaviour analysis.

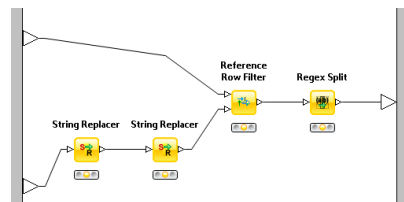


**Figure B.29.:** KNIME Image pre-processing Process path meta node. This meta node compares original images to files in the Enhanced folder and excludes from analysis those images that have been processed already.

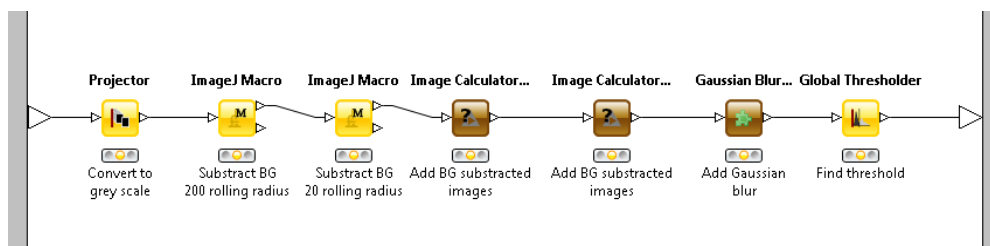


**Figure B.30.:** KNIME Image pre-processing Calculation meta node. This meta node subtracts the background and enhances the contrast, while a Gaussian blur further de-speckles the image.

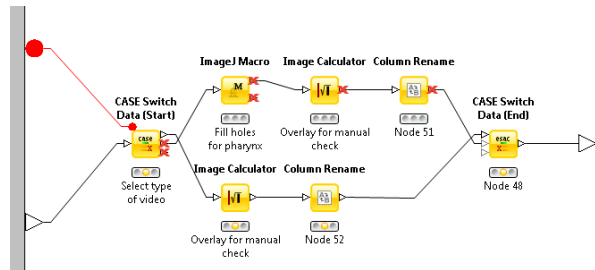


**Figure B.31.:** KNIME Image pre-processing *Animal* stage meta node. This meta node runs a hole fill script on the silhouette image, closing gaps. It also generates an overlay image for manual quality control.

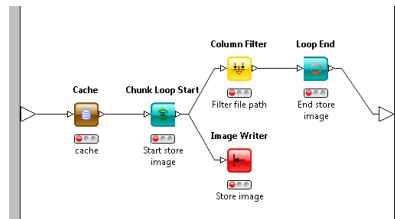


**Figure B.32.:** KNIME Image pre-processing *Save images* meta node. This meta node stores the silhouette images in the *Enhanced* folder as *jpg* files.

### B.1.7. KNIME Analysis of pump frequency through kymographs

This workflow was written for Dr. Elisabeth Fischer during her doctoral studies and applied for data analysis in her thesis as well as a peer reviewed publication [512]. The workflow uses a neuronal network for feature calling in kymographic analysis of pharynx pump events in experiments devised during her work. All data experiments and data analyzed with this workflow were planned, acquired and preprocessed by Dr. Elisabeth Fischer.

**Table B.9.:** KNIME Analysis of pump frequency through kymographs summary

Type	Description
KNIME version	2.12
KNIME Extensions	R, XLS export, Math Formula
Third-party software	R (ggplot2)
Input files	Folder with Kymograph grey values, MovieStartEnd, MovieOffset
Output files	ManualCorrected files, 3 Excel tables with results, Pump behavior images

The folder for analysis contains Kymograph grey values text files named as "MovieNumber Genotype AnimalNumber" (i.e. "1 N2 1.txt"). This file is a tab separated, comma as decimal separator, three column table with header. The column order is: RowID, Time and GreyValue. The workflow searches for minima in the grey value plot and trains a 4 layer, 10 neurons per layer, feedforward neuronal network to these features (resilient backpropagation (Rprop) multilayer perceptron (MLP), [514]). User supervision and export of manual corrected minima calling is used for improving the MLP performance. After tagging all minima in all files, the branch of the workflow analyzes the data, exports images and excel tables with grouped results. Due to the data acquisition properties, many corrections had to be performed in the data set to achieve synchronization. These steps can be bypassed with careful data acquisition. These data corrections require the files MovieStartEnd and MovieOffset. MovieStartEnd is a tab separated, four column with header text file; columns are MovieNumber, Genotype, StartFrame and EndFrame. MovieOffset is a tab separated, two column with header text file; columns are Kymograph grey values name and Offset.

**B.1.7.0.13. Pseudo code** The workflow in pseudo code is as follows:

1. Read folder content
2. If a Kymograph grey values file does not have a corresponding ManualCorrected file, do:
  - a) List all Kymograph grey values without corresponding ManualCorrected file
  - b) Read all ManualCorrected files
  - c) Train MLP on ManualCorrected files
  - d) Get first Kymograph grey values
  - e) Extract MovieNumber, Genotype and AnimalNumber from file name
  - f) Read Kymograph grey values and append meta data
  - g) Normalize grey values
  - h) If pump event as maxima, user input is required to invert the normalized grey values.
  - i) Exclude missing data
  - j) Calculate angles between every three data points in normalized plot
  - k) For each data point, append column with angle to prior and next data point
  - l) Calculate angle difference for each data point between data point before and after it
  - m) Calculate change in normalized grey value between data point and its preceding data point
  - n) Call minima based on threshold for calculated values
  - o) MLP application on data, with thresholded calls as primers
  - p) Manual supervision and correction of minima call
  - q) Create file name for export of manual corrected data
  - r) Export ManualCorrected file
  - s) Manual reset of workflow
3. Read all ManualCorrected files
4. For each ManualCorrected file, do:
  - a) Index all pump events
  - b) For each pump event, do:

- i. Find minima
  - ii. Calculate contraction duration
  - iii. Find end of relaxation based on standard deviation of normalized grey values
  - iv. Enforce relaxation to end with start of next pump
  - v. Calculate relaxation time
  - vi. Calculate pump duration
  - vii. Calculate time between two pump events (denominated refractory time)
  - viii. Enforce refractory time to be at least one time frame long
- c) Read `MovieStartEnd` and `MovieOffset` files
  - d) Correct double mathematics artifact
  - e) Filter data points according to `StartFrame` and `EndFrame`
  - f) Correct time frame based on `Offset`
  - g) Set start time to 0
  - h) Calculate instantaneous pump frequency
  - i) Create file path for image export
  - j) Use rule engine to describe the pump period
  - k) Plot normalized grey value versus time with background color describing pump period
  - l) Export image
  - m) Group data based on pump period description
  - n) Add zeros to not observed periods
  - o) Create two tables: `Description grouped data` and `Raw data`
5. Export `Description grouped data` Excel table
  6. Group `Description grouped data` by genotype
  7. Statistics on percentage of time spent per genotype in each period description
  8. Export percentage of time Excel table
  9. Group `Raw data` by pump index and `Kymograph grey values` file
  10. Group resulting table by mean pump frequency and genotype
  11. Count percentage of time spent per genotype in each frequency ( $1.0 \text{ Hz} \pm 0.5 \text{ Hz}$ )
  12. Export analysis to Excel table

**B.1.7.0.14. Workflow scheme** The workflow schematic is depicted in figure B.33. The lower part of the workflow runs the supervised feature calling required to tag pumps in the kymographic analysis. Therefore, `ManualCorrected` files are passed by the `Find new files` metanode (figure B.34) to the `Iterate list of files` metanode to be read (figure B.35). `Kymograph grey values` files without associated `ManualCorrected` files are sent for tagging, furthermore `ManualCorrected` files are used by the MLP learner. The `Prepare file paths` metanode adds metadata from the file path to the data table of the `Kymograph grey values` file (figure B.36). The `Read Results` metanode reads the `Kymograph grey values` file and normalizes the grey value (figure B.37). Manual input is necessary to invert the normalized grey values. The `Process results` metanode calculates angles between line spanning the data points in the normalized grey values as well as the difference in the grey value between data points (figure B.38). This data is required by the `Tagger` metanode for fixed rule tagging of minima (figure B.39). These minima are passed to the MLP predictor as primer for the location of the minima. The corrected minima location are then manually supervised and the resulting `ManualCorrected` table is exported. Manual reset of the workflow is required to process a further `Kymograph grey values` file.

The upper part of the workflow analyzes the `ManualCorrected` data and exports pump statistics to excel tables. The `Data processing` metanode has options for synchronizing videos and single `Kymograph grey values` files. This metanode also processes the raw data and generates the raw result table (figure B.40). These are not required if data acquisition is performed in a standardized manner. The pump events are indexed by the `Index pumps` metanode (figure B.41) and each pump passes the `Calculate Pump properties` metanode where pump duration, contraction, relaxation and refractory times are calculated (figure B.42). The results are synchronized in the `Clean and prepare data` metanode and the instantaneous pump frequency is calculated (figure B.43). Pump descriptions are added by fixed rules and used to define the color of the background of a normalized grey value plot. One plot per `Kymograph grey values` file is exported. Statistics on the time spent per pump description grouped by genotype is exported to an excel table for further processing. Further, `Frequency` metanode performs a descriptive statistical analysis of the raw result table grouped by genotype on the instantaneous pump frequency. This data is exported in an excel table for further processing.



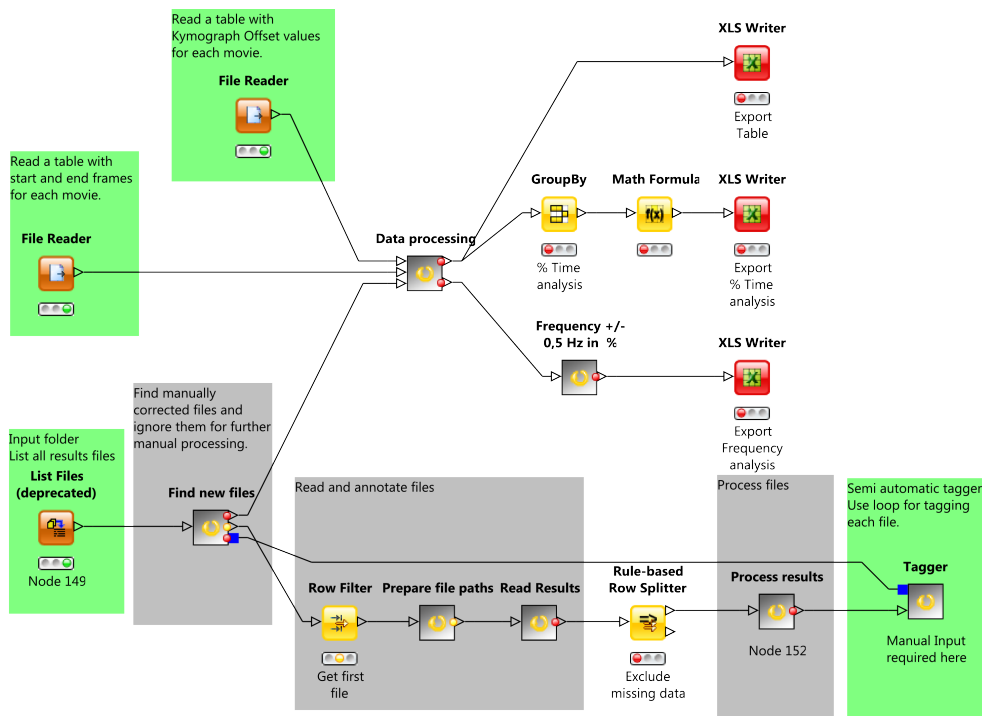


**Figure B.33.:** KNIME Kymograph analysis workflow. This workflow searches for all pump events measured by kymographic analysis of terminal bulb movement with a manually supervised MLP. Pump characteristics per genotype are calculated and exported to excel tables for further processing. Furthermore, for each kymograph, a normalized grey value plot with background coloring of the pump description is exported.

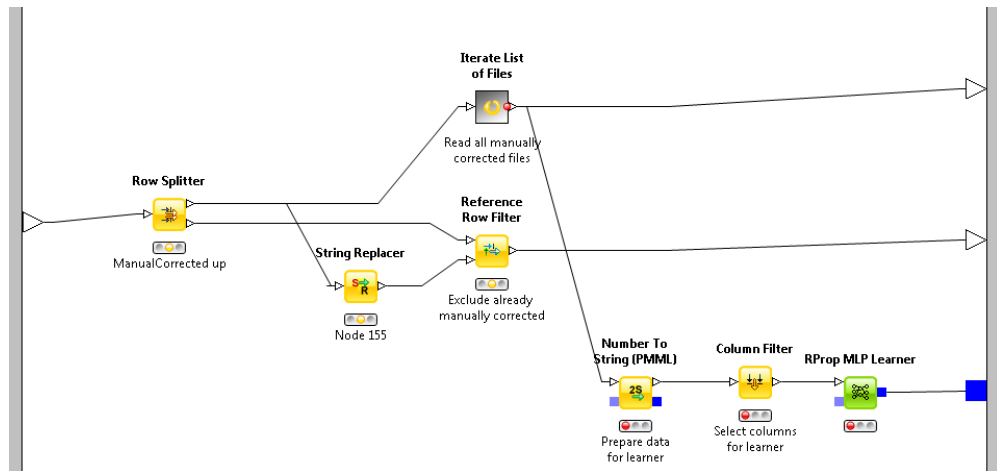


**Figure B.34.:** KNIME Kymograph Find new files metanode internal. This metanode searches for Kymograph grey values files and associated ManualCorrected files. Orphan Kymograph grey values files are passed for manually supervised tagging, while ManualCorrected files are read by the Iterate list of files metanode and used by the MLP learner.

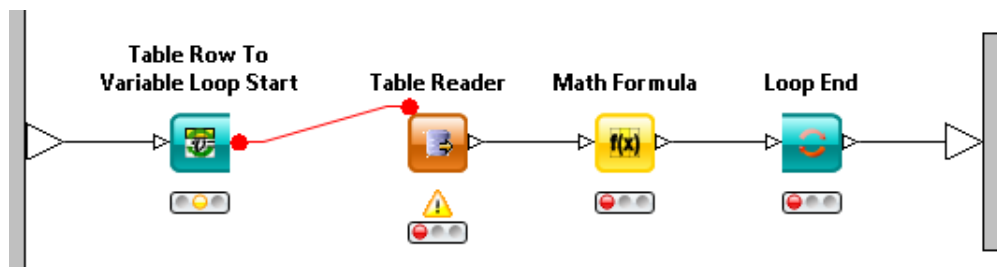


**Figure B.35.:** KNIME Kymograph Iterate list of files metanode internal. This metanode reads all ManualCorrected files and ensures the grey values are set as double.

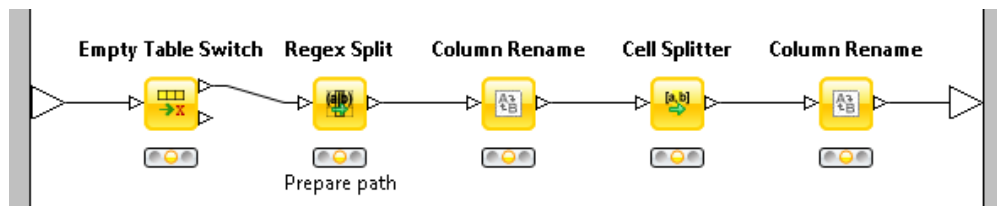


**Figure B.36.:** KNIME Kymograph Prepare file paths metanode internal. This metanode extracts meta data from the file path.

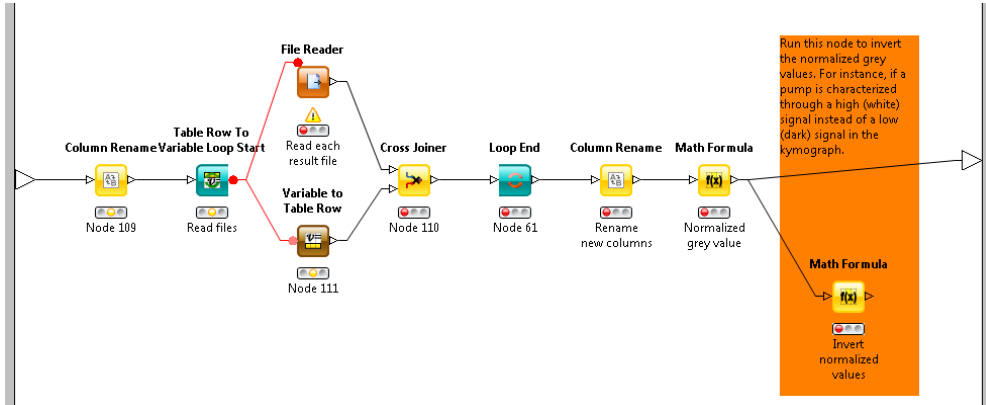


**Figure B.37.:** KNIME Kymograph Read Results metanode internal. This metanode reads the Kymograph grey values file, adds the meta data and calculates the normalized grey value. Manual input is necessary to invert the normalized grey value in cases where the pumps are defined by maxima instead of minima.

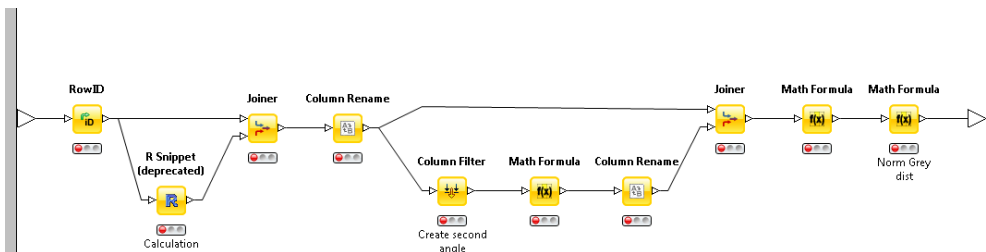


**Figure B.38.:** KNIME Kymograph Process results metanode internal. This metanode calculates angles between data points in the normalized grey value as well as the difference of the normalized grey value between data points. This information is required by the following node for tagging minima.

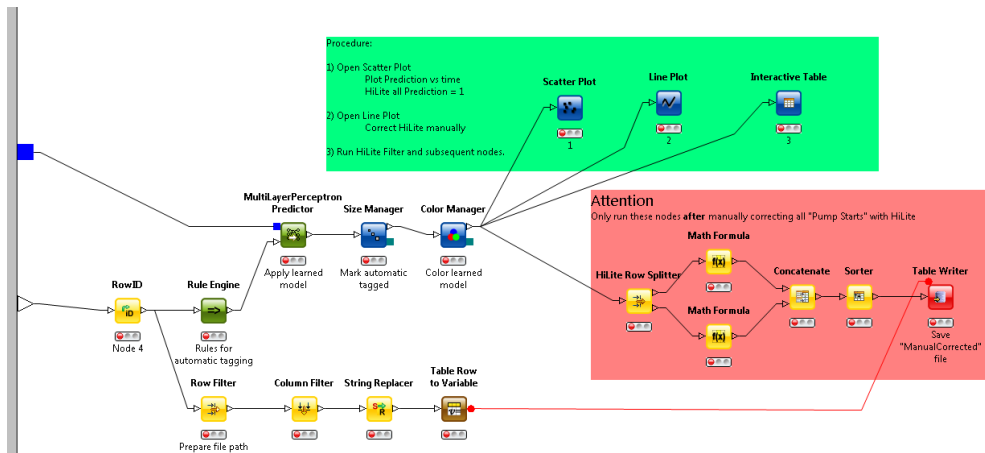


**Figure B.39.:** KNIME Kymograph Tagger metanode internal. This metanode applies a fixed rule for minima calling, these are passed to the MLP predictor as primer for minima search. User supervised data is saved as a ManualCorrected file.

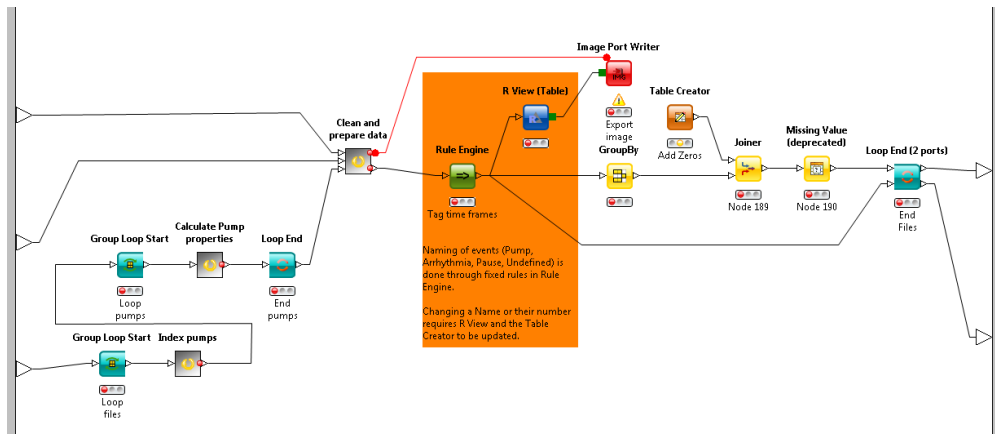


**Figure B.40.:** KNIME Kymograph Data processing metanode internal. This metanode synchronizes movies as well as single Kymograph grey values files. It then processes the raw data to a raw result table as well as exports plots of the normalized grey values with background colored to the pump description as set by the user.

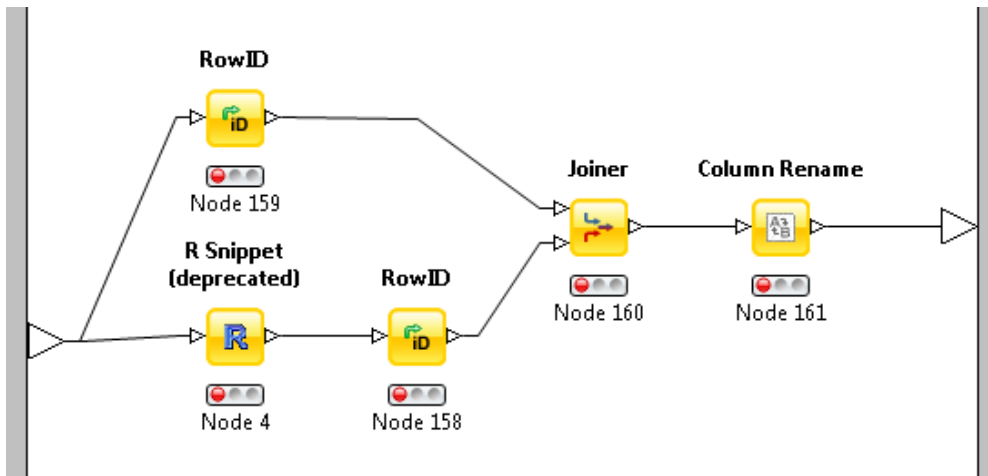


Figure B.41.: KNIME Kymograph Index pumps metanode internal. This metanode indexes each pump in a Kymograph grey values file.

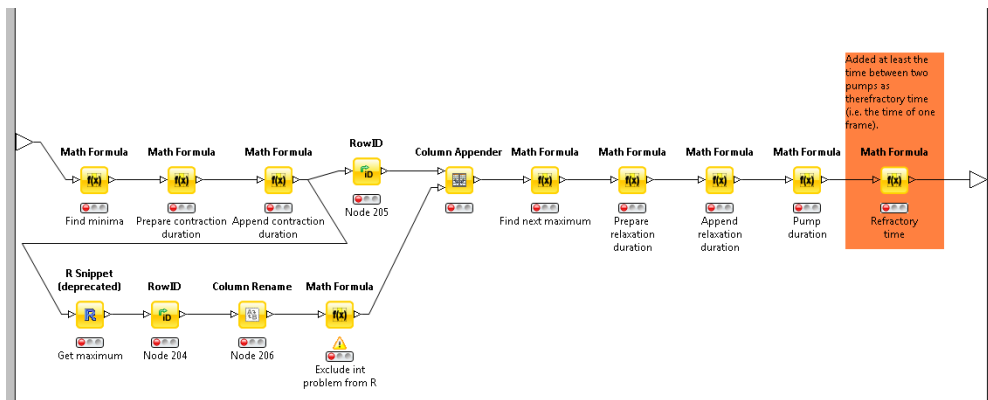


Figure B.42.: KNIME Kymograph Calculate Pump properties metanode internal. This metanode calculates the pump, pump contraction, pump relaxation and the refractory times.

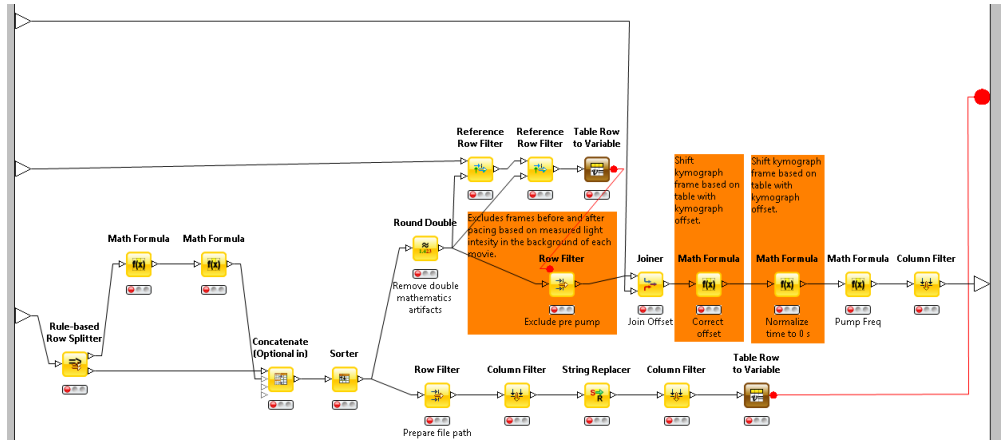


Figure B.43.: KNIME Kymograph Clean and prepare data metanode internal. This metanode synchronizes the raw data and calculates the instantaneous pump frequency.

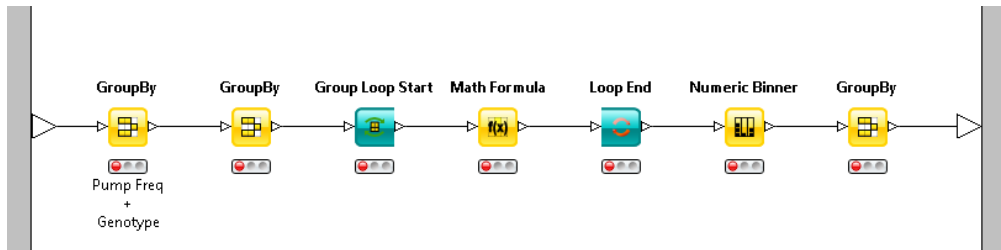


Figure B.44.: KNIME Kymograph Frequency metanode internal. This metanode performs a statistical analysis on the distribution of pump events according to the instantaneous pump frequency binned in Hz.

### B.1.8. KNIME synchronization and analysis of mPSCs

This workflow synchronizes mPSCs from electrophysiological recordings in a user defined window size (i.e. amount of data points per mPSC). The rise time  $\tau_{on}$  and the decay time  $\tau_{off}$  are calculated for every mPSC and user defined quality settings filter the output depending on the quality of the fit function. Optionally, the workflow exports a fit plot for every mPSC. Furthermore, the mPSCs which passed quality control, are plotted superimposed with mean and standard deviation per user defined time domain as well as a superimposed plot of means of the user defined time domains.

**Table B.10.:** KNIME synchronization and analysis of mPSCs summary

Type	Description
KNIME version	3.1.2
KNIME Extensions	R, Math Formula
Third-party software	R (libraries ggplot2, plyr)
Input files	Original Recordings, mPSC analysis
Output files	Tables: SynchmPSCs, Raw $\tau_{on}$ / $\tau_{off}$ , Filtered $\tau_{on}$ / $\tau_{off}$ , Variables Images: Superimposed mPSCs per time domain, superimposed mPSCs means, optional mPSC plot with $\tau_{on}$ / $\tau_{off}$ fit curve.

The input must be organized into folders as follows: .

GroupName

DataType

FileName. GroupName defines the group or genotype that was used to generate the data. DataType must be either "OR" for original recordings or "mPSCs" for mPSC analysis data. FileName must be the same in both folders to ensure that mPSC analysis is associated to the original recording. The original recording file must be a tab separated, dot as decimal separator two column, no headers \*.asc file. First column is time

s

and second column is amplitude

A

, both with scientific E notation. The mPSC analysis data must be a tab separated, dot as decimal separator 18 column, no headers \*.asc file. The column contents are: mPSC ID, Time [ms], Amplitude [pA], Rise [ms], Decay [ms], Area [fC], Baseline [pA], Noise, Group, Channel, 10-90 Rise [ms], Half Width [ms], Rise 50 [ms], Peak Dir (positive or negative), Burst #, Burst E#, 10-90 Slope, Rel Time [ms].

The workflow is subdivided in three parts. The upper part searches for original recording data and associated mPSC analysis data, and synchronizes the mPSCs. The resulting table is exported as SynchmPSCs files to the mPSCs folder. The mid part of the workflow fits a mono exponential rise / decay formula to each mPSC. A user defined quality control setting passes only mPSCs with  $\tau_{on} / \tau_{off}$  calculated from fit curves with acceptable quality. Raw (with all  $\tau_{on} / \tau_{off}$ ) and filtered data tables are exported, as well as a table with the value of all used variables. The lower part of the workflow extracts the filtered mPSCs from the SynchmPSCs files and plots them either superimposed per time domain or their means superimposed.

**B.1.8.0.15. Pseudo code** The workflow in pseudo code is as follows: User input of variables: WindowSize and ComputeAll

For Synchronization of mPSCs, do:

1. List folder with Original Recordings, mPSC analysis and SynchmPSCs tables
2. Extract meta data from folder name structure: GroupName and DataType
3. If ComputeAll set to 0, exclude mPSC analysis files with corresponding SynchmPSCs files from further processing steps
4. For each mPSC analysis file, do:
  - a) Find corresponding Original Recordings file.
  - b) Send Original Recordings and mPSC analysis file paths and variables to R section B.2.4, p. 292
  - c) Create SynchmPSCs file name
  - d) Save R result table as SynchmPSCs file

For  $\tau_{on} / \tau_{off}$  calculation, do:

1. List folder with Original Recordings, mPSC analysis and SynchmPSCs tables
2. Extract meta data from folder name structure: GroupName and DataType
3. For each mPSC analysis file, do:
  - a) Read mPSC analysis file



- b) Name columns
  - c) Add meta data to table
  - d) Exclude mPSCs that have another mPSC during their rise or decay time
  - e) Exclude mPSCs that have another mPSC in the same time window
  - f) Read associated SynchmPSCs file
  - g) Pass only mPSCs from SynchmPSCs data that were not excluded from mPSC analysis data
  - h) Read associated Original Recordings file and calculate acquisition period from first two time stamps
  - i) Add period to mPSC analysis data
4. Calculate the end of the synchronization window
  5. Extract SynchmPSCs data points during the rise / decay time of each mPSC
  6. For each mPSC file, fit mono-exponential curve in R (section B.2.5, p. 293)
  7. Save raw data table
  8. Exclude mPSCs with low quality of fit
  9. Exclude mPSCs in time frames not analyzed for other experiments
  10. Save filtered data table
  11. Save table with state of variables

For plotting, do:

1. List folder with SynchmPSCs tables
2. Read file filtered data table
3. For each mPSC in filtered data point, recover the synchronized window data
4. Plot all mPSCs per time frame with Mean+SD
5. Plot mPSCs Mean+SD per group

**B.1.8.0.16. Workflow scheme** This workflow is subdivided into three sections. User input is required in the first column of nodes, while optional are found in the meta nodes. The first section synchronizes the mPSCs (figure B.45). User input for variables are processed in the Variables meta node (figure B.46) and passed to the List files meta node (figure B.47). This nodes generates two list of files for R mPSC synchronization (figure B.48, section B.2.4, p. 292). The R meta node exports file tables with the synchronized mPSCs for further analysis.

The second section of this workflow calculates the kinetic properties of the mPSCs (figure B.49). This workflow first reads the synchronized mPSCs (figure B.50) while filtering out mPSCs that are too near to each other or when the mPSC file properties show that a previous mPSC decay time is in the same range as its rise time (figure B.51 and figure B.52, respectively). The data acquisition rate of each mPSC file is converted to time frequency in the Get Period meta node (figure B.53). The synchronized and filtered mPSCs are sent to the Calculate meta node for kinetic analysis (figure B.54). There, the Synch Win end meta node extracts the last data point of a mPSC to which the fit shall be applied (figure B.55). The raw results are stored to a file as well as processed in the Quality Control meta node, where poor fit statistics are filtered out (figure B.56). The mPSCs that passed quality control are stored in a filtered results table for further analysis together with a table containing the user input for further reference.

The third part of the workflow generates two plot types, either with all mPSCs together with Mean+SD per time frame or Mean+SD per group for all time frames (figure B.57). The input consists of all synchronized mPSC files as well as the filtered output from the Tau calculation workflow above. The later is required to filter the raw table and only plot the mPSCs that went into further calculations, a task performed in the Filter meta node (figure B.58).

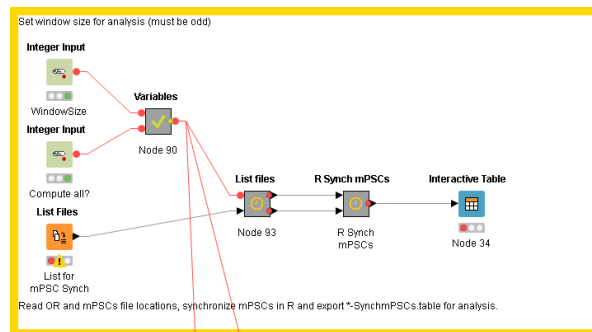


Figure B.45.: KNIME synchronizing mPSCs workflow.

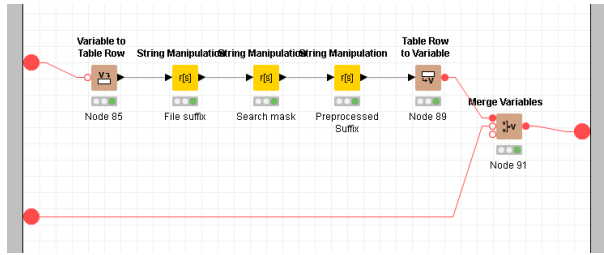


Figure B.46.: KNIME synchronizing mPSCs Variables meta node.

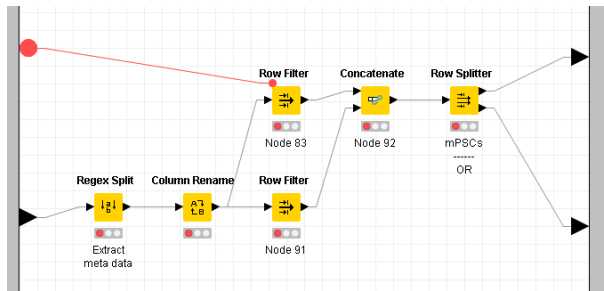


Figure B.47.: KNIME synchronizing mPSCs List files meta node.

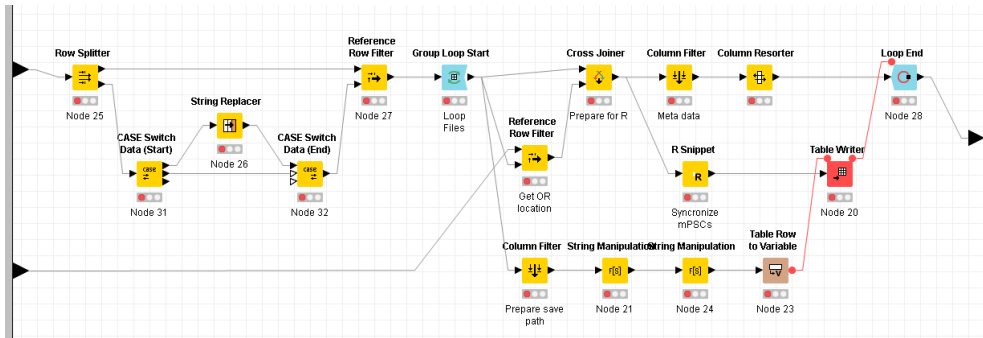


Figure B.48.: KNIME synchronizing mPSCs R meta node.

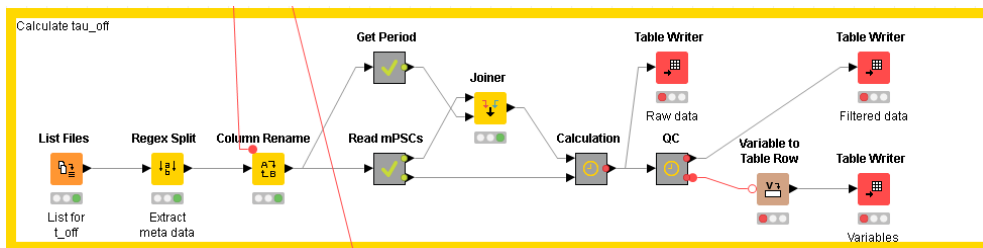


Figure B.49.: KNIME mPSC calculate Tau workflow.

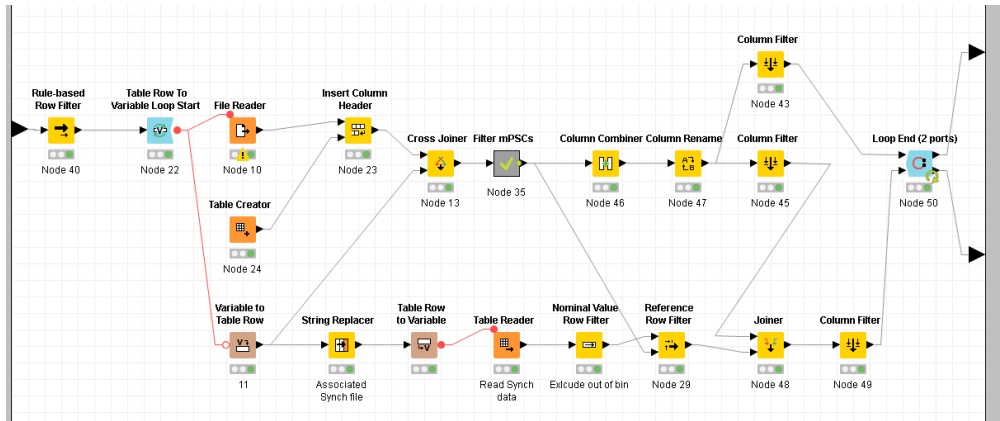


Figure B.50.: KNIME mPSC calculate Tau - Read meta node.

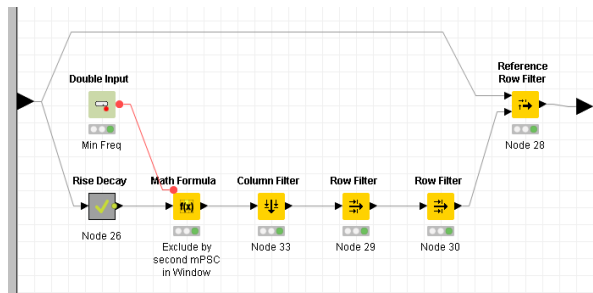


Figure B.51.: KNIME mPSC calculate Tau - Filter meta node.

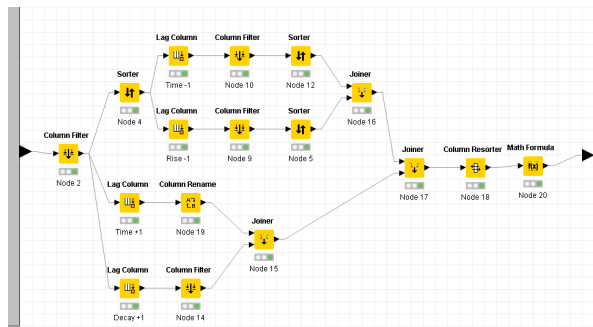


Figure B.52.: KNIME mPSC calculate Tau - Rise decay filter meta node.

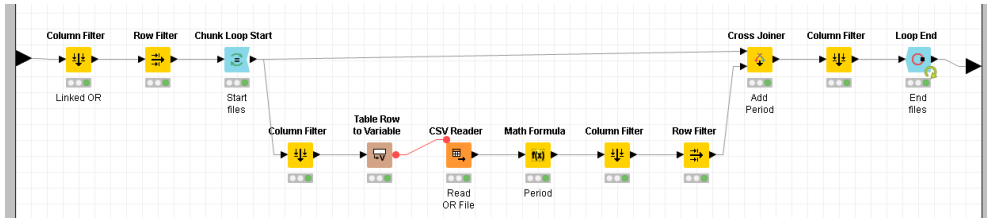


Figure B.53.: KNIME mPSC calculate Tau - Get period meta node.

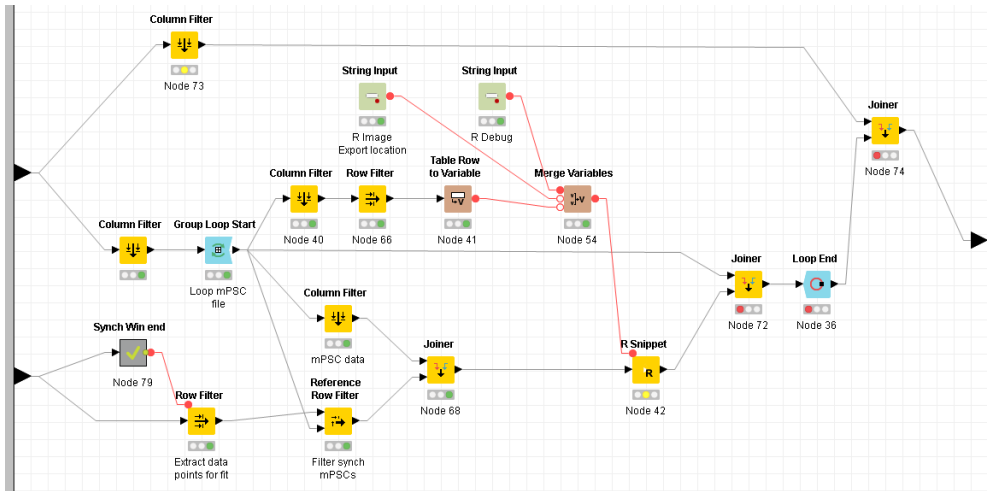


Figure B.54.: KNIME mPSC calculate Tau - Fit meta node.

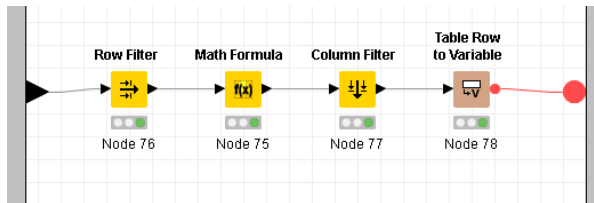


Figure B.55.: KNIME mPSC calculate Tau - Synch meta node.

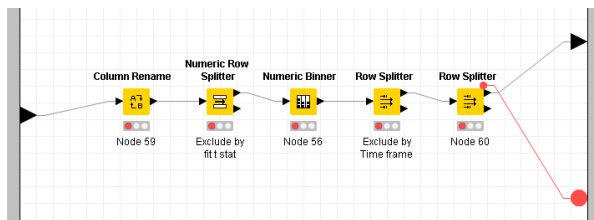


Figure B.56.: KNIME mPSC calculate Tau - Quality control meta node.

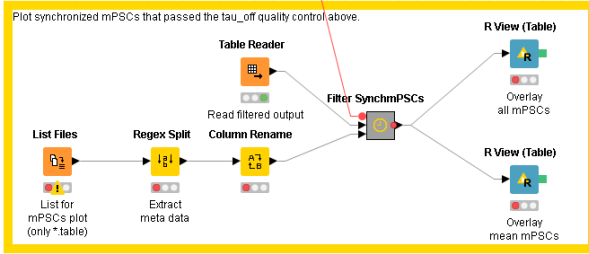


Figure B.57.: KNIME plot mPSCs workflow

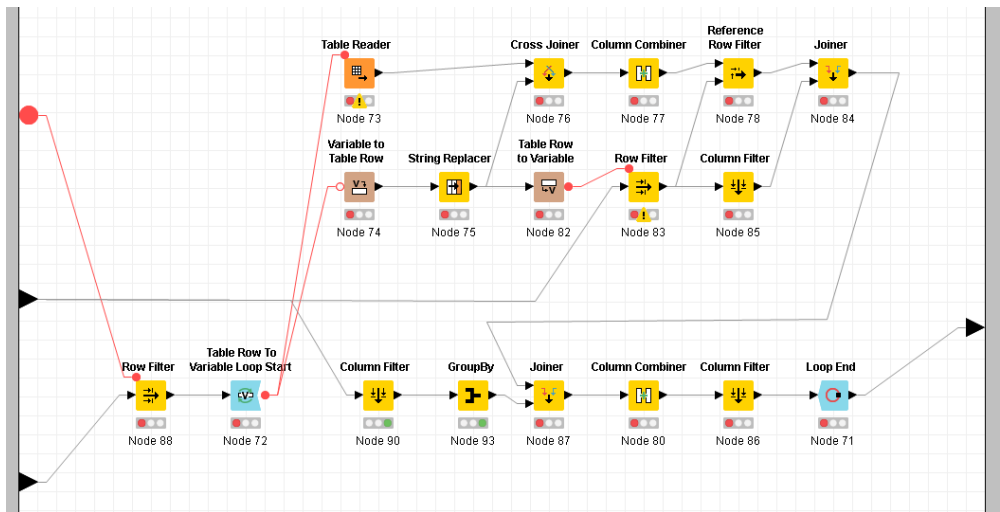


Figure B.58.: KNIME plot mPSCs - Filter meta node.

## B.2. R Scripts

R is freely available programming language for statistical computation. The following R scripts were written during the course of this thesis. A table summarizes the required R version, libraries, third-party software as well as file inputs and file outputs. A description of the required files and a pseudo code is given. The listing of the script follows.

### B.2.1. EM ROI distance calculation

Two R scripts were written to calculate the distance between two tagged features in an image.

#### B.2.1.1. EM ROI linear distance

This script calculates the minimal distance between two features.

Table B.11.: EM ROI linear distance summary

Type	Description
R version	3.2.1
R libraries	–
Third-party software	–
Input files	Two coordinate files
Output files	Table with minimal distance and coordinate pairs

The location for both required coordinate files are defined by KNIME B.1.5. The minimal distance between both features as well as the coordinates for the nearest points is passed back to KNIME as result table. Multiple result rows are returned, in case there are more than two coordinates with the least linear distance in between. This script calculates all possible distances and is therefore very inefficient for objects with many coordinate data points.

**B.2.1.1.1. Pseudo code** The workflow in pseudo code is as follows:

1. Open both coordinate files

2. Calculate an euclidean distance matrix for all possible coordinate pairs
3. Search for the shortest distance
4. Create a result table with all instances of the shortest distance and the coordinate pairs
5. Return the result table



### B.2.1.2. EM ROI distance through plasma membrane

This script calculates the minimal distance between two features following the plasma membrane ROI. In the case that the ROI of the feature of interest does not intersect with the plasma membrane ROI, the plasma membrane coordinate nearest to the feature of interest is used.

**Table B.12.:** EM ROI distance through plasma membrane summary

Type	Description
R version	3.2.1
R libraries	–
Third-party software	–
Input files	Three coordinate files
Output files	Table with minimal path and coordinates

The location for the required coordinates files are defined by KNIME B.1.5. The minimal path through the plasma membrane between both features as well as the coordinates for the nearest points is passed back to KNIME as result table. Multiple result rows are returned, in case there are more than two coordinates with the least path distance in between. This script calculates all possible distances and is therefore very inefficient for objects with many coordinate data points, especially because it calculates all distances to plasma membrane coordinates.

**B.2.1.2.1. Pseudo code** The workflow in pseudo code is as follows:

1. Open coordinate files
2. Calculate the perimeter of the plasma membrane ROI
3. Calculate an euclidean distance matrix for all possible coordinate pairs between features and plasma membrane
4. Search for the shortest distance between features and plasma membrane
5. Create a table with all instances of the shortest distance and the coordinate pairs of the features and the plasma membrane
6. Calculate the path distance through the plasma membrane between all coordinate pairs from the table
7. Search for the shortest paths through the plasma membrane perimeter

8. Create a result table with all instances of the shortest path and the coordinate pairs of the features and the plasma membrane
9. Return the result table

## B.2.2. Multimodal illumination tracker data visualization

This script imports data from KNIME Multimodal illumination tracker data analysis B.1.1 and returns a visualization as line plot of Mean with SEM.

**Table B.13.:** Multimodal illumination tracker data visualization summary

Type	Description
R version	3.2.1
R libraries	ggplot2
Third-party software	–
Input files	Automatic from KNIME B.1.1
Output files	Optional store visualization

This script requires manual input, as listed in table B.14.

**Table B.14.:** Multimodal illumination tracker data visualization manual input

Line	Variable	Description
12	xmin	Start of light indication bar.
12	xmax	End of light indication bar.
15	cbPalette	User defined color palette.
20	ggtitle	Title of visualization.
20	xlab	Title of abscissa.
20	ylab	Title of ordinate.
23	name	Description of group.
25	labels	New group names.
28	fill	Color of the light indication bar.

**B.2.2.0.2. Pseudo code** The workflow in pseudo code is as follows:

1. Get user input
2. Import data
3. Calculate SEM
4. Plot line graph of Mean with SEM

### B.2.3. Behavioral data cluster analysis

This script calculates the similarity of a behavior response over time across groups with a DTW and hierarchical clustering analysis and exports a dendrogram and a heat map of the result table. The script also allows for data normalization prior to calculation.

**Table B.15.:** Behavioral data cluster analysis summary

Type	Description
R version	3.2.1
R libraries	ape, dtw, gplots, colorRamps
Third-party software	–
Input files	Folder with csv files
Output files	Visualization

The script reads `FolderName\FileName.csv` files with following specifications: no header, one row per group, first column `GroupID`, tab separated and “.” as decimal separator. This script requires manual input, as listed in table B.16.

**Table B.16.:** Multimodal illumination tracker data visualization manual input

Line	Variable	Description
29	categories	Number of colored coded hierarchical clusters.
32	mypal	List of colors for cluster color coding.
34	HeatMapColor	Color ramp for heat map.
37	PlotSparklines	Export sparklines of smoothed graph.
40	subtractBaseline	Subtract baseline prior to analysis, baseline defined as mean of values in a range.
42	baselineStart	Start of range for baseline calculation.
43	baselineEnd	End of range for baseline calculation.
47	FileNames	List of file names to analyze, as <code>FileName</code> in <code>FolderName\FileName.csv</code> .
50	FolderName	Full folder path to files, as in <code>FolderName\FileName.csv</code> .

**Table B.16.:** (continued)

Line	Variable	Description
57	PlotThese	List files to export, given as TRUE/FALSE, for the five following possible analysis: Heat map, Heat map with lowess, Heat map with z-score, Heat map with z-score and lowess and Heat map with lowess and z-score.
60	lowessF	Lowess smoothing span value, between 0 to 1.

**B.2.3.0.3. Pseudo code** The workflow in pseudo code is as follows:

1. Load libraries
2. Read user input and define variables
3. For FileNames listed, do
  - a) Read file
  - b) If subtractBaseline set to TRUE, do
    - i. Calculate mean of each row from column baselineStart to baselineEnd
    - ii. Subtract mean from all data columns
  - c) If "Heatmap" create data table
  - d) If "Heatmap lowess" create lowess smoothed data table
  - e) If "Heatmap z-score" create z-score normalized data table
  - f) If "Heatmap z-score lowess" create lowess smoothed data table on z-score normalized data
  - g) If "Heatmap lowess z-score" create a z-score normalization data table on lowess smoothed data
  - h) For all data tables, do
    - i. Calculate the distance matrix by DTW
    - ii. Hierarchical cluster the distance matrix
    - iii. Cut the tree as defined by categories
    - iv. Plot dendrogram with heat map
    - v. Export image as svg

## B.2.4. Synchronize mPSCs

This script is called by KNIME (section B.1.8, p. 277) and synchronizes mPSCs stored in a mPSC file to a fixed window length with data from the corresponding original recording file.

**Table B.17.:** Synchronize mPSCs summary

Type	Description
R version	3.2.1
R libraries	–
Third-party software	–
Input files	Pointers and variables from KNIME section B.1.8, p. 277
Output files	Synchronized mPSCs to KNIME section B.1.8, p. 277

The script receives file pointers and variables from KNIME. It reads the mPSC as well as the original recording files. For each mPSC in the mPSC file, it searches for the corresponding time point in the original recording. It then stores a window of data points centered on the mPSC maximum amplitude. Time frame qualifiers are appended to the list and returned to KNIME.

**B.2.4.0.4. Pseudo code** The workflow in pseudo code is as follows:

1. Import variables from KNIME
2. Read mPSC and original recording files
3. Correct order of magnitude to match both files
4. Create result lists
5. For each mPSC in mPSC file do
  - Find corresponding time point in original recording file
  - Add all data points in window length centered at the mPSC from the original recording file to results list
  - Correct edge mPSCs, if window length longer than original recording
6. Generate data frame from result lists
7. Rename columns and return to KNIME

## B.2.5. Fit mPSCs

This script is called by KNIME (section B.1.8, p. 277) and fits a mono-exponential curve to the input data. The output to KNIME is a table of fit parameters as well as quality of fit. Optionally, this script stores fit plots for each mPSC for manual control of fit quality.

**Table B.18.:** Synchronize mPSCs summary

Type	Description
R version	3.2.1
R libraries	–
Third-party software	–
Input files	Pointers and variables from KNIME section B.1.8, p. 277
Output files	mPSC fit parameters to KNIME section B.1.8, p. 277

Data and variables are imported from KNIME. Data is assigned the correct order of magnitude before splitting the table according to mPSC IDs. A mono-exponential curve is fit to the data and parameters of the fit are stored to a result table. An error message is passed in case of fit failure. If required, a point plot of the original data with a line plot of the fit as well as confidence intervals is exported for manual control. Finally, the result table is returned to KNIME.

**B.2.5.0.5. Pseudo code** The workflow in pseudo code is as follows:

1. Read KNIME input
2. Correct order of magnitude
3. Split data frame according to mPSC IDs
4. Create result table
5. For each mPSC do:
  - Get baseline for this mPSC
  - Fit mono-exponential curve
  - If fit successful, extract fit properties and save to results table
  - Test computed baseline versus mPSC table result and export a warning if

not equal

- If required, plot a dot plot with fit and confidence interval as line plot
  - If fit not successful, return an error message
6. Rename results table columns for KNIME
  7. Return results table to KNIME



## B.3. MatLab Scripts

### B.3.1. Minis to Histogram

This script bins the output from Mini Analysis Program (Version 6.0.7, Synaptosoft Inc., 2042-A Ellery Ave. Fort Lee, NJ 07024 (USA)) mPSC output into user defined bins for a visualization as Histogram of amplitudes in a Microsoft Excel x1s file.

**Table B.19.**

Type	Description
MATLAB version	7.5.0
MATLAB toolbox	–
Third-party software	replaceinfile.m, Microsoft Excel
Input files	Folder with asc files, config.txt
Output files	Result table in Excel

The script consist of four files. The graphical user interface (GUI) `Minis2Histogram.m` and `Minis2Histogram.fig` file, the script `JL_histogram.m` file for binning and file conversion, and the external script `replaceinfile.m` (©2009, Pekka Kumpulainen) for character replacement in a file.

After the path in `set MATLAB`, run `Minis2Histogram` in order to open the GUI. Select folder containing the `asc` files for analysis (set `File` type to file extension if differing from `asc`). Set `Amplitude block size` variable to the size of one histogram bin. Load the time frame configuration file (`config.txt`) for binnig the time domain. The configuration file has three columns tab separated and “.” as decimal separator. The first column is a string with the name of the time domain, the second column defines the start of the time bin, while the last column defines the end of the time bin. Time bins must not be in ordered, but they may overlap. Press `Save` to export a Microsoft Excel x1s formatted table with the mPSC occurrence binned for a amplitude histogram visualization.

**B.3.1.0.6. Pseudo code** The workflow in pseudo code is as follows:

1. Get user input
2. Create an options table with the user input
3. Read `config.txt` file

4. For each file to be analyzed, do
  - a) If required, convert decimal separator from “,” to “.”
  - b) For each data point in file, do
    - Calculate to which bin the data point is associated
    - Get time frame
    - Increment the result table for the data point associated bin
  - c) Add zeros for non populated bins
  - d) For each time frame, do
    - i. Create a min / max normalized data table
    - ii. Statistics on normalized and absolute count data tables
5. Export data tables to Microsoft Excel

## B.4. ImageJ scripts

ImageJ is an open source software for scientific image analysis. A table summarizes the required ImageJ version, plug-ins, third-party software as well as file inputs and file outputs. A description of the required files and the script as pseudo code is given. The following ImageJ script was written during the course of this thesis.

### B.4.1. EM ROI quantification

This script searches for appropriately tagged EM images and saves the analysis output from ImageJ for further processing in KNIME B.1.5. This script requires modifications in the source code before running the analysis in ImageJ.

Table B.20.: ImageJ EM ROI quantification summary

Type	Description
ImageJ version	1.47v
ImageJ plug-ins	–
Third-party software	–
Input files	EM images, ImageJ ROIs
Output files	ROI statistic, ROI coordinates, Overlay image

The script stores overlay images `tif` of the original image with the tagged ROIs previously manually stored from ImageJ. In order to link a ROI file to an image, the ROI file from ImageJ must be stored in a zip file. The zip file must be saved in the same folder as the image and named `"ImageName_X_RoiSet"`, where `ImageName` is the name of the image to link this ROI collection to and `X` is a description of the ROI set. The script allows the ROI descriptions listed in table B.21.

**Table B.21.:** ROI descriptions

<b>x</b>	<b>Description</b>
CIS	Cisterna (Note: not Golgi membrane disk)
DCV	Dense Core Vesicle
DDCV	Docked Dense Core Vesicle
DP	Dense projection
DSV	Docked Synaptic Vesicle
ENDO	Endosome
PM	Plasma Membrane
SV	Synaptic Vesicle
UNKNOWN	Unknown feature
UNKNOWN-Type-2	Unknown feature

Furthermore, a variable called `OnlyOverlay` (line 38) can be toggled between 0 and 1. In the former case, the whole analysis is performed, while in the latter case only updated overlay images are created. This option is useful for modification of the overlay colors used to tag the different types of ROIs.

**B.4.1.0.7. Pseudo code** The script in pseudo code is as follows:

1. Create an array of the folders with images
2. For each folder do
3. {
4. Create arrays for ROI descriptions and ROI colors
5. Set ImageJ measurements options to `area perimeter bounding shape feret's skewness redirect=None decimal=3`
6. If required, create sub-folders for Results, Overlays and Coordinates
7. List all images in folder

8. For each image, do
9. [
  10. Open image
  11. If `OnlyOverlay = 0`, do
    - a) Search for associated ROI zip files
    - b) For each ROI zip file, do
      - i. Open ROI zip file
      - ii. For each ROI file, do
        - A. Measure ROI
        - B. Append meta data (File path, Image name, Image extension, ROI description, ROI name)
        - C. Save result table to folder Results as `ImageName_X_Results.txt`
        - D. Export ROI coordinates to folder Coordinates as `ImageName_X_ID.txt`, where ID is the position of the ROI in the zip file.
  12. If ROI description PM exists, do
    - a) For each associated ROI zip file, do
      - i. Open all ROIs in zip file
      - ii. Color ROIs as defined in `ROI colors`
  13. Save `Overlay-ImageName` image in `Overlay` folder
  14. ]
  15. }

## **B.5. Canon G9 and Arduino code**

Google Code, where this project was hosted, has been canceled and data will not be available after 2016. This section contains the listings of the required programs to synchronize a Canon G9 camera with an Arduino based shutter, based on a system described in my Diploma Thesis. The program was improved to allow increased complexity in light pulse protocols.

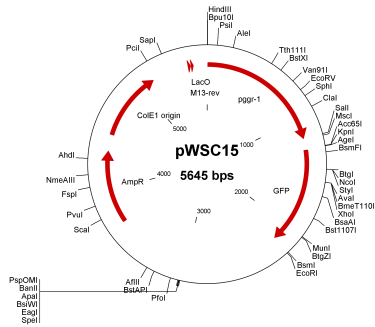
### **B.5.1. Canon G9 code**

The Canon G9 requires the freeware firmware from canon hack development kit (CHDK), a copy is included in the digital material accompanying this thesis. Furthermore, a simple script for either take still images or movies has to be loaded in the CHDK menu.

### **B.5.2. Arduino code**

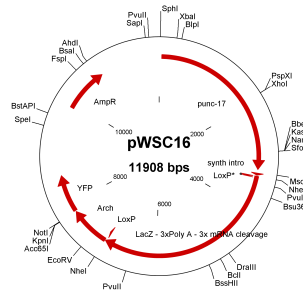
The Arduino based shutter requires the program WormNudger for operation. This program requires the common libraries "Servo", "LiquidCrystal" and "stdio", as well as the deprecated library "Buttons", a copy of the latter is included in the digital material accompanying this thesis.





charts/pWSC15.PNG

Figure C.3.: pWSC15 plasmid chart.

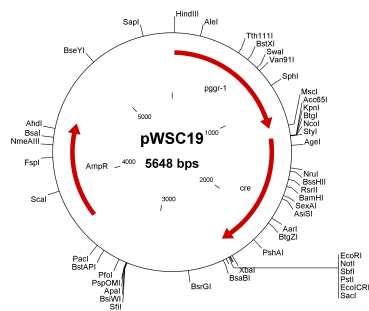


charts/pWSC16.PNG

Figure C.4.: pWSC16 plasmid chart.

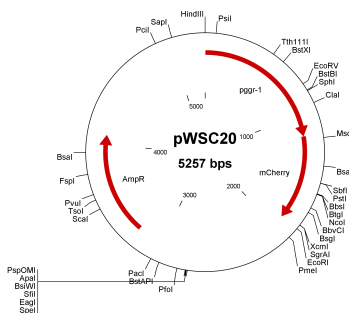






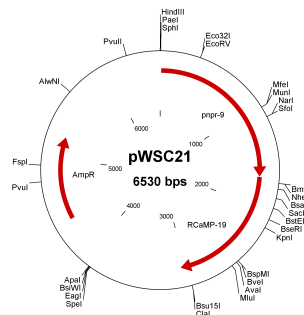
charts/pWSC19.PNG

Figure C.7.: pWSC19 plasmid chart.



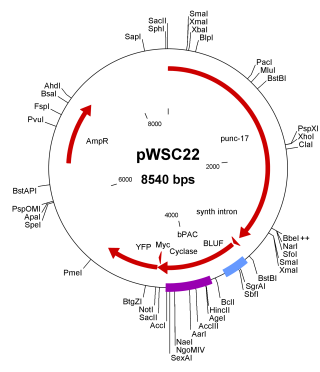
charts/pWSC20.PNG

Figure C.8.: pWSC20 plasmid chart.



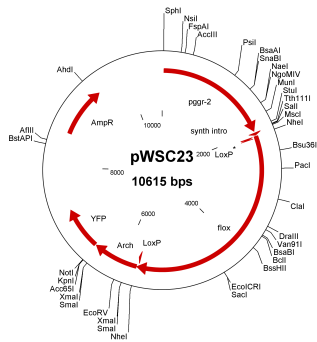
charts/pWSC21.PNG

Figure C.9.: pWSC21 plasmid chart.



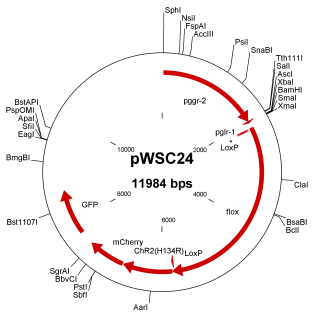
charts/pWSC22.PNG

Figure C.10.: pWSC22 plasmid chart.



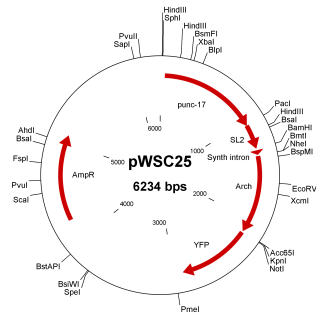
charts/pWSC23.PNG

Figure C.11.: pWSC23 plasmid chart.



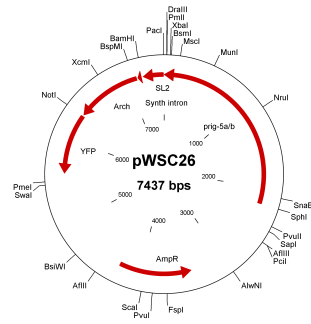
charts/pWSC24.PNG

Figure C.12.: pWSC24 plasmid chart.



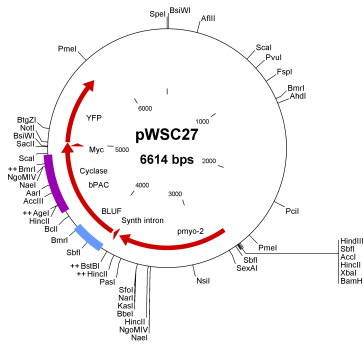
charts/pWSC25.PNG

Figure C.13.: pWSC25 plasmid chart.



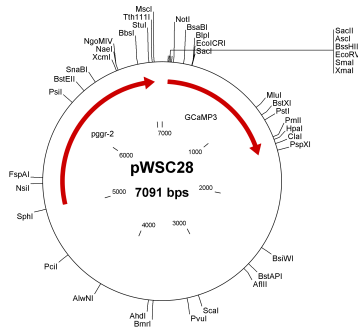
charts/pWSC26.PNG

Figure C.14.: pWSC26 plasmid chart.



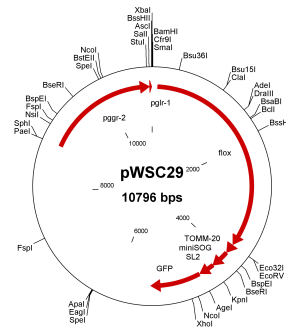
charts/pWSC27.PNG

Figure C.15.: pWSC27 plasmid chart.



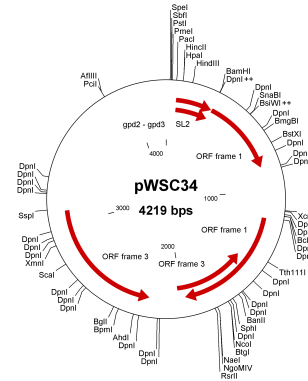
charts/pWSC28.PNG

Figure C.16.: pWSC28 plasmid chart.



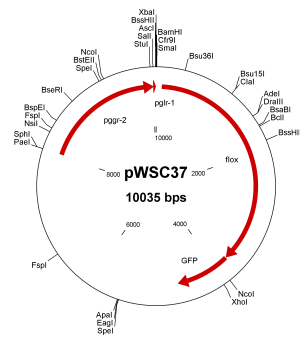
charts/pWSC29.PNG

Figure C.17.: pWSC29 plasmid chart.



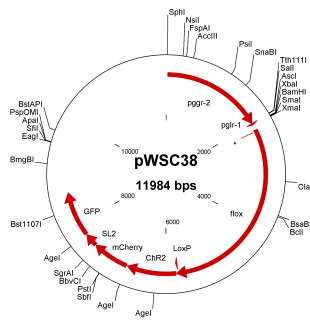
charts/pWSC34.PNG

Figure C.18.: pWSC34 plasmid chart.



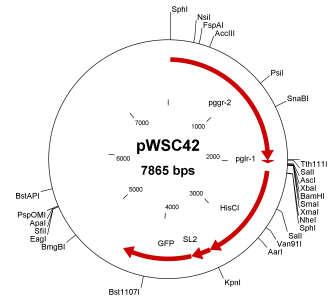
charts/pWSC37.PNG

Figure C.19.: pWSC37 plasmid chart.



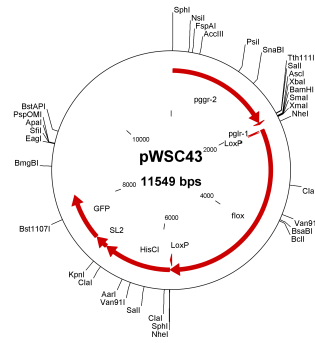
charts/pWSC38.PNG

Figure C.20.: pWSC38 plasmid chart.



charts/pWSC42.PNG

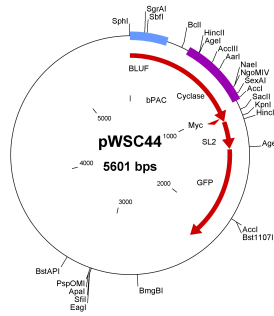
Figure C.21.: pWSC42 plasmid chart.



charts/pWSC43.PNG

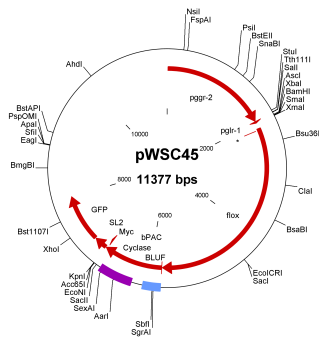
Figure C.22.: pWSC43 plasmid chart.





charts/pWSC44.PNG

Figure C.23.: pWSC44 plasmid chart.



charts/pWSC45.PNG

Figure C.24.: pWSC45 plasmid chart.

## D. Publications and personal involvement

List of publications published during this thesis with a brief description of my personal involvement in each project.

1. In Husson *et al.* (2012) [486], I improved a *C. elegans* behavior tracker [515] by adding the capability of applying light stimulus for optogenetic applications as well as a graphical user interface. I also performed video acquisition and analysis of behavior in animals with ChR2 expressed in PVD mechanosensory neurons.
2. In Husson *et al.* (2013) [516], I co-authored a review on current behavior trackers for *C. elegans*.
3. In Bazzone *et al.* (2013) [517], I tested the feasibility of *C. elegans* neuronal cell culture analysis by solid supported membrane electrophysiology. Results were not published, only an introduction to the method with proteoliposomes was shown.
4. In Kittelmann *et al.* (2013) [397], I helped analyze data as well as automated a workflow for electrophysiology data analysis.
5. In Cohen *et al.* (2014) [518], I performed behavior tracking and data analysis of nicotinic acetylcholine receptor subunit mutants.
6. In Costa *et al.* (2014) [510], I authored a manuscript delineating the application of light activatable adenylyl cyclases as optogenetic tools.
7. In Schüler *et al.* (2015) [512], I created a semi-automated workflow for analysis of pharyngeal pumping frequency based on an artificial neuronal network.

# Acknowledgments

**Prof. Dr. Alexander Gottschalk** Thank you for allowing me to work in such an exciting thesis project and giving me the academic freedom to pursue my own ideas. The RIS project would have never been one without this long lasting incentive. I appreciate all the scientific discussions and the mentoring as well as the help in crafting my scientific career.

**Prof. Dr. Martin Grininger** Thank you for being the second referee of my thesis, the scientific career advices as well as the amusing conversations every now and then.

**Anke Hermann, Caspar E. Glock, Jonas P. Weil, Lisa Gottschlich, Marlene Steiener, Ulf Einsfelder** Thank you for selecting me as your adviser during your laboratory rotations. I learned a lot from you and will definitely remember of the long hours to get to: gonad recombination as last resort; three guys tracking a neuron and watching it go live; cloning pain and lots of laughs about the cactus; achieving single cell expression for the first time; generating cross plans in A3 pages and not getting crazy; characterizing weird promoters. Thank you all!

**Petrus van der Auwera, Lukas Anneser** Thank you for joining forces and dedicating your PhD thesis to the RIS project as well. I'll miss the nightly philosophical transactions, the enthusiasm to get things done (and automated!) as well as all the ideas that seemed to sparkle from all over.

**Andrea Wachner, Angela Piater, Karin Schöffner, Kathrin Carlsburg, Susanne Fondacaro** Thank you for the administrative support and all the patience in the world to get some forms back.

**Alexander Hirschhäuser, Alexandra Oranth, Barbara Janósi, Bojana Languille, Christian Schultheis, Christina Schüler, Christine Molenda, Cornelia Schmitt, David Hain, Elisabeth Fischer, Florian Csintalan, Frank Becker, Heike Fettermann, Ivan Alcantara, Jana Liewald, Jatin Nagpal, Karen Erbguth, Kerstin Zehl, Kirill Essine, Marcial Engel, Martin Brauner, Martin Schneider, Mona Höret, Negin Azimi-Hashemi, Oleg Tolstenkov, Sebastian Wabnig, Steven Husson, Szi-chieh Yu, Thilo Henß** Thank you for all the help provided during this work as well as the moments

of joy in the coffee and lunch breaks.

**Can, Mamãe and Tanja** Thank you for the long hours spell checking my work!

**Andre Bazzone, Bianca G. M. Bricio, Björn Weber, Denise E. Kuwabara, Dietmar Janka, Gustavo Barreira, Holger Biehl, Juliana M. R. Moreno, Katharina Barth, Max Witter, Michael R. Costa, Phillip A. B. Galli and Teresa Ulmer** Thank you for the long lasting friendship, you are the best friends one could wish for!

**Eva und Walter** Vielen Dank für eure Unterstützung durch all diese Jahre! Na wollen wir hoffen, dass ich nicht mehr immer so müde bin.

**Ka, Mamãe, Papai, Opapa, Erika e Aires** Muito obrigado por toda a ajuda, por terem sempre confiado em mim e por, mesmo estando tão longe, sempre poder contar com vocês. Espero poder visitar vocês logo novamente! Mamãe, obrigado por segurar as pontas no final!

**Tanja und Cecilia** Danke, dass ihr beide so viel Verständnis in diesen vielen Jahren hattet. Diese Arbeit ist auch zu einem großen Teil nur dadurch entstanden, dass wir viel gemeinsame Zeit aufgeben mussten. Diese Arbeit ist euch beiden gewidmet, denn ohne eure Unterstützung in allen anderen Aspekten des Lebens wäre sie nie beendet worden. Vielen Dank, in Liebe, euer Wagner.

## Personal information

Surname(s) / First name(s)

Address(es)

Email(s)

Nationality(-ies)

Date of birth

Gender

### Steuer Costa, Wagner

Raimundstraße 100, 60320 Frankfurt am Main, Germany

wagner@steuercosta.de

Brasilian, German. Born in São Paulo, SP, Brasil

May 17, 1986

male

## Education and training

2010 – current

Johann Wolfgang Goethe-Universität Frankfurt am Main

PhD in Neurobiology

Supervisor: Prof. Dr. Alexander Gottschalk

2005 – 2010

Diploma in Biochemistry

Johann Wolfgang Goethe-Universität Frankfurt am Main

Mother tongue(s)

Other languages

### Portuguese

English, German, Spanish

## Awards

2012

Hermann-Willkomm-Stiftung

Travel grant received for the EMBO *C. elegans* Neurobiology meeting.

2010 – 2012

QSL Support

Received for continuous work on the organizing the international Genetically Engineered Machine (iGEM) competition team in Frankfurt.

2009 – 2010

eLF2009

Received for continuous work on the eLearning project BioKemika. The financial aid allowed further development of the project to address more students and focus on interdisciplinarity.

2008 – 2009

SeLF2008

SeLF - studentische eLearning-Förderung 2008: Received a financial aid for creating and organizing the project BioKemika.

## Publications

2015

Schüler, C., Fischer, E., Shaltiel, L., **Steuer Costa, W.**, Gottschalk, A. (2015) Arrhythmogenic effects of mutated L-type Ca<sup>2+</sup>-channels on an optogenetically paced muscular pump in *Caenorhabditis elegans*. *Scientific Reports* 5:14427

2014

Cohen, E., Chatzigeorgiou, M., Husson, S. J., **Steuer Costa, W.**, Gottschalk, A., Schafer, W. R., and Treinin, M. (2014) *Caenorhabditis elegans* nicotinic acetylcholine receptors are required for nociception. *Molecular and cellular neurosciences* 59, 85–96

**Steuer Costa, W.**, Liewald, J., and Gottschalk, A. (2014) Photoactivated adenylyl cyclases as optogenetic modulators of neuronal activity. *Methods Mol. Biol.* 1148, 161–175

- 2013 Bazzone, A., **Steuer Costa, W.**, Braner, M., Calinescu, O., Hatahet, L., and Fendler, K. (2013) Introduction to solid supported membrane based electrophysiology. *J Vis Exp*, e50230
- Kittlmann, M., Liewald, J. F., Hegermann, J., Schultheis, C., Brauner, M., **Steuer Costa, W.**, Wabnig, S., Eimer, S., and Gottschalk, A. (2013) In vivo synaptic recovery following optogenetic hyperstimulation. *Proceedings of the National Academy of Sciences* 110, E3007-16

- 2012 Husson, S. J<sup>1</sup>., **Steuer Costa, W.**<sup>1</sup>, Schmitt, C., and Gottschalk, A. (2012) Keeping track of worm trackers. *WormBook*, 1–17

Husson, S. J., **Steuer Costa, W.**, Wabnig, S., Stirman, J. N., Watson, J. D., Spencer, W. C., Akerboom, J., Looger, L. L., Treinin, M., Miller, D. M., Lu, H., and Gottschalk, A. (2012) Optogenetic Analysis of a Nociceptor Neuron and Network Reveals Ion Channels Acting Downstream of Primary Sensors. *Current Biology*

## Conference presentations

- 2016 Poster – Berlin, DE – Fast optogenetic cAMP modulation of neurotransmission via neuropeptide signals & synaptic vesicle loading
- 2015 Poster – Frankfurt, DE – Optogenetic cAMP-mediated modulation of cholinergic transmission involves neuropeptide signaling and synapsin-dependent SV mobilization
- 2014 Oral – Madison, WI, USA – Effect of cAMP on behavior and synaptic morphology
- 2013 Oral – Heidelberg, DE – Enhancement of cholinergic output in *C. elegans* by bPAC
- Poster – Göttingen, DE – Enhancement of cholinergic output in *C. elegans* by the *Beggiatoa sp.* photo-activatable adenylyl cyclase
- 2012 Poster – Heidelberg, DE – bPAC, a new photo-activatable adenylate cyclase as an optogenetic tool in *C. elegans*
- 2009 Poster – Cambridge, UK – Optogenetics tools to dissect a nociceptive neuronal network and neuropeptide signalling pathways in *C. elegans*

---

<sup>1</sup>both authors contributed equally